Advances in Civil Engineering

Bamboo/Wood Composites and Structures

Lead Guest Editor: Dongsheng Huang
Guest Editors: Minjuan He and Ying Hei Chui

Bamboo/Wood Composites and Structures

Advances in Civil Engineering

Bamboo/Wood Composites and Structures

Lead Guest Editor: Dongsheng Huang
Guest Editors: Minjuan He and Ying Hei Chui

Contents

Experimental Study on an Innovative Hollow Concrete Floor System Assembled with Precast Panels and Self-Thermal-Insulation Infills
Liang Gong, Zhongfan Chen, Yan Feng, Sihan Ruan, and Liuhui Tu
Research Article (13 pages), Article ID 6663412, Volume 2021 (2021)

A Review of the Methods for Predicting the Effective In-Plane Shear Modulus of Cross-Laminated Timber (CLT)
Mehsam Tanzim Khan, Ying Hei Chui, and Dongsheng Huang
Review Article (15 pages), Article ID 6616559, Volume 2021 (2021)

Temperature and Stress Effects on the Compressive Creep Behavior of Parallel Strand Bamboo
Yanyan Liu, Yulin Bian, Dong He, Jiao Liu, and Aiping Zhou
Research Article (9 pages), Article ID 6637572, Volume 2021 (2021)

Research on the Seismic Performance of Straw Panel-Infilled Concrete Frame by Shaking Table Test
Jia Zhu, Yuling Bian, and Aiping Zhou
Research Article (12 pages), Article ID 6669967, Volume 2021 (2021)

Mechanical Properties and Strength Grading of Engineered Bamboo Composites in China
Siyuan Tang, Aiping Zhou, and Jiannan Li
Research Article (13 pages), Article ID 6666059, Volume 2021 (2021)

Sustainability Design Considerations for Timber-Concrete Composite Floor Systems
Md Abdul Hamid Mirdad, Hossein Daneshvar, Thomas Joyce, and Ying Hei Chui
Research Article (11 pages), Article ID 6688076, Volume 2021 (2021)

Cyclic Behavior and Modeling of Bolted Glulam Joint with Cracks Loaded Parallel to Grain
Jing Zhang, Zhi-Fang Liu, Yong Xu, Mai-Li Zhang, and Liu-Cheng Mo
Research Article (16 pages), Article ID 6612886, Volume 2021 (2021)

An Inelastic Theoretical Model regarding the Load-Carrying Capacity of PSL Bending Component
Baolu Sheng, Yuling Bian, Dong He, and Aiping Zhou
Research Article (8 pages), Article ID 6677450, Volume 2021 (2021)

Experimental Investigation on the Load-Carrying Capacity of Steel-to-Laminated Bamboo Dowel Connection I: Single Fastener with Slotted-In Steel Plate under Tension
Zhaoyan Cui, Liuhui Tu, Ming Xu, Zhongfan Chen, and Qingfeng Xu
Research Article (10 pages), Article ID 6683589, Volume 2021 (2021)

Bamboo/Wood Composites and Structures Shear and Normal Strain Distributions in Multilayer Composite Laminated Panels under Out-of-Plane Bending
Jan Niederwestberg, Jianhui Zhou, Ying Hei Chui, and Dongsheng Huang
Research Article (15 pages), Article ID 6637853, Volume 2021 (2021)

FE Modeling for Bolted Wood Connection Using a Porous Constitutive Model
Huazhang Zhou and Xiaoqiang Zhou
Research Article (8 pages), Article ID 6621333, Volume 2020 (2020)

Flexural Properties of Steel-Bamboo Composite Slabs in Different Connection Methods
Hui Zhong, Qifeng Shan, Jialiang Zhang, Xiaocun Zhang, and Yushun Li
Research Article (10 pages), Article ID 6639789, Volume 2020 (2020)

Application and Analyzation of the Vision-Based Structure Model Displacement Measuring Method in Cassette Structure Shaking Table Experiment
Wang Yanhua, Wang Cheng, Feng Yan, Dai Bowen, and Wu Gang
Research Article (12 pages), Article ID 8869935, Volume 2020 (2020)

Study on Flexural Behaviour of Box Section Bamboo-Steel Composite Beams
Qifeng Shan, Jialiang Zhang, Keting Tong, and Yushun Li
Research Article (9 pages), Article ID 8878776, Volume 2020 (2020)

Field Test and Simulation Analysis of Thermal Performance of Bamboo Steel Composite Wall in Different Climate Regions
Qifeng Shan, Keting Tong, Xiaocun Zhang, and Yushun Li
Research Article (10 pages), Article ID 8854156, Volume 2020 (2020)

Hindawi
Advances in Civil Engineering
Volume 2021, Article ID 6663412, 13 pages
https://doi.org/10.1155/2021/6663412

Research Article

Experimental Study on an Innovative Hollow Concrete Floor System Assembled with Precast Panels and Self-Thermal-Insulation Infills

Liang Gong,[1,2] **Zhongfan Chen**,[1,2] **Yan Feng**,[1,2] **Sihan Ruan**,[1,2] **and Liuhui Tu**[1,2]

[1]*Key Laboratory of RC&PC Structures of Ministry of Education, Southeast University, Nanjing 210096, China*
[2]*School of Civil Engineering, Southeast University, Nanjing 210096, China*

Correspondence should be addressed to Zhongfan Chen; 101003944@seu.edu.cn

Received 18 November 2020; Accepted 12 July 2021; Published 27 July 2021

Academic Editor: Michael Yam

This paper presents an innovative hollow concrete floor system comprising hollow precast panels and self-thermal-insulation infills. The precast panels are connected by welded reinforcement bars and cast-in-situ concrete joints. To study the vertical load-carrying capacity and the working mechanism of this innovative floor system, a static loading test was carried out on a 1/2 scale model. The specimen consists of six precast slab members, four precast reinforced concrete beams and columns, respectively. Experimental and simulation results related to the crack development and vertical load-carrying capacity were analyzed. It is found that the innovative floor system could meet the capacity requirements of the Chinese code. Furthermore, the crack development of the innovative system shows similar characteristics with the solid floor. To explore the feasibility of the existed analysis methods, the specimen was simulated and compared by nonlinear analysis in ABAQUS. The comparison illustrates that the analogue cross beam method is more accurate and suitable for the simulation of the innovative hollow concrete floor system.

1. Introduction

As a reliable construction building material, concrete could meet the requirements of demanding construction conditions, different shaped structural components, and harsh environment for its mature construction technologies and superior properties [1–3]. With the increasing industrialization and commercialization of civil engineering, the requirements of buildings have converted to large-span structures, which present new challenges to the concrete floor system [4–6].

To eliminate the inherent limits of the traditional concrete floor system and extend its use in modern structures, researchers all over the world have conceived different kinds of effective solutions. The innovations mainly focused on new patterns of floor systems [7].

In the 1960s, Mueller invented the B-Z reinforced concrete cellular plate [8], which is a kind of cast-in-situ concrete hollow slab. Experimental research on this new type of floor was carried out by Franz [9] and the results showed that the stiffness of the hollow floor was equivalent to the solid flat slab. Hendler [10] improved the floor system by inserting a block of foamed plastic in the cavity of the hollow slab. Influential factors, such as the height of the slab, compressive strength of the concrete, and the patterns of the joint, were all carefully investigated. The corresponding calculation methods to estimate the load-carrying capacity and initial stiffness were proposed [11].

In recent decades, the precast concrete structures have become a preferable choice for their prominent advantages, i.e., high efficiency, standardization, and environmental friendliness [12]. In China, several innovative floor systems were also developed to exploit the highest efficiency of precast panels and to meet the requirements of large-span structures [13]. Ma proposed a Vierendeel-sandwich-plate floor system [14], which is comprised of two layers of ribbed reinforced concrete slab connected by reinforced concrete shear keys at the intersection. Through the design and

construction of a real-life project, the feasibility of this new floor system was verified. Other kinds of novel floor systems, i.e., PK prestressed composite slab floor system [15], the assembled monolithic hollow-ribbed floor [16], prefabricated PC floor system [17], and other new systems [18–22], were all investigated, and the results were satisfactory.

This paper presents a new type of floor system, which consists of hollow precast panels, self-thermal-insulation infills, joints with welded reinforcement, and cast-in-situ concrete beams. The hollow panels were prefabricated in the manufacturing factory with two different patterns (Figure 1), which can meet various requirements in actual construction. The self-thermal-insulation infill, i.e., the foam concrete, was inserted in the cavity of the hollow concrete panels to enhance the thermal insulation properties and vertical stiffness at the same time. The precast concrete panels were connected with the cast-in-place joint and welded reinforcements for larger span buildings, as shown in Figure 2. This type of floor system is of the advantages in both mechanical performance and manufacturing efficiency, such as (1) reduced self-weight: the light-weighted foam concrete accounts for 48% of the total volume of the floor, thus it is 44.7% lighter than the same sized solid floor; (2) enhanced floor height: there will be spare room since the bottom plate is flat, and the pipeline can be arranged in the middle of the plate as the equipment layer; (3) superior sound and thermal insulation: the filled lightweight foamed concrete improves the sound and thermal insulation of the floor; (4) high construction efficiency: the prefabrication degree reaches 87.5%, which accelerates the construction speed enormously.

To study the working mechanism of the innovative floor system and verify its effectiveness, a 1/2 scale single-span simply supported floor was tested through a static load experiment. The results related to the crack development, initial stiffness, and vertical load-carrying capacity were analyzed.

2. Experimental Investigation

2.1. Material Properties. The steel rods used in the precast and cast-in-place components are HRB 400, according to GB 50010-2010 [23]. The diameter of the steel bars encompasses four different sizes, i.e., 16 mm, 10 mm, 8 mm, and 3.5 mm. Mechanical properties of the steel bars were tested by the test method of GB/T 228.1-2010 [24]. Results are collected in Table 1.

The concrete is C30 in the columns and beams and C40 in the cast-in-situ joint and the slab, according to GB 50010-2010. Compressive and tensile tests were all performed on the standard cubic specimens sized 150 mm. The material properties are presented in Table 2.

2.2. The Similarity Ratio. Due to the limitation of the test platform, the test specimen was designed in a 1/2 scale. The component's size, load, and additional mass are designed in strict accordance with the similarity theory to ensure the model and the prototype share similar working conditions. For scale models, the relationship between the elastic modulus, density, geometry sizes, and gravitational acceleration is presented as follows:

$$\frac{S_E}{\left(S_g S_p\right)} = S_l, \tag{1}$$

where S_E is the similarity constant of elastic modulus, S_g is the similarity constant of gravity acceleration, S_ρ is the similarity constant of material density, and S_l is the similarity ratio of geometric size.

The material used in the scaled model is identical to those of the prototype; thus, the similarity constant related to material properties is equal to 1. Based on the similarity constant of geometry and material, S_ρ can be calculated as 2. It is impossible to adjust the density without changing its volume for a specific material. To meet the material similarities of both density and mechanics, additional weights were added to the model. Other similarity relationships are all calculated and presented in Table 3.

2.3. Specimen Preparation. A one-storey frame was designed to explore the vertical load-carrying capacity and working mechanism of the innovative hollow concrete floor system. The specimen is presented in Figure 3, comprised of three different components, i.e., the beams, columns, and the innovated hollow slab. The cross section of the four columns is 300 mm × 300 mm, which is designed according to the axial compression ratio in the GB 50011-2010 [25]. The ratio of reinforcement and selection of steel bars (Figure 3) was identical to both the prototype and the requirements in GB 50011-2010. Four beams of 200 mm × 350 mm × 4800 mm were employed to support the floor. Similar to the columns, the reinforcement and size conform to meet a criterion up to the standards.

The location of the cast-in-situ joints was designed according to the original building. There were three post-cast concrete joints in the floor system, including two transverse joints and one longitudinal joint. The longitudinal joint was located in the middle of the span, and the transverse joint was located at 1/3 and 2/3 of the span. The width of the joint was determined to be 200 mm according to the length of the reinforcement connection. Every two adjacent precast panels were connected through welded reinforcement and cast-in-situ concrete joint, as presented in Figure 4. The reinforcement bars were evenly distributed in the concrete joint with a diameter of 8 mm and an average distance of 75 mm, respectively.

The floor system in Figure 5 needs to bear the required area load with limited deflection and crack according to GB 50010-2010, on which static load experiment was conducted.

Before the test, white paint and grids were painted on the bottom surface of the floor to determine the cracking position, and the grid spacing shall be 200 mm. The protective scaffolds were located 100 mm below the bottom of the slab for protection without restricting the free deformation of the floor.

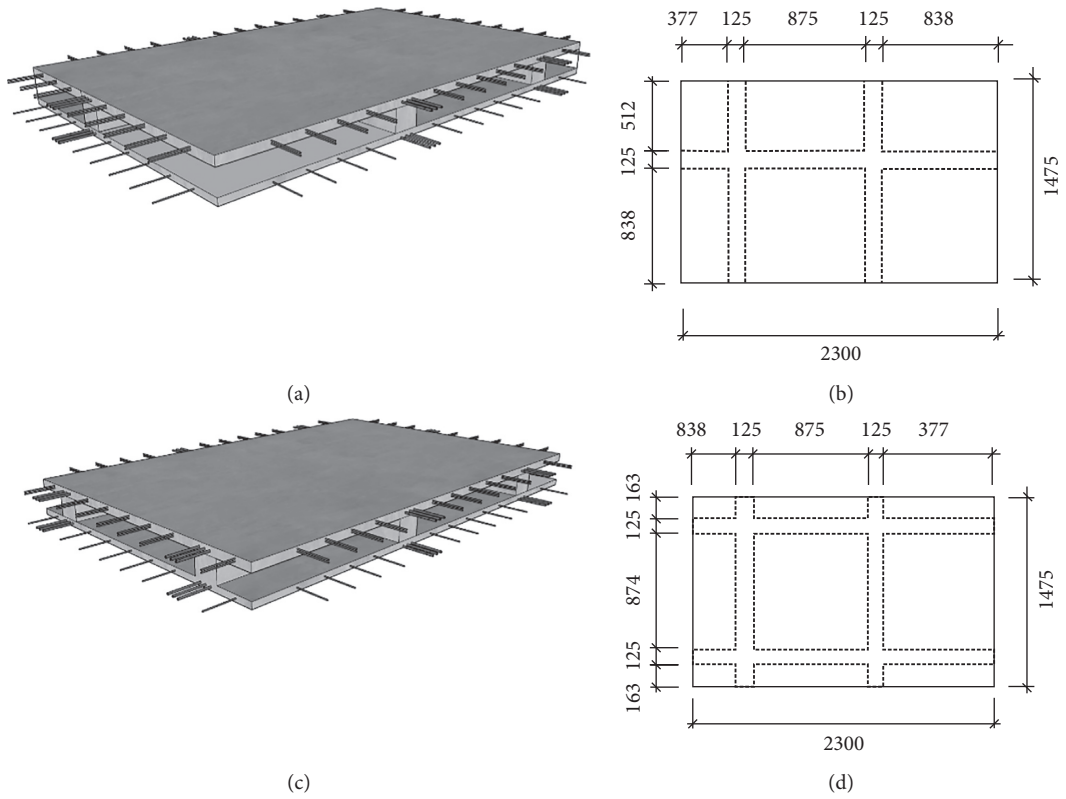

Figure 1: Precast hollow concrete panels: (a) type I; (b) details of type-I panel; (c) type II; (d) details of type-II panel (unit: mm).

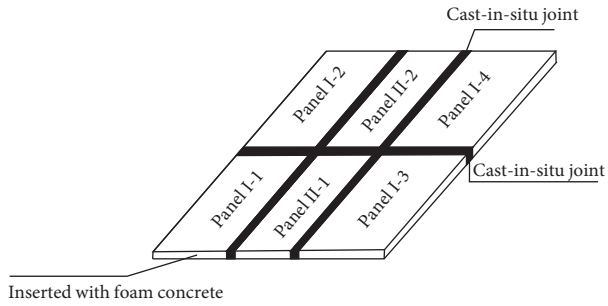

Figure 2: Innovated hollow composite concrete floor system assembled with precast panels and self-thermal-insulation infills.

Table 1: Material properties of steel bars.

Tensile strength	Diameter (mm)	Yield strength (MPa)	Young's modulus (GPa)	Passion ratio
Longitudinal bar in beams and columns	16	386.7	211.19	0.28
Stirrup in beams and columns	10	394.1	209.53	0.28
Longitudinal bar in ribbed beams	8	390.1	209.31	0.28
Stirrup in ribbed beams	8	390.1	210.03	0.28
Longitudinal bar in slab	3.5	306.2	210.57	0.28

Table 2: Material properties of concrete.

Position of the concrete	Compressive strength, f_{cu} (MPa)	Elastic modulus, E_c (MPa)
Concrete in beams and columns	28.5	30500
Concrete in ribbed beams	40.9	32200
Concrete in slab	40.9	32200
Foam concrete	0.5	2550

Table 3: Similarity constant of the specimen.

	Parameter	Dimension	Similarity relationship
Material properties	Strain, σ	FL^{-2}	$S_E = S_\sigma = 1$
	Stress, ε	—	1
	Elastic modulus, E	FL^{-2}	$S_E = 1$
	Passion's ratio, υ	—	1
Geometry	Length, l	L	$S_l = 1/2$
	Displacement, χ	L	$S_\chi = S_l = 1/2$
	Angular displacement, θ	—	1
	Area, A	L^2	$S_A = S_l^2 = 1/4$
	Moment of inertia, I	L^4	$S_I = S_l^4 = 1/16$
Load	Concentrated load, P	F	$S_P = S_E S_l^2 = 1/4$
	Line load, ω	FL^{-1}	$S_\omega = S_E\ S_l = 1/2$
	Area load, q	FL^{-2}	$S_q = S_E = 1$
	Moment, M	FL	$S_M = S_E S_l^3 = 1/8$

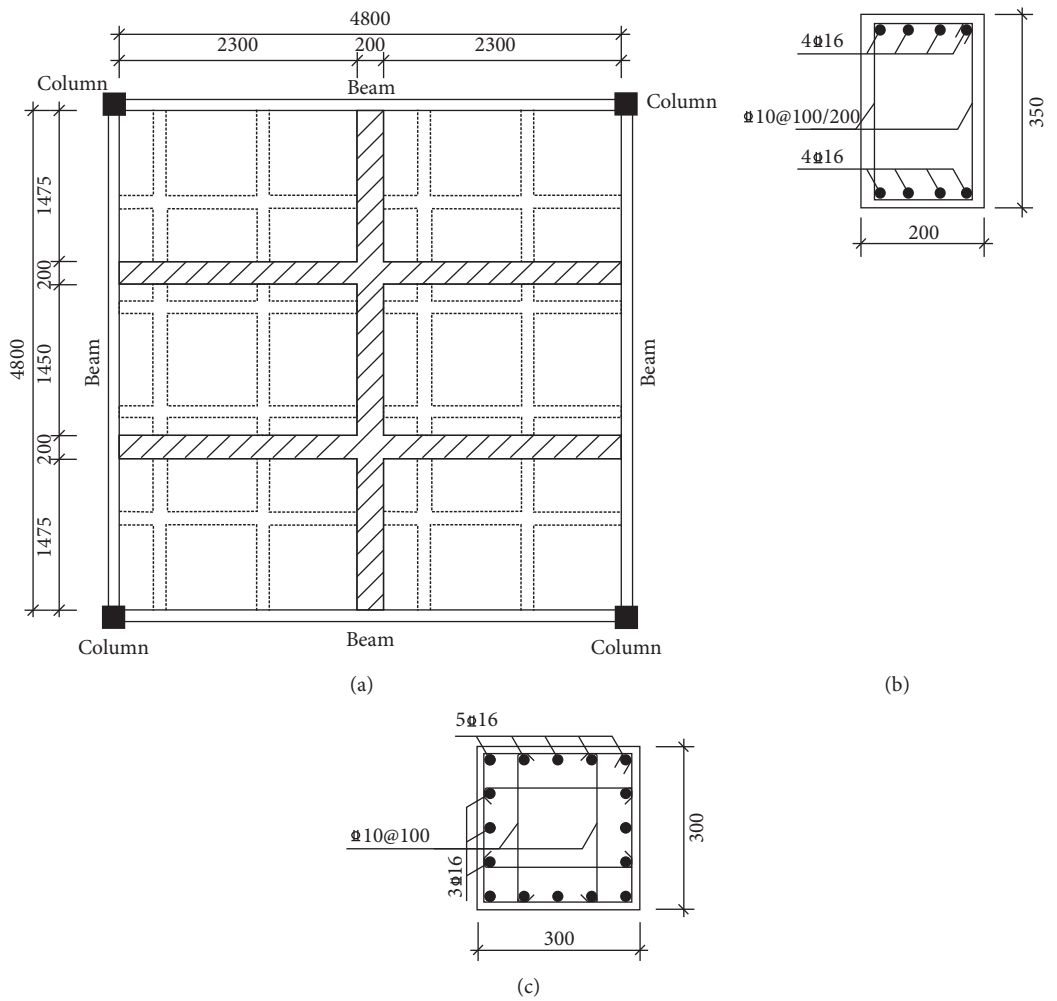

Figure 3: Detailed sizes of the innovated floor specimen: (a) schematic picture of the floor system; (b) beam; (c) column.

2.4. Load Protocol. Table 3 shows that the similarity ratio of stress and strain is equal to 1, indicating that the stain and stress got from the 1/2 scale are identical to those of the prototype. The area load could be directly calculated since $S_q = 1$.

Mass bags were used to exert a uniformly distributed area load on the floor (see Figure 6). The transverse and longitudinal gap between each stack of sandbags was 10 cm, larger than the requirements of GB/T50152-2012 [26] to avoid the arch effect after the deformation of the specimen.

(a) (b)

Figure 4: The joint between two adjacent precast panels. (a) Welded steel bars. (b) Cast-in-situ concrete beam.

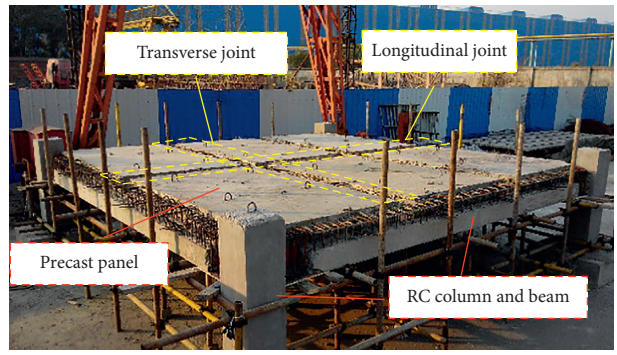

Figure 5: Tested specimen.

Figure 6: Area load exerted of the slab.

Three loading steps are included in the experiment, i.e., preloading, static loading, and unloading. Before the start of the static loading, preloading was conducted to check the stability of the structural support and eliminate the malfunctions of instruments and equipment. The static loading is designed according to the test methods of GB/T50152-2012 with ten main steps. After each stage of loading, the load was maintained for 15–20 minutes. The data collection and crack description were carried out after the structural deformation became stable. After the test, the mass bags on the floor were removed in batch, and the cracking of the concrete on the bottom surface of the floor could be observed after complete unloading.

The loading protocol is presented in Table 4.

2.5. Sensor Distribution. Three types of sensors, i.e., the displacement transducer, the strain gauges, and the crack width observation instruments, were used during the test. The deformation of the slab was monitored with displacement transducers arranged as Figure 7. Due to the symmetry of the structure, the displacement meters were distributed on the 1/4 side of the floor area.

The strain of steel bars was recorded with 2 mm × 1 mm strain gauges. The layout of strain gauges mainly focused on the comparison of strain along the ribbed beam at different

Table 4: Load protocol of the experiment.

Load grade no.	Area load (kN/m^2)	Accumulated area load (kN/m^2) (MPa)	Last time (min)
0	2.66	2.66	—
1	0.94	3.6	15–20
2	0.94	4.54	15–20
3	0.78	5.32	960
4	0.94	6.26	15–20
5	0.94	7.20	120
6	0.94	8.14	15–20
7	0.94	9.08	15–20
8	0.94	10.02	15–20
9	0.94	10.96	15–20
10	0.94	11.9	15–20
11	0.94	12.84	15–20

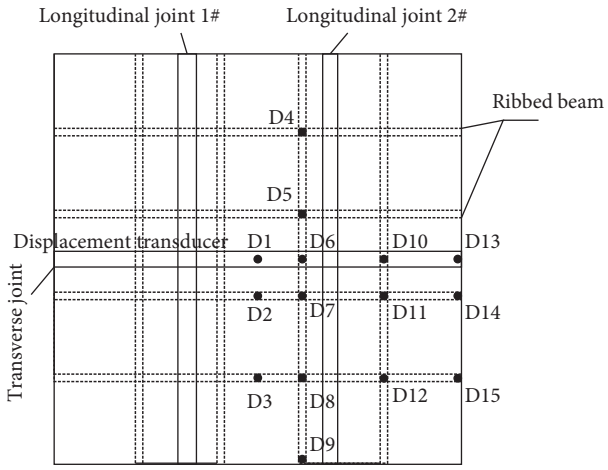

Figure 7: Arrangement of displacement transducers on the bottom surface.

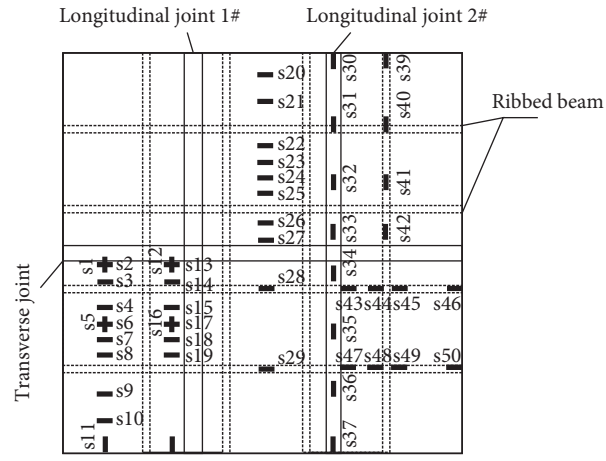

Figure 8: Layout of the strain gauges on steel bars.

positions and their differences with the others, as presented in Figure 8. The gauges were fixed on the steel bar before the cast of concrete. Glue and bandage were applied to the gauge and the outer layer of the conductor to avoid damage during concrete pouring.

To explore the stress development of the floor under different loads for later theoretical and numerical analysis, concrete strain gauges (8 mm × 2 mm) were arranged on the top and bottom surface of the floor. Figure 9 illustrates the layout of strain gauges on the concrete slab.

3. Experimental Results

3.1. Experimental Observation. The deflection and crack development were monitored and logged while loading, which can be concluded as follows.

At the initial loading stages, the deflection in the middle of the slab increased with the load. No cracks were found at other parts of the slab bottom except for some shrink fractures. When the load reached 6.26 kN/m^2 (the 4th load), a small number of tiny cracks parallel to the direction of the joint appeared on the interface between the new and old concrete. The cracks mainly appeared in the middle of the joint.

With the accumulated load increasing from 6.26 kN/m^2 to 8.14 kN/m^2, the cracks parallel to the longitudinal interface of the joint furtherly developed and extended to the transverse direction. The interfaces between the new and old concrete of the longitudinal joint cracked, and the maximum width was about 0.2 mm.

When the 7$_{th}$ area load reached 9.08 kN/m^2, almost all the surfaces of the joints cracked and slight cracks appeared at the bottom of the grid plate near the middle of the span. There were no cracks on the floor at the non-joint position. And the area load is slightly greater than the normal use load, which is 8.5 kN/m^2 according to GB 50009-2012. Thus, the maximum crack met the requirements of normal use.

After the area load of the slab reached 10.02 kN/m^2 (8$_{th}$ load), the cracks on the precast slab occurred. Most of the cracks were located near the diagonal line and no cracks were found at the bottom of the rib beam. When the load increased to 10.96 kN/m^2 (9$_{th}$ load), several diagonal cracks developed in the middle of the floor and passed through the bottom of the rib beam. When the load reached 11.9–12.84 kN/m^2, a large number of cracks appeared in the middle of the span. The width of one crack increased to approximately 1.5 mm, which forced the loading process to stop due to security reasons.

The load in the experiment was greater than the requirements of both normal use and ultimate loading capacity according to GB 50009-2012, which verified the

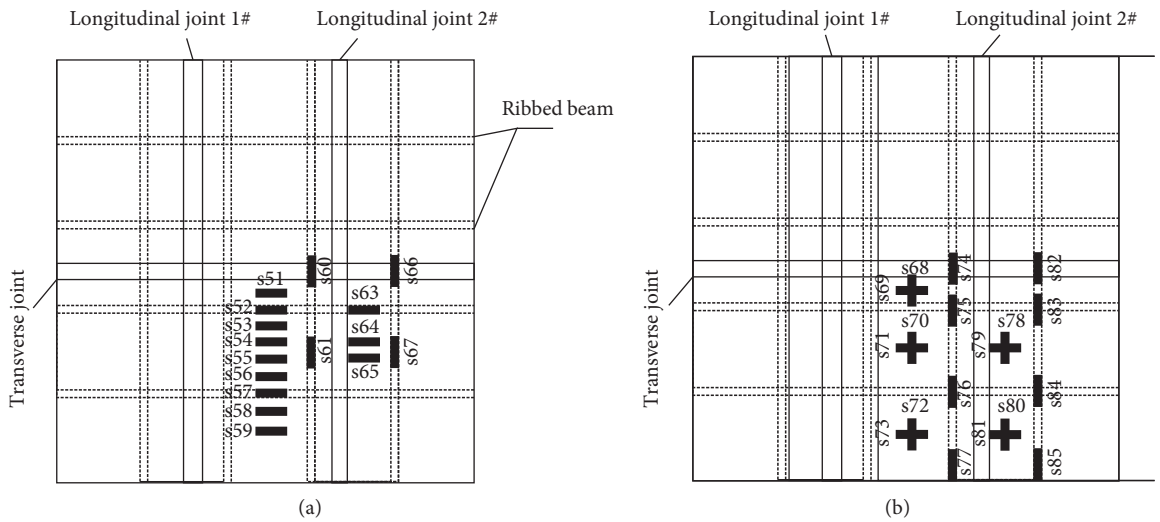

Figure 9: Layout of the strain gauges on concrete slab: (a) top surface; (b) bottom surface.

effectiveness and practicability of this innovative floor system. It can be observed that the main crack of the concrete is X-shaped (Figure 10), which is similar to that of the solid floor [27, 28]. The initial cracks occurred mainly in the joints, indicating the interfaces of cast-in-situ joint and precast panels are still the weaker section. Besides that, it is suggested to improve the bond performance of concrete at the joint and increase the roughness of concrete at the joint.

3.2. Load-Deflection Relationship. The load-deflection curve of the innovative floor system is presented in Figure 11(a), where the deflection is obtained from the D1 displacement transducer, and the area load is from the accumulated mass bags. Other displacement transducers present a similar increase trend. Figure 11(b) shows the deflection of displacement transducers along the ribbed beam, which contains the logged data along the cast-in-situ concrete joint.

It can be found that the innovative floor system basically meets the requirements of engineering application. Under the area load of 12.84 kN/m^2, the maximum deflection of the floor is 15.75 mm, which meets the deflection limit $L/300$ according to GB 50010-2010.

3.3. Stress Distribution. The stress distribution of the bottom surface of the concrete slab is illustrated in Figure 12(a). It is found that the compressive strains on the top surface of the concrete slab are all less than 800 $\mu\varepsilon$, within elastic range. Part of the tensile strains exceeded the elastic limit of 300 $\mu\varepsilon$, resulting in the crack in the bottom surface of the concrete slab. The strain increased with the area load. The strain gauges were mainly arranged in the steel rods of the bottom layer, of which the maximum strain is shown in Figure 12(b). The steel rods in the middle position approximately reached the softening stage, which verifies the rational reinforcement ratio of the design.

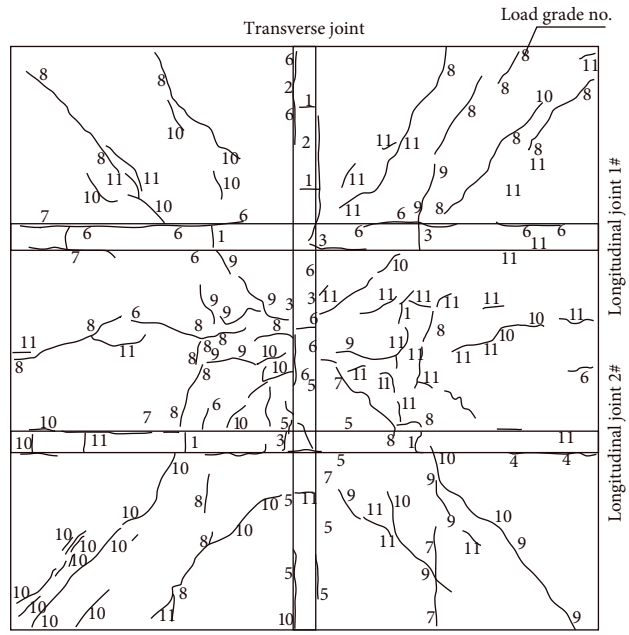

Figure 10: The cracks on the bottom surface of the slab.

4. Comparison of the Load-Deflection Relationship with Existing Methods

Two different calculation methods according to JGJ/T 268-2012 [29], i.e., analogue cross beam method and analogue slab method, were used for both cast-in-situ slab and assembled slab. By simplifying the hollow slab into beams or thinner slab through specific principles, the maximum deflection under the design load could be calculated. The innovative floor system has no related research. Even though the corresponding limit conditions should be met when using these formulas to calculate the bearing capacity, there are still many reasonable hypotheses and empirical relationships regarding the load-carrying capacity that is worth consulting. In this section, the feasibility of the existing

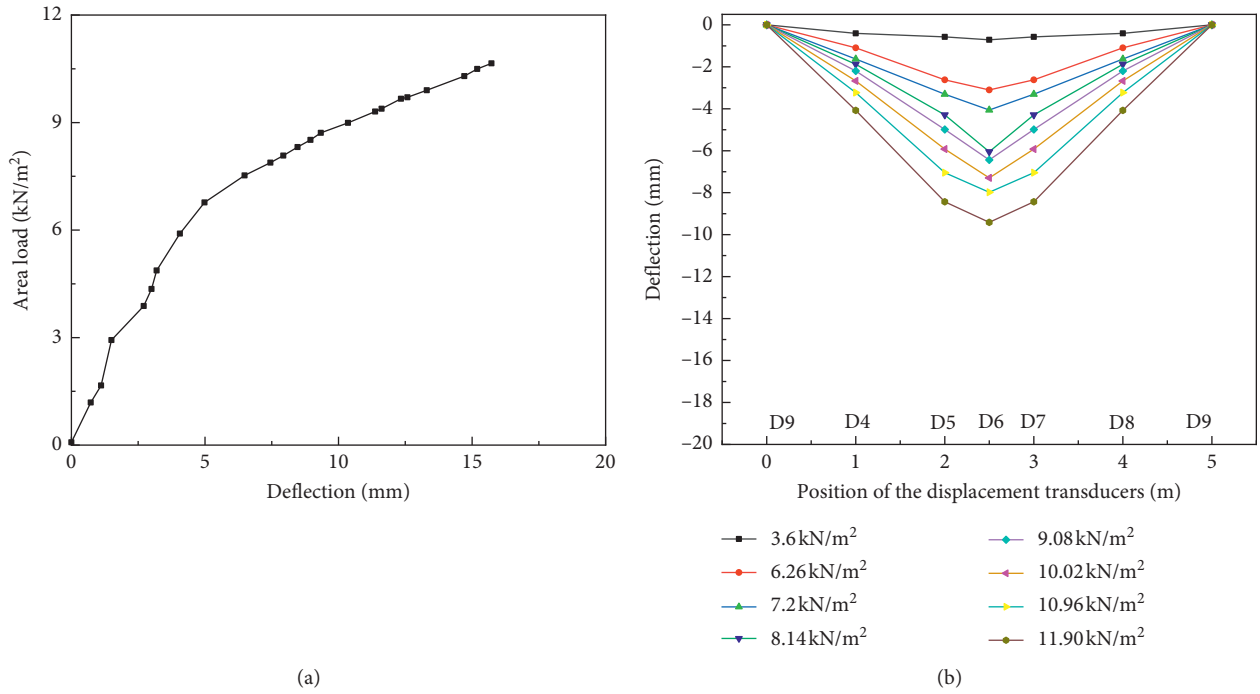

Figure 11: Experimental results: (a) load-deflection relationship of D1; (b) deflection along the ribbed beam under different area loads.

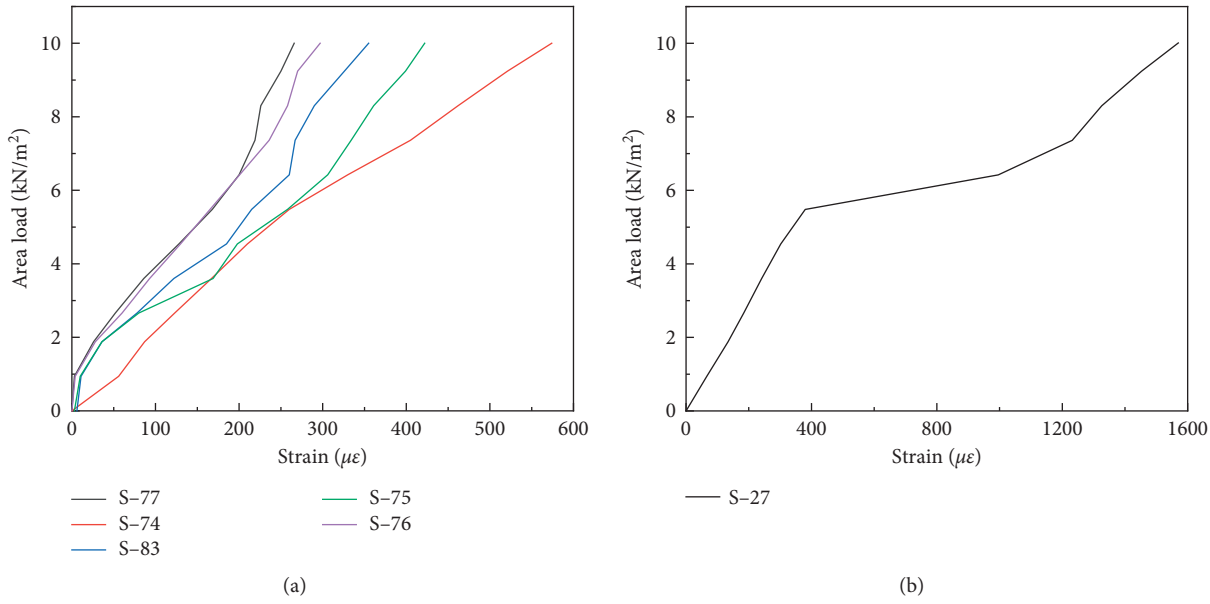

Figure 12: Strains of concrete and steel rods recorder in the test: (a) strain on the concrete of the top surface; (b) strain of the steel rods in the bottom layer.

designed methods was compared based on the experimental results.

4.1. Introduction of Existing Design Methods. Equations (2) and (3) present the calculation method for the analogue cross beam method (Figure 13) and analogue slab method (Figure 14), respectively. For the analogue cross beam method, the continuous slab is simulated by some scattered beams (the number should be larger than 5) with the same span. The sizes of the analogue cross beam are calculated with the principles that (1) the transformed beams share the same bending stiffness with the hollow slab and (2) the heights of the slab and beam remain identical; thus, the width can be calculated as follows:

$$b_b = \frac{I}{I_0} b_0, \tag{2}$$

where b_b is the width of the analogue cross beam, the hollow slab is divided into serval average slab strips, b_0 represents the width of the hollow slab strips, I is the moment inertia of

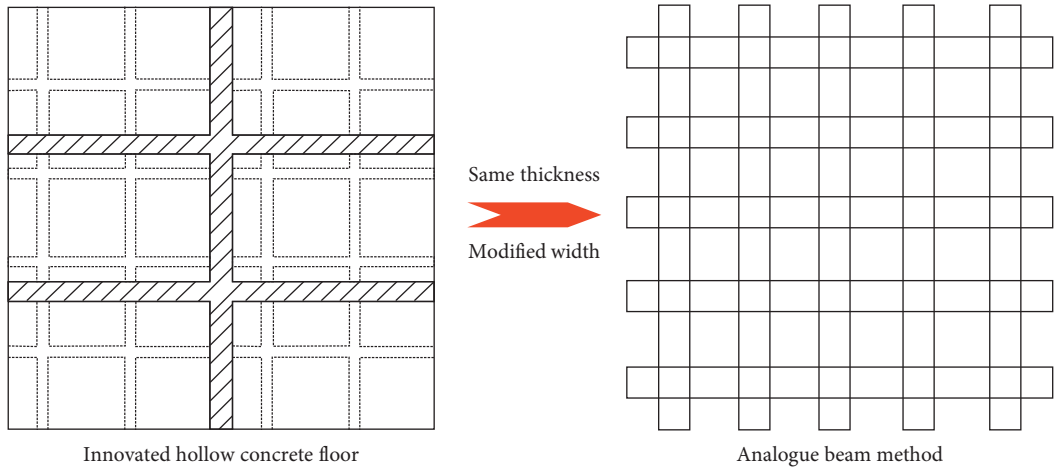

Figure 13: Schematic picture of analogue beam method.

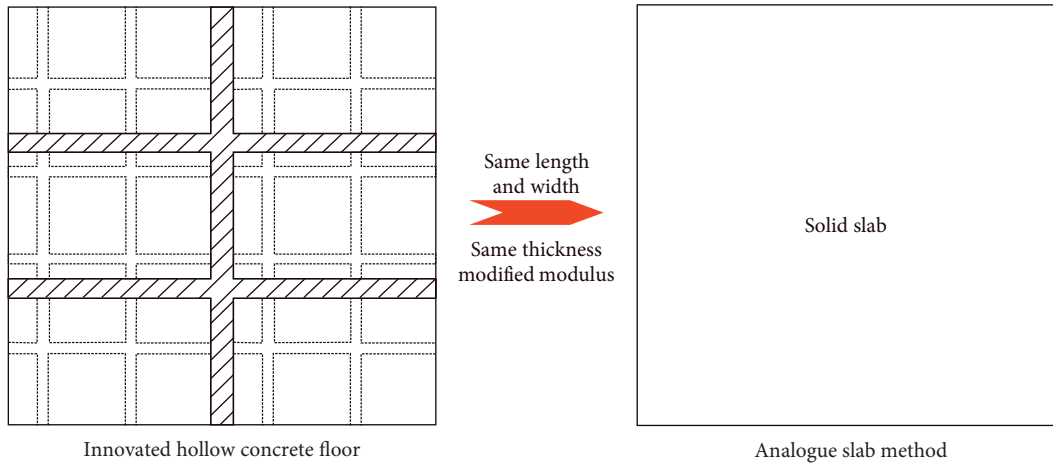

Figure 14: Schematic picture of analogue slab method.

the analogue cross beam, and I_0 stands for the moment inertia of the hollow slab.

For the analogue slab method, the hollow concrete slab is simulated with a solid slab of the same thickness and rectified modulus of concrete. When using the analogue slab method, the requirements are that (1) the distance between ribbed beams should be larger than 2 b_0, and (2) if the difference of the two-way stiffness of concrete hollow floor can be ignored, it should be calculated as isotropic slab; otherwise, it needs to be calculated as an anisotropic slab. The modulus of the concrete and infills when calculated as the isotropic slab is calculated through the formulas below:

$$E = \frac{I}{I_0} E_c, \tag{3}$$

where E is the modified modulus of the analogue slab and E_0 is the modulus of the concrete and infills.

4.2. Discussion of Feasibility of Existing Design Methods. To simulate the nonlinear behavior of the innovated floor system, analogue beam and slab methods are all calculated in ABAQUS, where the mechanical parameters of concrete and steel rods in Tables 1 and 2 are used. And the sizes of the calculated models are strictly identical to the calculation results presented in Table 5.

Detailed sizes of the innovative floor system in ABAQUS are the same as those in Figure 3. As aforementioned, the foam concrete works as infills to improve the heat insulation of the floor. Thus, only the elastic modulus of the foam concrete in Table 2 is adopted to define their orthogonal characteristics in the linear elastic stage. While the behavior of concrete and steel bars in other parts turns out to be in the range of elastic-plastic, the whole life stage, i.e. elastic stage, softening stage, and strengthening stage, should be included in the strain-stress relation. Figures 15–17 illustrate the stress and strain relations of foam concrete, steel bars, and C30 concrete, respectively. The finite element model and its corresponding mesh are shown in Figure 18.

The element type of C3D8R (three-dimensional eight-node linear brick elements with reduced integration) in ABAQUS was chosen to simulate the large deformation of slab. The four corners are all hinged to simulate the boundary of the experiment.

Table 5: Detailed information and simulation results of the analogue slab and beam methods.

Calculation methods	Modified width (mm)	Modified modulus (MPa)	Number of beams
Analogue cross beam method	700	—	5
Analogue slab method	—	20700	—

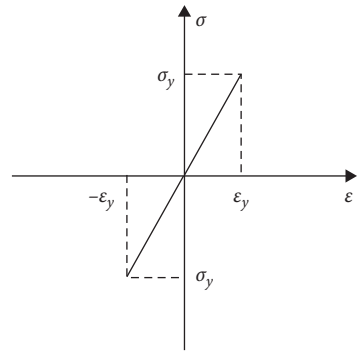

Figure 15: Strain-stress relationship of foam concrete.

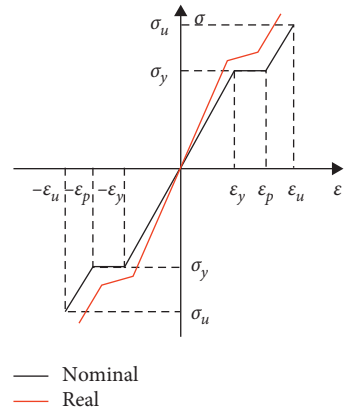

Figure 16: The strain-stress relationship of steel bars.

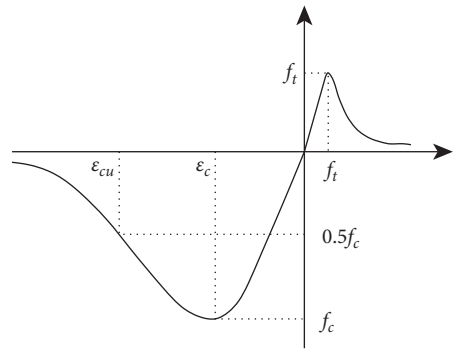

Figure 17: Strain-stress relationship of concrete.

The simulation results are collected in Figure 18; it is observed that the analogue cross beam method and analogue slab method present similar deformation patterns, where the maximum deflection is of little difference. The initial stiffnesses of the two analogue methods are all greater than the experimental results, which reveals that the calculation methods in JT/G 268-201 are conservative enough. The load-deflection curves of the experimental results were compared with those of analogue cross beam and slab method, which is presented in Figure 19.

Compared with the analogue slab method, the maximum deflection in the analogue cross beam method is 11.03 mm, which is +3.6% greater than the experimental results. The initial stiffness of the innovative floor system is recognized as

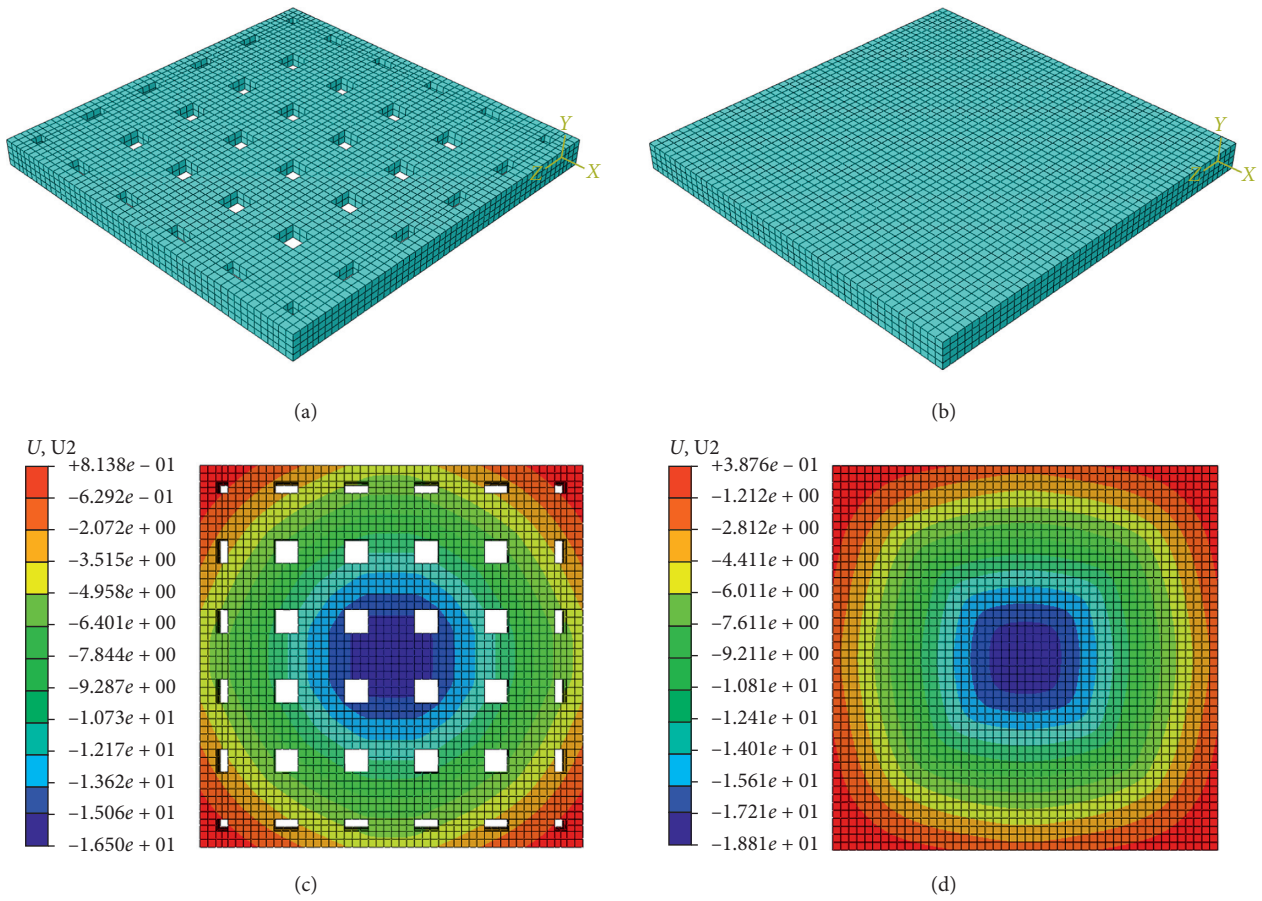

Figure 18: Finite element models and simulation results: (a) finite element model of analogue cross beam method; (b) finite element model of analogue slab method; (c) simulation results of the analogue cross beam method; (d) simulation results of the analogue slab method.

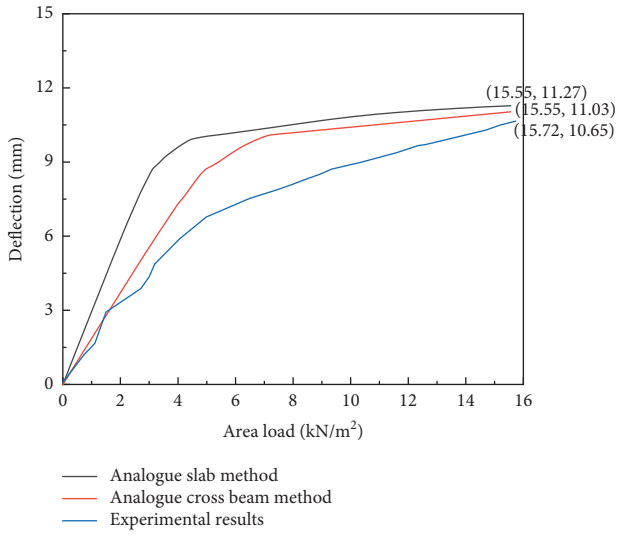

Figure 19: Comparison of the load-deflection relationship between the experiment and analogue methods.

the tangent of the load-deflection curve. And the absolute error of the initial stiffness between the experiment and the analogue cross section method is less than 12%, which is more accurate than that of the analogue slab method. From the analysis above, the conclusion is that the analogue cross beam method according to the JT/G 268-201 is more suitable for the prediction of deflection and initial stiffness in both elastic and elastoplastic stages.

5. Conclusions

To test the load-carrying capacity and working mechanism of an innovative floor system, a vertical static loading test and finite element analysis of a 1/2 scale floor model were conducted. Based on experimental and analytical results, the following conclusions can be drawn:

(1) The innovative floor system meets the requirements of the engineering application. Under the area load of 12.67 kN/m^2, the maximum deflection of the floor is 15.75 mm, which meets the deflection limit $L/300$ under the normal service limit. Besides that, the maximum strains of steel rods and compressive concrete are both within elastic range. The experimental results all indicate that the innovative floor is safety enough in both load-carrying capacity and deflection.

(2) The development of cracks firstly occurred in the bottom of the joints, while the final distribution of cracks in the bottom of the test floor is identical to

that of the solid floor. Thus, the following can be concluded:

(a) The stress distribution of the new floor system is similar to that of the solid two-way slab floor
(b) The joint is still the weaker section, where the bond performance and roughness of the interface between the cast-in-situ concrete and precast panels should be improved

(3) Two different kinds of simulation methods, i.e., the analogue cross beam method and the analogue slab method, were conducted to explore their efficiency in evaluating nonlinear behaviors. The analogue cross beam method is more accurate and more suitable, where the absolute error of maximum deflection is less than 5%.

Data Availability

The XLSX data used to support the findings of this study are available from the corresponding author upon request.

Conflicts of Interest

The authors declare that there are no conflicts of interest regarding the publication of this paper.

Acknowledgments

The study was supported by the National Key Research and Development Project (2018YFC1100402-05) and the National Natural Science Foundation of China (52078120) which are gratefully acknowledged.

References

[1] D. Ding, *Calculation of Reinforced Concrete Floor*, Press of science and technology, Shanghai, China, 1954, in Chinese.
[2] P.-C. Aitcin, "Concrete structure, properties and materials," *Canadian Journal of Civil Engineering*, vol. 13, no. 4, p. 499, 1986.
[3] R. B. Fleischman, C. J. Naito, J. Restrepo, R. Sause, and S. K. Ghosh, "Seismic design methodology for precast concrete diaphragms part 1: design framework," *PCI Journal*, vol. 50, no. 5, pp. 68–83, 2005.
[4] D. Arditi, U. Ergin, and S. Günhan, "Factors affecting the use of precast concrete systems," *Journal of Architectural Engineering*, vol. 6, no. 3, pp. 79–86, 2000.
[5] G. Polat, "Factors affecting the use of precast concrete systems in the United States," *Journal of Construction Engineering and Management*, vol. 134, no. 3, pp. 169–178, 2008.
[6] Q. Jiang, K. Zhang, Y. Feng, X. Chong, and J. Huang, "Out-of-plane flexural behavior of full precast concrete hollow core slabs with lateral joints," *Structural Concrete*, vol. 21, no. 5, 2020.
[7] S. C. Wang, C. S. Wang, Q. Wang, X. F. Tian, and L. Duan, "Flexural behaviors of full-scale prestressed concrete hollow slab girders with composite strengthening," *Journal of Traffic and Transportation Engineering*, vol. 18, no. 2, pp. 31–41, 2018.
[8] G. Fertigteil-Vertrieb, *B-Z Reinforced Concrete Cellular Plate for One-Way and Two-Way Stress Directions for High Loads and Large Span*, Engineering Design Brochure, Mannheim, Germany, 1965.
[9] G. Franz, *Test Report Extract on A Model of The Cellular Flat Plate*, South China University of Technology, Taipei, Taiwan, 1965.
[10] E. H. Hendler, "Cellular flat plate construction," *Journal Proceedings*, vol. 65, no. 2, pp. 81–86, 1968.
[11] K. S. Elliott, "Experimental and theoretical investigation of precast concrete hollow-cored slabs used as horizontal floor diaphragms," *Magazine of Concrete Research*, vol. 66, no. 12, pp. 585–602, 2014.
[12] L. Chung, S.-H. Lee, S.-H. Cho, S.-S. Woo, and K.-K. Choi, "Investigations on flexural strength and stiffness of hollow slabs," *Advances in Structural Engineering*, vol. 13, no. 4, pp. 591–601, 2010.
[13] E. H. Fahmy, Y. B. I. Shaheen, M. N. Abou Zeid, and H. M. Gaafar, "Ferrocement sandwich and hollow core panels for floor construction," *Canadian Journal of Civil Engineering*, vol. 39, no. 12, pp. 1297–1310, 2012.
[14] A. A. Yee and D. Hon, "Structural and economic benefits of precast/prestressed concrete construction," *PCI Journal*, vol. 46, no. 4, pp. 34–42, 2001.
[15] Y. Huang, K. Ma, H. Zhang, J. Xiao, and S. Jiang, "Study and application of Vierendeel-sandwich-plate floor framing in multistoried and tall building," *Journal of Building Structures*, vol. 18, no. 6, pp. 55–64, 1997.
[16] Y. Pan, "Study of load-bearing properties of PK prestressed composite slab," Master dissertation, University of Hunan, Changsha, China, 2009, in Chinese.
[17] W. Niu, "Experimental and theoretical study on waffle hollow-core composited floor," Master dissertation, University of Hunan, Changsha, China, 2009, in Chinese.
[18] R. Pang, "Research on the mechanical property and seismic design method of new type precast RC diaphragms," Master dissertation, Southeast University, Nanjing, China, in Chinese.
[19] C. Naito, L. Cao, and W. Peter, "Precast concrete double-tee connections, part 1: t," *PCI Journal*, vol. 54, no. 1, pp. 49–66, 2009.
[20] S. Spadea, M. Rossini, and A. Nanni, "Design analysis and experimental behavior of precast concrete double-tee girders prestressed with carbon-fiber-reinforced polymer strands," *PCI Journal*, vol. 63, no. 1, pp. 72–84, 2018.
[21] Q. Jiang, K. Zhang, Y. Feng et al., "Out-of-plane flexural behavior of full precast concrete hollow-core slabs with lateral joints," *Structural Concrete*, vol. 21, 2020.
[22] D. d. L. Araújo, M. W. R. Sales, R. P. M. Silva, C. d. F. M. Antunes, and M. d. A. Ferreira, "Shear strength of prestressed 160 mm deep hollow core slabs," *Engineering Structures*, vol. 218, Article ID 110723, 2020.
[23] National standard of the People's Republic of China, *Code for Design of Concrete Structures*, China Architecture & Building Press, Beijing, China, 2015.
[24] National standard of the People's Republic of China, *Metallic Materials – Tensile Testing - Part 1: Method of Test at Room Temperature*, China Standard Press, Beijing, China, 2011.
[25] National standard of the People's Republic of China, *Code for Seismic Design of Buildings*, China Architecture & Building Press, Beijing, China, 2016.
[26] National standard of the People's Republic of China, *Standard for Test Method of concrete Structures*, China Architecture & Building Press, Beijing, China, 2012.
[27] J. Hegger, T. Roggendorf, and F. Teworte, "FE analyses of shear-loaded hollow-core slabs on different supports,"

Magazine of Concrete Research, vol. 62, no. 8, pp. 531–541, 2010.

[28] M. Abramski, A. Albert, K. Pfeffer, and J. Schnell, "Experimentelle und numerische untersuchungen zum tragverhalten von stahlbetondecken mit kugelförmigen hohlkörpern," *Beton- und Stahlbetonbau*, vol. 105, no. 6, pp. 349–361, 2010.

[29] National standard of the People's Republic of China, *Technical Specification for Cast-In-Situ concrete Hollow Floor Structures*, China Architecture & Building Press, Beijing, China, 2012.

Hindawi
Advances in Civil Engineering
Volume 2021, Article ID 6616559, 15 pages
https://doi.org/10.1155/2021/6616559

Review Article

A Review of the Methods for Predicting the Effective In-Plane Shear Modulus of Cross-Laminated Timber (CLT)

Mehsam Tanzim Khan,[1] **Ying Hei Chui**,[1] **and Dongsheng Huang**[2]

[1]*Department of Civil and Environmental Engineering, University of Alberta, Edmonton T6G 2R3, Canada*
[2]*National Engineering Research Center of Biomaterials, Nanjing Forestry University, Nanjing 210037, China*

Correspondence should be addressed to Mehsam Tanzim Khan; mehsamta@ualberta.ca

Received 12 November 2020; Accepted 14 June 2021; Published 24 June 2021

Academic Editor: Daniele Baraldi

Cross-laminated timber (CLT) is a type of engineered wood product that offers both high in-plane and out-of-plane load-bearing capacity. It is slowly becoming an alternative material for building high-rise structures. However, there is no current standard or regulation for determining the shear modulus of CLT under in-plane loading condition, which is a very important property for its use as structural members. Few methods have been proposed over the last decade to determine the in-plane shear modulus of CLT. Almost all of the methods proposed until now have their strengths and weaknesses. In this paper, some of the prominent methods for determining the in-plane shear modulus of CLT are described and analysed. The descriptions along with the critical discussions will facilitate a better understanding and might pave the way to further enhancements of the method(s) to determine the in-plane shear modulus of CLT.

1. Introduction

Most of the traditional timber structures have been built based on the light-wood framework system, which is an assembly of regularly spaced dimension lumber members that are fastened together to create structural components. Due to the re-emergence of global interest in timber structures and the introduction of a relatively new category of engineered wood products called mass timber panel (MTP), it has now become possible to construct more complex and long-span timber structures. This type of construction utilizing MTPs is termed mass timber construction. Mass timber construction is making headway in the construction industry in North America and some European countries. Use of mass timber panel can revolutionize the timber construction industry as it opens the door to "building tall with structural wood."

Cross-laminated timber (CLT) is a relatively new engineered wood product that began to be commercially produced in the mid-1990s and is categorized as a type of MTP. For a long time, the utilisation of CLT was limited to some German-speaking countries, where the product is known as Brettsperrholz (BSP) [1]. The use of CLT is increasing because of its benefits compared to concrete and steel [2]. CLT usually consists of an odd number of layers (3, 5, 7, or 9 are the most common) of orthogonally glued timber boards/laminates. Each layer consists of adjacent boards which may or may not be edge-glued on the narrow face, depending on the manufacturer and the product type. CLT offers high load-carrying capacity under both in-plane and out-of-plane loading conditions due to the orthogonal arrangement of the laminates. For this reason, it can be used as both wall or edge-wise bending beam elements under in-plane loading condition and floor diaphragm panels under out-of-plane loading condition. Research has also proved that CLT is highly energy-efficient, and it has a high capacity for storing moisture and thermal energy. A 100 mm thick CLT has a very small thermal transmittance value of around 1.0 W/m^2-K, which is a measure of resistance to the movement of heat, and an equivalent air layer thickness of SD 2–5 m, which is a measure of resistance to moisture diffusion compared to a meter of air's resistance to moisture diffusion [3, 4].

When CLT is used under in-plane loading condition as beam, lintel, or wall panel, one major benefit of CLT is its high tensile strength perpendicular to the beam axis, which makes it less susceptible to crack formation in the perpendicular to the grain direction of the laminates of each layer [5]. CLT has been reported to have higher in-plane shear strength than other similar engineered wood products like glulam [1]. In order to get the full benefit of CLT panels under in-plane loading condition, detailed knowledge and investigation of all the relevant mechanical properties are indispensable. In-plane elastic properties (shear modulus (G) and bending modulus (E), as well as shear stiffness (GA) and bending stiffness (EI), are some of the vital parameters of CLT for its use in structural members [6]. Aside from their use in ultimate limit state (ULS) design, to meet the requirements of serviceability limit states (SLSs), the design checks require elastic properties as input parameters [7]. Therefore, it is necessary to accurately characterize the elastic properties and stiffness of CLT under in-plane loading condition for their structural application as beams, lintels, or wall elements.

Several recent studies have attempted to predict the in-plane shear modulus (G) of CLT panels by different methods. Among these, the methods developed by Brandner et al. [6], Flaig and Blaß [5], and Bogensperger et al. [1] have gained prominence. Brandner et al. [6] used the constitutive equations of the laminates and developed a semiempirical method to predict the in-plane shear modulus of CLT. Flaig and Blaß [5] treated CLT under in-plane loading condition as a transversely loaded beam. Following the beam analogy, they formulated an analytical model to predict the in-plane shear modulus of CLT. Bogensperger et al. [1] employed finite element analysis to develop a model for predicting the in-plane shear modulus of CLT. Among other studies, the studies conducted by Turesson et al. [8] and Andreolli et al. [9] are noteworthy. Turesson et al. [8] proposed some reduction factors from finite element analysis for a range of configurations of CLT which, when multiplied by the in-plane shear modulus of the laminates of the CLT, give the value of the effective in-plane shear modulus of the whole CLT. Andreolli et al. [9] subjected square-shaped CLT specimens to diagonal compression tests with an ad-hoc test setup and experimentally measured the shear modulus of CLT.

Though there have been a few investigations on the in-plane shear modulus of CLT, a comprehensive analysis and comparison of the available methods to determine the shear modulus is not available to date. Recognizing this gap in the body of knowledge, this paper will focus on a detailed comparative analysis of the available methods for the determination of the shear modulus value, along with some recommendations. Thus, this paper can act as an exhaustive summary of almost all the contemporary methods for determining the in-plane shear modulus of CLT and will facilitate further research on the in-plane shear modulus of CLT.

2. Discussion

As discussed in the previous section, several methods for the determination of the in-plane shear modulus of CLT as proposed by different researchers are prevalent. The methods were only briefly introduced in the previous section. In this section, the methods proposed by Brandner et al. [6], Flaig and Blaß [5], Bogensperger et al. [1], Turesson et al. [8] and Andreolli et al. [9] will be discussed in detail. All of these methods emphasize on determining the shear modulus of a non-edge-glued CLT. In edge-glued CLT, since the adjacent laminates of each layer are bonded, the CLT deforms as a whole continuous unit under shear stress and behaves similar to a piece of lumber. Thus, the shear modulus of edge-glued CLT is commonly taken to be equivalent to the shear modulus of the lumber forming the CLT [8].

2.1. Brandner Method. Brandner et al. [6] adopted the test configuration of Kreuzinger and Sieder [10] and proposed a method to determine the shear modulus of CLT from a simple compression test conducted on a differential CLT section. Instead of testing full scale CLT panels, Brandner et al. [6] opted for smaller CLT specimens to realize a continuous load path in the test samples, to achieve pure shear failure mode, and to minimize the test implementation cost.

In the test configuration proposed by Kreuzinger and Sieder [10], a rectangular section is cut out at 45° angle to the direction of the outer longitudinal layers of the CLT. The rectangular section has a length of 1500 mm and a width of 500 mm. This section is then subjected to a compressive load (F) as exhibited in Figure 1.

In Figure 1, x and y directions are the global horizontal and vertical directions of the system, respectively (the global coordinate system), and x_M and y_M are the directions of the fibres of the outer longitudinal layers and the transverse (cross) layers of the CLT, respectively (the local/material coordinate system). The local coordinate system is rotated counter-clockwise by an angle of 45° with respect to the global coordinate system. Under the action of the compressive load (F), the stress state of the CLT section cut out at 45° constitutes pure shear (τ_{xMyM}) combined with pure compression (σ_{yM}) in the local coordinate system. In the global coordinate system, only the vertical stress component (σ_y) is created on the CLT section. Using stress-strain relationships from the plate theory (in-plane stresses), the constitutive equations for the material of the CLT in the local coordinate system are given as

$$\begin{pmatrix} \varepsilon_{xM} \\ \varepsilon_{yM} \\ \gamma_{xMyM} \end{pmatrix} = \begin{pmatrix} \frac{1}{E_{xM}} & 0 & 0 \\ 0 & \frac{1}{E_{yM}} & 0 \\ 0 & 0 & \frac{1}{G_{xMyM}} \end{pmatrix} \begin{pmatrix} \sigma_{xM} \\ \sigma_{yM} \\ \tau_{xMyM} \end{pmatrix}, \quad (1)$$

where ε_{xM}, ε_{yM}, and γ_{xMyM} are the strain components and σ_{xM}, σ_{yM}, and τ_{xMyM} are the stress components. E_{xM} is the weighted modulus of elasticity in the x_M direction, and E_{yM} is the weighted modulus of elasticity in the y_M direction.

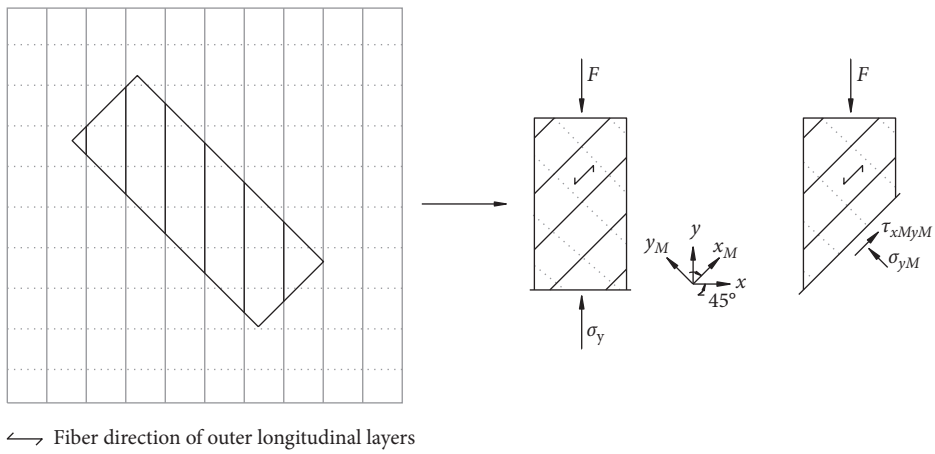

Figure 1: Internal stresses and external loading of the rectangular CLT cut out at 45° angle from larger CLT panels according to Brandner et al. [6].

G_{xMyM} is simply the shear modulus of the CLT section. E_{xM} and E_{yM} can be determined as follows by the method of weighted average:

$$E_{xM} = \frac{\sum t_{xM}E_0 + \sum t_{yM}E_{90}}{t_{\mathrm{CLT}}};$$
$$E_{yM} = \frac{\sum t_{yM}E_0 + \sum t_{xM}E_{90}}{t_{\mathrm{CLT}}}, \tag{2}$$

where t_{xM} is the thickness of each longitudinal layer, t_{yM} is the thickness of each transverse layer, E_0 is the modulus of elasticity of each layer parallel to the grain, E_{90} is the modulus of elasticity of each layer perpendicular to the grain, and t_{CLT} is the total thickness of CLT.

$S_{xMyM} = \begin{pmatrix} (1/E_{xM}) & 0 & 0 \\ 0 & (1/E_{yM}) & 0 \\ 0 & 0 & (1/G_{xMyM}) \end{pmatrix}$ in (2) is the flexibility matrix in the local coordinate system which can be transformed to the global coordinate system (S_{xy}) using the following transformation:

$$S_{xy} = TS_{xMyM}T^T, \tag{3}$$

where

$$T = \begin{pmatrix} \cos^2\alpha & \sin^2\alpha & -\sin\alpha\cos\alpha \\ \sin^2\alpha & \cos^2\alpha & \sin\alpha\cos\alpha \\ 2\sin\alpha\cos\alpha & -2\sin\alpha\cos\alpha & \cos^2\alpha - \sin^2\alpha \end{pmatrix}, \tag{4}$$

where α is the angle between the local and the global coordinate systems, which in this case is 45°. For $\alpha = 45°$, the flexibility matrix in the global coordinate system is given by

$$S_{xy} = \begin{pmatrix} \frac{0.25}{E_{xM}} + \frac{0.25}{E_{yM}} + \frac{0.25}{G_{xMyM}} & \frac{0.25}{E_{xM}} + \frac{0.25}{E_{yM}} - \frac{0.25}{G_{xMyM}} & \frac{0.5}{E_{xM}} - \frac{0.5}{E_{yM}} \\ \frac{0.25}{E_{xM}} + \frac{0.25}{E_{yM}} - \frac{0.25}{G_{xMyM}} & \frac{0.25}{E_{xM}} + \frac{0.25}{E_{yM}} + \frac{0.25}{G_{xMyM}} & \frac{0.5}{E_{xM}} - \frac{0.5}{E_{yM}} \\ \frac{0.5}{E_{xM}} - \frac{0.5}{E_{yM}} & \frac{0.5}{E_{xM}} - \frac{0.5}{E_{yM}} & \frac{1}{E_{xM}} + \frac{1}{E_{yM}} \end{pmatrix}. \tag{5}$$

Thus, the flexibility matrix given in (5) is the flexibility of the CLT section in the global directions with the properties transformed from the local material directions to the global directions. Now, in the global coordinate system, the constitutive equations for the material of the CLT are given as

$$\begin{pmatrix} \varepsilon_x \\ \varepsilon_y \\ \gamma_{xy} \end{pmatrix} = \begin{pmatrix} \frac{1}{E_x} & 0 & 0 \\ 0 & \frac{1}{E_y} & 0 \\ 0 & 0 & \frac{1}{G_{xy}} \end{pmatrix} \begin{pmatrix} \sigma_x \\ \sigma_y \\ \tau_{xy} \end{pmatrix} = \left[S_{xy}\right] \begin{pmatrix} \sigma_x \\ \sigma_y \\ \tau_{xy} \end{pmatrix}, \tag{6}$$

where, similar to (1), ε_x, ε_y, and γ_{xy} are the strain components and σ_x, σ_y, and τ_{xy} are the stress components in the global directions. E_x is the modulus of elasticity in the x direction, and E_y is the modulus of elasticity in the y direction. G_{xy} is the shear modulus of the CLT section (G_{xMyM} and G_{xy} are synonymous). The flexibility matrix S_{xy} given in (6) is equivalent to that given by (5). The only difference between them is as follows: one is derived from the local material directions and transformed into the global directions, while the other is given directly in the global axes.

From the direction of load application on the rectangular section, it can be observed that $\sigma_x = 0$ and $\tau_{xy} = 0$ since only vertical compressive load is acting on the section. Thus, under the vertical compressive load, a discrete stress state σ_y with an associated strain ε_y is formed which follows the simple constitutive relation $\sigma_y = E_y\varepsilon_y$. σ_y is the stress acting in the vertical direction on the CLT section, and ε_y is the associated strain. From the vertical load-deflection behaviour of the CLT section, the modulus of elasticity in the vertical direction, E_y can be determined. Now, considering the (2,2) element of the flexibility matrix given in equations (5) and (6), and their equivalency, the following relationship holds:

$$\frac{1}{E_y} = \frac{0.25}{E_{xM}} + \frac{0.25}{E_{yM}} + \frac{0.25}{G_{xMyM}}. \tag{7}$$

Rearranging (7), the shear modulus can be determined using

$$G_{xMyM} = \frac{1}{\left(\left(4/E_y\right) - \left(1/E_{xM}\right) - \left(1/E_{yM}\right)\right)}, \tag{8}$$

where E_y is determined from vertical load-deflection behaviour of the CLT section and E_{xM} and E_{yM} are estimated from the material properties of the laminates that form the CLT. Equation (8) represents the final form of Brandner et al.'s [6] model to predict the shear modulus of CLT. The test setup used by Brandner et al. [6] is shown in Figure 2. The CLT section is placed in between the machine actuator head at the top and the support (machine base) at the bottom. Measurement crosses are placed concentrically on the specimen to measure both the vertical and the horizontal deflection.

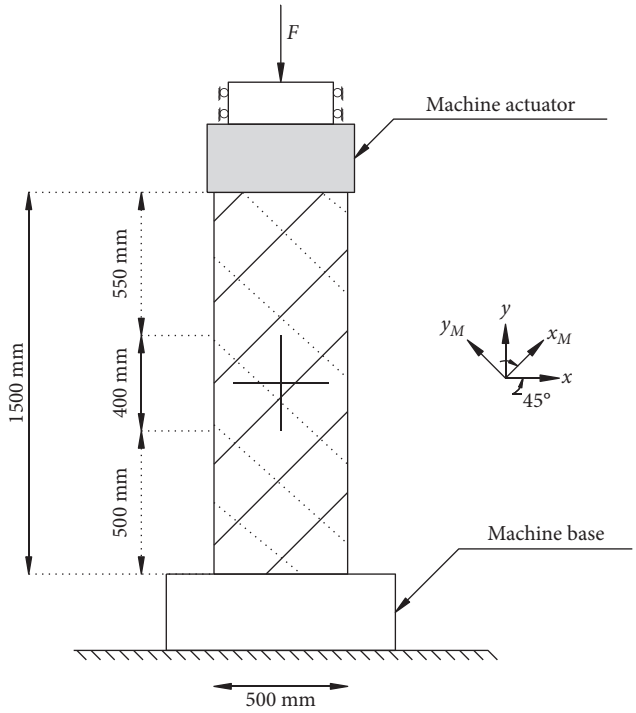

Figure 2: Test setup used by Brandner et al. [6]. The specimen is placed between the machine base and the machine actuator.

The test configuration adopted by Brandner et al. [6] was motivated by noting the difficulties faced in determining shear properties on a full-scale CLT diaphragm, as had been performed by Andreolli et al. [9] and Bogensperger et al. [1]. The simple compression test can be conducted in almost any laboratory that has a compression test machine without the need for any complicated instrumentation. The intended and assumed failure mode in this configuration is the gross-shear failure mode, which is initiated by the longitudinal shearing failure (shear failure parallel to the grain) in all the layers of the CLT considering the gross cross-section of CLT. The in-plane deformation (both vertical and horizontal) of the CLT specimen under compressive load was determined on both side faces using centrically placed measurement crosses with a gauge length of 400 mm. The height-to-width ratio of the specimen used in Brandner et al. [6] tests was 1500 mm/500 mm = 3/1. Through finite element analysis, it was verified that this height-to-width ratio of the specimen did not lead to any stress concentrations at the middle of the specimen. Also, the middle of the specimen was under a state of constant shear stress. Thus, deformation measurements were taken in this middle region of the specimen as exhibited in Figure 2.

Shear modulus values were experimentally determined by Brandner et al. [6] using two approaches, (a) by using (8), with the value of E_y measured from the load-deformation data in the vertical direction of the test configuration of Figure 2, and standardized moduli of elasticity, E_0 and E_{90} according to the stress class of the lumbers of each layer of the CLT; (b) with the approach standardized in EN 408 [11]. The second approach involved measuring the local shear deformations of a specimen in a bending test. Details of this approach can be found in the standard EN 408 [11]. The

shear modulus values using these two approaches differed by about 10%, the latter approach yielding higher values. Brandner et al. [6] noted the higher deflection in the vertical direction compared to the horizontal direction in the compression test setup as a possible reason for the lower value given by the first approach. Among the two approaches, the first approach led to higher variability in the shear modulus values.

From (1), it can be observed that the off-diagonal elements, which are related to Poisson's ratio, have been ignored. Furthermore, in estimating E_{xM} and E_{yM}, E_0 might be considered as the modulus of elasticity of each layer parallel to the grain direction of the laminates of the layer and E_{90} is the modulus of elasticity of each layer perpendicular to the grain direction of the laminates of that layer. While assuming E_0 of each layer to be equal to the E_0 of the laminates of the layer might be appropriate, assuming E_{90} of each layer to be equal to the E_{90} of the laminates might be an overestimation. The rationale behind this is, for each layer, the continuity of the laminates which is maintained when stresses parallel to the grain (fibre) direction are considered and the laminates can be considered to be fully effective in resisting the stresses. On the other hand, when stresses perpendicular to the grain (fibre) direction are considered, the continuity of laminate is disrupted at the boundary between two adjacent laminates due to the presence of edge-gaps and inadequate bonding (for CLT without edge-gluing or narrow face bonding), and the full capacity of the laminates might not be effective in resisting the stresses. Thus, assuming the modulus of elasticity of the layer perpendicular to the grain direction of the laminates equal to the modulus of elasticity of the laminate material perpendicular to the grain may lead to an overestimation of the stiffness property. Also, the specimen size adopted in the test configuration is still fairly sizeable, which led to heavy specimens and the need to use lifting equipment in the test laboratory.

2.2. Flaig and Blaß Method. According to Flaig and Blaß [5], when CLT is subjected to in-plane transversal forces, the overall shear deformation in the CLT can be considered to be the superposition of two components: (1) shear deformation within the laminates of the CLT and (2) rotational and translational deformation of the crossing areas between the laminates of the longitudinal and the transversal layers. The first component arises from the shear strain within the laminates of the CLT, and it is equivalent to the shear deformation in wood material. This is the only component of shear deformation in an edge-glued CLT (CLT with narrow face bonding). The second component arises from the mutual displacement and rotation that occur in the crossing area between the laminates of the longitudinal and the transversal layers in a CLT without narrow face bonding [12]. The glued connection between the longitudinal and transverse layers (crossing area) of the CLT can be considered as rigid; however, the wood fibres at the vicinity of the adhesive layer in the crossing areas can undergo significant deformation under transverse loads. This leads to the mutual displacement and rotation that occur in the crossing area, or more precisely, at the vicinity of the crossing area. Since shear deformation within the laminate is the only component of shear deformation in an edge-glued CLT, the shear modulus of an edge-glued CLT can be considered to be comparable to that of a solid lumber and it was not considered in the Flaig and Blaß [5] study.

The two components of shear deformation in a differential CLT section that arise due to the action of the shear force T on all faces are illustrated in Figure 3. The strain γ_S in the left picture is the first component of the shear deformation, and γ_{CA} in the right picture is the second component of the shear deformation. Some implicit assumptions of the Flaig and Blaß [5] model are as follows: (1) the CLT is loaded on edge as a beam; (2) the transverse loads acting on the CLT beam are perpendicular to the direction of the grain of the outer longitudinal layers, and (3) the direction of the grain of the outer longitudinal layers is aligned with the beam axis.

Along the length or width of the CLT, in sections which coincide with gaps between adjacent laminates of the same layer, the shear forces have to be transferred to the subsequent layer in the CLT thickness direction through the crossing areas. This leads to the development of shear stress in the crossing areas. The second component of the overall shear deformation arises from the stress acting in the crossing areas. This second component of the overall shear deformation can again be broken down into two mechanisms, translational and the rotational. The translational deformation (γ_{yx}) originates from unidirectional shear stresses acting parallel to the beam axis (Figure 4(a)), while the rotational deformation (γ_{tor}) is caused by torsion as shown in Figure 4(b).

The strain components are given by the following relationships:

$$\begin{aligned}\gamma_{yx} &= \frac{2\tau_{yx}}{Kw(m-1)} \\ &= \frac{12V}{Kw^3m^3n_{CA}},\end{aligned} \tag{9}$$

$$\begin{aligned}\gamma_{\text{tor}} &= \frac{2\tau_{\text{tor}}}{Kw} \\ &= \frac{6V}{Kw^3n_{CA}}\left(\frac{1}{m}-\frac{1}{m^3}\right).\end{aligned} \tag{10}$$

In the above equations, τ_{yx} is the shear stress acting parallel to the beam axis of the CLT and it is caused by the variation of the bending moment along the beam axis. If the CLT does not have narrow face bonding, the differential normal forces that arise from the change of the bending moment along the beam axis have to be transferred through the crossing areas between the longitudinal and the transverse layers. This is the source of the shear stress τ_{yx}. τ_{tor} is the torsional shear stress which arises from the eccentricity between the centre lines of the laminates of the longitudinal layers with respect to the central plane of the CLT beam (the horizontal plane through the midheight of the CLT beam). The torsional shear stress is assumed to be constant within the beam thickness and uniformly distributed within the

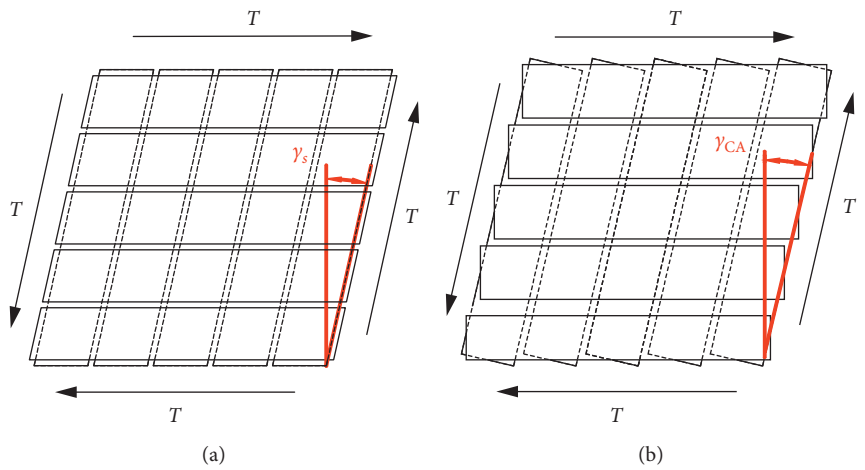

Figure 3: The two components of the overall shear deformation: (a) shear deformation within the laminates; (b) rotational and translational deformation in the crossing areas [12].

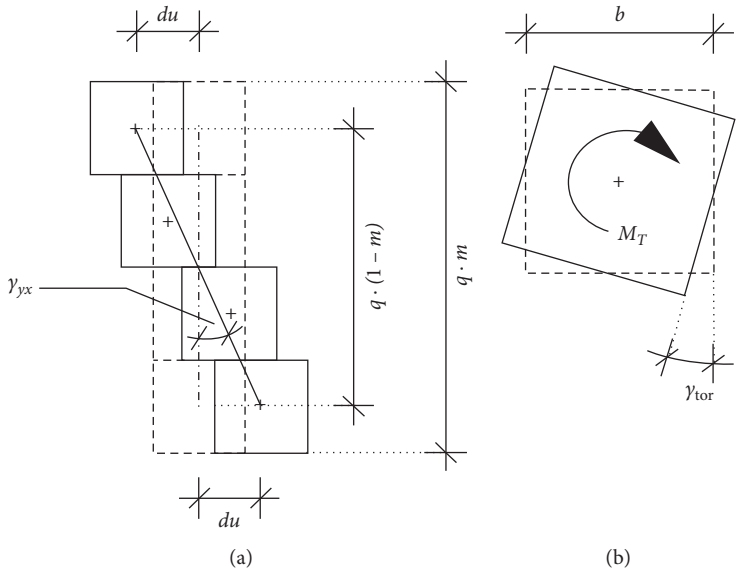

Figure 4: Shear strain components in the crossing areas due to (a) the translational deformation mechanism and (b) the rotational deformation mechanism [5].

beam height. The latter assumption is only possible if the laminates of the transverse layers remain straight (do not undergo any rotation) in the deformed beam. This torsional shear stress leads to rolling shear stresses in the laminates. K is the slip modulus, a measure of the stiffness of the crossing areas with the unit of force/(length)^3. In (9) and (10), no distinction has been made between the stiffness of the crossing areas under the two separate mechanisms (e.g., slip modulus and torsional modulus). The same K value is used as the measure of stiffness under both mechanisms. w is the width of all the laminates, which is taken as constant for all the layers. Information on CLT with laminates of different widths in the longitudinal and transverse layers can be found in Blaß and Flaig [13]. m is the number of longitudinal laminates within the beam height direction. V is the shear force acting on a section of the CLT beam, and n_{CA} is the number of glue lines between the longitudinal and transverse layers in the beam width direction.

From (9) and (10), it can be observed that the number of laminates in the longitudinal layers have a pronounced effect on the shear deformations. However, in CLT beams having a large number of laminates in the longitudinal layers, the last term in (10) becomes very small and can be ignored.

For CLT with a rectangular cross-section, the constitutive equation for the crossing area is

$$\tau = \left(\gamma_{yx} + \gamma_{\text{tor}}\right) G_{\text{eff},CA}, \tag{11}$$

where $G_{\text{eff},CA}$ is the shear modulus of the crossing area and τ is the shear stress acting in the crossing area. To estimate this shear stress from the shear force acting in the gross cross-section (considering the whole thickness and width of the CLT), a shear correction factor has to be used:

$$\tau = k_{\text{shear}} \frac{V}{A_{\text{gross}}}, \tag{12}$$

where A_{gross} is the gross cross-sectional area and k_{shear} is the shear correction factor, assumed to be 5/6 by Flaig and Blaß [5] which is a value commonly used for rectangular cross-sections [14], and V is the shear force acting in the whole CLT gross cross-section. Thus, the shear modulus of the crossing area is given by

$$\begin{aligned} G_{\text{eff},CA} &= \frac{6V}{5A_{\text{gross}}\left(\gamma_{yx} + \gamma_{\text{tor}}\right)} \\ &= \frac{Kw^2m^2n_{CA}}{5t_{\text{CLT}}\left(m^2+1\right)}, \end{aligned} \tag{13}$$

where t_{CLT} is the total thickness of the CLT beam and the terms on the right side of (12) have been derived by substituting the values of γ_{yx} and γ_{tor} from equations (9) and (10). Finally, the shear deformations in the laminates and the deformation of the crossing areas are superimposed by the following formalism:

$$\begin{aligned} \gamma_{\text{eff,CLT}} &= \gamma_{\text{eff},CA} + \gamma_{\text{lam}}, \\ \gamma_{\text{eff},CA} &= \gamma_{yx} + \gamma_{\text{tor}}, \\ \tau &= \gamma_{\text{eff},CA} G_{\text{eff},CA} = \gamma_{\text{lam}} G_{\text{lam}} \\ &= \gamma_{\text{eff,CLT}} G_{\text{eff,CLT}} \\ &= \left(\gamma_{\text{lam}} + \gamma_{\text{eff},CA}\right) G_{\text{eff,CLT}}, \\ \tau &= \left(\frac{\tau}{G_{\text{lam}}} + \frac{\tau}{G_{\text{eff},CA}}\right) G_{\text{eff,CLT}}, \\ G_{\text{eff,CLT}} &= \left(\frac{1}{G_{\text{lam}}} + \frac{1}{G_{\text{eff},CA}}\right)^{-1}, \end{aligned} \tag{14}$$

where $\gamma_{\text{eff,CLT}}$ is the overall shear deformation in the CLT beam, $\gamma_{\text{eff},CA}$ is the total shear deformation of the crossing areas due to the two mechanisms, and γ_{lam} is the shear deformation within the laminates. τ is the shear stress acting on the crossing area as before, and also in the laminates and the whole CLT. Thus, τ is the effective shear stress acting on the CLT. G_{lam} is the mean shear modulus of the laminates (Flaig and Blaß [5] assumed all the laminates of the CLT to have the same shear modulus) of the CLT, and $G_{\text{eff,CLT}}$ is the effective shear modulus of the whole CLT. Equation (14) represents the final closed form solution of the Flaig and Blaß [5] model to predict the shear modulus of CLT.

The determination of the stiffness of the crossing areas (slip modulus, K in (9) and (10)) is a challenge as discussed by Blaß and Flaig [13], and the results of the studies carried out by Blaß and Görlacher [15] and by Jöbstl et al. [16] have a significant discrepancy. Blaß and Flaig [13] carried out four-point bending tests on CLT beams. From the measured shear-free and apparent moduli of elasticity of the CLT beams, the effective shear modulus values of the CLT beams were evaluated. Using the effective shear modulus value, the slip modulus of a crossing area was determined using (13) and (14) and a laminate shear modulus of 690 N/mm^2, which is the characteristic value of the shear modulus of lumber of nominal strength class C24 according to EN 338 [17].

The shear modulus values tabulated in Flaig and Blaß [6] are determined the measured shear-free and apparent moduli of elasticity of the CLT beams under four-point bending tests. No ad hoc test setup for measurement of shear modulus was made. The problem with the four-point bending test is that the shear deformations under bending test might be very small depending on the span-to-depth ratio (L/h) of the CLT beam. Nevertheless, Flaig and Blaß [6] found that the shear modulus of CLT beam increases with the number of layers of CLT.

Though Flaig and Blaß [6] pointed out that the shear stress component τ_{yx} varies in the beam width direction for CLT in which the ratio of $t_{\text{long},k}/n_{CA,k}$ ($t_{\text{long},k}$ is the thickness of the k-th longitudinal layer and $n_{CA,k}$ is the number of glue lines the k-th longitudinal layer shares with adjacent transverse layers) is not constant for all the longitudinal layers, it was assumed that this shear stress variation in the beam width direction can be ignored. Danielsson and Serrano [18] pointed out that, this assumption is inaccurate, and this shear stress component is significantly influenced by the lay-up parameters $t_{\text{long},k}/t_{\text{net,long}}$ ($t_{\text{net,long}}$ is the sum of the thicknesses of the longitudinal layers), n_{CA}, and $n_{CA,k}$. For the calculation of shear stress component τ_{tor}, Danielsson and Serrano [18] also noted that the assumption of equal torsional moments for all crossing areas in the beam height direction is inaccurate in the Flaig and Blaß [5] model. Danielsson and Serrano [18] found the torsional moments and shear forces to be significantly greater close to the centre line of the beam compared to the upper and lower parts of the beam. The findings of Danielsson and Serrano [18] might have implications on the method of effective shear modulus determination proposed by Flaig and Blaß [5].

2.3. Bogensperger Method. Bogensperger et al. [1] took advantage of the regular periodic geometric structure of CLT elements and modelled the smallest unit cell for mechanical treatment, called the "representative volume subelement (RVSE)." The unit cell which is repeated over the whole volume of the CLT is called the "representative volume element (RVE)." The RVE can be decomposed to even smaller building blocks called the "representative volume subelement (RVSE)." The representative volume subelement comprises of a cut out of two orthogonal laminates in two adjacent layers of CLT, usually each of them extending over half of the thickness of each layer. This further decomposition of RVE into RVSE is justified if an infinite number of layers of CLT are assumed. The RVSE is surrounded by two planes of symmetry on the two sides. The RVE and RVSE are shown in Figure 5.

From Figure 5, it can be observed that, if there are n number of layers in CLT, the number of glue planes and thus the number of RVSE are $(n-1)$. Also, each RVSE is

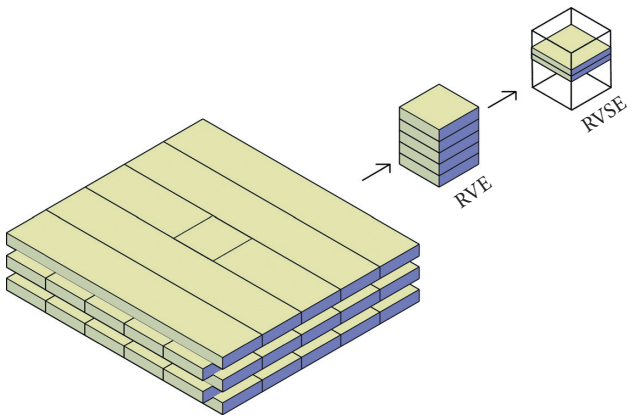

Figure 5: A full-sized CLT panel decomposed to an RVE and then subsequently to an RVSE.

composed of one glue plane and two orthogonal laminates on either side of the glue plane. Bogensperger et al. [1] assumed the thickness of the thinner of the two glued laminates to be the controlling thickness of the RVSE, as a conservative approach to calculation of the resulting shear stresses. However, the thickness of the outermost RVSEs in a CLT is equal to either twice the thickness of the outer laminate or the ordinary thickness of the inner laminate, whichever is less. To illustrate the thickness of the RVSE in detail, the RVSEs that constitute a 5-layer CLT are shown in Figure 6.

As the CLT in Figure 6 is a 5-layer CLT, it has 4 RVSEs. For the 4 RVSEs in Figure 6, the thickness of each RVSE is given in Table 1.

The overall thickness of all the RVSEs is equal to the sum of the thickness of all the RVSEs, which is always smaller than or equal to the overall geometric thickness of the CLT.

Under in-plane shear forces, shear stresses are generated in such a way that the narrow faces of the laminates of each layer remain stress-free. These narrow faces usually have glue lines in an edge-glued CLT while they lack glue lines in a non-edge-glued CLT. Shear stresses are transferred to the adjacent RVSEs at the vertical and horizontal pairs of planes of periodicity only. This means that shear stresses are not transferred to adjacent laminates of the same layer in a non-edge-glued CLT. The complete in-plane shear mechanism in an RVSE can be decomposed into two parts: (a) pure shear mechanism with full shear force transmission at the narrow faces of all boards (mechanism 1, Figure 7); (b) local stress redistribution caused by torsional moments acting on both sides of the gluing interface on the wide faces of the laminates (mechanism 2, Figure 8). These two mechanisms superimpose to create a stress-free condition at the narrow faces (Figure 9(a)). This fulfils the condition of no shear stress transmission to adjacent laminates of the same layer through the narrow faces.

The mechanism 1 corresponds to the state of uniform shear across the total thickness of the RVSE (Figure 9(b)). This state occurs in homogeneous CLTs with narrow face bonding (edge-gluing). Under this mechanism, full shear force is transmitted at the narrow faces of the laminates.

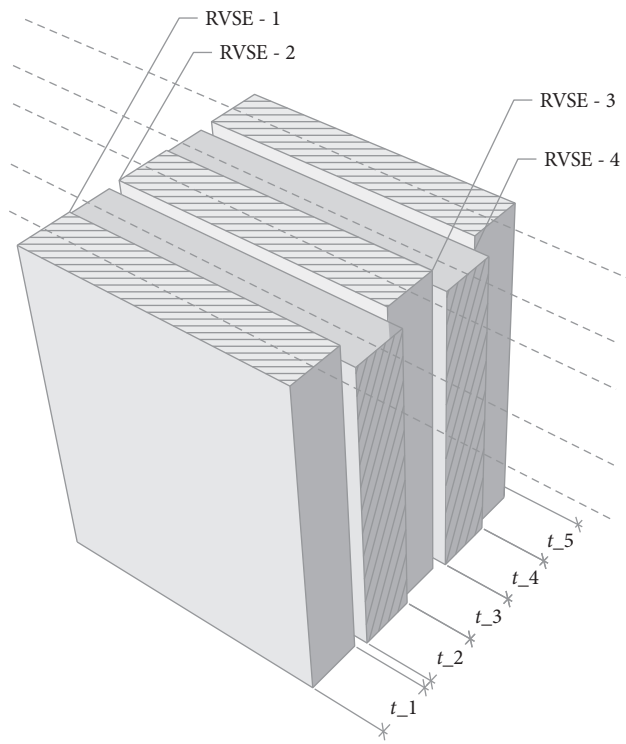

Figure 6: Idealized RVSE for a 5-layer CLT according to Bogensperger et al. [1].

Table 1: Idealized thicknesses of all the RVSEs for the CLT in Figure 6

RVSE designation	Thickness
RVSE–1	$\min(2t_1, t_2)$
RVSE–2	$\min(t_2, t_3)$
RVSE–3	$\min(t_3, t_4)$
RVSE–4	$\min(t_4, 2t_5)$

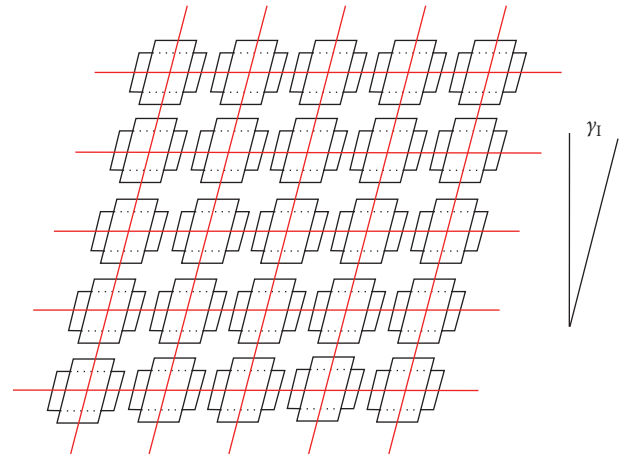

Figure 7: Pure shear mechanism, mechanism 1 [1].

Therefore, the relevant shear stiffness under mechanism 1 is equivalent to the mean shear modulus of the laminates parallel to the grain (G_{lam}). Mechanism 2 corresponds to a complicated state of torsion-like behaviour in the

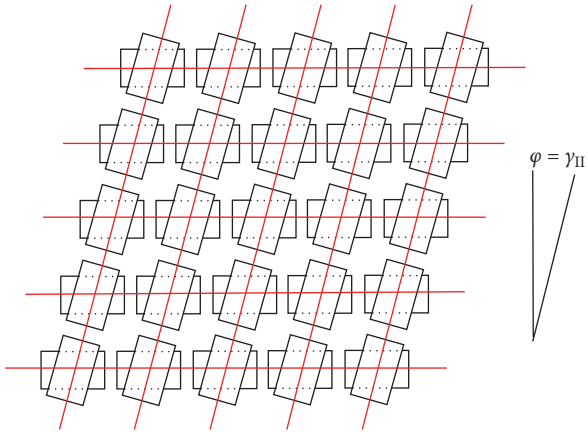

Figure 8: Local stress redistribution due to torsional moments, mechanism 2 [1].

thickness direction of the RVSE extending between the two planes of symmetry of the RVSE (Figure 9(c)). Bogensperger et al. [1] adopted a simple classical torsional beam model which extends in plate thickness direction and is loaded by oppositely directed torsional moments with uniform distribution, acting antisymmetrically to the midplane of the RVSE. The assumed torsional model corresponds to the condition of restrained warping. The relevant effective shear stiffness (G_{eff}) under mechanism 2 is still unknown and is assumed to be equal to $G_{eff,2} = G_{lam}/2$ (Moosbrugger et al. [19] and Bogensperger et al. [1]).

The shear deformation of mechanism 1 (γ_1) and mechanism 2 (γ_2) are given by (15) and (16), respectively:

$$\gamma_1 = \frac{\tau_0}{G_{lam}}, \tag{15}$$

$$\gamma_2 = \frac{6\tau_0}{G_{lam}}\left(\frac{t}{w}\right)^2, \tag{16}$$

where τ_0 is the nominal shear stress associated with the RVSE. G_{lam} is the mean shear modulus of the laminates of the CLT parallel to grain. t is the mean thickness of the laminates, and w is the mean laminate width or the mean distance between stress relief cuts of CLT. As discussed previously, only a simple torsional behaviour was assumed to derive (16). The torsional shear deformation of this simple torsional beam model is given by

$$\gamma_2 = \frac{TL}{G_{eff,2}J}, \tag{17}$$

where T is the torsional moment acting on the two sides of the RVSE at the two planes of symmetry (two outer sides). L is the length from the midplane of the RVSE to the plane of symmetry. $G_{eff,2}$ is the effective shear modulus under mechanism 2, and J is the polar moment of inertia. These terms are given by the following expressions according to Bogensperger et al. [1]:

$$\begin{aligned} T &= \tau_0 t a^2, \\ L &= \frac{t}{2}, \\ G_{eff,2} &= \frac{G_{lam}}{2}, \\ J &= \frac{w^4}{6}. \end{aligned} \tag{18}$$

The torsional moment results from the nominal shear force, $\tau_0 \cdot t \cdot w$, and w is the torsional moment arm of the nominal shear force. The length from the midplane of the RVSE to the plane of symmetry is $t/2$. $G_{lam}/2$ is the assumed value of $G_{eff,2}$. Finally, considering the simple torsional beam model, the torsional constant is assumed to be equal to the polar moment of inertia, J which for a square cross-section is given by $w^4/6$. Inputting these expressions into (17) will lead to 16.

Now, adding the shear deformation of the two mechanisms will give the total shear deformation of the CLT, which is

$$\gamma = \gamma_1 + \gamma_2. \tag{19}$$

If G is the effective shear modulus of the whole CLT with the superposition of both the mechanisms,

$$\begin{aligned} \frac{\gamma_1}{\gamma} &= \frac{(\tau_0/G_{lam})}{(\tau_0/G)}, \\ \text{or } &\frac{(\tau_0/G_{lam})}{(\tau_0/G_{lam}) + (6\tau_0/G_{lam})(t/w)^2} \\ &= \frac{G}{G_{lam}} \\ &= \frac{1}{1 + 6(t/w)^2} \\ \text{or } G &= \frac{G_{lam}}{1 + 6(t/w)^2}. \end{aligned} \tag{20}$$

Equation (20) provides a simple relation between the effective shear modulus of the CLT under in-plane loading condition and the mean shear modulus of the laminates that make up the CLT. However, as some assumptions were made regarding the shear deformation under mechanism 2 and as it can only be approximated with equation (20), Bogensperger et al. [1] carried out a finite element study for achieving better mechanical results. Also, equation (20) does not recognize the effect of the finite number of layers of CLT in predicting the shear modulus from the shear mechanism of RVSE. Instead, equation (20) assumes an infinite number of layers of the CLT. According to Turesson et al. [8], this results in an overestimate of the actual shear modulus of the CLT. The effect of the finite number of layers on equation (20) was investigated by Silly [20], and in order to account for the finite number of layers in a CLT, a correction factor

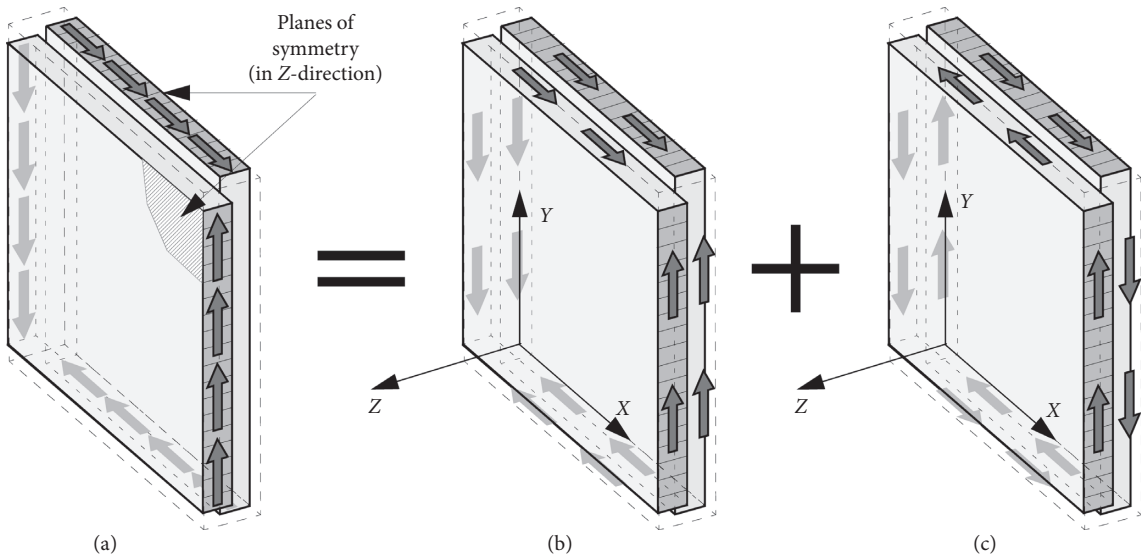

Figure 9: Superposition of shear mechanisms (a) original situation, (b) partial state of pure shear mechanism (mechanism 1), and (c) partial state of torsion-like behaviour (mechanism 2) [19].

was proposed. The proposed correction factor (α_T) to predict the effective shear modulus is

$$\alpha_T = p\left(\frac{t}{w}\right)^q;$$
$$t = \frac{\text{total thickness of CLT}}{\text{number of layers in CLT}}, \tag{21}$$

where t is the mean thickness of all the layers of CLT and w is the laminate width of the CLT (usually a constant value for each type of CLT). The values of p and q in estimating the correction factor are given in Table 2 according to Silly [20] and Bogensperger et al. [1].

With the correction factor, the shear modulus is approximated by

$$G = \frac{G_{\text{lam}}}{1 + 6\alpha_T\left((t/w)\right)^2}. \tag{22}$$

Equation (22) represents the final form of the Bogensperger et al. [1] model to predict the shear modulus of CLT. Bogensperger et al. [1] assumed a mean value of the width and the thickness of the laminates in developing the model to predict the shear modulus of CLT. Though CLT with unequal width of the laminates of each layer is not common, the assumption of an equal mean thickness of all the layers means that the method cannot be applied to CLT with unequal layer thicknesses. Also, the simple torsional beam model for the shear mechanism 2 in (17) does not represent the correct state of the torsion in the RVSE when the width-to-thickness ratio of each layer is low [8]. A more accurate representation of the shear state in the RVSE can be made using the theory of elasticity.

2.4. Andreolli Method. Andreolli et al. [9] noted some of the shortcomings of the different methods mentioned in the European standard EN 16351 [21] to determine the in-plane

Table 2: p and q values of the correction factor for determining shear modulus.

No. of layers	3	5	7
p	0.53	0.43	0.39
q	−0.79	−0.79	−0.79

characteristics of CLT. Among these methods, the four-point bending test is not always useful in determining shear properties as bending stresses are predominant compared to the shear stresses in the bending test. Other test methods conducted on small-sized specimens focus on testing of single nodes of CLT (with only one glued crossing area between the longitudinal and the transverse layers). Tests on single nodes are usually done to determine the shear strength values under different failure modes. However, they cannot provide any information on the stiffness of CLT and it is uncertain whether they are representative of the global behaviour of the whole CLT panel.

Considering the shortcomings of the previously proposed test methods, Andreolli et al. [9] proposed a diagonal compression test setup to determine some of the in-plane properties of CLT. The test setup is illustrated in Figure 10. For this test, square-shaped CLT specimen of 1 m side length was used. The load was applied under displacement control at a constant rate of 0.04 mm/s. The load was transferred to the specimen using reinforced steel angles (seen in the upper and lower corner of the specimen in Figure 10). The deformation of the specimen was measured on both the side faces. A total of eight instruments were positioned on the panel as shown in Figure 10. Four LVDTs measured the horizontal (w_x) and vertical (w_y) deformations of the central core of the specimen (the central core is the square zone located in the centre of the specimen with a diagonal length equal to 40% of the specimen diagonal, shown in Figure 10 with dashed lines), two wire potentiometers measured the

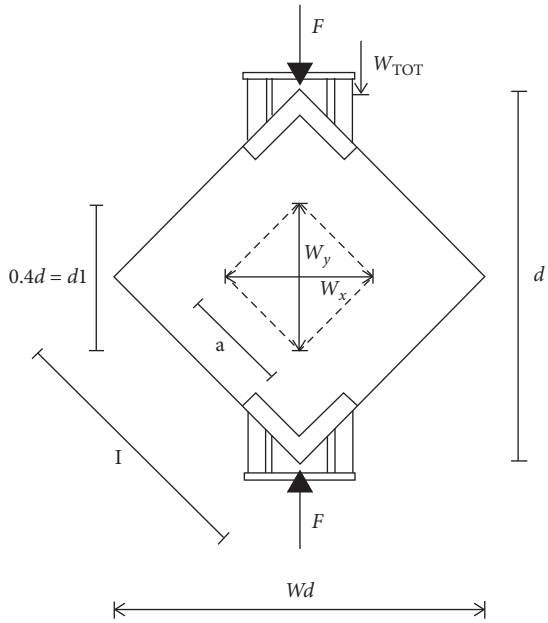

Figure 10: Diagonal compression test setup [8].

total deformation along the horizontal diagonals (w_d) and two inductive displacement transducers measured the absolute vertical displacements (w_{TOT}) of the machine head. A load cell was used to measure the applied force. The main goal of the diagonal compression test is to introduce a state of pure shear stress inside the CLT. For simplified treatment of the stress condition inside the CLT under diagonal compression, uniform stress distribution can be assumed. However, the actual stress distribution inside is more complex. The state of uniformity of stress is grossly violated, and in the central core zone, the shear stress is higher than other parts of the CLT.

Andreolli et al. [9] used Frocht's [22] solution to estimate the average value of the shear stress acting in the core zone from the assumed uniform stress distribution, which is given by

$$\begin{aligned}\tau_{\text{core}} &= 1.429\overline{\tau} \\ &= \frac{1.429F}{\sqrt{2}A},\end{aligned} \tag{23}$$

where F is the applied vertical force from the machine actuator and A is the cross-sectional area of the specimen in the direction parallel to the four sides of the specimen. Thus, $A = l \times t_{\text{CLT}}$, where l is the length of the specimen as seen in Figure 10 and t_{CLT} is the thickness of the specimen. The factor 1.429 in (23) accounts for the fact that the shear stress inside the central core zone is higher than the shear stress occurring outside the central core zone. The stress calculated using $F/\sqrt{2}A$ in (23) gives the value of the stress if uniform stress distribution is considered throughout the CLT. Andreolli et al. [9] suggested this factor by averaging the ratios of the actual the shear stress in the core zone to the shear stress calculated using $F/\sqrt{2}A$ along the horizontal (along w_x) and vertical (along w_y) diagonal of the central core zone.

The average shear strain of the core zone is given by

$$\gamma = \frac{2\Delta v}{d_1}. \tag{24}$$

The derivation of (24) can be explained with the help of the deformed shape of the core zone (Figure 11).

Δv in (24) is the average change in the core diagonal of length d_1 as measured by the four LVDT transducers, thus $\Delta v = (w_{x,\text{side 1}} + w_{x,\text{side 2}} + w_{y,\text{side 1}} + w_{y,\text{side 2}})/4$. In Figure 11, the deformed shape is shown with dotted lines. a is the length of the core zone. From small-displacement approximations,

$$\begin{aligned}\cos(90 - \gamma) = \sin\gamma \approx \gamma, \\ \Delta v^2 \approx 0.\end{aligned} \tag{25}$$

Using cosine law of triangle,

$$\begin{aligned}d_1 - \Delta v &= \sqrt{a^2 + a^2 - 2 \cdot a \cdot a \cdot \cos(90 - \gamma)}, \\ \text{or } (d_1 - \Delta v)^2 &= a^2 + a^2 - 2 \cdot a \cdot a \cdot \cos(90 - \gamma) \\ \text{or } d_1^2 + \Delta v^2 - 2d_1\Delta v &= a^2 + a^2 - 2 \cdot a \cdot a \cdot \cos(90 - \gamma) \\ \text{or } -2d_1\Delta v &= -d_1^2\gamma \\ &[\Delta v^2 \approx 0 \text{ and from the undeformed shape,} \\ &\quad d_1^2 = a^2 + a^2] \\ \text{or } \gamma &= \frac{2\Delta v}{d_1}.\end{aligned} \tag{26}$$

Finally using (23) and (24), the shear stress versus shear strain curve of the core zone is produced for each specimen. Regression analysis is carried out on the data points to get a best-fit line. Then, the slope of the best-fit line within the 10%–40% range (this range is actuated following the provisions of EN 408 [11]) of the maximum applied load $F_{\max}$ gives the value of the in-plane shear modulus of CLT, G.

Andreolli et al. [9] conducted diagonal compression test on four types of CLTs: (1) CLT with narrow face bonding; (2) CLT with narrow face bonding but with shrinkage cracks; (3) CLT without narrow face bonding and with stress relief cuts; (4) CLT without narrow face bonding. The first type of CLT gave the highest value of shear modulus, which was comparable to that of solid lumber material.

Turesson et al. [23] discussed some of the drawbacks of the diagonal compression test. The contact area between the CLT panel and the steel angles (which act as supports) provides some additional restraint to the deformation of the CLT in the horizontal direction. As a result, the CLT panels are not deformed in the vertical and horizontal direction by the same amount. The factor 1.429 used to calculate the shear stress in the core zone does not consider this unequal deformation issue. Furthermore, the simplified deformed shape exhibited in Figure 11, in which both the vertical and

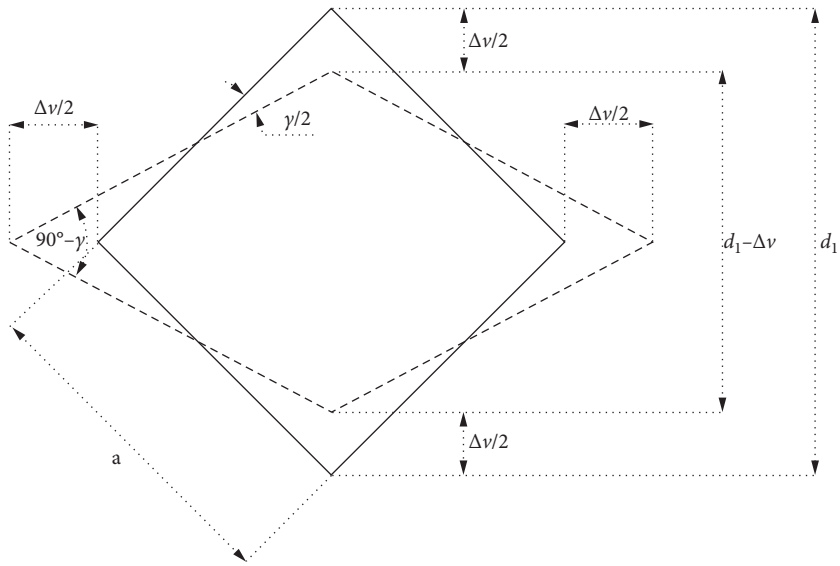

Figure 11: The central core zone in the undeformed (represented by solid lines) and deformed (represented by dashed lines) shape.

horizontal deformation is assumed to be equal ($\Delta v/2$), is not representative of the actual deformed shape of the core zone due to the unequal deformation in the vertical and horizontal direction. This might lead to inaccurate value of the shear modulus determined using Andreolli et al.'s [9] method based on the geometry of the deformed shape. Considering this shortcoming, Turesson et al. [23] developed a picture frame test setup, which is essentially an improvement over that used by Andreolli et al. [9]. According to Turesson et al. [23], CLT panels can be deformed along the horizontal and vertical diagonals proportionately by the same amount using the picture frame setup, which was not the case for specimen in the diagonal compression test of Andreolli et al. [9]. However, the picture frame test setup by Turesson et al. [23] will not be described here as the principle is the same as that of Andreolli et al. [9].

2.5. Turesson Method. Turesson et al. [8] carried out finite element analysis to derive some reduction factors, which when multiplied by the shear modulus value of the lumber forming the CLT (assuming each layer of CLT is formed with the same grade of lumber), will give the effective shear modulus value of the whole CLT. The reduction factor (k_{88}) ranges from a value of 0 to 1. According to Turesson et al. [8], its value is 1 for an edge-glued CLT and for a non-edge-glued CLT, it is always less than 1. While Bogensperger et al. [1] only analysed idealised representative volume subelements of CLT as discussed previously, Turesson et al. [8] analysed whole sized (1.28 m × 1.28 m) 3-layered and 5-layered CLT panels using finite element methods.

In their study, Turesson et al. [8] modelled the whole CLT panels and analysed them using proper boundary conditions by finite element analysis. Shear force was applied on the sides of the panels as surface traction forces. A simplified model of the CLT panel is shown in Figure 12. Two corner nodes were restrained against translation in the vertical and horizontal direction to prevent any rigid body motion of the panel. The

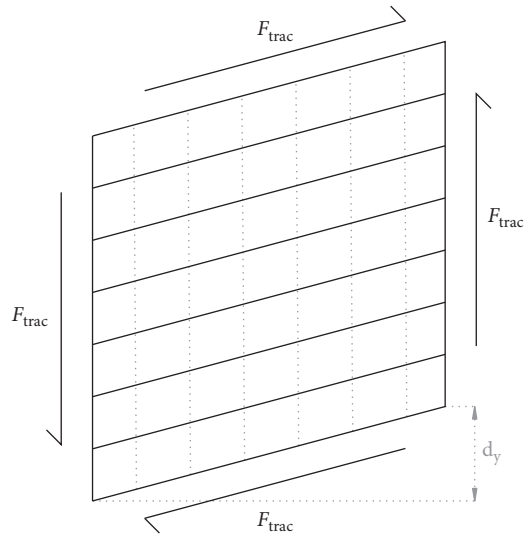

Figure 12: Finite element model of the CLT panel. The reduction factor was calculated using equation (27).

two corners on the left edge of the panel were restrained from any movement. The right edge of the panel was shifted by an amount of d_y under the action of shear force:

$$k_{88} = \frac{F_{trac}}{t_{CLT} d_y G_{lam}}, \tag{27}$$

where F_{trac} is the applied traction force in the finite element analysis software, t_{CLT} is the total thickness of the CLT, d_y is the displacement of the CLT due to the shear force, and G_{lam} is the mean shear modulus value of the laminates of the CLT.

As reflected in (27), the reduction factors were calculated relative to the shear modulus of the laminates of the CLT, G_{lam}. From the finite element analysis, Turesson et al. [8] generated charts for determining the value of the factor based on width of the laminates and thickness of each layer.

From the large range of values of the width of the laminates and thickness of the layers, practical values used in real-life CLTs can easily be determined from the charts. Turesson et al. [8] also suggested an equation to predict the correction factors based on curve fitting methods. Nevertheless, Turesson et al. [8] only studied 3- and 5-layer CLT panels, and the results cannot be extended to CLT panels with a greater number of layers.

2.6. Comparison of the Methods and Analysis of the Results. Unlike the Flaig and Blaß [5] method, Brandner et al.'s [6] method requires test results for each specific type of CLT as the E_y value will vary depending on the type of CLT. In other words, the Brandner et al. [6] model to predict the shear modulus of CLT might be considered a semiempirical approach while the Flaig and Blaß [5] model is more of a mechanics-based approach. Large-scale tests on CLT panels were carried out by Zimmerman and McDonnell [24] to determine the effective in-plane shear modulus of full-size CLT panels. The effective shear modulus values were compared against the values predicted by Flaig and Blaß [5] and Brandner et al. [6] models. From the comparison, it was observed that both methods gave underestimated values of the effective shear modulus compared to the test results. However, the values predicted by the Flaig and Blaß [5] method were further off from the test results compared to the values predicted by Brandner et al.'s [6] method. It should be noted that CLTs in the large-scale panel tests were under constant axial compression during testing which might have contributed to relatively higher effective shear modulus values. Zimmerman and McDonnell [24] also reported that the predicted effective shear moduli using these Flaig and Blaß [5] and Brandner et al. [6] methods differed by approximately a factor of two.

Flaig and Blaß [5] provided a plot of the effective shear modulus of CLT calculated using (14) with a shear modulus value of 690 MPa for the laminates and a slip modulus (K) value of 5 N/mm^3. The width of the laminates (w) has a big influence on the shear modulus value. As discussed previously, the shear modulus predicted by the Flaig and Blaß [5] method is dependent on the number of adjacent laminates in the longitudinal layers (m). However, for CLTs with the same width of the laminates, with an increasing number of laminates in the longitudinal layers (m), the difference in the predicted shear modulus values gradually decreases. The shear modulus value can be taken as constant if the number of laminates in the longitudinal layers is equal to or exceeds 10. In Figure 13, the shear modulus values of CLT predicted by the Flaig and Blaß [5] method with G_{lam} = 690 MPa, K = 5 N/mm^3, and m = 10 have been compared with the shear modulus determined by Andreolli et al. [9] and Brandner et al. [6] methods for CLT with comparable physical properties. It can be observed that the Flaig and Blaß [5] method underestimates the shear modulus value compared to the other two methods which corroborate the findings of Zimmerman and McDonnell [24]. A possible reason for the underestimated values of shear modulus by the Flaig and Blaß [5] method is the use of an inappropriate value of K. As discussed by Blaß and Flaig [13], the determination of an appropriate value of K poses a challenge in reality.

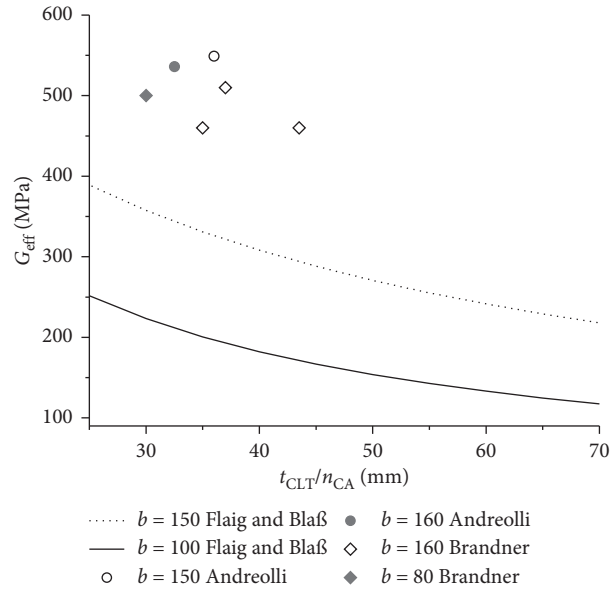

Figure 13: Effective shear modulus vs. $t_{\text{CLT}}/n_{\text{CA}}$ for CLT. The laminate width (b) is in mm.

Turesson et al. [8] suggested some shear modulus values of CLT using finite element analysis and compared these values to the experimental values of Brander at al. [6]. The difference in the values was between 0.4% and 6.9%. Brandner et al. [5] compared the shear modulus values determined from their compression tests to those predicted using the mechanical model given by Bogensperger et al. [1]. Brandner et al. [5] reported that the shear modulus values determined from the two methods were overall coherent, except for some CLTs with stress reliefs. For reducing the effects of shrinkage-swelling stresses and subsequent formation of cracks with the change of surrounding moisture content in CLT panels, stress relief was introduced by making cuts in the longitudinal laminates of the CLT panels [25]. A detailed description of CLT stress relief cut can be found in the CLT Handbook [26]. In a practical scenario, in CLTs with stress reliefs, some additional stiffness is developed due to (i) the residual bridge at the groove of the relief (the bridge occurs as the grooves are not always such that the cuts extend the full thickness of each layer) and (ii) unintentional penetration of the adhesive into the reliefs. In Figure 14, the effective shear modulus value of CLT as a fraction of the shear modulus of the laminates of the CLT determined by the methods proposed by Bogensperger et al. [1], Brandner et al. [6], Turesson et al. [8] and Andreolli et al. [9] has been plotted against the mean layer thickness-to-width of laminates ratio for CLTs with a different number of layers. Here, t_{mean} is the total thickness of the CLT divided by the number of layers and w is the width of the laminates of the CLT. For the shear modulus values from Andreolli et al. [9], the qualifier "equal" represents an equal thickness of all layers, "unequal" represents an unequal thickness of all

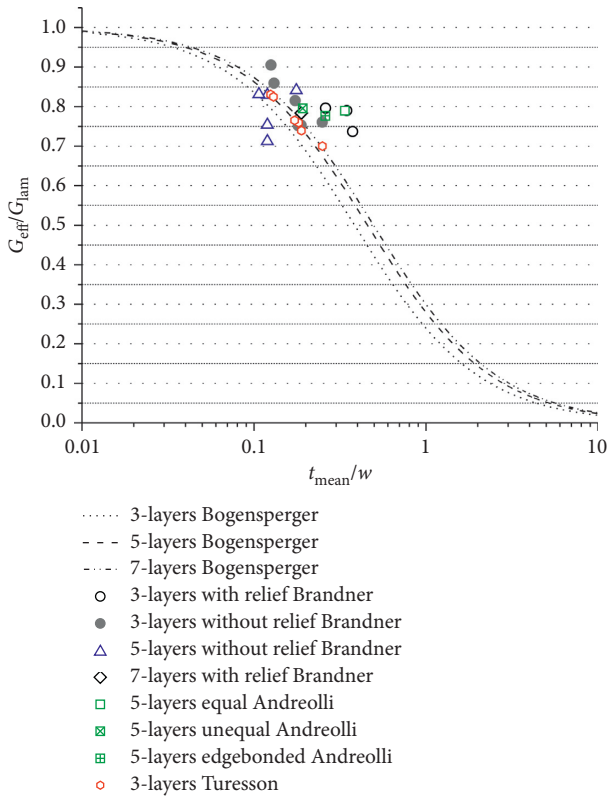

Figure 14: Effective shear modulus of CLT vs. geometric ratio t_{mean}/w.

layers, and "edgebonded" represents an edge-glued CLT. The shear modulus of an edge-glued CLT with the presence of shrinkage cracks from the study of Andreolli et al. [9] has been presented along with the shear modulus of all other non-edge-glued CLTs in Figure 14. The shear modulus value of the edge-glued CLT is similar to those of the non-edge-glued CLTs. The reason for this is the edge-glued CLT in Andreolli et al.'s [9] study had developed considerable shrinkage cracks, which eventually happens in all edge-glued CLTs in real life due to the effect of moisture-induced stresses caused by the change in surrounding moisture content. After the formation of shrinkage cracks, the behaviour of an edge-glued CLT becomes closer to that of a non-edge-glued CLT and it no longer exhibits high shear modulus values concordant with that of solid lumber.

From Figure 14, it can be observed that the shear modulus values from all the four methods are closely clustered and Brandner et al. [6] and Andreolli et al. [9] methods give slightly overestimated shear modulus values compared to Bogensperger et al.'s [1] method. Turesson et al.'s [8] method gives shear modulus values very close to those from Bogensperger et al.'s [1] method.

Turesson et al. [23] reported that Brandner et al.'s [6] method is increasingly becoming accepted as the most appropriate test setup for determining the gross shear properties of CLT. However, ensuring a pure shear stress condition remains a problem in this method. The Flaig and Blaß [5] method is very convenient as it does not require any physical testing and only the material properties of the CLT are required as input parameters. The Flaig and Blaß [5] method has the potential to become widely accepted if the relevant shear stiffness of the crossing areas under the two separate mechanisms can be properly quantified. Bogensperger et al. [1] and Turesson et al. [8] methods are mainly dependent on numerical modelling and simulation of CLT using finite element methods. As it is the case for all finite element methods, some simplified approximations are always present. For example, modelling the glue layer alone poses a challenge and the results can be drastically different depending on the method used to model the glue layer in the finite element analysis software. Andreolli et al.'s [9] method is also a very good experimental method for determining the shear modulus, but the test setup implementation remains a problem due to the large sample sizes and the requirement of fabricating special fixtures. Thus, all the methods described in this paper have some pros and cons. Each of these methods has room for improvement through further research.

3. Conclusions

Five methods for the determination of the in-plane shear modulus of CLT have been discussed in this paper. Each method has some advantages and disadvantages. Some of them require physical testing, while others are just prediction models that require the material properties of CLT as input parameters. The highlights of the five methods are as follows:

(1) The Brandner method is a semiempirical approach which gives shear modulus values close to the values from large-scale CLT panel tests. The size of the specimens used in this method is fairly large, which is cumbersome.

(2) The Flaig and Blaß method is a mechanics-based analytical approach. However, determination of one of the input properties of the analytical model and the stiffness of the crossing areas remains a challenge.

(3) The Bogensperger method is a combination of analytical and numerical approach. The analytical part of this method relies on some simplified assumptions, which might not be very accurate.

(4) The Andreolli method involves experimental determination of the shear modulus from a diagonal compression test. The geometric assumptions made in this method might not be appropriate due to the nonuniform deformation in the vertical and horizontal direction.

(5) In the Turesson method, shear modulus was found from numerical modelling. A prediction model was proposed from numerical analysis; however, the model is valid for only 3- and 5-layered CLT panels.

Further research is needed to develop a method that can accurately predict the shear modulus of CLT and that takes into account the shortcomings of all the current methods. Thus, the full potential of CLT can be utilised.

Data Availability

Most of the data have been taken from other literature studies as this is a review paper. However, the authors of this paper have reproduced all the graphs used in this paper from different sources. All the reproduced data used in this paper are available upon request from the authors of this paper.

Conflicts of Interest

The authors declare that there are no conflicts of interest regarding the publication of this paper.

Acknowledgments

Financial support to this research was provided by the Natural Sciences and Engineering Research Council of Canada (NSERC) Industrial Research Chair grant program and industrial partners: FPInnovations, Western Archrib, Landmark Group, Canadian Wood Council, ACQBuild, MTC Solutions, and Rotho Blaas. Test material was provided by Nordic Structures. Their contributions are gratefully acknowledged.

References

[1] T. Bogensperger, T. Moosbrugger, and G. Silly, "Verification of CLT-plates under loads in plane," in *Proceedings of the 11th World Conference on Timber Engineering*, Riva del Garda, Italy, June 2010.

[2] M. Shahnewaz, M. S. Alam, T. Tannert, and M. Popovski, "Cross laminated timber walls with openings: in-plane stiffness prediction and sensitivity analysis," in *Proceedings of the Annual Conference of the Canadian Society for Civil Engineering*, London, UK, June 2016.

[3] H. Ferk, "Some building science aspects for building with CLT," in *Proceedings of the European Conference on Cross Laminated Timber (CLT)-Focus Solid Timber Solutions*, pp. 207–250, Bath, UK, 2013.

[4] M. Jeleč, D. Varevac, and V. Rajčić, "Cross-laminated timber (CLT)—a state of the art report," *Gradjevinar*, vol. 70, 2018.

[5] M. Flaig and H. J. Blaß, "Shear strength and shear stiffness of CLT-beams loaded in plane," in *Proceedings of the CIB 2013*, Vancouver, Canada, May 2013.

[6] R. Brandner, P. Dietsch, J. Dröscher, M. Schulte-Wrede, H. Kreuzinger, and M. Sieder, "Cross laminated timber (CLT) diaphragms under shear: test configuration, properties and design," *Construction and Building Materials*, vol. 147, pp. 312–327, 2017.

[7] J. Zhou, Y. H. Chui, M. Gong, and L. Hu, "Elastic properties of full-size mass timber panels: characterization using modal testing and comparison with model predictions," *Composites Part B: Engineering*, vol. 112, pp. 203–212, 2017.

[8] J. Turesson, S. Berg, and M. Ekevad, "Impact of board width on in-plane shear stiffness of cross-laminated timber," *Engineering Structures*, vol. 196, Article ID 109249, 2019.

[9] M. Andreolli, M. A. Rigamonti, and R. Tomasi, "Diagonal compression test on cross laminated timber panels," in *Proceedings of the 13th World Conference on Timber Engineering*, Quebec, Canada, August 2014.

[10] H. Kreuzinger and M. Sieder, "Einfaches Prüfverfahren zur Bewertung der Schubfestigkeit von Kreuzlagenholz/Brettsperrholz," *Bautechnik*, vol. 90, no. 5, pp. 314–331, 2013.

[11] CEN, *EN 408+A1: Timber Structures–Structural Timber and Glued Laminated Timber–Determination of Some Physical and Mechanical Properties*, CEN, Brussels, Belgium, 2010.

[12] M. Flaig and N. Meyer, "A new test configuration to determine the slip modulus of connections between crosswise bonded boards," in *Proceedings of the Experimental Research with Timber*, pp. 77–84, Prague, Czech Republic, May 2014.

[13] H. J. Blaß and M. Flaig, "Stabförmige bauteile aus brettsperrholz," *Karlsruher Berichte zum Ingenieurholzbau, Bd. 24*, KIT Scientific Publishing, Karlsruhe, Germany, 2012.

[14] G. R. Cowper, "The shear coefficient in timoshenko's beam theory," *ASME: Journal of Applied Mechanics*, vol. 33, no. 2, pp. 335–340, 1966.

[15] H. J. Blaß and R. Görlacher, "Zum trag- und verformungsverhalten von brettsperrholzelementen bei beanspruchung in plattenebene," *Bauen Mit Holz*, vol. 104, pp. 34–41, 2002.

[16] R. A. Jöbstl, T. Bogensperger, and G. Schickhofer, "Mechanical behaviour of two orthogonally glued boards," in *Proceedings of the 8th World Conference on Timber Engineering*, pp. 357–364, Lahti, Finland, June 2004.

[17] CEN, *EN 338: Structural Timber-Strength Classes*, CEN, Brussels, Belgium, 2009.

[18] H. Danielsson and E. Serrano, "Cross laminated timber at in-plane beam loading–prediction of shear stresses in crossing areas," *Engineering Structures*, vol. 171, pp. 921–927, 2018.

[19] T. Moosbrugger, W. Guggenberger, and T. Bogensperger, "Cross laminated timber wall segments under homogeneous shear—with and without openings," in *Proceedings of the 9th World Conference on Timber Engineering*, Portland, OR, USA, August 2006.

[20] G. Silly, "Numerische studien zur drill- und schubsteifigkeit von brettsperrholz (BSP)," Diploma thesis, Institute for Timber Engineering and Wood Technology, Graz University of Technology, Graz, Austria, 2010.

[21] CEN, *En 16351: Timber Structures–Cross Laminated Timber–Requirements*, CEN, Brussels, Belgium, 2015.

[22] M. M. Frocht, "Recent advances in photoelasticity and an investigation of the stress distribution in square blocks subjected to diagonal compression," *ASME Transactions*, vol. 55, pp. 135–153, 1931.

[23] J. Turesson, A. Björnfot, S. Berg et al., "Picture frame and diagonal compression testing of cross-laminated timber," *Materials and Structures*, vol. 52, p. 66, 2019.

[24] R. B. Zimmerman and E. Mcdonnell, "Framework—a tall re-centering mass timber building in the United States," in *Proceedings of the New Zealand Society for Earthquake Engineering Conference*, Wellington, New Zealand, April 2017.

[25] M. He, X. Sun, Z. Li, and W. Feng, "Bending, shear, and compressive properties of three- and five-layer cross-laminated timber fabricated with black spruce," *Journal of Wood Science*, vol. 66, no. 1, p. 38, 2020.

[26] E. Karacabeyli and S. Gagnon, *Canadian CLT Handbook*, FP Innovations, Pointe-Claire, Canada, 2nd edition, 2019.

Hindawi
Advances in Civil Engineering
Volume 2021, Article ID 6637572, 9 pages
https://doi.org/10.1155/2021/6637572

Research Article

Temperature and Stress Effects on the Compressive Creep Behavior of Parallel Strand Bamboo

Yanyan Liu[1], **Yulin Bian**[2], **Dong He**[3], **Jiao Liu**[1] and **Aiping Zhou**[1]

[1]*National Engineering Research Center of Biomaterials, Nanjing Forestry University, No. 159 Longpan Road, Nanjing 210037, Jiangsu, China*
[2]*Wuxi Vocational Institute of Commerce, No. 809 Qianhu Road, Wuxi 214153, Jiangsu, China*
[3]*Dongfang Tubine Co., Ltd., No. 666 Jinshajiang Road, Deyang 618000, Sichuan, China*

Correspondence should be addressed to Yanyan Liu; liuyanyan@njfu.edu.cn

Received 25 November 2020; Accepted 25 May 2021; Published 4 June 2021

Academic Editor: Quoc-Bao Bu

Parallel strand bamboo (PSB) is an engineered bamboo product fabricated using crushed bamboo fiber bundles. Recently, this product finds applications in the civil engineering field. It is expected that the use of this composite will continue to grow because of its excellent mechanical performance, relatively low variability in material properties, and shape standardization. Modern bamboo structures made from PSB composites may be subjected to temperature variations during service. So far, however, there has been little discussion about the temperature-dependent creep. In this study, an investigation was carried out on the short-term behavior of the compressive property of PSB. A stress range of 8 to 64 MPa over a temperature range of 25°C to 75°C was considered in the 24-hour creep tests. In addition, Burgers model was adopted to describe the short-term creep behavior of PSB. Temperature and stress effects on the creep compliance of the Burgers model were also discussed.

1. Introduction

Parallel strand bamboo (PSB), a kind of engineered bamboo product, is made from raw bamboo strands which are compressed along the grain direction under high pressure. It has been proved that PSB has excellent mechanical properties and is an important alternative to traditional constructional materials [1–4]. This engineered bamboo product is considered to have great potential to be used as structural columns, beams, and flooring materials in the construction industry [5–8]. Biomaterials, such as wood and bamboo, are classified as viscoelastic materials at normal operating load, temperature, and moisture content. The viscoelastic behavior-induced microvoids and microcracking may lead to stiffness degradation and consequently develop macrocracks resulting in the premature failure of structures, of which the stress is significantly lower than expected. To avoid the creep rupture of a structural member, design codes require reductions in static strength to account for long-term performance. Therefore, it is necessary to evaluate the creep and relaxation of biomaterials since this property may affect their long-term performance.

More recently, a considerable amount of literature has been published, including mechanical properties of PSB, fracture toughness, fire resistance, and performance of PSB columns/beams [7–14]. However, few writers have been able to draw on any systematic research into the viscoelastic properties of PSB. To the authors' knowledge, no single study exists which discusses the variation of tensile/compressive properties of PSB during a wider temperature range and a time duration. Modern bamboo structures made from PSB may be subjected to temperature variations during service. For instance, on winter nights, the temperature on the surface of some structural members can reach below 0°C. In a hot climate under direct sun, however, the temperature can even rise to over 50°C [15]. Hence, characterization of PSB creep behavior under a wide temperature range is important to ensure confidence in structure design and to assess potential failure due to excessive deformation or rupture.

Over the past few decades, there have been several investigations into the creep behavior of wood and wood-based composites. 10-hour creep tests of SPF under constant temperature and humidity were performed by Kuwamura [16]. He states that when the stress level exceeds 80% of the static strength, the creep strain transitions from the secondary stage to the tertiary stage and terminates in fracture. Kobbe et al. [17–21] conducted short- and long-term creep tests on wood-based composites to evaluate the creep behavior and concluded that they are very sensitive to the magnitude of the applied load, temperature, and relative humidity changes. The overall effect of temperature was an acceleration of creep with increasing temperature. In recent times, several investigations were devoted to creep behavior of raw bamboo material [22–24]. The effects of the environmental condition and the specimen part (outer or inner culm of the bamboo stem) have been clarified. Wu [25] conducted tensile and compressive creep tests of PSB at a stress range between 10% and 40% of tensile/compressive strength under constant temperature and relative humidity. The material exhibited linear viscoelastic behavior within the applied stress levels.

The time-dependent behavior of PSB, however, is not well understood at elevated temperatures, and very little information is available. The present study sets out to assess the temperature effect on the creep behavior of PSB composites. The creep tests over a stress range of 8 MPa to 32 MPa and a temperature range of 25° to 75°C were conducted in a temperature-controlled environmental chamber. The relative humidity was set at 50%. The results and analysis from creep tests were reported in detail. Moreover, the Burgers model was adopted to evaluate the creep behavior, and the creep compliance of the Burgers model was discussed.

2. Experimental

2.1. Material and Manufacturing. The experimental material used in this study was manufactured using 5-year-old Moso bamboo from the Jiangxi province of China. Firstly, bamboo culms were split into strips which are 2 m long with a section of 15 mm in width and 3 mm in thickness. The bamboo strips were carbonized for 140 min. The temperature and pressure were 130°C and 0.3 MPa, respectively. Carbonation treatment can improve the weatherability and dimensional stability of the PSB product and reduce shrinkage and swelling deformation. The bamboo strips were then dried at 80°C temperature until they reached a moisture content of approximately 11%. After carbonizing and drying treatment, the strips were crushed into rough bamboo strands. The strands were then impregnated with water-soluble phenolic resin. The solid content of resin and the impregnation time were 25% and 14 min, respectively. Then, the strands were compressed under a pressure of 4 MPa at 160°C to make PSB panels. The curing time is related to the thickness of the PSB panel, generally 1 min/mm.

2.2. Creep Test Procedure. All the specimens used in this study were designed per ASTM D2990-17 [26]. As shown in Figure 1, the manufactured PSB panels were cut into specimens of 100 mm length with a section of 25 mm × 25 mm.

Creep tests are very sensitive. Thus, applying constant load and no shock during the creep test are expected. The creep tests were conducted in a temperature-controlled environmental chamber controlled to 50% relative humidity. Three temperature levels of 25°C, 50°C, and 75°C and three stress levels of 8 MPa, 16 MPa, and 32 MPa were selected. Initially, the stress level of 64 MPa was also selected. However, the specimens at the stress level of 64 MPa and the temperature of 50°C and 75°C failed prematurely. Only at 25°C, strain data under the stress of 64 MPa were recorded during the whole creep test. Thus, we also reported the results of 64 MPa in Section 3.1. Specimen temperatures during the creep tests were maintained within a tolerance of ±1°C to the target temperature. The average value of the ultimate static strength of PSB is 106.7 MPa at 25°C and drops to 42.7 MPa at 75°C. Hence, the lowest stress level 8 MPa was about 7.5% of the compressive strength at 25°C and 18.7% of that at 75°C. The highest stress level 32 MPa was about 30% of the compressive strength at 25°C and 74.9% of that at 75°C. All the specimens were preconditioned for the target temperature. Each creep test lasted 24 hours. The load, deformation, and time were recorded immediately following loading and at an interval of 15 s in the first hour and then at an interval of 75 s for the next 23 hours. The test setup and environmental chamber arrangement are shown in Figure 2(a), whereas the schematic representation is shown in Figure 2(b).

Since scatter in the properties is unavoidable in PSB, creep tests set at each test condition were repeated three times to improve the confidence of the test results. These specimens were named "Temperature-stress-No." For example, the specimens tested at 25°C and 8 MPa were named "25°C-8 MPa-1/2/3." The average results using three separate specimens were adopted for discussion.

3. Results and Discussion

3.1. Creep Behavior at Room Temperature. The time-dependent behavior of PSB specimens at 25°C and different stress levels is displayed in Figure 3. All the specimens showed similar behavior, and no creep rupture was observed.

The specimens first suffered an instantaneous strain upon loading. The instantaneous strain was expected to be more pronounced for greater loading. Such behavior can be seen in Figure 3. The strain then increased over time. This time-dependent response is creep strain. Creep behavior of wood composites is generally considered to have three stages [27, 28]. As shown in Figure 4, they are primary, secondary, and tertiary stages. Generally, primary creep occurs in a relatively short period of time. During the primary stage, the strain usually increases with a continuously decreasing strain rate. Then, the secondary creep stage with a constant strain rate is usually reached. The duration of the secondary stage is related to material properties, the level of sustained loading, and the loading condition. The tertiary stage usually indicates progressive failure of the material. It is clear that, at the

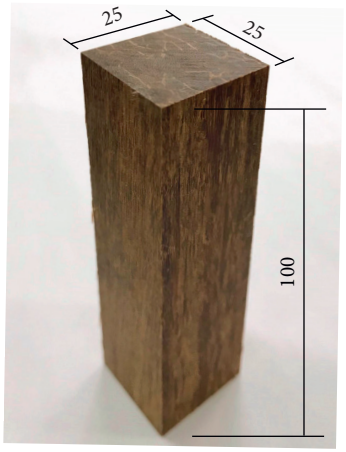

Figure 1: PSB specimen for the compressive creep test (unit: mm).

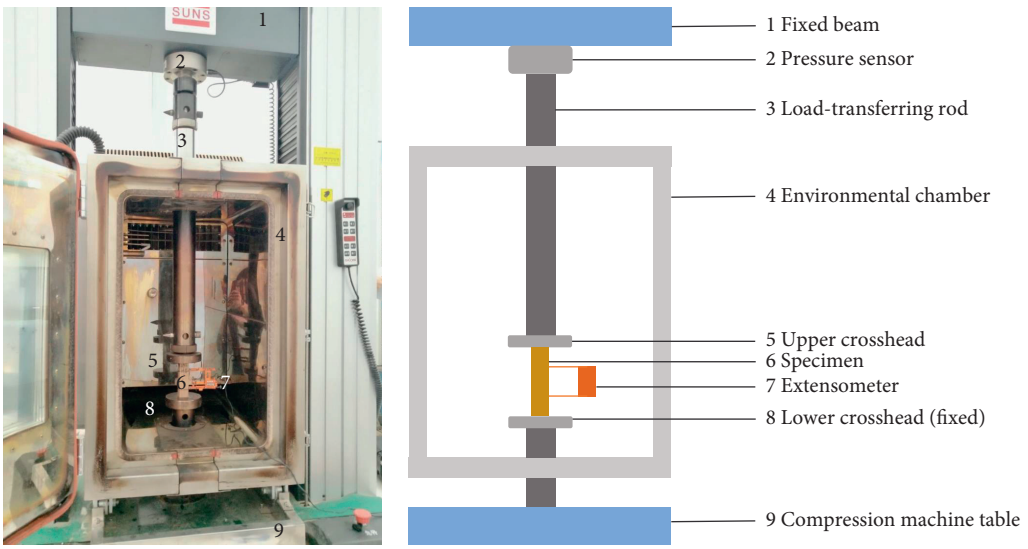

Figure 2: Experimental setup used in this study. (a) Test setup for loading. (b) Schematic of the test setup.

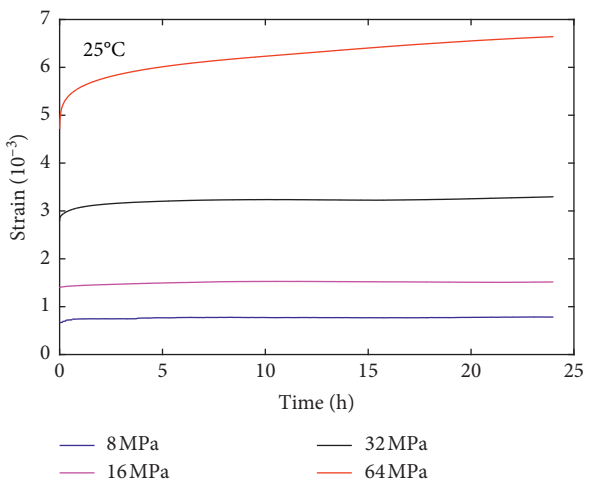

Figure 3: Creep behavior of PSB at 25°C and different stress levels.

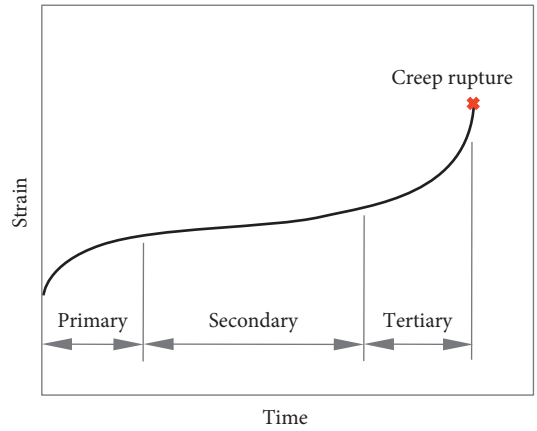

Figure 4: Three stages of the creep curve.

end of the tests, all specimens stay in the secondary creep stage.

The creep responses in the range of 8–64 MPa at 25°C are similar such that creep strains increase over time. As shown in Figure 3, the stress levels had an influence on the amount of creep strain of PSB material. The higher the level of sustained loading, the larger the creep strain. From the figure, we can see that, at the end of the tests, the creep strain was 0.79×10^{-3} under the stress level of 8 MPa. The creep strain increased to 3.30×10^{-3} at the stress level of 32 MPa and further increased to 6.64×10^{-3} at the stress level of 64 MPa. These results suggest that, at the temperature of 25°C, the increase in creep strain was proportional to the increase in stress within the range of this study.

When observing the creep curves plotted in Figure 3, note that the strain rate at 64 MPa is higher than the lower stress level. The observed difference may indicate the existence of a change in the creep mechanism at the high stress level. At lower stress levels, the creep is mainly induced by the molecular motions, while at higher stress levels, the creep may be dominated by the damage that occurred in the material.

3.2. Creep Behavior at Elevated Temperature. Considering the variation of seasonal temperatures in the south area of China, temperature variations at the surface of structural members are estimated to range from 25°C to 75°C.

Figure 5 may help us understand the temperature effect on creep behavior. At a constant stress level, the creep strain increased with the temperature. A possible explanation for this might be that exposure to high temperatures reduces the stiffness of PSB material [11]. At the stress levels of 8 MPa and 16 MPa, the creep strain at the end of the test was increased 2 times when the temperature was increased from 25 to 75°C. In the creep test under 75°C with the sustained load of 32 MPa, two specimens (75°C-32 MPa-1 and 75°C-32 MPa-3) failed within 24 hours. Therefore, the creep curve of 75°C in Figure 5(c) is not the average result, but the result of specimen 75°C-32 MPa-2.

It can be seen from Figures 3 and 5 that the temperature and stress level have a great influence on the amount of creep strain of PSB material. However, the strain rate appeared to be unaffected by the temperature and stress levels, except for the case with the stress of 32 MPa and temperature of 75°C.

Although this study was not intended to investigate the creep rupture of PSB material, specimen failure was recorded at the stress level of 32 MPa. As shown in Figure 6, the specimens enter the tertiary stage when the load is maintained for 17-18 hours. The creep deformation increases sharply, leading to creep rupture, indicating the likelihood of some material damage resulting from the increased temperature and sustained loading in this case. Such results suggest that although the bamboo-based structure is designed at low stress levels, high temperature and long time may still cause large creep deformation and even material failure.

4. Modeling of Creep

4.1. Burgers Model. To evaluate the time-dependent behavior of PSB material, a reliable and widely accepted model is needed. The generalized Kelvin model has been proven to apply to a variety of viscoelastic materials [29, 30]. Since this study focuses on the short-term creep behavior, the Burgers model which can be seen as a simple generalized Kelvin model consisting of one Kelvin unit is adopted here.

The Burgers model consisting of a Maxwell unit and a Kelvin unit in series is reasonably simple, as shown in Figure 7(a). Considering a creep test of a PSB specimen under compression, the behavior of the Burgers model can be understood as the combination of the element behavior connected in series in Figure 7(a). Thus, the total strain of the Burgers model at time t is decomposed into three parts:

$$\varepsilon(t) = \varepsilon_1(t) + \varepsilon_2(t) + \varepsilon_3(t), \quad (1)$$

where ε_1, ε_2, and ε_3 are the strain of the spring, Newton's dashpot, and the Kelvin unit, respectively. Given the stiffness and viscosity of the elements in the Burgers model, ε_1, ε_2, and ε_3 can be expressed as

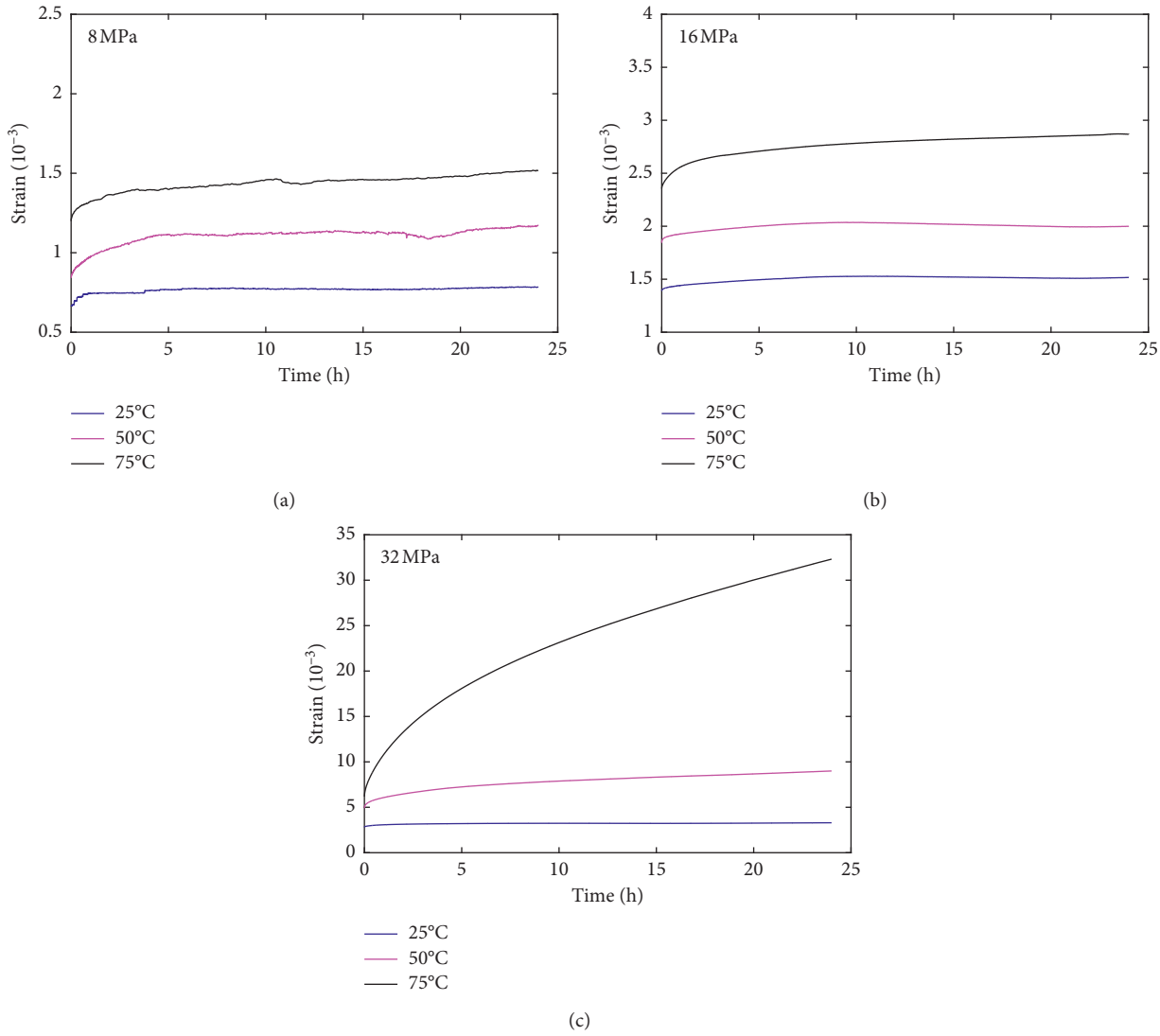

Figure 5: Creep behavior of PSB at temperatures between 25 and 75°C. (a) Creep test results at constant loading of 8 MPa. (b) Creep test results at constant loading of 16 MPa. (c) Creep test results at constant loading of 32 MPa.

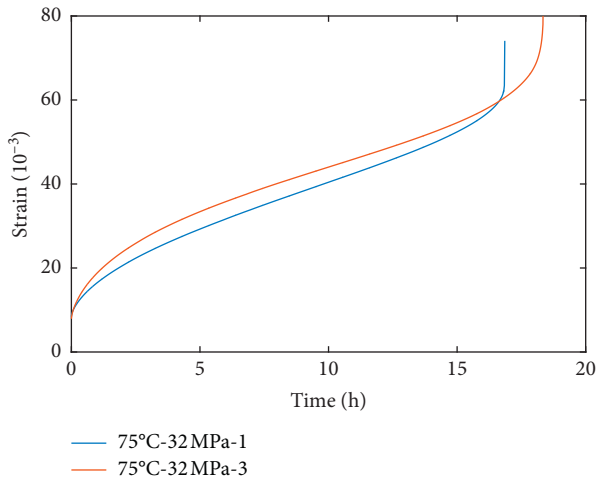

Figure 6: Creep rupture of specimens at 75°C and 32 MPa.

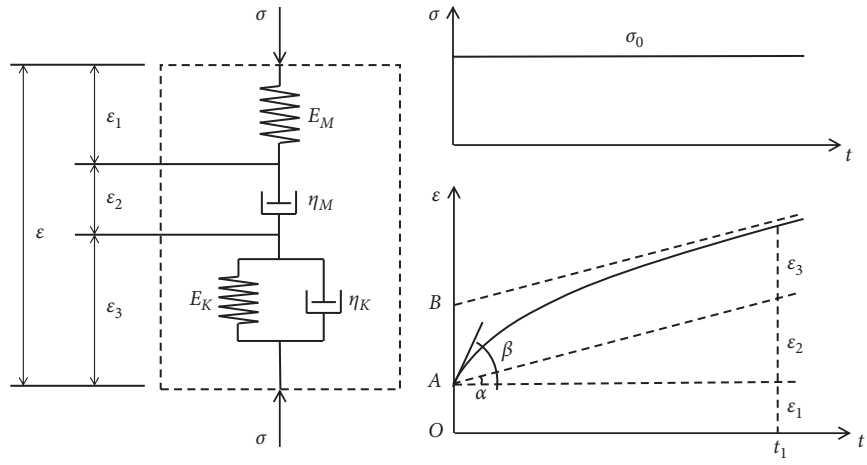

Figure 7: Burgers model. (a) Schematic illustration. (b) Creep response under a constant load.

$$\varepsilon_1 = \frac{\sigma}{E_M}, \tag{2}$$

$$\dot{\varepsilon}_2 = \frac{\sigma}{\eta_M}, \tag{3}$$

$$\dot{\varepsilon}_3 + \frac{E_K}{\eta_K}\varepsilon_3 = \frac{\sigma}{\eta_K}, \tag{4}$$

where E_M and η_M are the stiffness and viscosity of the Maxwell unit, respectively, and E_K and η_K are the stiffness and viscosity of the Kelvin unit, respectively.

The creep response of the Maxwell model is the sum of the spring and Newton's dashpot:

$$\varepsilon_1(t) + \varepsilon_2(t) = \frac{\sigma}{E_M} + \frac{\sigma}{\eta_M}t. \tag{5}$$

On the right-hand side of (5), the first term represents the instantaneous elastic strain since the spring will act immediately upon loading. The second term represents viscous flow because it takes time for the dashpot to build up the strain.

The creep behavior of the Kelvin model is expressed by solving first-order nonhomogeneous ordinary differential equation (4) with the initial condition $\varepsilon_3(0) = 0$. Thus,

$$\varepsilon_3(t) = \frac{\sigma}{E_K}\left(1 - e^{-\left(E_K/\eta_K\right)^t}\right). \tag{6}$$

The right-hand term of (6) represents delayed elasticity of the Kelvin model. Then, the creep strain of the Burgers model can be expressed as follows:

$$\varepsilon(t) = \frac{\sigma}{E_M} + \frac{\sigma}{\eta_M}t + \frac{\sigma}{E_K}\left(1 - e^{-\left(E_K/\eta_K\right)^t}\right). \tag{7}$$

Differentiating (7) yields the creep rate $\dot{\varepsilon}$:

$$\dot{\varepsilon}(t) = \frac{\sigma}{\eta_M} + \frac{\sigma}{\eta_K}e^{-\left(E_K/\eta_K\right)^t}. \tag{8}$$

Based on the knowledge of the physical response of simple elements in the Burgers model, the material constants E_M, η_M, E_K, and η_K can be determined as follows:

$$\overline{OA} = \frac{\sigma}{E_M}, \tag{9a}$$

$$\tan\alpha = \frac{\sigma}{\eta_M}, \tag{9b}$$

$$\overline{AB} = \frac{\sigma}{E_K}, \tag{9c}$$

$$\tan\beta = \frac{\sigma}{\eta_M} + \frac{\sigma}{\eta_K}, \tag{9d}$$

where the four values $\overline{OA}$, $\overline{AB}$, α, and β illustrated in Figure 7(b) are obtained from the creep curve.

Figure 8 compares the Burgers model with the creep test results. Both primary and secondary creep stages can be well represented by the Burgers model. The comparison demonstrates the effectiveness of this model to evaluate the short-term creep behavior of this material.

4.2. Creep Compliance. The creep response of Burgers model (7) may also be written in the form

$$\varepsilon(t) = \sigma J(t) = \sigma\left(J_0 + J_\eta t + J_K\left(1 - e^{(-t)/\tau}\right)\right), \tag{10}$$

and $J(t)$ is defined as the creep strain resulting from unit stress, known as the compliance function. It is the viscoelastic material property used to describe behavior during creep loading. J_0 is the initial compliance. It is time independent and only related to the elastic modulus of the spring in the Maxwell unit. J_η is the delayed compliance due to the viscosity of the dashpot in the Maxwell unit. J_K and τ are the delayed compliance and retardation time due to the Kelvin unit in the Burgers model.

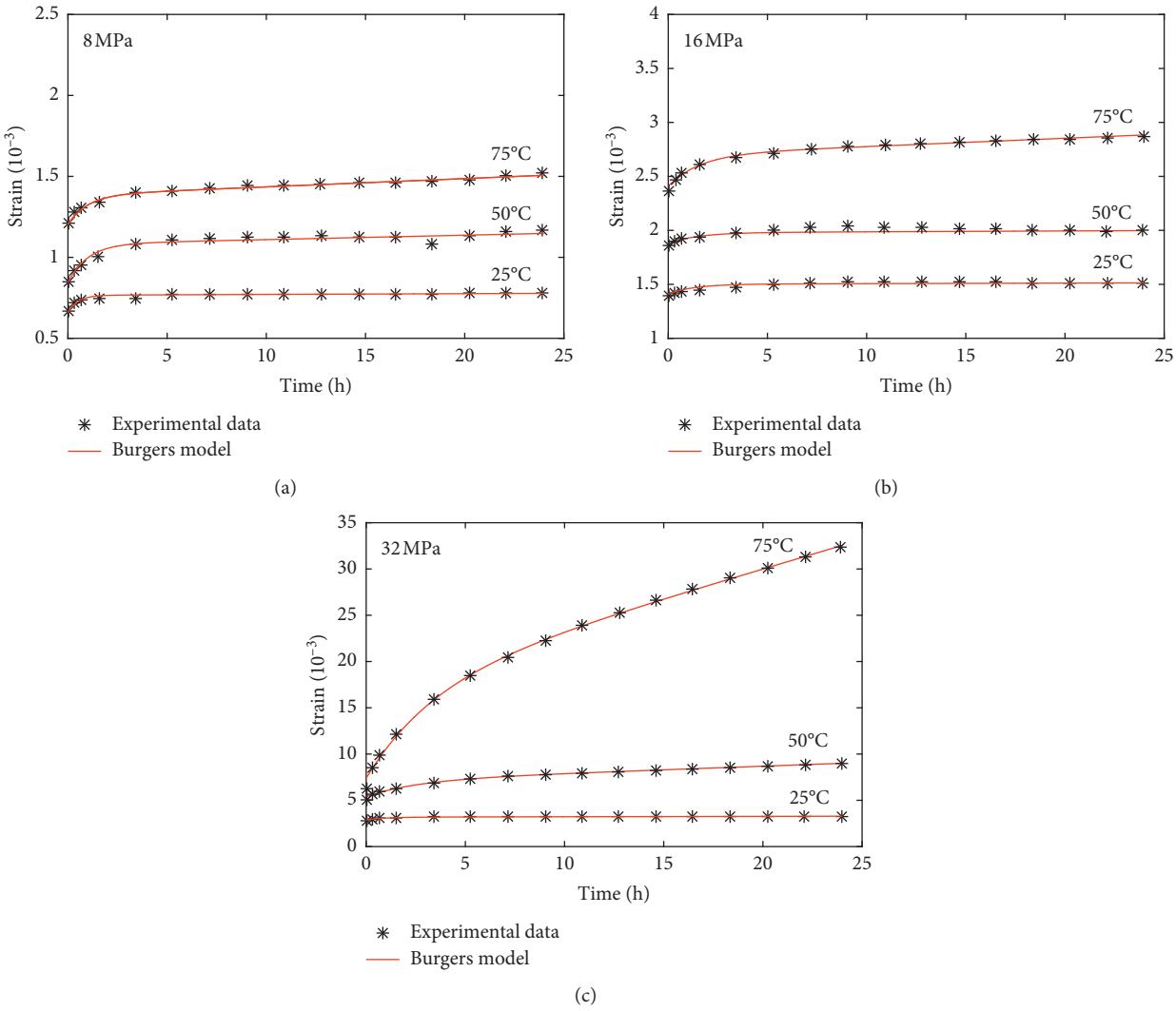

Figure 8: Measurements and Burgers model predictions for creep strain. (a) At constant loading of 8 MPa. (b) At constant loading of 16 MPa. (c) At constant loading of 32 MPa.

Table 1: Creep compliance and retardation time.

Condition	J_0	J_η	J_K	τ
25°C-8 MPa	823.3	0.6	134.3	0.5
50°C-8 MPa	1055	3.4	297.8	1.0
75°C-8 MPa	1495	6.4	224.9	1.2
25°C-16 MPa	881.4	0.3	57.1	1.3
50°C-16 MPa	1175	0.5	61.5	1.5
75°C-16 MPa	1566	4.8	181.2	1.6
25°C-32 MPa	902.3	1.3	91.6	1.0
50°C-32 MPa	1686	24.3	543.3	2.6
75°C-32 MPa	2307	198.2	3110	3.4

The compliance J_0, J_η, J_K and the time quantity τ are key characteristic properties of the model. Indeed, no knowledge of each element in the Burgers model is necessary. The creep response of a material can be completely characterized provided the creep compliance is known. The compliance can be derived from the data collected in the creep tests, as summarized in Table 1.

Figure 9 compares creep compliance values determined using different stress levels at elevated temperatures. Evaluating the compliance shows that compliance is temperature dependent. There is an increasing trend with temperature, especially at higher stress level. At a temperature of 25°C, the compliance values are basically identical when the loads are no more than 32 MPa, 30% of the static strength. This

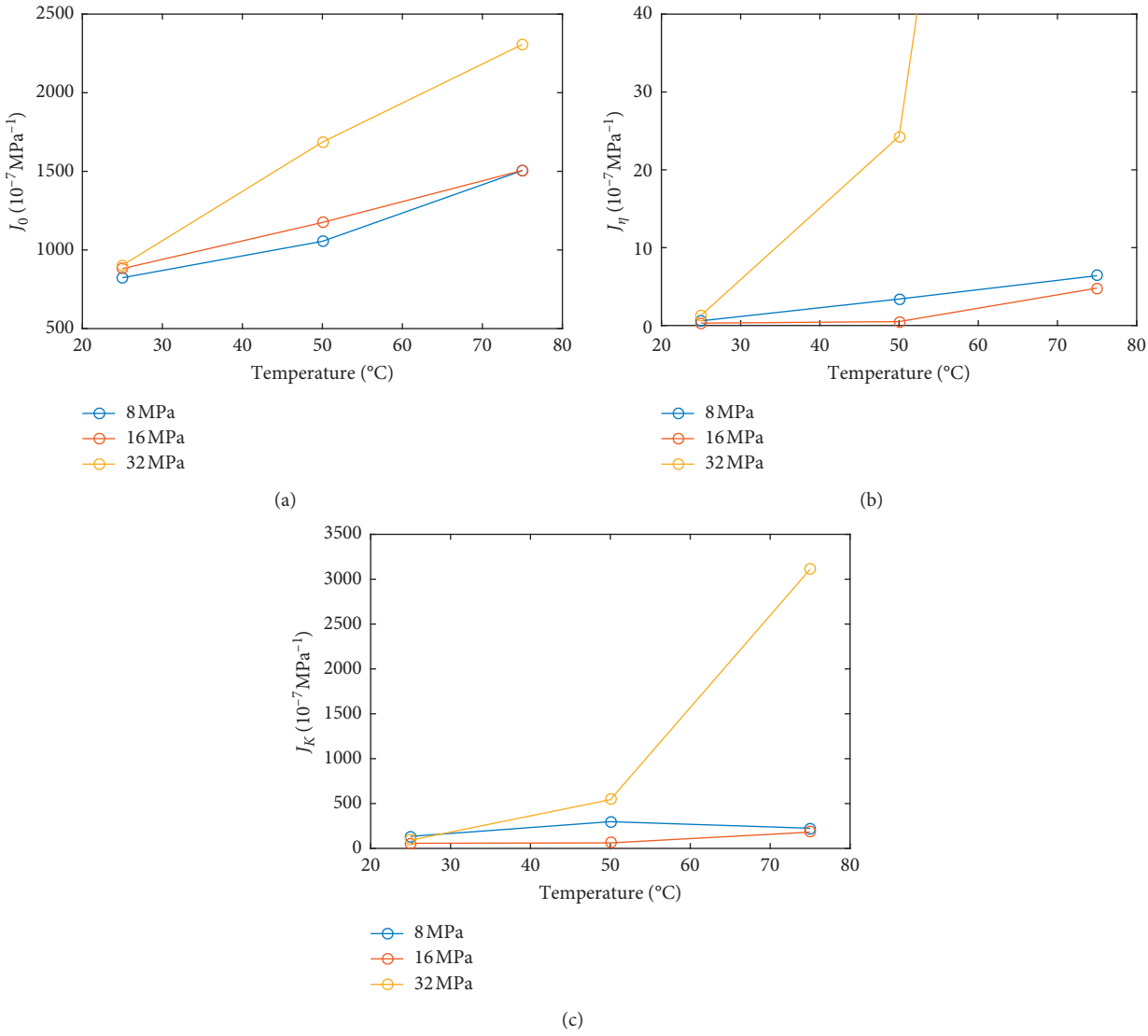

Figure 9: Evaluation of the creep compliance. (a) Initial compliance J_0. (b) Delayed compliance J_η. (c) Delayed compliance J_K.

indicates the linear viscoelastic behavior of PSB at relatively low temperature and under relatively low stress. High temperature and stress level may increase the creep compliance, leading to larger creep deformation.

5. Conclusions

The present study was designed to investigate the temperature and stress effect on the compressive creep behavior of PSB. The creep tests over a stress range of 8 MPa–32 MPa and a temperature range of 25°C–75°C were conducted in a temperature-controlled environmental chamber. At a constant load, the creep strain showed an increasing trend with the temperature. Elevated stress and temperature levels resulted in a noticeable higher creep rate, possibly indicating the existence of a different creep mechanism compared with relatively low stress and temperature conditions. Creep rupture observed in the creep test under 32 MPa and 75°C demonstrates that although the bamboo-based structure is designed at low stress levels, high temperature and a long time may still cause large creep deformation and even material failure.

Burgers model has proven to be an effective model for short-term creep behavior of PSB material. Using the Burgers model, the primary and secondary creep stage was predicted with accuracies at all stress and temperature levels. The creep compliance of the Burgers model is basically identical at 25°C when the load is no more than 32 MPa, indicating the linear viscoelastic creep behavior of PSB at relatively low temperature and stress. High temperature and stress levels may increase the creep compliance, leading to larger creep deformation. While the Burgers model can be helpful in interpreting observed creep behavior, the model is only valid for conditions within the range of this study. In

the future study, it is necessary to demonstrate the effectiveness of the model when used outside the conditions studied.

Data Availability

The data used to support the findings of this study are available from the corresponding author upon request.

Conflicts of Interest

The authors declare that they have no conflicts of interest.

Acknowledgments

The authors gratefully acknowledge the financial support provided by the National Natural Science Foundation of China (Grant nos. 51978338 and 52008212).

References

[1] X. Sun, M. He, and Z. Li, "Novel engineered wood and bamboo composites for structural applications: state-of-art of manufacturing technology and mechanical performance evaluation," *Construction and Building Materials*, vol. 249, Article ID 118751, 2020.

[2] C. Y. T. Ming, W. K. Jye, and H. A. I. Ahmad, "Mechanical properties of bamboo and bamboo composites: a review," *Journal of Advanced Research in Materials Science*, vol. 35, no. 1, pp. 7–26, 2017.

[3] A. Kumar, T. Vlach, L. Laiblova et al., "Engineered bamboo scrimber: influence of density on the mechanical and water absorption properties," *Construction and Building Materials*, vol. 127, pp. 815–827, 2016.

[4] D. Huang, Y. Bian, A. Zhou et al., "Experimental study on stress-strain relationships and failure mechanisms of parallel strand bamboo made from phyllostachys," *Construction and Building Materials*, vol. 77, pp. 130–138, 2015.

[5] B. Sharma, A. Gatoo, M. Bock et al., "Engineered bamboo: state of the art," *Construction Materials*, vol. 168, pp. 57–67, 2015.

[6] B. Sharma, A. Gatoo, M. Bock et al., "Engineered bamboo for structural applications," *Construction and Building Materials*, vol. 81, pp. 66–73, 2015.

[7] D. Huang, Y. Bian, D. Huang et al., "An ultimate-state-based-model for inelastic analysis of intermediate slenderness PSB columns under eccentrically compressive load," *Construction and Building Materials*, vol. 94, pp. 306–314, 2015.

[8] X. Wang, A. Zhou, and Y. H. Chui, "Load-carrying capacity of intermediately slender parallel strand bamboo columns with a rectangular cross section under biaxial eccentric compression," *Bioresources*, vol. 13, pp. 313–330, 2018.

[9] M. Xu, Z. Cui, Z. Chen et al., "The charring rate and charring depth of bamboo scrimber exposed to a standard fire," *Fire and Materials*, vol. 42, pp. 750–759, 2018.

[10] Y. Zhong, H. Ren, and Z. Jiang, "Effects of temperature on the compression strength parallel to the grain of bamboo scrimber," *Materials*, vol. 9, no. 6, Article ID 436, 2016.

[11] M. Xu, Z. Cui, Z. Chen et al., "Experimental study on compressive and tensile properties of a bamboo scrimber at elevated temperatures," *Construction and Building Materials*, vol. 151, pp. 732–741, 2017.

[12] F. K. Liew, S. Hamdan, M. R. Rahman, and M. Rusop, "Thermomechanical properties of jute/bamboo cellulose composite and its hybrid composites: the effects of treatment and fiber loading," *Advances in Materials Science and Engineering*, vol. 2017, Article ID 8630749, 10 pages, 2017.

[13] D. Huang, B. Sheng, Y. Shen et al., "An analytical solution for double cantilever beam based on elastic-plastic bilinear cohesive law: analysis for mode I fracture of fibrous composites," *Engineering Fracture Mechanics*, vol. 193, pp. 66–76, 2018.

[14] Z. Huang, D. Huang, Y. H. Chui et al., "A bi-linear cohesive law-based model for mode II fracture analysis: application to ENF test for unidirectional fibrous composites," *Engineering Fracture Mechanics*, vol. 213, pp. 131–141, 2019.

[15] J. Long, *Thermal and Moisture Stress Analysis of Bamboo Buildings Based on Heat and Mass Transfer Method of Porous Medium*, Hunan University, Hunan, China, 2013, in Chinese.

[16] H. Kuwamura, "Creep limit of wood under parallel-to-grain compression," *Journal of Structural and Construction Engineering AIJ*, vol. 77, no. 681, pp. 1691–1700, 2012, in Japanese.

[17] R. G. Kobbe, "*Creep behavior of a wood-polypropylene composite*," M.S. thesis, Washington State University, Pullman, WA, USA, 2005.

[18] P. E. Nur Yazdani, E. Johnson, and S. Duwadi, "Creep effect in structural composite lumber for bridge applications," *Journal of Bridge Engineering*, vol. 9, pp. 87–94, 2004.

[19] J. Tissaoui, *Effects of long-term creep on the integrity of modern wood structures*, Ph.D. thesis, Virginia Polytechnic Institute and State University, Blacksburg, VA, USA, 1996.

[20] T. Liu, "Creep of wood under a large span of loads in constant and varying environments," *Holz als Roh- und Werkstoff*, vol. 51, pp. 400–405, 1993.

[21] D. M. Holzer, J. R. Loferski, and D. A. Dillard, "A review of creep in wood: concepts relevant to develop long-term behavior predictions for wood structures," *Wood and Fiber Science*, vol. 21, pp. 376–392, 1989.

[22] X. Ma, X. Liu, Z. Jiang et al., "Flexural creep behavior of bamboo culm (Phyllostachys pubescens) in its radial direction," *Journal of Wood Science*, vol. 62, pp. 487–491, 2016.

[23] J. Gattron, K. A. Harries, and Q. Xu, "Creep behavior of bamboo," *Construction and Building Materials*, vol. 66, pp. 79–88, 2014.

[24] T. Tsubaki and T. Nakano, "Creep behavior of bamboo under various desorption conditions," *Holzforschung*, vol. 64, pp. 489–493, 2010.

[25] P. Wu, "Experiment and analysis on creep properties of reconsolidated bamboo," Master's thesis, Northeast Forestry University, Harbin, China, 2015.

[26] ASTM D2990-17, *Standard Test Methods for Tensile, Compressive, and Flexural Creep and Creep-Rupture of Plastics*, ASTM International, West Conshohocken, PA, USA,, 2017.

[27] I. Smith, E. Landis, and M. Gong, *Fracture and Fatigue in Wood*, John Wiley and Sons Ltd., West Sussex, UK, 2003.

[28] R. G. Kobbe, "*Creep behavior of a wood-polypropylene composite*," M.S. thesis, Washington State University, Whitman country, Pullman, WA, USA, 2005.

[29] A. Shukla and Y. M. Joshi, "Boltzmann superposition principle for a time-dependent soft material: assessment under creep flow field," *Rheologica Acta*, vol. 56, pp. 927–940, 2017.

[30] M. M. Hassani, F. K. Wittel, S. Hering et al., "Rheological model for wood," *Computer Methods in Applied Mechanics and Engineering*, vol. 283, pp. 1032–1060, 2015.

Hindawi
Advances in Civil Engineering
Volume 2021, Article ID 6669967, 12 pages
https://doi.org/10.1155/2021/6669967

Research Article

Research on the Seismic Performance of Straw Panel-Infilled Concrete Frame by Shaking Table Test

Jia Zhu,[1,2] **Yuling Bian**,[3] **and Aiping Zhou**[1]

[1]*National Engineering Research Center of Biomaterials, Nanjing Forestry University, Nanjing 210037, China*
[2]*School of Architecture and Transportation Engineering, Guilin University of Electronic Technology, Guilin 541004, China*
[3]*Wuxi Vocational Institute of Commerce, 809 Qianhu Rd., Wuxi 214153, China*

Correspondence should be addressed to Yuling Bian; bianyuling@wxic.edu.cn

Received 23 December 2020; Revised 21 February 2021; Accepted 24 April 2021; Published 5 May 2021

Academic Editor: Jian Ji

Infill wall-frame interaction-induced damage and failure have been found in many previous earthquakes due to the inappropriate estimation of the stiffness of infill walls. It is a common knowledge of design philosophy that properly lowering the lateral stiffness of infill wall may significantly improve the seismic performances of concrete frames. Fabricated straw wall, a sandwich-type structure with tenon and groove, is proposed as a new type of lightweight and environment-friendly infill wall. The lateral stiffness is much lower than that of masonry infill wall. Shaking table tests were carried out for a concrete frame structure with fabricated straw wall, as well as for a frame with masonry infill wall for comparison. Results show that failure modes of them are different. Plastic hinges took place at the ends of beams in the frame with fabricated straw infill wall, different from the frame with masonry infill wall where the plastic hinges emerged at the ends of columns. Numerical analysis was conducted to verify and illustrate the failure mechanism. It indicates that the straw panel-infilled concrete frame well matches the design philosophy and presents better seismic performance.

1. Introduction

Masonry infill wall used as partial wall of reinforced concrete frame structures is usually treated as the nonstructural component in design philosophy. However, masonry infill wall exerts a significant effect on the stiffness of frame structures [1–4] and the structural dynamic performances [5]. Design codes [6, 7] take a natural vibration period reduction factor to account for the stiffness contribution of the masonry infill walls; e.g., the factor is specified as 0.6–0.9 by the Chinese code [7].

The current design philosophy poses serious problems, as it did in the case of Wenchuan earthquake. On May 12, 2008, an Ms8.0 earthquake struck Wenchuan area where masonry infill wall is extensively adopted. A 3-story building of frame structure in Beichuan is shown in Figure 1 [8]. To set street shops for the building, few infill walls were set on the ground floor, while many infill walls were arranged on other floors, making the ground floor much weaker than other layers. Finally, all the bottom columns broke at ends, and the whole building inclined dramatically. The same type of failure is presented in Figure 2 [9]. It is a damaged column of a 6-story building in Dujiangyan city. Its ground floor acted as a garage with no walls. Infill walls on the upper floors made the stiffness vary greatly between the first and second story, so the damage of bottom columns occurred.

Witnessing all these damages and failure induced by the interaction between the masonry infill wall and concrete frame [2, 4, 9], the significant role of masonry infill walls in frame structures is gradually realized. Related experiments [10–12] and numerical analyses [13–15] are conducted by different scholars. Some codes [16, 17] recommend struts to represent masonry infill walls in calculations. However, due to the scattered data offered by different experiments, along with the difficulty in modeling brittle materials [18], a widely accepted method to precisely consider the masonry stiffness is still absent.

To eliminate the great disparity in lateral stiffness between stories generated by masonry infill walls, arranging

Figure 1: Damage of a 3-story frame structure [8].

Figure 2: Damage of the bottom columns of a 6-story building [9].

masonry infill walls equivalently on each story is a simple way. However, this method is generally not practical, since the main entrances, garage, or stores are often set on the first floor. Due to the need for rational use of space, the layout of masonry infill walls on first floor is quite limited. An effective approach is to lower the stiffness of the masonry infill wall directly. Either decreasing their total number or replacing the masonry with other proper materials would work. By proposing a sandwich-type of fabricated straw panel, the latter method is chosen and studied.

2. Fabricated Straw Brick

To properly replace the masonry bricks, a sandwich-type of fabricated straw panel is advanced. With a low elastic modulus [19], straw panels own much lower stiffness compared with masonry bricks [20]. Due to the flexible tenon connection between straw panel and frame, a certain deformation is allowed under horizontal loads and actions. Thus, the interaction between the straw panel infill wall and concrete frame is weak. It also shares the characteristics of sound insulation and self-heat insulation [21–24]. Meanwhile, the straw panels are remarkably fire-resistant considering the compactness [25].

The proposed straw panel is a sandwich structure with tenon and groove, consisting of a low-density straw board ($\rho \leq 400\,kg/m^3$) and 2 high-density straw boards ($\rho \geq 700\,kg/m^3$). The low-density board with good thermal insulation and sound insulation performance is used as the lining, of which 2 high-density boards are placed on both sides. The lower end of the low-density lining board is a groove. The high-density outer panel and the low-density lining board are staggered to form a tenon and groove. Considering the requirements of the building modulus and the conditions in the transportation and construction process, the size of the straw panel is decided as shown in Figure 3.

Shaking table tests were carried out for a straw panel-infilled frame, as well as for a masonry infilled frame for comparison, to study their seismic performance.

3. Experimental Investigation

3.1. Experimental Design

3.1.1. Similitude of the Model. Scale models are used in the shaking table tests, which are representative of the prototype structure according to a certain similar relationship. The designed similitude of model is presented in Table 1.

3.1.2. Experimental Model Design. The test models of the frame structures are 1/3 scale models of the prototype structure. Two identical reinforced concrete frames are designed for comparison. Each frame is a 1-bay, 3-story structure, filled with masonry bricks or straw panels, respectively. All frame beams, columns, and floor (roof) panels are cast-in-place.

In order to ensure the consistency of these 2 concrete frames, synchronous construction and simultaneous pouring are adopted, and each layer of steel and concrete is obtained from the same batch of materials. (For the convenience of description in this article, the frame with masonry bricks is called brick frame, and the frame with straw panels is called straw frame.) The geometrical sizes of models are presented in Tables 2 and 3 .

According to the Chinese Code for Design of Concrete Structures [26], the component layout and the reinforcement diagrams of components in the test structures are designed and shown in Figures 4–6 . The straw brick is presented in Figures 3 and 7, and the photo of test structures is shown in Figure 8.

3.1.3. Construction and Installation of Infill Walls. As the brick frame is filled with masonry bricks, its infill wall was constructed in accordance with the requirements of the Chinese current code [27].

There are currently no relevant regulations or specifications as references for straw frame, so the installation plan was determined based on the principle of structural stability, the geometrical sizes of straw brick, and the suggestions of the manufacturer's technicians. Figure 9 illustrates the connections between straw components and frame; specific installation steps are as follows:

(1) While the straw bricks with tenon and groove are easy to connect with each other vertically, vertical long straw strips were needed to link the boards horizontally with air nails to enhance the integrity of

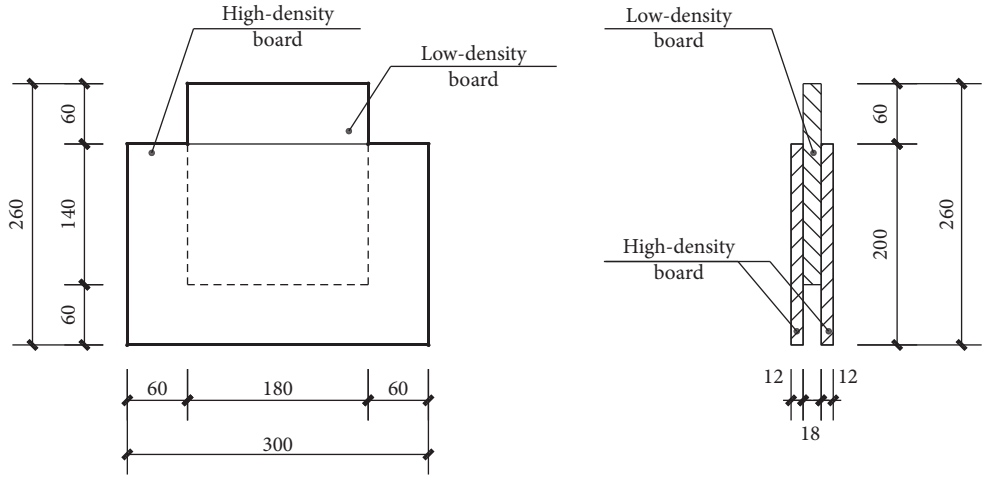

Figure 3: Geometrical sizes of a straw brick (unit: mm).

Table 1: Designed similitude of the model.

Type	Physical properties	Dimension	Similitude	Similarity constant
Material features	Stress	FL^{-2}	$S_\sigma = S_E$	1
	Modulus of elasticity	FL^{-2}	S_E	1
	Mass density	FT^2L^{-4}	$S_\rho = S_E/S_l$	3
Geometrical features	Length	L	S_l	1/3
	Mass	$FL^{-2}T^2$	$S_m = S_\rho S_l^3$	1/9
Dynamic features	Stiffness	FL^{-1}	$S_k = S_E S_l$	1/3
	Acceleration	LT^{-2}	$S_a = S_l/S_t^2$	1

Table 2: Geometrical sizes of models (unit: m).

Structure	Length	Width	Height
Prototype structure	4.5	4.5	9
Test structures	1.5	1.5	3

Table 3: Geometrical sizes of components (unit: mm).

Structure	Column		Beam		Slab
	H_c	B_c	H_b	B_b	
Prototype structure	300	300	300	150	120
Test structures	100	100	100	50	100

the straw wall. The straw strips, with the basic geometric size of 120 mm × 18 mm × 900 mm, could be perfectly stuck between two horizontally adjacent straw boards, as shown in Figure 9.

(2) Straw strips and frame beams are fixed by embedded parts to avoid slipping and falling off during the vibration. The 10-centimeter-long steel bars in Figure 9 acted as the embedded parts whose diameter is 12 mm. Proper holes were reserved at the ends of the straw strips for the embedded parts.

(3) To prevent the straw wall from falling off or tilting out of the frame, steel plates were used to fix the straw wall to the frame. The steel plates were coated with glue to ensure the connection between the straw wall and frame.

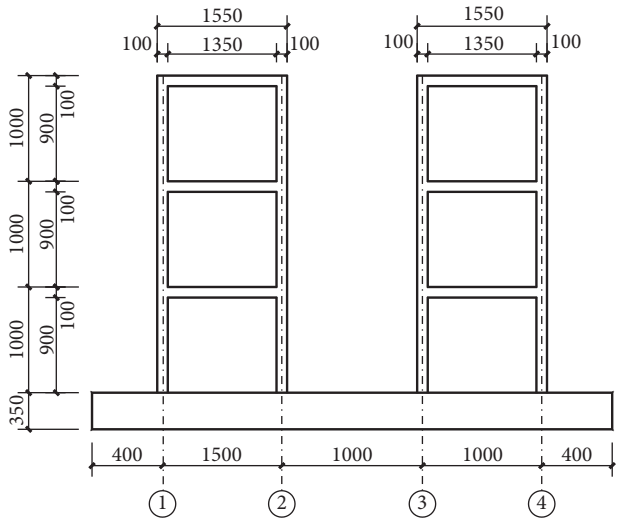

Figure 4: Front elevation view of test structures (unit: mm).

(4) In order to guarantee the connections, all straw components were checked before installation, those of which with large deviation in geometrical sizes were screened out.

(5) The installation order from bottom to top and from right to left was followed to ensure that the first straw board at the floor level fits the floor correctly, and that straw boards fits well with the neighboring straw strips.

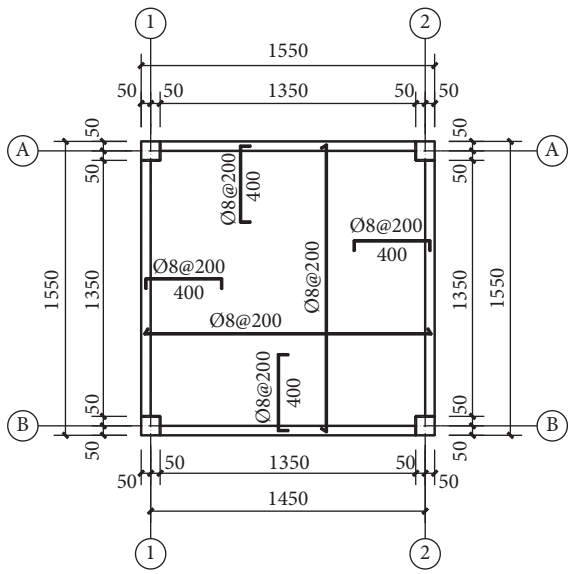

Figure 5: Reinforcement diagram of floor slab (unit: mm).

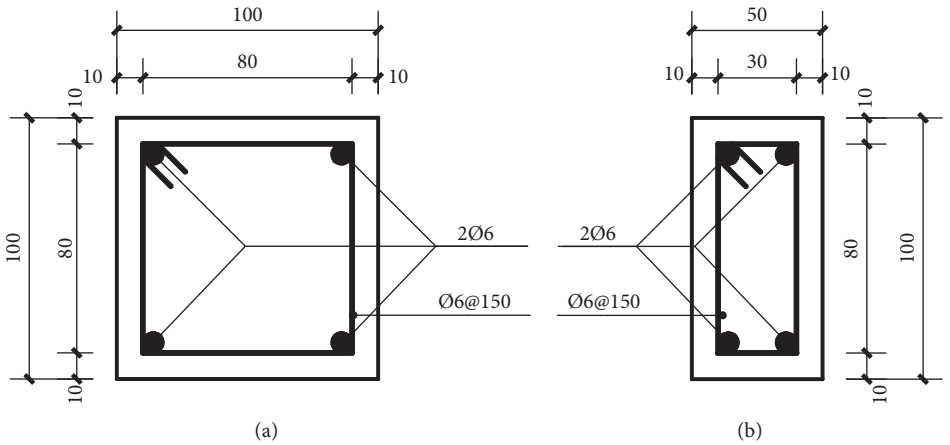

Figure 6: Reinforcement diagrams of columns and beams (unit: mm). (a) Column. (b) Beam.

Figure 7: The straw brick.

Figure 8: Test structures on shaking table.

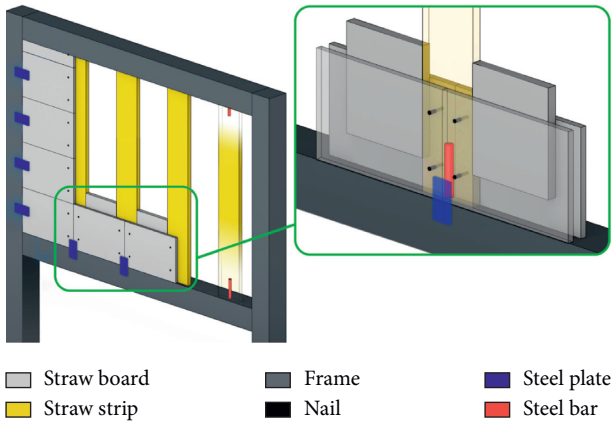

Figure 9: Connections between straw components and frame.

(6) By conducting the above steps, construction deviation accumulated on the last row of straw boards. Standard straw boards were cut on-site to ensure that the size of the last row and column meets the requirements.

(7) After all installations were complete, the straw strips and straw boards were connected with air nails. 20 mm air nails with an interval of 10 cm were adopted.

3.1.4. Experimental Materials. The parameters of experimental materials are shown in Table 4.

3.2. Shaking Table Test

3.2.1. Apparatus. This test was carried out on the earthquake simulation shaking table of the Civil Engineering Test Center in Southeast University. The vibration table is an assembled single-degree-of-freedom seismic simulation vibration table, which is mainly composed of a foundation, a table, a dynamic actuator, a controller, an oil source system, and a data acquisition and analysis system.

3.2.2. Spectrum Waves and Load Cases. According to the Chinese current code [7], 3 seismic waves were selected as the input waves in the experiment, namely, the EL Centro wave, the Taft wave, and an artificial wave. In the experiment, the seismic waves are firstly scaled with the acceleration peak value according to the working conditions. And the duration is compressed according to the similar coefficient, which is 23.2 s at last. All of them then work as the excitation input for the test.

During the test, the EL Centro wave, Taft wave, and the artificial wave were successively input in one way horizontally. White noise with a peak acceleration of 35 cm/s^2 was employed before and after each stage to test the dynamic characteristics of the structures. Ground motions were selected based on the Chinese current code [7] for research. The testing cases are presented in Table 5.

3.2.3. Measuring Point Layout and Data Collection. After the models had been installed, the measuring points were arranged. 7 magnetic accelerometers (numbered a1–a7) and 7 pull-wire displacement meters (numbered D1–D7) were employed during the tests. An acceleration sensor and a displacement meter were arranged on the ② axis and ④ axis of each floor elevation, roof, and vibration table base of the models, as shown in Figure 10.

The AdCRAS dynamic data collection system developed by Nanjing Anzheng Software Company was adopted in the test. The system is able to collect the acceleration and displacement response of the model under various working conditions. The sensitivity of acceleration sensor and displacement meter is shown in Table 6.

3.3. Test Results and Discussion

3.3.1. Experimental Observations. In the case of gradually increasing the peak acceleration of seismic waves, the occurrence and specific development of cracks are explained as follows:

(1) Under the Peak Ground Acceleration (PGA) of 35 cm/s^2, the horizontal shaking of the models was inconspicuous. No visible cracks appeared on the models.

(2) Under the PGA of 70 cm/s^2, cracks appeared at the bottom of the brick frame beams, and tiny cracks took place at the top of the bottom columns.

(3) Under the PGA of 140 cm/s^2, previous cracks expanded with low amplitude, and a few horizontal cracks appeared at the top of the bottom column in the brick frame.

(4) Under the PGA of 220 cm/s^2, micro cracks on the top of the bottom column in the brick frame began to expand, and cracks appeared in all four columns with a maximum length of 6 cm. Meanwhile, diagonal cracks took place in both ends of the 1st floor beams in the straw frame, as shown in Figure 11.

(5) Under the PGA of 400 cm/s^2, top cracks of bottom column in brick frame continued expanding, some of which expanded to the full section. Meanwhile, micro cracks appeared on top of the column in the second story. Cracks in the 1st floor beam of the straw frame expanded, especially in the beams along the shaking direction. During vibration, the gap between straw panels and beams caused by the deformation of the straw frame was observed.

(6) Under the PGA of 620 cm/s^2, cracks on the bottom column in the brick frame all extended to the full cross section; the maximum width of which is 2 mm. Cracks in the beams of the 1st and 2nd floor of the straw frame grew, and those of the 1st floor even extended to the full cross section.

(7) Under the PGA of 800 cm/s^2, the width of the cracks on the bottom column in the brick frame increased to 3 mm, and cracks appeared at the bottom of some columns. The maximum width of the crack at the beam ends in the straw frame is about 2 mm. The gap between the straw panels and the columns at the top story was between 3 cm and 5 cm.

Table 4: Parameters of experimental materials.

Material	Concrete	Steel	Masonry brick		Mortar	Straw brick	Straw strip
			Elastic modulus (MPa)	Grade		Density	Density
Parameter	C25	HPB235	2400	MU10	M5	559 kg/m^3	700 kg/m^3

Table 5: Testing cases.

Stage	Case no.	Input wave	Peak acceleration (cm/s^2)		Stage	Case no.	Input wave	Peak acceleration (cm/s^2)	
			Target value	Measured value				Target value	Measured value
1	1	White noise	35	48	5	17	White noise	35	42
	2	EL Centro	35	28		18	EL Centro	400	493
	3	Taft	35	49		19	Taft	400	405
	4	Artificial wave	35	64		20	Artificial wave	400	278
2	5	White noise	35	40	6	21	White noise	35	47
	6	EL Centro	70	92		22	EL Centro	620	531
	7	Taft	70	107		23	Taft	620	539
	8	Artificial wave	70	144		24	Artificial wave	620	531
3	9	White noise	35	45	7	25	White noise	35	39
	10	EL Centro	140	214		26	EL Centro	800	530
	11	Taft	140	216		27	Taft	800	562
	12	Artificial wave	140	206		28	White noise	35	59
4	13	White noise	35	43		29	EL Centro	1100	576
	14	EL Centro	220	280		30	Taft	1100	715
	15	Taft	220	417					
	16	Artificial wave	220	348					

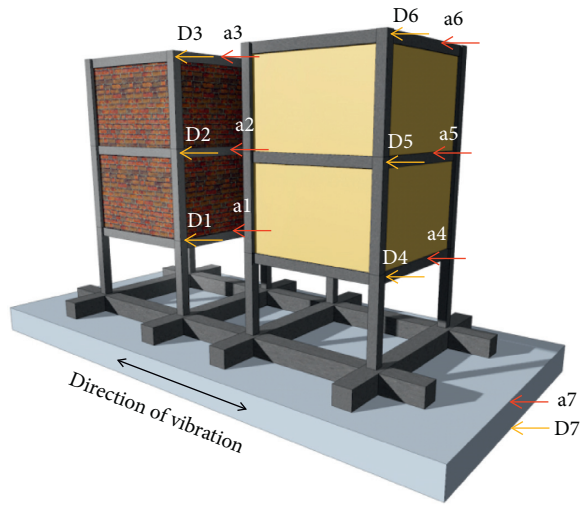

Figure 10: Layout of measuring point.

Table 6: Sensitivity and measuring range of sensors.

Accelerometer		Displacement meter		
Measuring point	Sensitivity (mV/m·s^2)	Measuring point	Sensitivity (V/m)	Measuring range (mm)
a1	10.02	D1	6.21	750
a2	9.92	D2	6.15	750
a3	9.90	D3	6.13	750
a4	10.16	D4	6.08	750
a5	9.92	D5	4.58	1000
a6	10.38	D6	4.57	1000
a7	10.22	D7	4.57	1000

Figure 11: Diagonal cracks in a beam of straw frame.

(8) Under 1100 cm/s^2, the bottom columns in the brick frame were twisted, the top of which showed obvious plastic hinge characteristics. The bottom columns in the straw frame twisted in a low amplitude. The local cracks of the brick wall were slightly developed, and the overall performance was good. The straw wall of the top layer of the A axis showed an outward inclining trend. At 1400 cm/s^2, the maximum width of cracks in the bottom column in the brick frame is around 5 mm, as shown in Figure 12. The cracks in the brick walls still developed locally and the walls still presented good integrity. The cracks at the beam ends on the 1st floor of the straw frame are about 3 mm, which all extended to the full sections. The straw wall at the top of axis A was about to crumble. At 1800 cm/s^2, displacement of the top layer in brick frame became too big. As the bottom column broke, the brick frame overturned as a whole, as shown in Figure 13. Straw frame remained intact.

3.3.2. Dynamic Characteristics of Structure. White noise was input on the table before and after the earthquakes at different cases. By performing frequency spectrum analysis on the horizontal acceleration data collected by the acceleration sensor under the action of white noise, the amplitude-frequency curve of the transfer function was acquired. So, the frequencies and damping ratios of the structures were obtained, which are shown in Figures 14 and 15 .

Results show that the attenuation law of the first-order frequency of the two models is basically the same, but the main reasons for the stiffness loss of the testing structures are different. It is also deduced from the damping ratios curve that the straw frame consumes more energy than the brick frame. Apparently, the straw frame with flexible connection has strong energy consumption capacity and is safer than brick frame structure under the action of big earthquakes.

3.3.3. Structural Displacement Response. The maximum interstory displacements and story drifts are shown in Table 7.

Figure 12: Crack in the bottom column of brick frame.

Figure 13: Crumble of the brick frame.

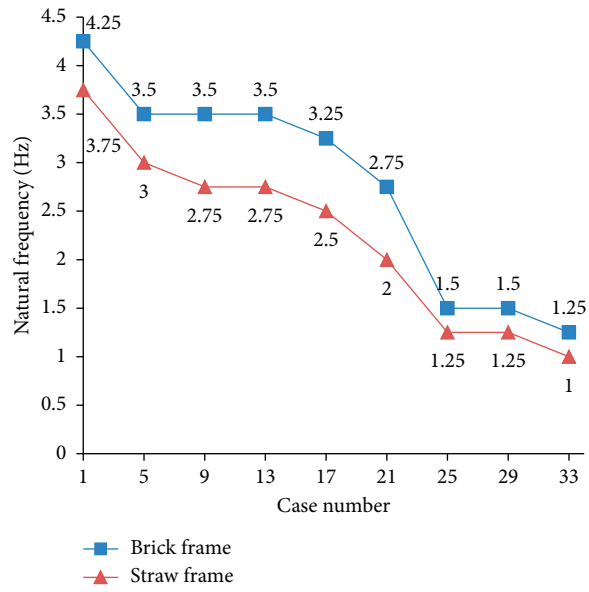

Figure 14: The frequencies of models in different cases.

Results show that the max inter story displacements in the brick frame are generally smaller than those of the straw frame under the same lateral actions, due to the extra stiffness the masonry wall brings. It is not difficult to explain why the max story displacements occurred in the first story of the brick wall, while max story displacements appeared in the first and third story of the straw frame. Because masonry

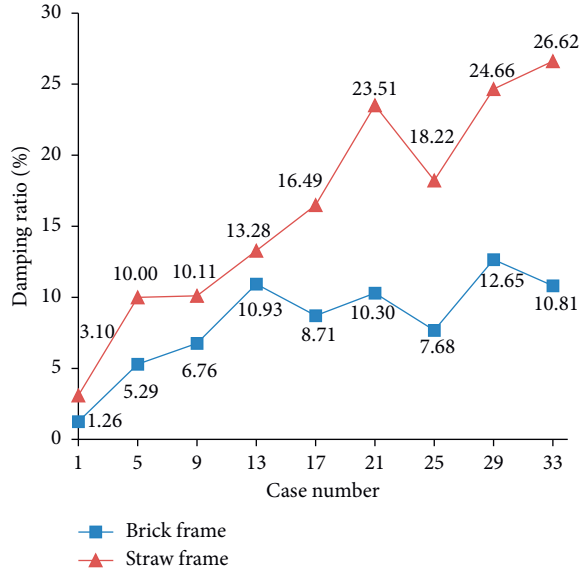

Figure 15: Damping ratios of models in different cases.

Table 7: Maximum interstory displacements and story drifts.

Peak acceleration (cm/s^2)	Brick frame			Straw frame		
	Max interstory displacement (mm)	Max story drift	Floor number	Max interstory displacement (mm)	Max story drift	Floor number
35	0.49	1/2041	1	0.48	1/2083	1
70	0.55	1/1818	1	0.76	1/1316	1
220	0.72	1/1389	1	0.83	1/1205	3
400	0.83	1/1205	1	1.03	1/971	3
620	1.07	1/935	1	1.85	1/541	1
800	2.39	1/418	1	2.77	1/361	1

walls offered extra stiffness, and restricted the deformation of brick frame, this makes the 1st layer much weaker, as no bricks are arranged there. Straw walls, however, brought little extra stiffness to the original structure, hardly affecting the deformation of straw frame.

4. Numerical Analysis

The objective of this section is to verify and illustrate the failure mechanism of test structures.

4.1. FEM Models. By using SAP2000 (version 22.1.0), numerical analysis models of frameworks were built based on experimental structures. The only difference of FEM models was the way that those infill walls were considered. Compression struts, with no mass, were adopted to represent the stiffness contribution of masonry walls, as code ASCE/SEI 41-06 [17] proposed. The width of strut was the same with the thickness of masonry infill walls, namely, 40 mm. And the depth of strut was calculated based on (equation (7)) [17], which was 148 mm. With low elastic modulus and flexible connection, however, straw wall was treated as nonstructure component, whose stiffness was ignored. Both the self-weight of masonry bricks and straw panels were considered as vertical linear loads on beams.

To study the failure mechanism, plastic hinges were defined at both ends of all columns and beams. Pushover analysis was conducted, with gradient horizontal loads being imposed on each floor. The FEM models of brick framework and straw framework are shown in Figures 16 and 17 . "H" in the figures represents plastic hinge; dimensionless values of the horizontal loads merely illustrate the ratio of acting pushover loads.

4.2. Numerical Results and Discussion. As pushover analysis proceeded, plastic hinges took place. Figures 18 and 19 show records of the pushover steps, where first hinges that reached C stage [16] appeared. In the straw framework, the first failure hinge emerged at the beam end of the 1st floor, while 7 other hinges appeared in other beams and columns. In the brick framework, first failure hinges took place only

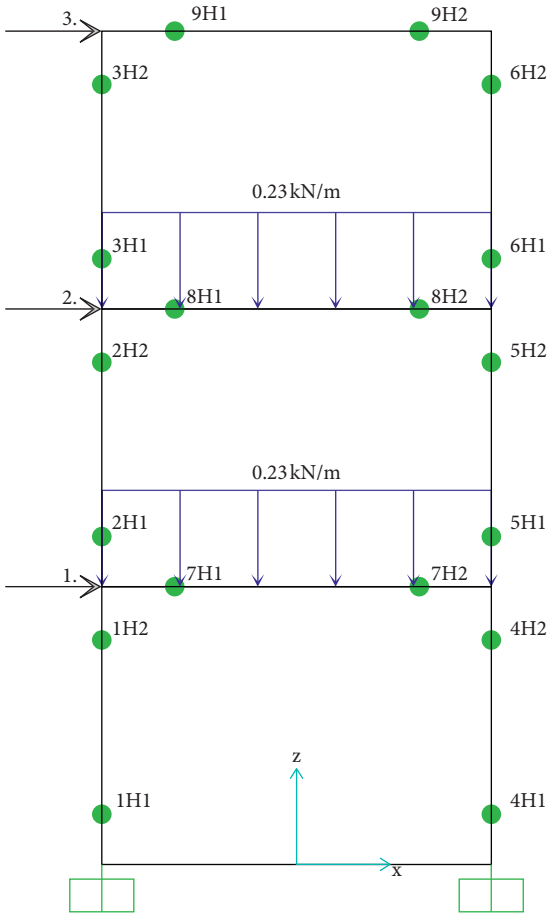

Figure 16: FEM model of straw framework.

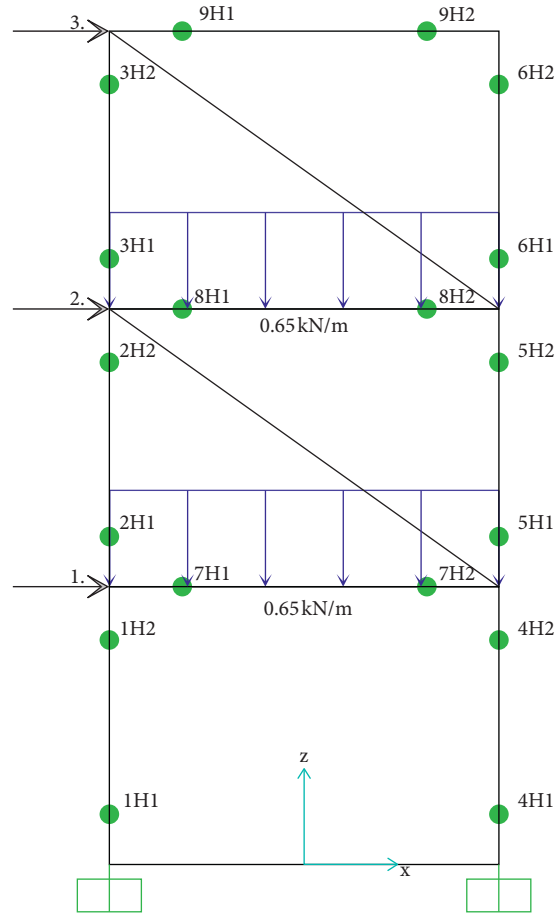

Figure 17: FEM model of brick framework.

at the column ends of the 1st floor. Table 8 lists the displacements, story displacements, and story drifts at the time.

Results show that before the failure of structure, the straw frame withstands greater lateral deformation than brick frame does under the same lateral action mode. From bottom to top, the story drifts of brick frame decrease dramatically than those of straw frame, which indicates that the masonry infill walls stupendously enhance the lateral stiffness of upper floors. However, when it comes to the story drifts of first stories, the brick frame apparently owns a bigger value. Above all, masonry infill walls on upper floors result in the localized increase of stiffness, leading to the redistribution of stress generated by lateral actions. This was presented in the form of a weaker first story, eventually a weaker frame than a straw frame or a bare one.

With the difference of these structures produced by unequal stiffness, the failure modes differ. Numerical analyses show that the first failure hinge took place at the end of the 1st floor beam in the straw frame, while the first failure hinges appeared at the ends of the bottom columns in the brick frame, which accords with the experimental observations above. Failure of beams undoubtedly brings about local damage, while it sometimes in turn protects the structures by absorbing and dissipating part of the seismic energy. However, as vertical load bearing members, the failure of columns would lead to the collapse of the whole structure. This is the reason why the Chinese code [7] recommends the notion of strong column and weak beam, making sure columns fail after beams to protect the living at its best in seldomly occurred earthquakes. In a word, straw frame presents better seismic performance than brick frame.

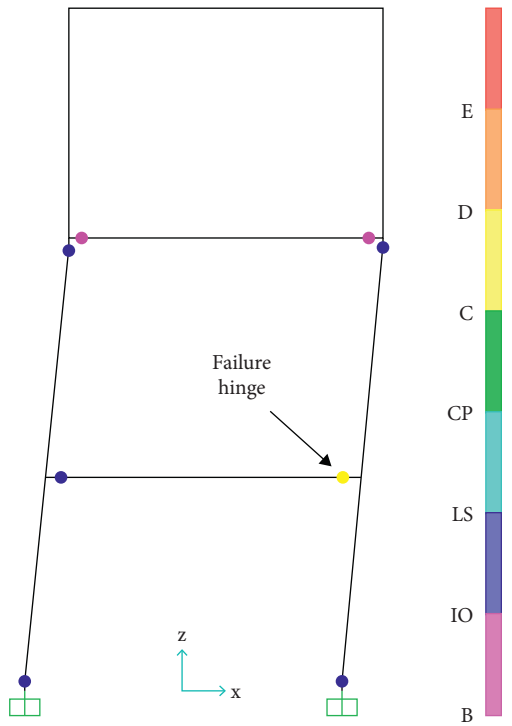

Figure 18: Hinges distribution of straw framework.

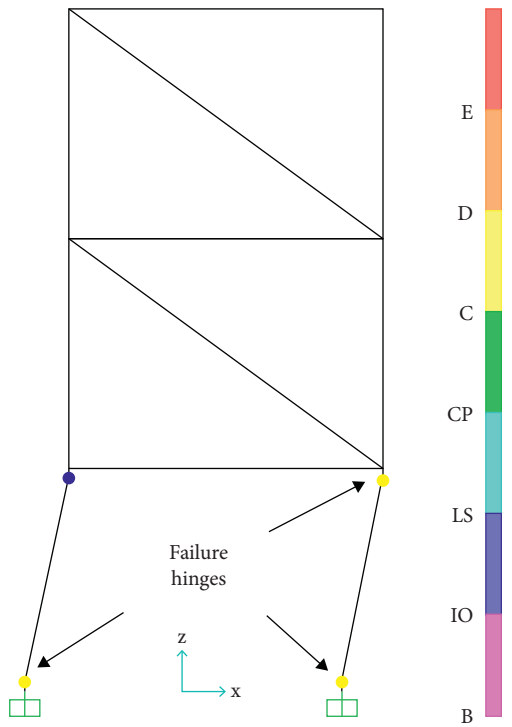

Figure 19: Hinges distribution of brick framework.

Table 8: Displacements and story drifts of numerical models when the first failure hinges appeared.

Framework	Displacement (mm)			Interstory displacement (mm)			Story drift		
	1st floor	2nd floor	3rd floor	1st floor	2nd floor	3rd floor	1st floor	2nd floor	3rd floor
Straw frame	20.40	40.64	45.74	20.40	20.24	5.10	1/49	1/50	1/196
Brick frame	26.03	27.06	27.49	26.03	1.03	0.43	1/39	1/971	1/2326

5. Conclusion

After the shaking table tests are conducted to study the seismic performance of a 1/3-scale straw panel-infilled frame in comparison with masonry infilled frame, along with the numerical analysis, the following conclusions are drawn:

(1) As the story drifts of brick frame are generally smaller than those of straw frame under the same load cases, the masonry walls greatly affect the stiffness of original frame. Consequently, ignoring the stiffness contribution of masonry infill walls in seismic design process is inappropriate and dangerous.

(2) According to the outcome of test results and numerical analysis, inconsistent layout of masonry infill walls along the vertical direction results in the disparity of lateral stiffness for successive stories, leading to the redistribution of stress generated by lateral actions. Eventually, the failure mode shifts to a brittle type, as the stress concentration firstly harms the columns in weak stories.

(3) The proposed straw panels, with lightweight and flexible connections, bring less mass and little extra stiffness to bare frames. Thus, great disparity of lateral stiffness along vertical direction will not be achieved. Consequently, the failure mode is consistent with that of the bare frame, in which the beams damage firstly and consume part of the seismic energy to ensure the whole structure resisting the seismic actions better. The damping ratios' curve also showed that the straw frame consumes more energy than the brick frame. With proper design, the straw panel-infilled frame is a good system combined with safety and flexibility in building space layout.

Data Availability

The data used to support the findings of this study are available from the corresponding author upon request.

Conflicts of Interest

The authors declare that they have no conflicts of interest regarding the publication of this paper.

Acknowledgments

This research was supported by the National Key R&D Program of China (Grant no. 2017YFC0703507), Basic Ability Improvement Program of Young- and Middle-Aged Scholar for the Education Office of Guangxi Zhuang Autonomous Region (Grant no. 2019KY0256), and Priority Academic Program Development of Jiangsu Higher Education Institutions (PAPD).

References

[1] I. Koutromanos, "Numerical modeling of masonry-infilled RC frames subjected to seismic loads," *Computers & Structures*, vol. 89, no. 11-12, pp. 1026–1037, 2011.

[2] F. De Luca, G. M. Verderame, F. Gómez-Martínez, and A. Pérez-García, "The structural role played by masonry infills on RC building performances after the 2011 Lorca, Spain, earthquake," *Bulletin of Earthquake Engineering*, vol. 12, no. 5, pp. 1999–2026, 2014.

[3] G. Blasi, D. Perrone, and M. A. Aiello, "Fragility functions and floor spectra of RC masonry infilled frames: influence of mechanical properties of masonry infills," *Bulletin of Earthquake Engineering*, vol. 16, no. 12, pp. 6105–6130, 2018.

[4] F. Braga, V. Manfredi, A. Masi, A. Salvatori, and M. Vona, "Performance of non-structural elements in RC buildings during the L'Aquila, 2009 earthquake," *Bulletin of Earthquake Engineering*, vol. 9, no. 1, pp. 307–324, 2011.

[5] P. G. Asteris, C. C. Repapis, E. V. Repapi, and L. Cavaleri, "Fundamental period of infilled reinforced concrete frame structures," *Structure and Infrastructure Engineering*, vol. 13, no. 7, pp. 929–941, 2017.

[6] Press CCI, *Technical Specification for Concrete Structures of Tall Building (JGJ3-2010)*, The Ministry of Housing and Urban-Rural Development of the People's Republic of China, Beijing, China, 2011.

[7] Press CCI, *Code for Seismic Design of Buildings (GB50011-2010)*, The Ministry of Housing and Urban-Rural Development of the People's Republic of China, Beijing, China, 2016.

[8] Research, C. A. O. B., *Photo Collection of 2008 Wenchuan Earthquake Damage to Buildings*, China Construction Industry Press, Beijing, China, 2008.

[9] Z. Z.-Q. Huang Dong-Sheng, "MAO long-quan investigations of building damages in mianzhu and dujiangyan due to 5·12 wenchuan earthquake," *Journal of Disaster Prevention and Mitigation Engineering*, vol. 30, no. 01, pp. 109–116, 2010.

[10] A. Stavridis, I. Koutromanos, and P. B. Shing, "Shake-table tests of a three-story reinforced concrete frame with masonry infill walls," *Earthquake Engineering & Structural Dynamics*, vol. 41, no. 6, pp. 1089–1108, 2012.

[11] M. Shabdin, N. K. A. Attari, and M. Zargaran, "Shaking table study on the seismic performance of an Iranian traditional Un-Reinforced Masonry (URM) building," *Structures*, vol. 27, pp. 424–439, 2020.

[12] H. Wijaya, "Effect of infill-wall material types and modeling techniques on the seismic response of reinforced concrete buildings," *Natural Hazards Review*, vol. 21, no. 3, 2020.

[13] M. H. Santhi, G. M. S. Knight, and K. Muthumani, "Evaluation of seismic response of soft-storey infilled frames," *Computers and Concrete*, vol. 2, no. 6, pp. 423–437, 2005.

[14] T. Suzuki, H. Choi, Y. Sanada et al., "Experimental evaluation of the in-plane behaviour of masonry wall infilled RC frames," *Bulletin of Earthquake Engineering*, vol. 15, no. 10, pp. 4245–4267, 2017.

[15] T. Salonikios, C. Karakostas, V. Lekidis, and A. Anthoine, "Comparative inelastic pushover analysis of masonry frames," *Engineering Structures*, vol. 25, no. 12, pp. 1515–1523, 2003.

[16] FEMA-440, *Improvement Of Nonlinear Static Seismic Analysis Procedures*, Applied Technology Council (ATC), Washington DC, USA, 2005.

[17] (ASCE), A. S. O. C. E., *Seismic Rehabilitation of Existing Structures (41-06)*, ASCE, Reston, VA, USA, 2007.

[18] P. G. Asteris, D. M. Cotsovos, C. Z. Chrysostomou, A. Mohebkhah, and G. K. Al-Chaar, "Mathematical micromodeling of infilled frames: state of the art," *Engineering Structures*, vol. 56, pp. 1905–1921, 2013.

[19] Z. Xu, Z. Chen, and S. Yang, "Seismic behavior of cold-formed steel high-strength foamed concrete shear walls with straw boards," *Thin-Walled Structures*, vol. 124, pp. 350–365, 2018.

[20] L. Jian, *The Experimental Investigation of the Straw Bale Wall under the Horizontal Loads*, Jilin Jianzhu University, Changchun, China, 2015.
[21] A. D. González, "Energy and carbon embodied in straw and clay wall blocks produced locally in the Andean Patagonia," *Energy and Buildings*, vol. 70, pp. 15–22, 2014.
[22] K. Li, "Analysis on energy saving and thermal insulation performance of improved straw brick in northern cold area," *Arabian Journal of Geosciences*, vol. 13, no. 16, 2020.
[23] D. Snoeck and N. De Belie, "From straw in bricks to modern use of microfibers in cementitious composites for improved autogenous healing - a review," *Construction and Building Materials*, vol. 95, pp. 774–787, 2015.
[24] F. Parisi, D. Asprone, L. Fenu, and A. Prota, "Experimental characterization of Italian composite adobe bricks reinforced with straw fibers," *Composite Structures*, vol. 122, pp. 300–307, 2015.
[25] F. S. Liu, J. Fan, and H. B. Bian, "A new cost effective building material: compacted wheat straw block," *Advanced Materials Research*, vol. 374-377, pp. 2599–2604, 2011.
[26] C. C. I. Press, *Code for Design of Concrete Structures (GB50010-2010)*, The Ministry of Housing and Urban-Rural Development of the People's Republic of China, Beijing, China, 2015.
[27] C. C. I. Press, *Code for Design of Masnory structures (GB50003-2011)*, The Ministry of Housing and Urban-Rural Development of the People's Republic of China, Beijing, China, 2011.

Hindawi
Advances in Civil Engineering
Volume 2021, Article ID 6666059, 13 pages
https://doi.org/10.1155/2021/6666059

Research Article

Mechanical Properties and Strength Grading of Engineered Bamboo Composites in China

Siyuan Tang,[1,2] **Aiping Zhou**,[1] **and Jiannan Li**[3]

[1]*National Engineering Research Center of Biomaterials, Nanjing Forestry University, Nanjing, China*
[2]*School of Architecture and Transportation Engineering, Guilin University of Electronic Technology, Guilin, China*
[3]*School of Civil Engineering, Changzhou Institute of Technology, Changzhou, China*

Correspondence should be addressed to Siyuan Tang; 404533342@163.com

Received 24 December 2020; Revised 1 March 2021; Accepted 29 March 2021; Published 22 April 2021

Academic Editor: Giosuè Boscato

Engineered bamboo composite (EBC) is a new high-strength anisotropic structural material, which has standardized sections and less inherent variability than the natural material. For safety reasons in structural applications, the characteristic values of mechanical behaviors are needed to build the design values utilized in practical application. Recent research studies on EBC focused on the mechanical properties from a single source, with little research on the sampling of the manufacturers. The present work investigates mechanical properties of two types of commercially available EBC—parallel strand bamboo (PSB) and laminated veneer bamboo (LVB). The main aim of this work is to evaluate the best probability distribution model (normal, lognormal, and Weibull) and mechanical properties for EBC in China and determine the characteristic values indicated by ASTM D2915. The mechanical properties in tensile, compression, and shear were evaluated using about 4300 small clear specimens from seven manufacturers in five raw bamboo origins of China. Based on the confidence band method, the strength grading of EBC subjected to compressive strength was developed with two predictors (density and MOE). By using intervals of each predictor, several strength grades were built. Each grade has the mean compressive strength, 5th percentile lower value ($R_{0.05}$), and characteristic value (R_k), which could be used in structural design. This research contributes to the establishment of EBC standards and is essential for further accepting these materials in structural engineering.

1. Introduction

Bamboo is a sustainable and natural material. It is a crucial forest resource other than timber. Therefore, bamboo has been used as a building material for thousands of years. Due to bamboo's circular hollow section and range of available sizes, the scope of possible structural applications for natural round culms is limited. Instead, EBCs have become more popular in academic and engineering application fields. In recent years, several forms of engineered bamboo composite have been rapidly developed and applied [1]. Figure 1 shows some examples of EBC structure.

China presents an enormous potential for EBC applications since Moso bamboo (the primary raw material of EBC) resources are widespread in natural forests and are cultivated over large areas in Mainland China, including Hunan, Jiangxi, Hubei, Zhejiang, Fujian, and Anhui Provinces (see Figure 2). The EBCs are bamboo-based composites designed for structural applications with specific mechanical properties, including parallel strand bamboo (PSB) and laminated veneer bamboo (LVB). The PSB is a composite of bamboo strand elements with bamboo fibers primarily orientated along the member's longitudinal axis (see Figure 3). LVB is also a composite of bamboo strand elements, edge-bonded to form veneer sheets of uniform sectional dimensions, which are then face-bonded to develop finished products, with bamboo fibers primarily oriented along the longitudinal axis of the member (see Figure 3).

The EBC shows the anisotropic behavior typical of natural bamboo, comparable to that of fiber reinforced composites [3, 4]. A significant number of experiments

(a) (b) (c)

Figure 1: Examples of EBC structure.

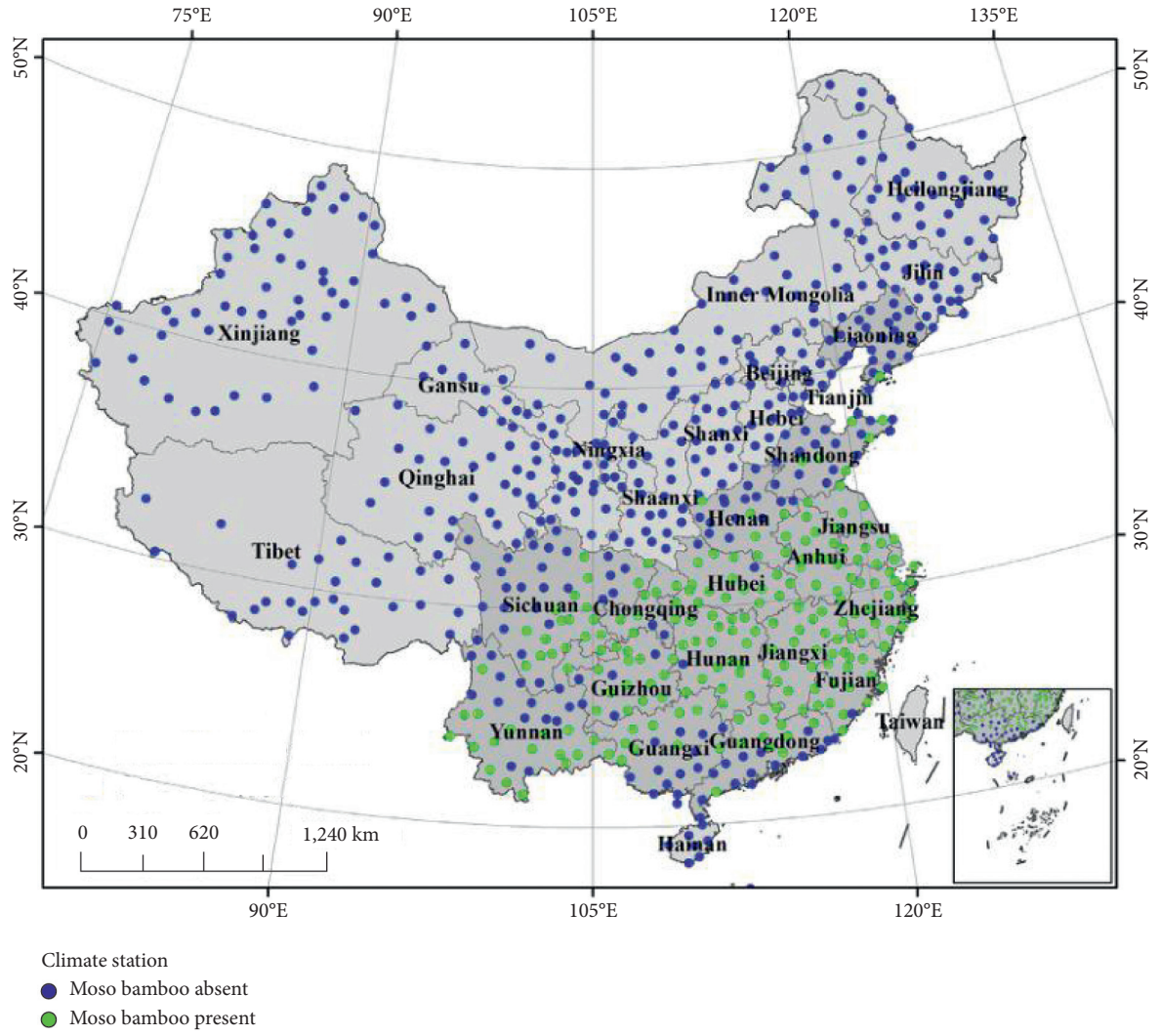

Figure 2: The information on the distribution of Moso bamboo in Mainland China by Shi [2].

have been conducted to investigate the mechanical properties of bamboo composites. Huang [5, 6] studied the mechanical properties of PSB by experiments and investigated stress-strain relationships and failure mechanisms in each stress state. Wei [7] provided a comprehensive research on the mechanical behavior and failure modes of bamboo scrimber (PSB) and laminated bamboo (LVB) and proposed the stress-strain models for EBC. Xiao [1, 8] studied the mechanical properties of glubam boards and found that the Weibull distribution and normal distribution are best fit for shear strength and the in-plane shear strength, respectively, and suggested the characteristic values and the design values. Sharma et al. [9] provided a comprehensive study that compares bamboo scrimber,

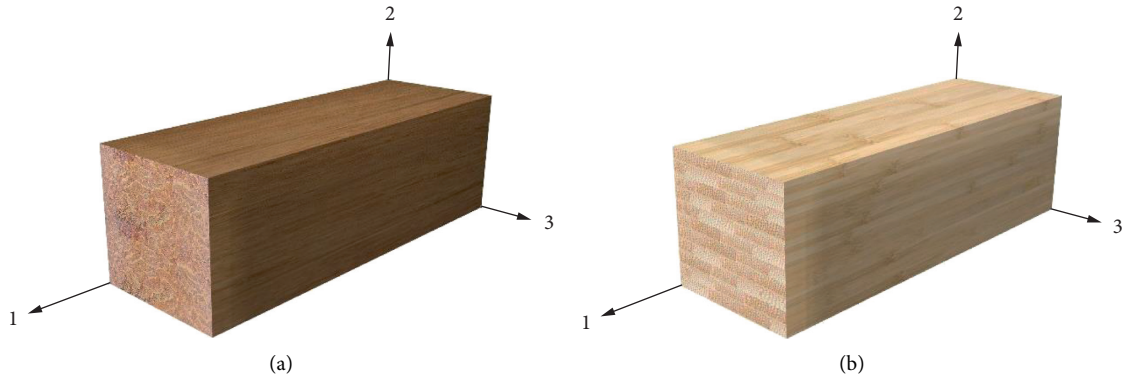

Figure 3: Engineered bamboo composites: parallel strand bamboo (a); laminated veneer bamboo (b).

laminated bamboo, timber, and engineered timber products for mechanical properties. Kumar et al. [10] studied the influence of bamboo scrimber densities on the mechanical properties and concluded that the density has significant influence on the mechanical properties of bamboo scrimber. There is no sampling and statistical research on the physical and mechanical properties of EBC products from different manufacturers, which makes the formulation of standards lack data reference.

The characteristic value is the representative value of a material property used for design. The standards [11, 12] define the 5th percentile value at the 75% confidence level for structural materials as characteristic value of strength, and the determination method includes nonparametric and parametric. The parametric approach calculates the characteristic value of strengths according to the estimated statistical average and standard deviation of the sample. The nonparametric approach is to sort the sample data from small to large to determine the strength corresponding to the data point as the characteristic value of strength. Therefore, it is vital to determine the characteristic values of mechanical property of EBC for engineering applications, and it is also the basis for determining its strength design value in the future.

EBC for structural applications has to be strength graded before its use. For economic reasons, the most important physical and mechanical properties (e.g., density, modulus, and strength) are the basic grading principles. For bamboo culm, Trujillo et al. [13] indicated that grading could be utilized based on physical properties and flexural stiffness. Nurmadina et al. [14] and Bahtiar [15, 16] studied several potentials, including *M*c, density, and linear mass, for bamboo culm both in flexural and compressive strength grading. The grading of timber and bamboo are constantly studied, but the strength grading of EBC subject to compressive properties is still missed.

In order to build the EBC standards and contribute to the use of EBC for structural purposes, this research aimed to determine the probability distribution and the characteristic value of the mechanical properties for EBC by tests. Afterward, the Indicating Properties (IPs) which were the best for predicting compressive strength of EBC were determined. The strength grading was developed by the confidence band method for EBC based on compressive properties. It will provide more design-relevant data for engineering applications.

2. Materials and Methods

2.1. Materials. In order to objectively reflect the mechanical properties of EBC in China, this study randomly took EBC products from seven manufacturers with raw materials from five primary bamboo origins. Different types of EBC from manufacturers were divided into nine groups. All of the EBC products were manufactured of Moso bamboo (*Phyllostachys pubescens*), and the material information is shown in Table 1. Each group of materials required the same batch of products from the same manufacturer. Test specimens were processed to the specified dimensions (Table 2) and transported to the laboratory.

2.2. Sample Size. The population is characterized by the sample, therefore enough sample size must be adopted. In this study, the sample size is obtained based on ASTM D2915 [13]. On the 95% confidence level, the required minimum sample size n of specimens is

$$n = \left(\frac{ts}{\alpha \overline{X}}\right) = \left(\frac{t}{\alpha}\mathrm{CV}\right)^2, \quad (1)$$

where s is the standard deviation of specimen values; $\overline{X}$ is the specimen mean value; CV is the coefficient of variation (it was assumed first as 0.1 for physical properties and 0.2 for mechanical properties); α is the estimate of precision, taken as 0.05; and t is the value of the t statistic, taken as 2.093 (physical properties) and 2 (mechanical properties) for 0.95 confidence level. The minimum number of specimens is 18 (physical properties) and 64 (mechanical properties) for each test based on the testing standard. To ensure an adequate test sample size, the number of specimens for physical properties and mechanical properties is 80.

2.3. Testing Methods. The mechanical properties of testing included tensile, compressive, and shear tests in both directions to the grain. The same method of testing was used for both PSB and LVB. The dimensions were measured

Table 1: The raw material information of engineered bamboo composites.

Group	Material	Origin of raw bamboo	Age of raw bamboo	Resin types	Manufacturer
EBC1	PSB	Jiangxi Province	4 years	Urea formaldehyde resin	Jiangxi Feiyu Bamboo Co., LTD
EBC2	PSB	Hunan Province	5 years	Phenol formaldehyde resin	Hunan Taohuajiang Bamboo Technology Co., LTD
EBC3	PSB	Fujian Province	5 years	Phenol formaldehyde resin	Fujiang Jinzhu Bamboo Co., LTD
EBC4	PSB	Zhejiang Province	3–5 years	Phenol formaldehyde resin	Guangyu Bamboo Industry Co., LTD
EBC5	PSB	Anhui Province	3–6 years	Phenol formaldehyde resin	Anhui Hongyu Bamboo Technology Co., LTD
EBC6	LVB	Jiangxi Province	5 years	Urea formaldehyde resin	Jiangxi Feiyu Bamboo Co., LTD
EBC7	LVB	Hunan Province	5 years	Phenol formaldehyde resin	Hunan Taohuajiang Bamboo Technology Co., LTD
EBC8	LVB	Fujian Province	3–5 years	Phenol formaldehyde resin	Shaowu Xingda Bamboo Co., LTD
EBC9	LVB	Zhejiang Province	5 years	Phenol formaldehyde resin	Zhejiang Shanglin Bamboo Co., LTD

thrice for each specimen. All parameters of dimension were measured using a vernier caliper with an accuracy of 0.001 mm. The EBC specimens were conditioned in a chamber at 65% (±5%) relative humidity and 20°C (±2°C) temperature prior to testing for one month.

Since the EBC is a new composite and no test standard has been established, the standards for timber structure and composite materials are referenced in studying the mechanical properties of EBC. For each group, density and moisture content were determined based on the specimens of compression in parallel to grain according to GB/T 1933 [17]: Method for determination of the density of wood and GB/T 1931 (air-dry method) [18], respectively. The tests of tensile and compressive were conducted following ASTM D143 [19]: Standard test methods for small clear specimens of timber. The tests of shear were in accordance with principles of ASTM D7078 [20]: Standard test method for shear properties of composite materials by V-notched rail shear method. The mechanical properties were measured with a universal testing machine using load cell of 100 kN capacity. Two strain gauges were affixed to the surface in the middle of the specimen to measure the strains along with two directions, namely, parallel and perpendicular to grain directions, respectively. The data logger (TML TDS-640) automatically recorded the load and the strains during the tests. The standards, test methods, number of specimens, and test parameters used are summarized in Table 2.

2.4. Data Analysis. Statistical distributions were fitted to the experimental data obtained by the maximum likelihood estimates method. The Kolmogorov–Smirnov [21] test was used to verify the goodness of fit analysis. Both methods were using the software MATLAB® version R2018b. In this study, the probability distributions were fitted with normal, lognormal, and Weibull models. The general equations for probability density functions and cumulative distribution functions are calculated using equations (2)–(7):

$$x - N(\mu, \sigma): f(x) = \frac{1}{\sqrt{2\pi}\sigma} e^{-(x-\mu)^2/2\sigma^2}, \tag{2}$$

$$F(x) = \Phi\left(\frac{x-\mu}{\sigma}\right), \tag{3}$$

$$x - L\left(\mu_{\ln}, \sigma_{\ln}^2\right): f(x) = \frac{1}{\sqrt{2\pi}\sigma_{\ln} x} e^{-\left(\ln x - \mu_{\ln}\right)^2/2\sigma_{\ln}^2}, \tag{4}$$

$$F(x) = \Phi\left(\frac{\ln x - \mu_{\ln}}{\sigma_{\ln}}\right), \tag{5}$$

$$x - W(k, \lambda): f(x) = \frac{k}{\lambda}\left(\frac{x}{\lambda}\right)^{k-1} e^{-(x/\lambda)^k}, \tag{6}$$

$$F(x) = 1 - e^{-(x/\lambda)^k}, \tag{7}$$

where x is the strength; μ is the mean value of the distribution; σ is the standard deviation; $\mu_{\ln}$ is the mean value of logarithmic; $\sigma_{\ln}$ is the standard deviation value of logarithmic; k is the shape parameter; and λ is the scale parameter.

In this study, the mean value of the best-fit distribution is used for the characteristic value of moduli. The 5th percentile value with 75% confidence level from test results shall be the characteristic value for strengths. According to the ASTM D2915, the characteristic value of strength corresponding to the 5th percentile value with 75% confidence level for the normal, lognormal, and Weibull distribution of the strengths can be calculated as follows:

$$\begin{aligned} f_{k,0.05} &= \mu - K_N \sigma, \\ f_{k,0.05} &= \mu_{\ln} - K_{\ln} \sigma_{\ln}, \\ f_{k,0.05} &= \overline{X} - K_W S, \end{aligned} \tag{8}$$

where μ is the mean of the normal distribution; σ is the standard deviation of the normal distribution; K_N is the confidence level factor of the normal distribution; $\mu_{\ln}$ is the

Table 2: Experimental methods for EBC.

Standard	Test method	Direction	n (for each group)	Loading rate (mm/min)	Dimensions (mm)
GB/T 1933 [17]	Density	—	80	—	25 × 25 × 100
GB/T 1931 [18]	Moisture content	—	80	—	
ASTM D143 -14 [19]	Compression	Parallel to grain	80	1.5	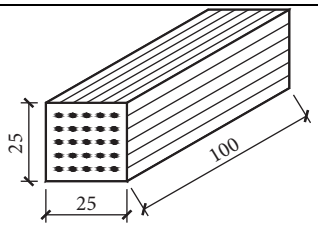
		Perpendicular to grain	80	1.5	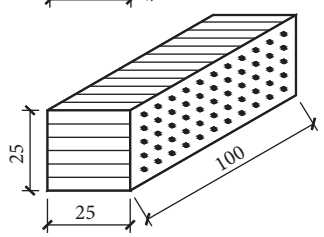
ASTM D143 -14 [19]	Tension	Parallel to grain	80	1	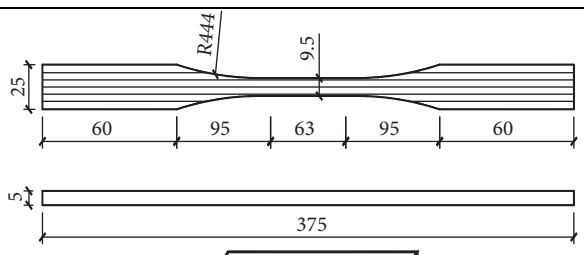
		Perpendicular to grain	80	1	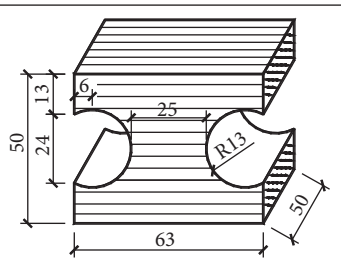
ASTM D7078 -12 [20]	Shear	Parallel to grain	80	1	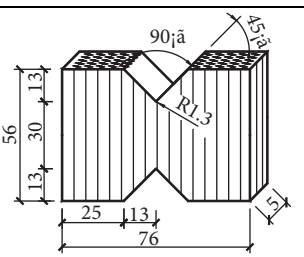
		Perpendicular to grain	80	1	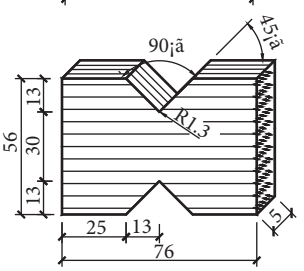

mean of the lognormal distribution; σ_{In} is the standard deviation of the lognormal distribution; K_{In} is the confidence level factor of the lognormal distribution;$\overline{X}$ is the mean of the Weibull distribution; S is the standard deviation of the Weibull distribution; and K_W is the confidence level factor of the Weibull distribution.

The EBC strength grading was conducted using a confidence band approach as described by Bahtiar et al. [16]. Statistical analysis was developed using correlation and linear regression. The parameters that had a strong correlation with strength will be considered potential predictors for EBC strength grading. Based on the confidence band in regression analysis, class intervals are created in similar ranges. According to the confidence band method, the 5th percentile lower value ($R_{0.05}$) was calculated using equation (9). Then, the adaptation is applied by substituting the standard deviation (S_{D}) value with standard error for estimation in regression (S_{E}) (equation (10)). Finally, the characteristic value for each class (R_{k}) was obtained with equation (11).

$$R_{0.05} = \widehat{y} - t_{(\nu,0.95)}\left(1 + \frac{1}{n} + \frac{(x-\overline{x})^2}{\Sigma(x-\overline{x})^2}\right)^{0.5} S_r, \quad (9)$$

$$S_E = \left(1 + \frac{1}{n} + \frac{(x-\overline{x})^2}{\Sigma(x-\overline{x})^2}\right)^{0.5} S_r, \quad (10)$$

$$R_k = R_{0.05}\left(1 - \frac{k_{0.05,0.75}S_E}{m\sqrt{n}}\right)^{0.5}, \quad (11)$$

where m is the average of strength from the test data; n is the sample size; $\overline{x}$ is the mean of predictor value; $\widehat{y}$ is the estimated strength when the predictor has x value; S_r is the standard error of regression; S_E is the standard error of prediction at a given value of x; $t_{(\nu,0.95)}$ is the one-tailed Student's t-distribution value with ν degree of freedom for 95% probability; and $k_{0.05,0.75}$ is the confidence level factor for 75% confidence and 5% probability, which is interpolated from confidence level factor table in ASTM 2915 [12].

3. Results and Discussion

3.1. Mechanical Properties. A summary of the mechanical property test results according to the procedure defined in standards is presented in Table 3. The test results are assembled in Figure 4 which shows column plots for mechanical properties. The average value is indicated with a vertical column, and a vertical black whisker denotes the width of the standard deviation.

It is shown that the moisture content of EBC ranges from 5.3% to 9.18%. There is a slight difference between PSB and LVB. However, the air-dry density of PSB is 0.98–1.31 g/cm^3, and LVB is 0.65–0.70 g/cm^3, respectively. Because of differences in manufacturing processes, adhesive content, and elements, PSB density is greater than LVB, which is closer to the density of raw bamboo.

In general, the mechanical behaviors of PSB and LVB are corresponding both parallel and perpendicular to the grain. However, the PSB groups are superior to that of LVB in mechanical properties except for EBC4, which has the lowest density (9.8 g/cm^3) of PSB. This is a rare and unexpected result. It is considered that this tendency is given by the fibers within the phenol formaldehyde resin which are not dense enough, leading to more imperfections. Because the tensile strength of EBC is mainly determined by the bamboo fiber, the tensile strength in parallel to the grain of PSB and LVB is extremely close to the tensile strength of bamboo. With the exception of EBC4, the compressive strength of PSB is in the range of 99.29–119.04 MPa, which is significantly higher than that of LVB in the range of 55.93–69.22 MPa.

To compare the variability in mechanical properties, the coefficient of variations (CV) are examined to the test results. Lower CV values suggest a smaller expected scattering in the corresponding variable. The compressive behavior in perpendicular to the grain shows the highest variability for all mechanical properties. It can be attributed to the inhomogeneity of the formaldehyde resin layer geometry, which leads to a nonhomogeneous fiber volume fraction over the sample volume. The group of EBC4 shows great variability in most tests for mechanical properties. It can be inferred that the density of PSB has a certain correlation with the strength parallel to the grain. Once the PSB density is less than the critical value, the mechanical properties will be significantly reduced, even lower than that of the LVB, whose density is smaller than that of PSB. Therefore, in the PSB manufacturing process, it is necessary to find and exceed the critical density, which makes the material manufacturing more homogeneous to reduce the nonhomogeneous fiber volume fraction.

3.2. Probability Distribution. In order to characterize the statistical distributions of mechanical properties for EBC, the test data are fitted to normal, lognormal, and Weibull models, and the goodness of fit analysis is conducted. Figure 5 shows the details of the best-fit distribution for the tension strength parallel to the grain of EBC5 as an example of the choice of distribution model. H indicates null hypothesis, and P is the probability of observing a test statistic as extreme as, or more extreme than, the observed value under the null hypothesis. D is computed from the largest difference (in absolute value) between the observed and theoretical cumulative distribution functions in the figure. The details of the best-fit probability distribution functions of mechanical properties are shown in Table 4 and Table 5. For most groups of EBC, the normal distribution best-fitted the tensile strength parallel to the grain and shear strength perpendicular to the grain and compressive properties, the Weibull model presented the best fit for both shear strength parallel to the grain and tensile strength perpendicular to the grain, and the lognormal distribution best-fitted the tensile and shear modulus, which is inconsistent with research studies on other composite materials [22]. Table 6 shows the recommended best-fit distribution functions of the mechanical properties for EBC.

Table 3: Summary of experimental results and characteristic values for EBC.

	EBC1	EBC2	EBC3	EBC4	EBC5	EBC6	EBC7	EBC8	EBC9
ρ (g/cm^3)	1.31 (0.04)	1.31 (0.06)	1.23 (0.06)	0.98 (0.06)	1.14 (0.05)	0.68 (0.04)	0.65 (0.04)	0.67 (0.02)	0.70 (0.05)
Mc_{mean} (%)	5.30 (0.04)	5.75 (0.07)	7.56 (0.06)	7.26 (0.05)	9.18 (0.06)	8.38 (0.04)	7.52 (0.03)	7.59 (0.04)	7.07 (0.06)
Compression									
$f_{c,0,mean}$ (MPa)	112.89 (0.08)	119.04 (0.08)	99.29 (0.04)	66.72 (0.11)	101.95 (0.06)	59.44 (0.07)	55.93 (0.09)	59.36 (0.08)	69.22 (0.06)
$f_{c,90,mean}$ (MPa)	46.15 (0.11)	51.19 (0.18)	47.64 (0.12)	27.09 (0.19)	35.54 (0.20)	15.1 (0.21)	16.08 (0.12)	15.24 (0.13)	16.37 (0.08)
$f_{c,0,k}$ (MPa)	97.66	102.73	91.49	53.44	90.24	51.79	46.94	50.94	61.50
$f_{c,90,k}$ (MPa)	46.15	51.19	47.64	18.13	35.54	15.10	16.08	15.24	16.37
$E_{c,0,mean}$ (GPa)	19.48 (0.08)	17.43 (0.10)	15.37 (0.05)	12.52 (0.10)	16.82 (0.10)	13.03 (0.07)	10.45 (0.09)	11.61 (0.08)	12.87 (0.06)
$E_{c,90,mean}$ (GPa)	4.04 (0.16)	4.53 (0.20)	3.88 (0.10)	2.77 (0.16)	3.44 (0.12)	1.87 (0.23)	1.87 (0.13)	2.19 (0.22)	2.01 (0.10)
Tension									
$f_{t,0,mean}$ (MPa)	141.73 (0.24)	130.60 (0.20)	133.19 (0.13)	99.91 (0.33)	125.86 (0.20)	127.71 (0.10)	124.25 (0.24)	103.71 (0.18)	117.05 (0.19)
$f_{t,90,mean}$ (MPa)	5.2 (0.22)	7.29 (0.15)	9.38 (0.21)	2.52 (0.31)	3.14 (0.34)	4.30 (0.18)	5.03 (0.11)	5.45 (0.31)	6.79 (0.18)
$f_{t,0,k}$ (MPa)	81.15	83.86	103.55	39.89	81.06	89.89	71.38	70.05	80.38
$f_{t,90,k}$ (MPa)	3.15	5.59	5.85	1.17	1.11	2.84	3.92	2.37	4.46
$E_{t,0,mean}$ (GPa)	19.11 (0.10)	16.58 (0.12)	14.48 (0.09)	14.02 (0.22)	16.96 (0.15)	13.19 (0.13)	12.82 (0.22)	9.82 (0.17)	11.56 (0.16)
$E_{t,90,mean}$ (GPa)	3.22 (0.26)	8.98 (0.26)	7.09 (0.25)	1.06 (0.22)	1.44 (0.25)	3.7 (0.24)	8.43 (0.26)	3.74 (0.25)	6.51 (0.26)
Shear									
$f_{s,0,mean}$ (MPa)	19.9 (0.19)	16.1 5 (0.24)	18.79 (0.16)	9.01 (0.29)	10.69 (0.26)	15.44 (0.17)	10.36 (0.28)	14.6 (0.17)	11.89 (0.20)
$f_{s,90,mean}$ (MPa)	26.11 (0.23)	40.35 (0.15)	34.45 (0.12)	20.77 (0.16)	32.63 (0.15)	18.49 (0.12)	21.68 (0.17)	17.87 (0.13)	12.83 (0.20)
$f_{s,0,k}$ (MPa)	12.77	8.88	12.54	4.05	5.19	10.75	4.89	9.69	8.16
$f_{s,90,k}$ (MPa)	15.44	29.48	27.28	14.44	23.92	14.63	15.17	13.68	8.24
$G_{s,0,mean}$ (GPa)	5.13 (0.13)	4.22 (0.12)	4.45 (0.10)	2.17 (0.15)	3.80 (0.10)	2.62 (0.14)	2.35 (0.15)	2.95 (0.11)	2.58 (0.10)
$G_{s,90,mean}$ (GPa)	5.8 (0.12)	5.03 (0.15)	4.62 (0.16)	2.77 (0.17)	4.45 (0.12)	2.99 (0.13)	2.86 (0.17)	3.06 (0.15)	2.54 (0.09)

Note. The coefficient of variation is shown in parentheses.

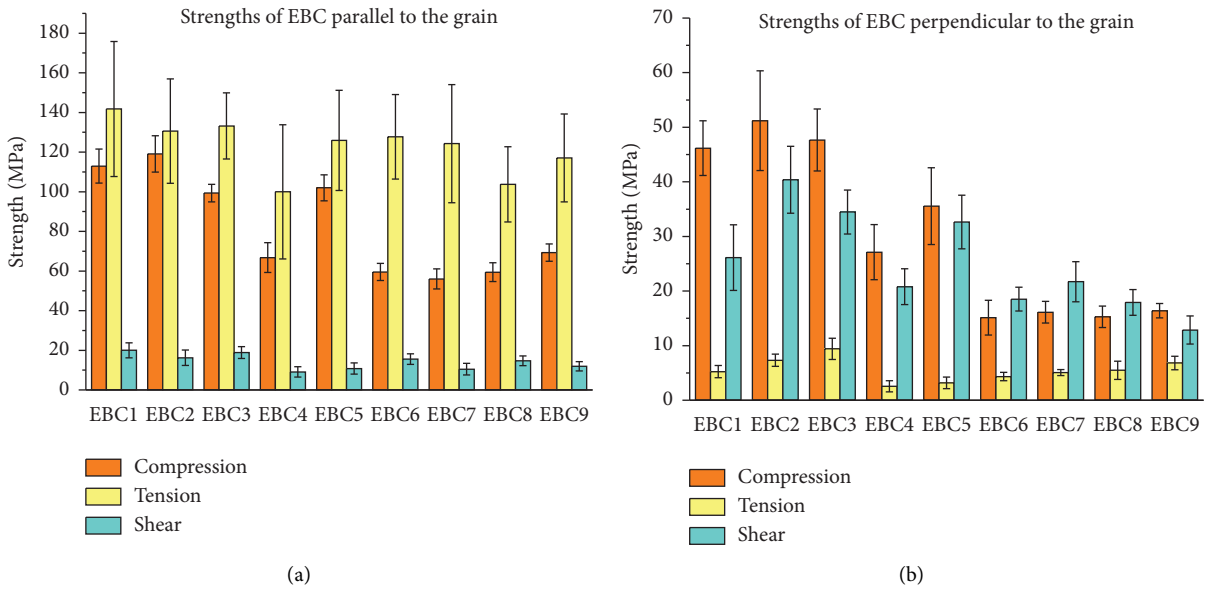

Figure 4: Continued.

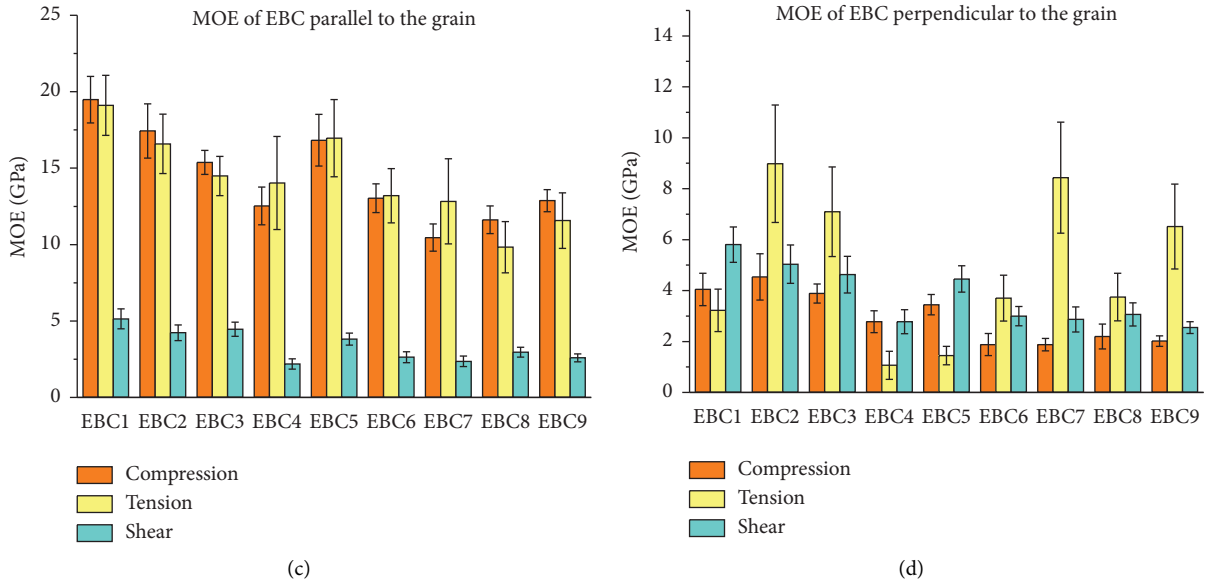

Figure 4: Strengths and moduli distributions of experimental data: strengths in parallel to the grain (a); strengths in perpendicular to the grain (b); moduli in parallel to the grain (c); moduli in perpendicular to the grain (d).

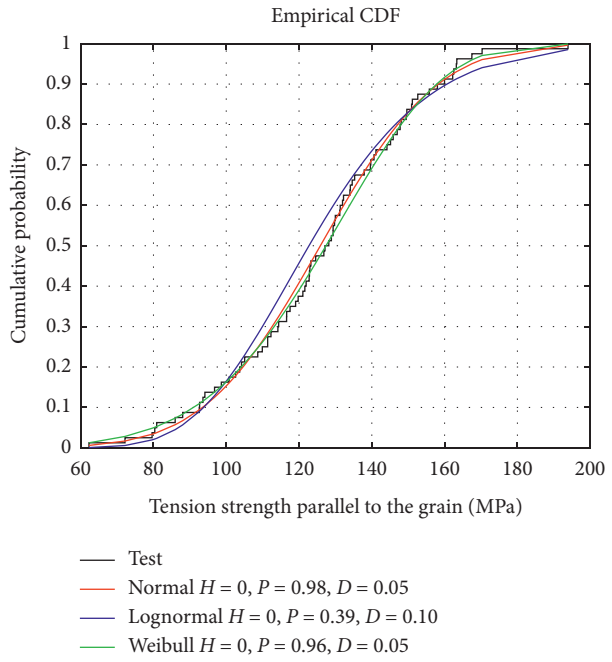

Figure 5: Example of the Kolmogorov–Smirnov tests for the goodness of fit analysis.

3.3. Strength Grading of EBC. The objective of this section was to develop the strength grading of EBC, which is expected that the results can be applied in structural design. The first step is to determine the potential predictors with a stronger correlation with compressive strength through correlation analysis, which was chosen as IPs. Density and MOE frequently show a strong correlation with strength properties of European hardwoods [23–25]. For this work, density and compressive modulus were chosen as potential predictors for compressive strength. To verify potential predictors, a simple linear regression was conducted between predictors (ρ and $E_{c,0}$) and response ($f_{c,0}$). According to the linear regression, the correlation coefficient between ρ and $f_{c,0}$ was in the range of 0.58–0.79, and between $E_{c,0}$ and $f_{c,0}$, it was 0.58–0.79 (Table 7). Hence the density and compressive MOE were selected as IPs for strength grading.

In this research, EBC grading based on compressive strength was established by the confidence band. The outlier and extreme values were justified and removed from further analysis by utilizing a 99% ellipse band and 95% predicted

Table 4: The details of the best-fit distribution functions of modulus for EBC.

Group	Compression		Tension		Shear	
	$E_{c,0}$	$E_{c,90}$	$E_{t,0}$	$E_{t,90}$	$G_{s,0}$	$G_{s,90}$
EBC1	$x-L$ (2.97, 0.08^2)	$x-N$ (4.04, 0.64^2)	$x-L$ (2.94, 0.10^2)	$x-N$ (3.22, 0.84^2)	$x-L$ (1.63, 0.13^2)	$x-L$ 1.49, 0.12^2)
EBC2	$x-N$ (17.39, 1.80^2)	$x-L$ (1.49, 0.19^2)	$x-L$ (2.80, 0.12^2)	$x-L$ (2.16, 0.26^2)	$x-L$ (1.43, 0.12^2)	$x-L$ (1.60, 0.15^2)
EBC3	$x-L$ (2.73, 0.05^2)	$x-L$ (1.35, 0.10^2)	$x-L$ (2.67, 0.09^2)	$x-L$ (1.93, 0.25^2)	$x-W$ (4.64, 9.86)	$x-W$ (4.92, 7.53)
EBC4	$x-N$ (9.43, 0.10^2)	$x-N$ (2.77, 0.43^2)	$x-L$ (2.62, 0.22^2)	$x-W$ (1.25, 3.36)	$x-L$ (0.77, 0.17^2)	$x-L$ (1.01, 0.16^2)
EBC5	$x-N$ (16.82, 1.69^2)	$x-N$ (3.44, 0.40^2)	$x-N$ (16.96, 2.53^2)	$x-W$ (1.58, 4.56)	$x-L$ (1.43, 0.12^2)	$x-L$ 1.49, 0.12^2)
EBC6	$x-N$ (13.03, 0.94^2)	$x-W$ (2.05, 4.82)	$x-N$ (13.19, 1.77^2)	$x-L$ (1.28, 0.25^2)	$x-N$ (2.62, 0.35^2)	$x-N$ (2.54, 0.23^2)
EBC7	$x-N$ (10.45, 0.89^2)	$x-N$ (1.88, 0.24^2)	$x-L$ (2.53, 0.22^2)	$x-W$ (9.26, 4.39)	$x-L$ (0.85, 0.14^2)	$x-N$ (2.99, 0.38^2)
EBC8	$x-L$ (2.45, 0.08^2)	$x-W$ (2.38, 5.10)	$x-L$ (2.27, 0.17^2)	$x-L$ (1.84, 0.26^2)	$x-N$ (2.95, 0.32^2)	$x-W$ (3.07, 5.95)
EBC9	$x-L$ (2.55, 0.06^2)	$x-N$ (2.01, 0.20^2)	$x-N$ (11.56, 1.82^2)	$x-L$ (1.29, 0.25^2)	$x-L$ (0.94, 0.10^2)	$x-L$ (1.11, 0.15^2)

Table 5: The details of the best-fit distribution functions of strengths for EBC.

Group	Compression		Tension		Shear	
	$f_{c,\ 0}$	$f_{c,\ 90}$	$f_{t,\ 0}$	$f_{t,\ 90}$	$f_{s,\ 0}$	$f_{s,\ 90}$
EBC1	$x-N$ (112.89, 8.57^2)	$x-N$ (46.15, 5.02^2)	$x-N$ (141.73, 34.09^2)	$x-W$ (5.63, 5.62)	$x-W$ (24.41, 6.23)	$x-N$ (26.11, 6.02^2)
EBC2	$x-N$ (119.04, 9.20^2)	$x-N$ (51.19, 9.13^2)	$x-N$ (130.60, 26.35^2)	$x-L$ (1.98, 0.15^2)	$x-W$ (17.64, 4.85)	$x-N$ (40.35, 6.13^2)
EBC3	$x-N$ (99.29, 4.40^2)	$x-N$ (47.64, 5.68^2)	$x-N$ (133.19, 16.72^2)	$x-W$ (10.13, 5.88)	$x-W$ (20.09, 6.77)	$x-N$ (34.45, 4.04^2)
EBC4	$x-N$ (66.72, 7.49^2)	$x-N$ (27.09, 5.05^2)	$x-N$ (99.90, 33.85^2)	$x-N$ (2.66, 0.84^2)	$x-L$ (2.16, 0.30^2)	$x-N$ (3.02, 0.17^2)
EBC5	$x-N$ (101.95, 6.59^2)	$x-N$ (35.54, 7.04^2)	$x-N$ (125.86, 25.27^2)	$x-W$ (3.51, 3.23)	$x-W$ (11.75, 4.20)	$x-W$ (34.65, 8.10)
EBC6	$x-N$ (59.44, 4.30^2)	$x-N$ (15.10, 3.18^2)	$x-N$ (127.71, 21.33^2)	$x-W$ (4.61, 6.60)	$x-W$ (16.51, 7.38)	$x-N$ (18.49, 2.18^2)
EBC7	$x-N$ (55.93, 5.07^2)	$x-N$ (16.08, 1.98^2)	$x-N$ (124.25, 29.80^2)	$x-N$ (5.03, 0.54^2)	$x-W$ (11.45, 4.06)	$x-W$ (23.19, 7.20)
EBC8	$x-N$ (59.36, 4.75^2)	$x-N$ (15.24, 1.97^2)	$x-N$ (103.71, 18.97^2)	$x-W$ (6.04, 3.77)	$x-W$ (15.60, 6.71)	$x-N$ (17.87, 2.36^2)
EBC9	$x-N$ (69.22, 4.36^2)	$x-N$ (16.37, 1.33^2)	$x-L$ (4.75, 0.19^2)	$x-W$ (7.30, 6.53)	$x-L$ (2.46, 0.20^2)	$x-N$ (12.83, 2.57^2)

Note.: $x-N\ (\mu, \sigma^2)$: $f(x) = (1/\sqrt{2\pi}\sigma)\exp(-(x-\mu)^2/2\sigma^2)$; $x-L\ (\mu_{\ln}, \sigma_{\ln}^2)$: $f(x) = (1/\sqrt{2\pi}\sigma_{\ln}x)e^{-(\ln x-\mu_{\ln})^2/2\sigma_{\ln}^2}$; $x-W\ (k, \lambda)$: $f(x) = (k/\lambda)(x/\lambda)^{k-1}e^{-(x/\lambda)^k}$.

Table 6: The recommended best-fit distribution functions of the mechanical properties for EBC.

Property	Best-fit distribution
$f_{c,\ 0}$	Normal
$f_{c,\ 90}$	Normal
$E_{c,\ 0}$	Normal
$E_{c,\ 90}$	Normal
$f_{t,\ 0}$	Normal
$f_{t,\ 90}$	2-P Weibull
$E_{t,\ 0}$	Lognormal
$E_{t,\ 90}$	Lognormal
$f_{s,\ 0}$	2-P Weibull
$f_{s,\ 90}$	Normal
$G_{s,\ 0}$	Lognormal
$G_{s,\ 90}$	Lognormal

Table 7: Correlation coefficients (R^2) between predictors and response for EBC.

	Compressive strength parallel to the grain ($f_{c,0}$)								
	EBC1	EBC2	EBC3	EBC4	EBC5	EBC6	EBC7	EBC8	EBC9
Density (ρ)	**0.60**	**0.73**	**0.72**	**0.62**	**0.75**	**0.58**	**0.64**	**0.63**	**0.79**
Compressive modulus ($E_{c,0}$)	**0.62**	**0.68**	0.58	**0.62**	**0.70**	**0.73**	**0.72**	**0.73**	**0.79**

Note. The correlations significant at $p < 0.05$ are displayed in bold.

band. The examples of ellipse confidence band analysis are shown in Figure 6.

Density and MOE were IPs for strength grading for EBC since they were strong correlation with compressive strength. Using the confidence band approach to perform regression analysis on the EBC for strength grading, R^2 is sufficiently high in the range of 0.44 to 0.87. Figure 7 shows the confidence bands used to develop the EBC strength grading. The confidence band method generates a continuous function, and the stair function can be used to

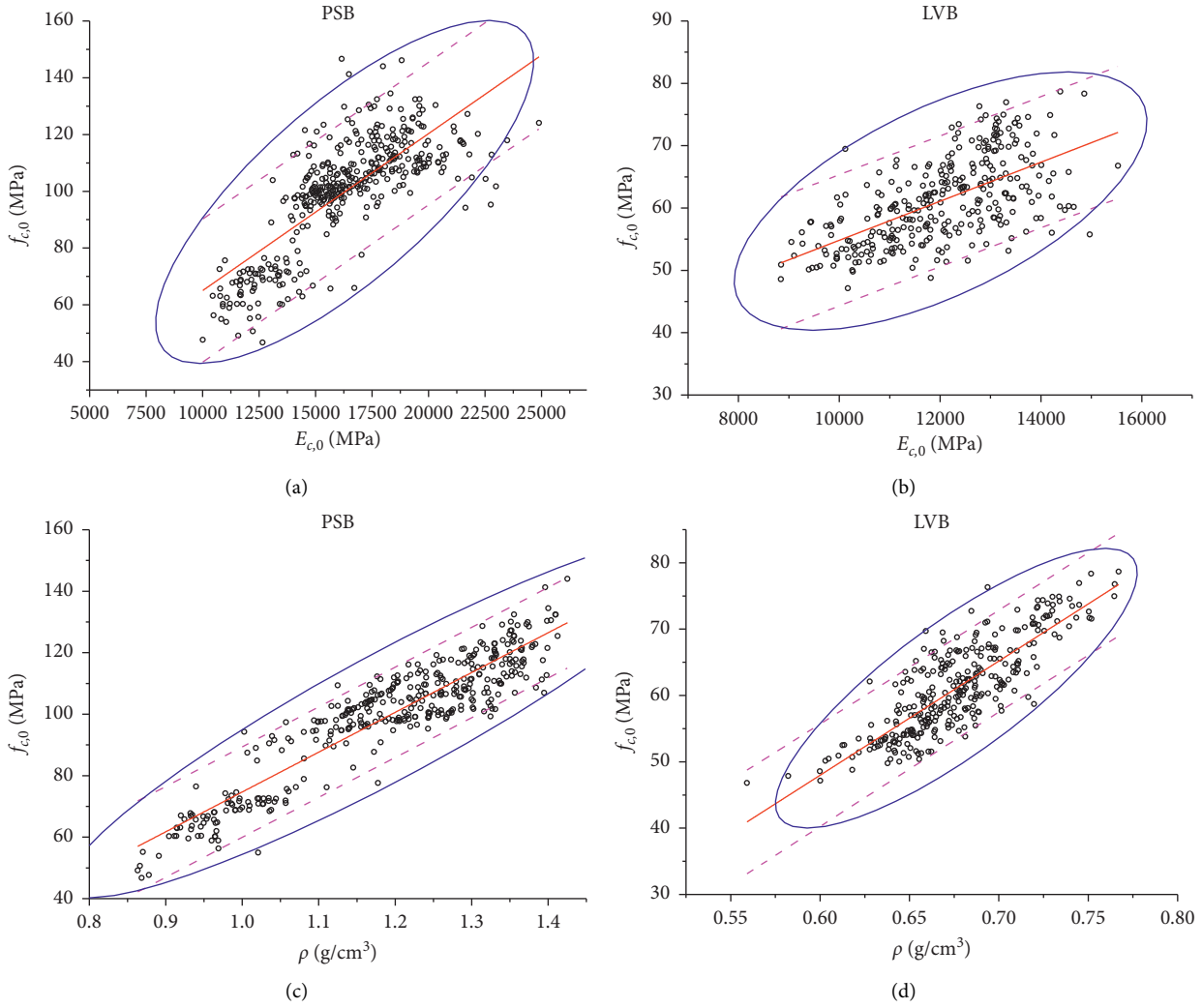

Figure 6: Ellipse band and predicted band analysis of linear regression: $f_{c,0}$ against $E_{c,0}$ for PSB (a); $f_{c,0}$ against $E_{c,0}$ for LVB (b); $f_{c,0}$ against ρ for PSB (c); $f_{c,0}$ against ρ for LVB (d).

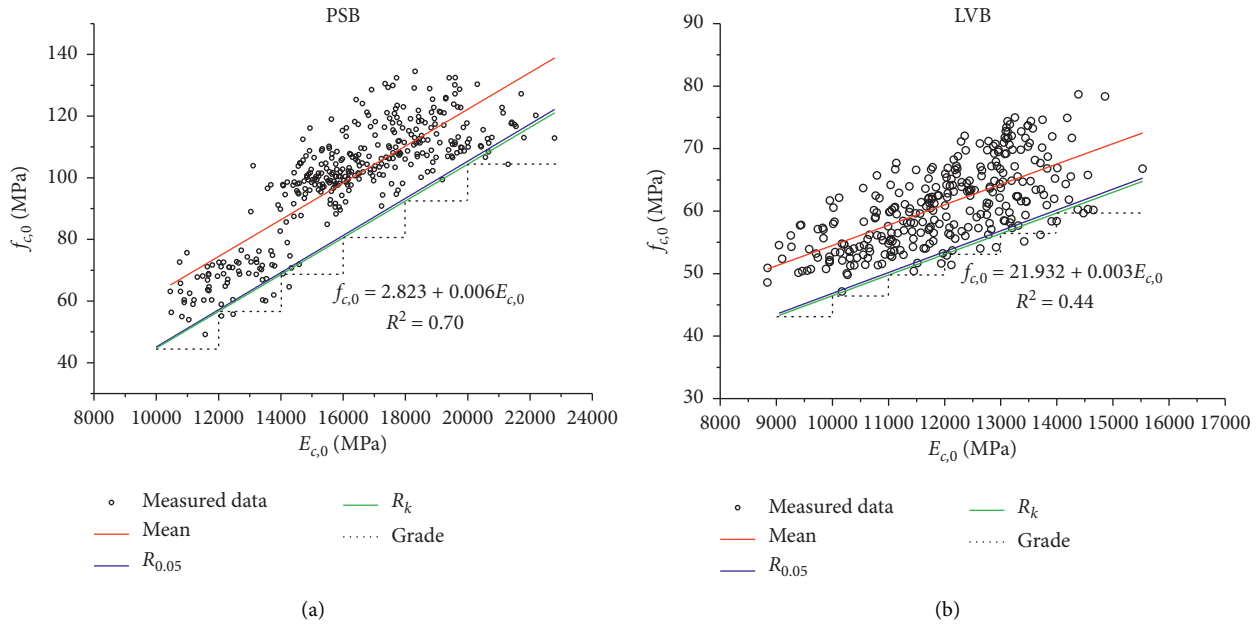

Figure 7: Continued.

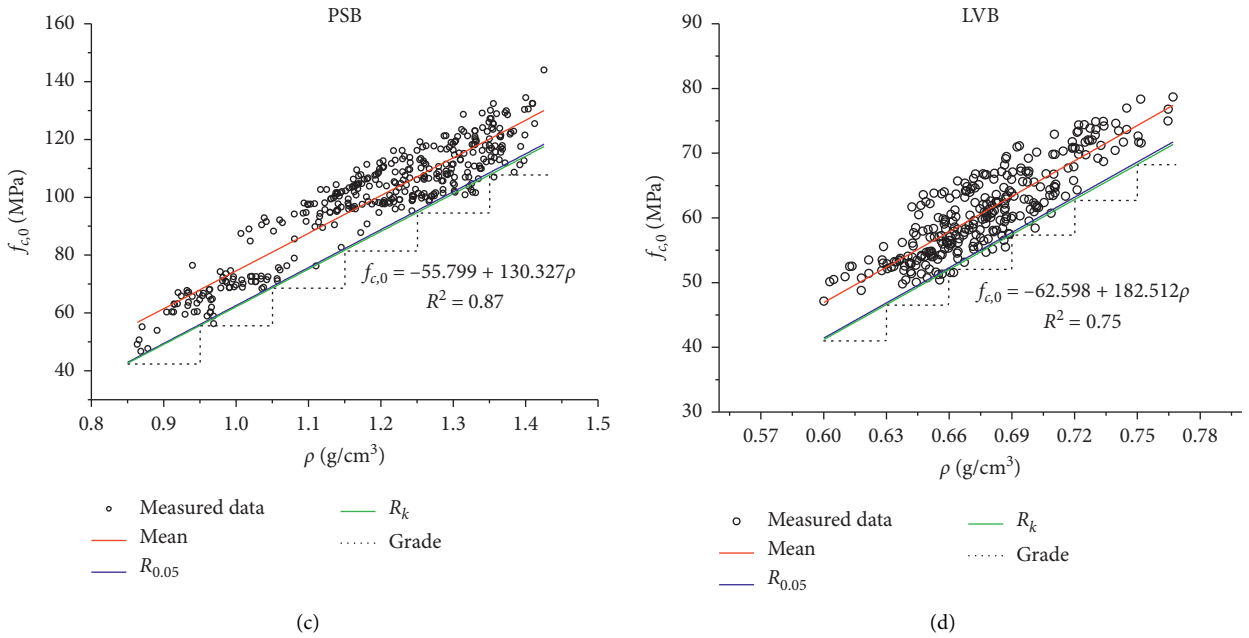

Figure 7: Compressive strength grading of EBC: based on compressive modulus for PSB (a); based on compressive modulus for LVB (b); based on density for PSB (c); based on density for LVB (d).

Table 8: Compressive strength grade classification of EBC based on compressive modulus.

Grade ($E_{c,0}$) Interval (MPa)	Compressive strength ($f_{c,0}$, MPa)		
	Mean	$R_{0.05}$	R_k
PSB			
10000–11999	63.10	51.12	50.70
12000–13999	72.58	63.16	62.64
14000–15999	98.13	75.20	74.58
16000–17999	108.71	87.24	86.52
18000–19999	115.16	99.28	98.46
≥20000	116.07	111.32	110.40
LVB			
9000–9999	54.00	45.21	44.80
10000–10999	55.41	48.55	48.11
11000–11999	58.74	51.89	51.42
12000–12999	63.08	55.23	54.73
13000–13999	66.45	58.57	58.04
≥14000	67.22	61.91	61.35

Table 9: Compressive strength grade classification of EBC based on density.

Grade (ρ) Interval (g/cm^3)	Compressive strength ($f_{c,0}$, MPa)		
	Mean	$R_{0.05}$	R_k
PSB			
0.85–0.949	61.17	49.47	49.12
0.95–1.049	71.24	62.58	62.14
1.05–1.149	87.58	75.69	75.16
1.15–1.249	101.93	88.80	88.18
1.25–1.349	111.45	101.92	101.20
≥1.35	121.94	115.03	114.22
LVB			
0.60–0.629	51.57	44.14	43.89
0.63–0.659	55.43	49.58	49.31
0.66–0.689	60.48	55.03	54.72
0.69–0.719	65.45	60.48	60.14
0.72–0.749	72.23	65.92	65.56
≥0.750	74.95	71.37	70.97

subdivide the function into several grades at the specified interval of IP. Each grade had $R_{0.05}$ and R_k of $f_{c,\ 0}$, which could be utilized in EBC structural design following a strength-based approach. Table 8 and Table 9 show the grading of PSB and LVB into strength grades based on density and MOE. The higher quality grades have higher strength. The designer can estimate the characteristic value of compressive strength based on the IPs according to Table 8 and Table 9 for modern engineered bamboo structural design.

4. Conclusions

This study statistically investigates the mechanical properties of two types of EBC for seven manufacturers with raw materials from five regions in China. To study the mechanical behaviors of groups for EBC, tensile, compressive, and shear tests were carried out on small clear specimens. The study utilized wood standards for characterization, determining the probability distributions and characteristic values for mechanical properties. Except for the PSB with lower density, the mechanical properties of PSB are generally higher than those of LVB.

In addition, the statistical parameters of the best-fit probability distribution models for mechanical properties can be utilized to determine the characteristic values and build the probabilistic design approach. The results are conducive to developing design standards and reliability evaluation practices for EBC structures and extending the particular applications in engineering.

Due to their more significant correlation coefficients, density and compressive modulus were considered the most suitable IPs for strength grading of EBC subject to compressive strength. According to the confidence band method, grade intervals are built in similar ranges, and the characteristic value in each grade can be calculated.

After comparing the results from different sources, it is found that although the results obtained from the test are similar, there is significant variation in the differences between different sources of the same material. The research shows that future work needs to determine the source of variation in testing and establish a complete reliability analysis and strength grading.

Nomenclature

$E_{c,0}$: Compressive modulus parallel to the grain
$E_{c,\ 0,\text{mean}}$: Mean compressive parallel to the grain
$f_{s,\ 0}$: Shear strength parallel to the grain
$f_{s,\ 0,\ k}$: Characteristic shear strength parallel to the grain
$E_{c,\ 90}$: Compressive modulus parallel perpendicular to the grain
$E_{c,\ 90,\ \text{mean}}$: Mean compressive modulus parallel perpendicular to the grain
$f_{s,\ 90}$: Shear strength perpendicular to the grain
$f_{s,\ 90,\ k}$: Characteristic shear strength perpendicular to the grain
$E_{t,\ 0}$: Tensile modulus parallel to the grain
$E_{t,\ 0,\ \text{mean}}$: Mean tensile modulus parallel to the grain
$G_{s,\ 0}$: Shear modulus parallel to the grain
$G_{s,\ 0,}$ mean: Mean shear modulus parallel to the grain
$E_{t,\ 90}$: Tensile modulus perpendicular to the grain
$E_{t,\ 90,}$ mean: Mean tensile modulus perpendicular to the grain
$G_{s,\ 90}$: Shear modulus perpendicular to the grain
$G_{s,\ 90,\ \text{mean}}$: Mean shear modulus perpendicular to the grain
$f_{c,\ 0}$: Compressive strength parallel to the grain
$f_{c,\ 0,\ k}$: Characteristic compressive strength parallel to the grain
Mc: Moisture content
Mc_{mean}: Mean moisture content
$f_{c,\ 90}$: Compressive strength perpendicular to the grain
$f_{c,\ 90,\ k}$: Characteristic compressive strength perpendicular to the grain
ρ: Mean air-dry density
MOE: Modulus of elastic
$f_{t,\ 0}$: Tensile strength parallel to the grain
$f_{t,\ 0,\ k}$: Characteristic tensile strength parallel to the grain
$f_{t,\ 90}$: Tensile strength perpendicular to the grain
$f_{t,\ 90,\ k}$: Characteristic tensile strength perpendicular to the grain.

Data Availability

The data used to support the findings of this study are available from the corresponding author upon request.

Conflicts of Interest

The authors declare that they have no conflicts of interest.

Acknowledgments

This research was supported by the National Natural Science Foundation of China (no. 51978338), Basic Ability Improvement Program of Young and Middle-Aged Scholar for the Education Office of Guangxi Province (no. 2019KY0236) and Priority Academic Program Development of Jiangsu Higher Education Institutions (PAPD).

References

[1] Y. Xiao, R. Z. Yang, and B. Shan, "Corrigendum to "Production, environmental impact and mechanical properties of glubam"" *Construction and Building Materials*, vol. 44, p. 805, 2013.

[2] P. J. Shi, "Precipitation is the most crucial factor determining the distribution of moso bamboo in Mainland China," *Global Ecology and Conservation*, vol. 22, 2020.

[3] S. Amada and S. Untao, "Fracture properties of bamboo," *Composites Part B-Engineering*, vol. 32, no. 5, pp. 449–457, 2001.

[4] F. Wang, Z. Shao, and Y. Wu, "Mode II interlaminar fracture properties of Moso bamboo," *Composites Part B: Engineering*, vol. 44, no. 1, pp. 242–247, 2013.

[5] D. S. Huang, A. P. Zhou, and Y. L. Bian, "Experimental and analytical study on the nonlinear bending of parallel strand bamboo beams," *Construction and Building Materials*, vol. 44, pp. 585–592, 2013.

[6] D. Huang, Y. Bian, A. Zhou, and B. Sheng, "Experimental study on stress-strain relationships and failure mechanisms of parallel strand bamboo made from phyllostachys," *Construction and Building Materials*, vol. 77, pp. 130–138, 2015.

[7] Y. Wei, "Stress-strain relationship model of glulam bamboo under axial loading," *Advanced Composites Letters*, vol. 29, 2020.

[8] Y. Xiao, Y. Wu, J. Li, and R. Z. Yang, "An experimental study on shear strength of glubam," *Construction and Building Materials*, vol. 150, pp. 490–500, 2017.

[9] B. Sharma, A. Gatóo, M. Bock, and M. Ramage, "Engineered bamboo for structural applications," *Construction and Building Materials*, vol. 81, pp. 66–73, 2015.

[10] A. Kumar, T. Vlach, L. Laiblova et al., "Engineered bamboo scrimber: influence of density on the mechanical and water absorption properties," *Construction and Building Materials*, vol. 127, pp. 815–827, 2016.

[11] B. S. Institution, *Bs En 384 - Structural Timber - Determination of Characteristic Values of Mechanical Properties and Density*, 2018.

[12] ASTM, *Practice for Sampling and Data-Analysis for Structural Wood and Wood-Based Products*, ASTM International West, Conshohocken, PA, USA, 2017.

[13] D. Trujillo, S. Jangra, and J. M. Gibson, "Flexural properties as a basis for bamboo strength grading," *Proceedings of the Institution of Civil Engineers - Structures and Buildings*, vol. 170, no. 4, pp. 284–294, 2017.

[14] N. N. Nurmadina, N. Nugroho, and E. T. Bahtiar, "Structural grading of Gigantochloa apus bamboo based on its flexural properties," *Construction and Building Materials*, vol. 157, pp. 1173–1189, 2017.

[15] E. T. Bahtiar, A. P. Imanullah, D. Hermawan, N. Nugroho, and fnm Abdurachman, "Structural grading of three sympodial bamboo culms (Hitam, Andong, and Tali) subjected to axial compressive load," *Engineering Structures*, vol. 181, pp. 233–245, 2019.

[16] E. T. Bahtiar, D. Trujillo, and N. Nugroho, "Compression resistance of short members as the basis for structural grading of Guadua angustifolia," *Construction and Building Materials*, vol. 249, 2020.

[17] China SAO, *Method for Determination of the Density of Wood*, GB/T 1933-2009, Macau, China, 2009.

[18] China SAO, *Method for Determination of Moisture Content of Wood*, GB/T 1931-2009, Macau, China, 2009.

[19] ASTM, *Standard Test Methods for Small Clear Specimens of Timber*, ASTM International West Conshohocken, Conshohocken, PA, USA, 2014.

[20] ASTM, *Standard Test Method for Shear Properties of Composite Materials by V-Notched Rail Shear Method*, ASTM International West Conshohocken, Conshohocken, PA, USA, 2012.

[21] B. P. Murphy, I. M. Chakravarti, R. G. Laha, and J. Roy, "Handbook of methods of applied statistics. Vol. I: techniques of computation, descriptive methods and statistical inference," *Applied Statistics*, vol. 17, no. 3, p. 293, 1968.

[22] J. P. Torres, L.-J. Vandi, M. Veidt, and M. T. Heitzmann, "The mechanical properties of natural fibre composite laminates: a statistical study," *Composites Part A: Applied Science and Manufacturing*, vol. 98, pp. 99–104, 2017.

[23] CEN, *Structural Timber – Strength Classes. EN 338. 2016*, European Committee for Standardisation, Brussels, Belgium.

[24] G. Riesco Muñoz, A. Remacha Gete, and F. Pedras Saavedra, "Implications in the design of a method for visual grading and mechanical testing of hardwood structural timber for designation within the European strength classes," *Forest Systems*, vol. 20, no. 2, pp. 235–244, 2011.

[25] A. Kovryga, P. Stapel, and J. W. G. van de Kuilen, "Mechanical properties and their interrelationships for medium-density European hardwoods, focusing on ash and beech," *Wood Material Science & Engineering*, vol. 15, no. 5, pp. 289–302, 2020.

Hindawi
Advances in Civil Engineering
Volume 2021, Article ID 6688076, 11 pages
https://doi.org/10.1155/2021/6688076

Research Article

Sustainability Design Considerations for Timber-Concrete Composite Floor Systems

Md Abdul Hamid Mirdad, Hossein Daneshvar, Thomas Joyce, and Ying Hei Chui

Department of Civil and Environmental Engineering, 9211 116 Street NW, University of Alberta, Edmonton, AB T6G1H9, Canada

Correspondence should be addressed to Md Abdul Hamid Mirdad; mdabdul@ualberta.ca

Received 19 December 2020; Revised 1 March 2021; Accepted 4 March 2021; Published 16 March 2021

Academic Editor: Claudio Mazzotti

Over the last few decades, there has been growing interest in the use of low-carbon materials to reduce the environmental impacts of the construction industry. The advent of mass timber panels (MTP), such as cross laminated timber (CLT), has allowed structural engineers to specify a low-carbon material for a variety of floor design considerations. However, serviceability issues such as vibration and deflection are limiting the construction of longer span timber-only floor systems and have encouraged the development of timber-concrete composite (TCC) systems. The use of concrete would negatively impact on the carbon footprint of the TCC floor system and should be minimized. The purpose of this study was to study the impact on embodied carbon in the TCC system, when the ratio of timber and concrete was varied for specific floor spans. Two MTP products were considered, CLT and glued laminated timber (GLT). The floors were designed to satisfy structural, acoustic, and vibration criteria, and the results were presented in the form of span tables. It was found that using thicker MTP instead of adding concrete thickness to meet a specific span requirement can lead to lower embodied carbon values. Increasing concrete thickness for long-span floor systems led to a reduction in allowable floor span due to the vibration criterion being the controlling design parameter. Increasing timber thickness also resulted in higher strength and stiffness to weight ratios, which would contribute toward reducing the size of lateral load resisting systems and foundations, resulting in further reductions in the embodied carbon of the entire structure.

1. Introduction

In recent years, the use of timber in multistorey residential and commercial buildings has increased worldwide, primarily inspired by consciousness surrounding the sustainability of timber as the primary structural material [1, 2]. Timber structures are generally associated with lower levels of embodied carbon due to lower emissions during the manufacturing of the timber products and the construction process. In addition, some life cycle accounting practices permit the inclusion of carbon sequestered from the atmosphere during tree growth that is captured within timber products for the duration of their life [3, 4]. Therefore, timber in construction can reduce greenhouse gas (GHG) emission in the atmosphere which is a major contributor to global warming. A new generation of engineered mass timber products known as mass timber panel (MTP), for example, glued laminated timber (GLT) and cross laminated timber (CLT), has the structural capacities to be used as a low-carbon alternative to steel and concrete for gravity and lateral load resisting systems in structures.

Construction with mass timber is approximately 25% faster than similar on-site concrete construction. It also requires 90% less construction traffic and 75% fewer workers which yields a much quieter job site [5]. The lighter weight and lower stiffness of timber-only floors can make them more susceptible to serviceability limit states such as vibrations and excessive deflections while satisfying the strength requirements. Therefore, in timber-concrete composite (TCC) floor systems, a structural concrete topping layer is provided over the timber beam or mass timber panel (MTP). The two components are connected by mechanical connectors, as shown in Figure 1, such as dowels

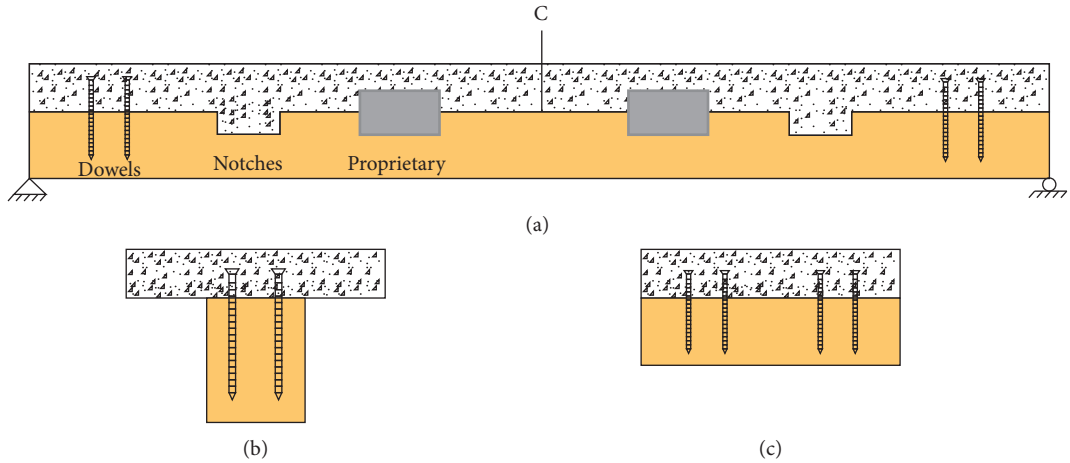

Figure 1: (a) Longitudinal section of a TCC system with dowel, notched, or proprietary connectors; cross section of a TCC floor (b) with timber beam and (c) with MTP.

(e.g., self-tapping screw (STS)), notches, or proprietary connectors (e.g., glued in plate/HBV plate). The added concrete increases the floor mass and stiffness which subsequently mitigates the vibrations and excessive deflection issues [6–8].

In TCC construction, the concrete slab resists compressive stress while timber primarily resists tensile stress generated by an out-of-plane bending action. In reinforced concrete design, the tensile strength of concrete is often neglected, and steel reinforcement is installed to resist the tensile stresses caused by bending. In the ultimate limit state design, the concrete is assumed to crack to about 2/3 of its depth under bending [9]. In TCC, this cracked area is replaced by the timber cross section. In TCC, minimum steel reinforcements are provided only to control and limit the cracking. The mechanical connector transfers the shear force between timber and concrete to provide a desired partial composite action. Using a timber panel instead of a timber beam in the TCC construction generates longer spans which also can reduce the floor height if they are used as a flat slab and is preferable in the mid-to-high rise construction [10]. Besides structural and serviceability performance, TCC provides enhanced performance over timber-only floors, including air-borne sound insulation, fire resistance, and thermal mass [9, 11, 12]. Since concrete is more carbon-intensive than timber but provides a larger contribution to stiffness and strength on a per unit volume basis, there should be an optimum ratio of concrete and timber in terms of embodied carbon for a specific design. Investigating the various floor parameters that affect this optimum concrete-timber ratio is the main goal of this study.

Embodied carbon (EC) is defined as the carbon footprint of a material. It considers the amount of greenhouse gas emissions that is released throughout the supply chain of a material or product, including all extraction, transport, processing, and fabrication activities of a material or product via cradle-to-gate, or cradle-to-site. Cradle-to-gate refers to a partial product life cycle associated with embodied carbon which considers all activities from resource extraction (cradle) to the factory gate (i.e., before it is transported to the consumer). Cradle-to-site extends the cradle-to-gate results to include transportation of the material or product to its site of use [13–15]. Embodied carbon differs from carbon footprint in that embodied carbon can only be associated with materials or products, whereas a carbon footprint could also measure the GHG emissions during the service life of a material, for example, in the operation of a building. Embodied carbon emissions from the building construction sector produce almost 11% of annual global GHG emissions [16]. Life cycle assessment (LCA) is a method for calculating the environmental impact, be it embodied carbon or total carbon footprint, of a product [17].

Despite the ongoing research in the field of timber structures, most of the timber standards around the globe including North America do not have a standardized method for designing TCC floor systems. Among several proposed methods, the Gamma method based on Annex B of Eurocode 5 [18] is generally used to account for the partial composite action [9, 19]. The closed-form solution of the Gamma method, commonly used by design engineers, was obtained based on the assumption of sinusoidal distributed load and smeared connection between concrete and timber. Recently, a more general analytical model [20] was developed to predict the load-carrying capacity for ultimate limit state based on potential failure modes [21] and effective bending stiffness for serviceability limit state with load-deflection response [22] of TCC floor systems with mechanical connectors. This new model does not have the same limiting assumptions on loading and connection as the Gamma method. The Gamma method is most appropriate for systems with stiff mechanical and glued connection but is considered less accurate in the case of flexible connectors [9]. With the assumption of linear-elastic behavior, the Gamma method is not capable of predicting system failure if the system exhibits nonlinear behavior at failure [23].

As the structural integrity of the TCC system primarily depends on interlayer mechanical connectors, analytical models have also been developed for directly calculating the

strength [24] and stiffness [25] of concrete-to-timber connection based on the component properties. These connection models allow the timber-concrete connection properties, which are required for TCC system design, to be calculated without the need to perform connection tests.

It is common practice in TCC floor design to choose the thickness of the concrete layer based on several requirements of concrete design standard such as anchorage of the fastener, limits for concrete crushing, minimum cover to reinforcement, sound transmission, and a minimum thickness for diaphragm action. Generally, concrete thicknesses of 75 mm to 100 mm are used in practice, though past studies have considered thicknesses as low as 30 mm (plus 20 mm timber interlayer) with self-tapping screws [26], 50 mm lightweight concrete with self-tapping screws [26], 57 mm with inclined self-tapping screws [27], and 48 mm with notches and dowels using steel fibre reinforcement to remove the cover requirements [28]. Ultrathin toppings of only 12.5 mm tested by [29] showed significant reductions in both stiffness and strength relative to comparable connections with inclined self-tapping screws in thicker concrete layers. Despite this, the topping was found to be effective in reducing the perception of human-induced vibrations by increasing the natural frequency [29]. Besides, high-strength concrete gives the option to reduce the thickness of the concrete slab in TCC by providing higher load-carrying capacity [30]. However, the stiffness of connectors in high-strength concrete is usually lower compared to normal weight concrete [31].

Research has shown that suitable indicators of human response to floor vibration are the fundamental natural frequency of the floor and the deflection of the floor under a concentrated load at the center of the floor [9, 19]. Hamm et al. [32] proposed a method for checking the vibration performance of TCC floors based on the natural frequency and static deflection under 2 kN load at the floor center. Hu et al. [33] proposed a vibration criterion for TCC floors based on the natural frequency and static deflection under 1 kN load at the floor center. From their study, vibration control span can also be calculated directly from the effective bending stiffness and mass per unit length of a 1 m wide strip TCC beam. Besides, CSA O86 [34] provides a vibration-based limitation on the allowable span for CLT floors, without accounting for potential composite behavior adequately. A previous study [35] investigated the embodied carbon of the TCC system with CLT up to 7 ply using the Gamma method [18] and satisfying the vibration criterion proposed by Hamm et al. [32] for floor spans. The study concluded that lower embodied carbon values can be found by using thicker CLT panels rather than adding the concrete topping. Also, the influence of the connector properties on the TCC design requirement was found to be limited beyond a moderate degree of composite action. In this study, the sustainability aspects of the TCC system are investigated by using a more detailed TCC design method with all possible thicknesses of CLT (up to 9 ply) and glued laminated timber (GLT). The vibration criterion proposed by Hu et al. [33] is used in the development of floor spans along with satisfying other structural, serviceability, and acoustic performance requirements.

2. Methodology

As stated above, the goal of this study is to investigate the impacts on design selection with respect to the main TCC floor components, namely, concrete and timber, for specific span requirements on the embodied carbon of the system. The allowable span for a TCC floor system can be developed by considering all ultimate limit states related to timber, concrete, and shear connectors, and serviceability limit states related to deflection and vibration. The ultimate and serviceability limit state requirements for TCC floors with different combinations of materials, dimensions, and connection characteristics were evaluated based on [20]. Although long-term behavior of TCC systems such as creep deflection may be critical, this was not considered since it will be shown later that short-term serviceability criteria, such as vibration, tend to govern the design [19, 33].

2.1. Ultimate Limit State. In ultimate limit states, a floor system might fail due to concrete crushing, timber crushing, or screw yielding, when the stress demand exceeds the capacity at concrete layer, timber layer, and shear connectors, respectively. The lowest capacity associated with these failure modes would govern the allowable floor span. In the developed analytical model [21, 22], the MTPC composite beam is divided into two subsystems under uniformly distributed load. In the first subsystem (subsystem 1), the connection is released and the deflection of the unconnected beam under an applied load is calculated. In the second subsystem (subsystem 2), the connectors are replaced by redundant shear force. According to [21], the slip at the interlayer of subsystem 1 and subsystem 2 can be calculated as follows:

$$\omega_{1,0} = \frac{w_r\left(h_c + h_i + h_t\right)\left(3L^2 n_r - n_r^3\right)}{96\left(E_c I_c + E_t I_t\right)},$$

$$\omega_{1,1} = \left[\frac{\left(E_c A_c + E_t A_t\right)}{E_c A_c E_t A_t} + \frac{\left(h_c + h_t + 2h_i\right)\left(h_c + h_t\right)}{4\left(E_c I_c + E_t I_t\right)}\right] \cdot \frac{n_r}{2}. \tag{1}$$

Here, L is the span, w is the uniformly distributed load, and n_i refers to the distance of each symmetrical screw row from midspan. The primary material and geometric parameters are specified as follows; h: depth, A: cross-sectional area, I: moment of inertia, E: modulus of elasticity, and b: width of the cross section of concrete slab, insulation, and MTP with the subscripts c, i, and t respectively.

By applying the displacement compatibility condition at the interface, the redundant shear force in the connectors with r number of connector rows along the span can be obtained based on the following matrix expression [21] as

$$\begin{Bmatrix} \omega_{1,0} \\ \omega_{2,0} \\ \vdots \\ \omega_{r,0} \end{Bmatrix} + \left[\begin{pmatrix} \omega_{1,1} & \omega_{1,2} & \cdots & \omega_{1,r} \\ \omega_{2,1} & \omega_{2,2} & \cdots & \omega_{2,r} \\ \vdots & \vdots & \ddots & \vdots \\ \omega_{r,1} & \omega_{r,2} & \cdots & \omega_{r,r} \end{pmatrix} + \begin{pmatrix} f & 0 & \cdots & 0 \\ 0 & f & \cdots & 0 \\ \vdots & \vdots & \ddots & \vdots \\ 0 & 0 & \cdots & f \end{pmatrix} \right] \begin{Bmatrix} X_1 \\ X_2 \\ \vdots \\ X_r \end{Bmatrix} = 0. \tag{2}$$

Here, $f = 1/k$ is the flexibility of the connection and k is the stiffness of the shear connector.

Then, the superposition method can be implemented to determine the vertical deflection [22] as follows:

$$\Delta_r = \frac{5w_r L^4 - 19.2X_r(h_c + h_t + 2h_i)(2L - n_r)n_r}{384(E_cI_c + E_tI_t)}. \tag{3}$$

Here, r is the number of connector rows along the span and X_r is the sum of shear forces in all the connectors between the midspan and the panel edge, which is equal to the resultant normal force at a given cross section.

The linear-elastic effective bending stiffness [22] of the MTPC composite system can then be written as

$$EI_{\text{eff}} = \frac{5w_1 L^4}{384\Delta_1}. \tag{4}$$

After yielding of each connector, the stresses in concrete and timber are checked to determine if either of them fails (e.g., concrete compression, timber tension, and/or shear) before yielding of the next connector.

According to [21], the axial stress in the members can be written as

$$\sigma_{t,N} = \frac{\sum_{i=1}^{n} X_i}{A_t}, \qquad \sigma_{c,N} = \frac{\sum_{i=1}^{n} X_i}{A_c}. \tag{5}$$

And the bending stress in the members of each subsystem can be written as

$$\sigma_{1,t} = \frac{M_t}{S_t}, \quad \sigma_{1,c} = \frac{M_c}{S_c}, \quad \sigma_{2,t} = \frac{\sum_{i=1}^{n} X_i\left((h_c + h_t + 2h_i)/2 \cdot E_tI_t / (E_cI_c + E_tI_t)\right)}{S_t}, \quad \sigma_{2,c} = \frac{\sum_{i=1}^{n} X_i\left((h_c + h_t + 2h_i)/2 \cdot E_cI_c / (E_cI_c + E_tI_t)\right)}{S_c}. \tag{6}$$

Here, M_t and M_c are the bending moment and S_t and S_c are the section modulus of timber and concrete, respectively. Therefore, the resultant axial stress in the members due to bending at the position of cross section is as follows:

$$\sigma_{t,B} = \sigma_{1,t} + \sigma_{2,t}, \qquad \sigma_{c,B} = \sigma_{1,c} + \sigma_{2,c}. \tag{7}$$

The stress distributions of the subsystems and the actual system are shown in Figure 2.

The extreme fibre stress of timber must not be greater than its factored bending strength as follows:

$$\sigma_{t,B/t} + \sigma_{t,N} \le f_b. \tag{8}$$

Here, f_b is the specified bending strength of the timber.

The shear stress in timber member can be calculated as follows:

$$\tau_{\max} = \frac{y_t^2 E_t V}{2EI_{\text{eff}}} < f_v, \quad \text{with, } y_t = \frac{h_t\left(\sigma_{t,N} + \sigma_{t,B}\right)}{2\sigma_{t,B}}. \tag{9}$$

Here, V is the applied shear force at the connector location due to the external load, y_t is the distance of the neutral axis of timber to the tension edge, and f_v is the specified shear strength of timber (rolling shear for CLT).

The top extreme fibre stress of concrete in compression must not be greater than its factored compressive strength and the bottom extreme fibre stress of concrete in tension must not be greater than its factored modulus of rupture as follows:

$$\sigma_{c,c} \le f_c', \qquad \sigma_{c,t} \le \left(0.6\lambda\sqrt{f_c'}\right). \tag{10}$$

Here, f_c' is the concrete specified compressive strength and λ is the modification factor for concrete density.

2.2. Serviceability Limit State

2.2.1. Vibration. Hu et al. [36] presented the following equation for the vibration-controlled span of TCC floors:

$$L \le \frac{\left((EI)_{\text{eff}}^{1m}\right)^{0.278}}{4.835m_L^{0.166}}, \tag{11}$$

where m_L is mass per unit length of 1 m wide strip of TCC beam (kg/m), L is the span (m), and EI_{eff} is the effective bending stiffness of the floor (Nm^2).

2.2.2. Deflection. The deflection can be calculated based on the load combination associated with serviceability limit state in CSA O86 [34]. The deflection under the specified load is required to be within the limit of L/180 and can be calculated as follows:

$$\Delta = \frac{5wL^4}{384EI_{\text{eff}}}, \tag{12}$$

where w is the uniformly distributed load (N/m).

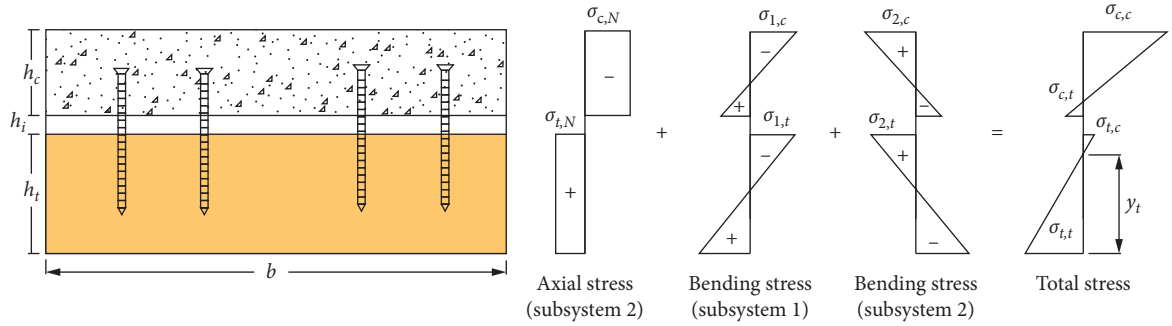

Figure 2: Stress distributions in the TCC system.

2.2.3. Acoustic Requirements. As required by the NBCC [37], the levels of noise or sound control should be adequate in a building. Sound transmission class (STC) is the main parameter to evaluate the acoustic performance of floor assemblies. Nonetheless, the determination of the exact STC of a floor is still of great difficulty using the modelling techniques, while a laboratory test is considered the most accurate way. Schmid [38] proposes a mathematical model for the estimation of the air-borne sound level which is consistent with STC. According to [38], within the area mass density range of 30 kg/m^2 to 800 kg/m^2, the mass law is practically applicable to the influence of the subfloor and concrete as follows:

$$\text{STC} = 20\ \log(m) + 7\ \text{dB}, \tag{13}$$

where m is the total mass per unit area (kg/m^2).

Based on the described methodology, the allowable spans were developed for a variety of TCC floor systems built with MTP (as in Figure 3), satisfying all the requirements stated earlier. The geometric and mechanical properties used in the design to develop the span table of TCC with MTP are presented in Table 1. Normal weight concrete of 35 MPa compressive strength at 28 days was assumed with a modulus of elasticity of 26600 MPa and density of 2300 kg/m^3. GLT made of No. 2 grade Spruce-Pine-Fir (S-P-F) lumber and E1 grade CLT made of 1950Fb-1.7E grade S-P-F lumber in longitudinal and No. 3/Stud S-P-F lumber in transverse layer were considered in the calculation for a width of 1 m, according to CSA O86 [34]. The density of lumber was 420 kg/m^3. The connector was fully threaded self-tapping screw of 11 mm diameter with a 45° insertion angle to timber grain and 100 mm penetration length. The connection stiffness and strength were calculated based on [24, 25], respectively, and are presented in Table 2. As required by the National Building Code of Canada (NBCC) [37], the appropriate load combinations were considered. The dead loads were obtained from the self-weight of the members and an additional superimposed load of 1 kPa while a live load of 2.4 kPa was considered for commercial occupancy.

The MATLAB software was used to perform repetitive calculations, based on the analytical equations presented in [21, 22]. The allowable span for a particular combination of floor parameters was obtained based on the shortest span that meets all structural and serviceability limit states. Table 3 presents the allowable spans of TCC floors when all appropriate design criteria are considered. It was found that all floor spans were governed by vibration for the stated applied load combinations, which generally agrees with the common practice [35]. In Table 3, the spacing of the connector was 250 mm along the span. The analysis was repeated for different MTP thicknesses as shown in Table 3. TCC systems with concrete thicknesses of 50, 75, and 100 mm for each MTP are included in Table 3. Here, 50 mm represents a practical lower bound and 100 mm is a typical upper bound found in practice. STC values for the floor configurations are also presented in Table 3. Based on this, the influence of the thickness of concrete on TCC effective bending stiffness, allowable floor span, and design decision for TCC through optimizing vibration and STC requirements are discussed below.

Table 3 also reports the embodied carbon content of each case study per square meter (kgCO_2eq/m^2) obtained from the LCA analysis using Athena Impact Estimator for Buildings [40] by considering concrete and timber elements only. Here, the cost or other environmental impacts from the material selection, for example, eutrophication or acidification potential and on-site construction are not accounted. For the purposes of this study, the commercial buildings were assumed to be located in Vancouver, Canada, as there are benchmarks for energy and emissions within various locations. To focus exclusively on near term embodied emissions, carbon storage in the timber material was excluded [41, 42]. The carbon intensity of the CLT from Athena was compared with available environmental product declaration values from major CLT producers in Canada [43, 44] and was found to overestimate the intensity by 15–30%. This implies that the results are shifted upwards slightly; however, that difference does not change the general conclusions. Based on this life-cycle analysis, the design decision for TCC through optimizing embodied carbon is discussed below.

3. Results and Discussion

3.1. Influence of MTP Thickness on TCC Bending Stiffness. In the TCC system, generally, effective bending stiffness and mass per unit area dictate the performance of the composite floor system. From Table 3, it can be seen that the effective bending stiffness of the TCC system increases marginally

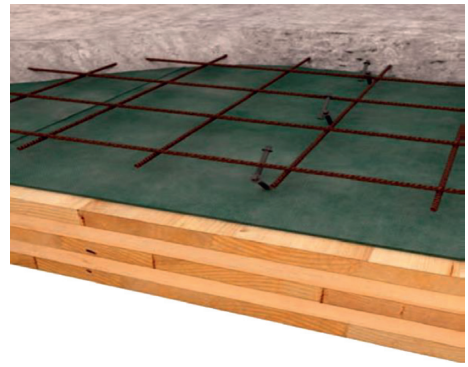

Figure 3: Type of TCC system with MTP and inclined self-tapping screws [39].

Table 1: Design properties of the concrete and MTP.

	Thickness (mm)	Modulus of elasticity (MPa)	Bending strength (MPa)	Shear strength (MPa)	Compressive strength (MPa)
Concrete	50, 75, 100	26600	—	—	35
GLT	89, 140, 186	9500	11.8	1.3	—
CLT	105, 175, 245, 315	11281	28.2	0.5	—

Table 2: Properties of the self-tapping screw.

MTP	Acoustic layer (mm)	Stiffness (kN/mm/screw)	Yield strength (kN/screw)
GLT	0	15.24	15.34
CLT	0	14.00	16.19
GLT	5	7.34	14.66
CLT	5	7.03	15.51

with the increase of concrete thickness but increases exponentially with the increase of timber thickness. From Figure 4, the timber thickness has a dominant effect on the effective bending stiffness of the TCC system compared to the thickness of concrete. Doubling the depth of concrete seems to make little difference to the stiffness but doubling the timber depth has a significant impact.

3.2. Influence of Concrete Thickness on TCC Floor Span. It is also noted that mass per unit area is influenced largely by concrete thickness because of the higher density of concrete (2300 kg/m^3) compared to timber (420 kg/m^3) and the system deflection decreases with the increase of concrete thickness. Therefore, the effective bending stiffness increases with a thicker MTP, but the total mass per unit area only increases marginally which yields a larger floor span. From Figure 5, it can also be seen that after a certain MTP thickness (approximately 150 mm), the added concrete thickness has minor and, in some case, a negative impact on the span length while, for MTP with thicknesses less than 150 mm, the span length increases with the increase of concrete thickness. Therefore, it can be concluded that, for TCC span longer than 7 m, the MTP thickness should be larger than 150 mm while keeping the concrete thickness within the range of 50–75 mm. Besides, for allowable TCC spans smaller than 7 m, a concrete thickness range of 75–100 mm is required if thinner MTP is selected.

3.3. Design Decision Based on Vibration Performance. The design of all the TCC floors was governed by the vibration criteria, which generally agrees with the common practice. In addition to changing the properties of the floor, the addition of concrete to the TCC floor increases the weight significantly because of the higher density of concrete compared to timber, which can subsequently create a demand for larger framing members and foundations due to an increase in dead and consequently seismic loads. The influence of the weight of TCC is similar to the influence of concrete thickness on the allowable span. Therefore, an increase in concrete thickness tends to reduce the allowable floor span due to a reduction in natural frequency which is detrimental to vibration performance.

3.4. Design Decision Based on Connector Properties. In the developed span Table 3, all possible MTP and concrete thicknesses were investigated with constant connection properties at 250 mm spacings and without an acoustic layer. A parallel span table was also developed for different connector properties as presented in Table 4, by adding 500 mm screw spacings, 5 mm of acoustic layer, and associated STC values for each span. It was found that there is a minimal benefit in increasing the stiffness of connection beyond a moderate threshold by adjusting the connection parameters such as connector spacings because the impact in effective bending stiffness is small. It was also found that, by doubling the number of connectors, the TCC floor span only increases by approximately 250 mm. Further, as the TCC designs were governed by stiffness-related design parameters, the yield strength of the connection was similarly not influential in the design outcome. Together these results indicate that the

Table 3: TCC allowable floor spans with associated embodied carbon for 250 mm spaced connectors.

MTP	MTP thickness (mm)	Concrete thickness (mm)	Effective stiffness ((10^6) Nm^2)	Span (m)	STC (dB)	Embodied carbon ($kgCO_2/m^2$ eq)		
						Total	Timber share	Reinforced concrete share
GLT	89	0	0.08	2.62	39	15.4	15.4	0.0
		50	1.87	4.98	49	39.0		23.6
		75	3.03	5.39	52	51.3		35.9
		100	4.9	5.92	55	62.6		47.2
	140	0	0.61	4.26	42	23.0	23.0	0.0
		50	4.61	6.26	49	46.6		23.6
		75	6.07	6.44	52	58.9		35.9
		100	8.22	6.75	55	70.2		47.2
	186	0	2.09	5.73	45	29.7	29.7	0.0
		50	8.91	7.39	49	53.3		23.6
		75	10.65	7.43	52	65.6		35.9
		100	13.06	7.60	55	76.9		47.2
CLT	105 (3 ply)	0	0.34	3.80	40	11.9	11.9	0.0
		50	2.7	5.47	49	35.5		23.6
		75	3.94	5.78	52	47.8		35.9
		100	5.88	6.21	55	59.1		47.2
	175 (5 ply)	0	1.73	5.50	44	18.2	18.2	0.0
		50	8.41	7.29	49	41.8		23.6
		75	10.04	7.33	52	54.1		35.9
		100	12.35	7.50	55	65.5		47.2
	245 (7 ply)	0	4.75	6.88	47	24.6	24.6	0.0
		50	19.65	9.01	49	48.2		23.6
		75	21.73	8.92	52	60.5		35.9
		100	24.43	8.93	55	71.8		47.2
	315 (9 ply)	0	10.2	8.16	49	31.0	31.0	0.0
		50	38.35	10.63	49	54.6		23.6
		75	40.94	10.46	52	66.9		35.9
		100	44.07	10.37	55	78.2		47.2

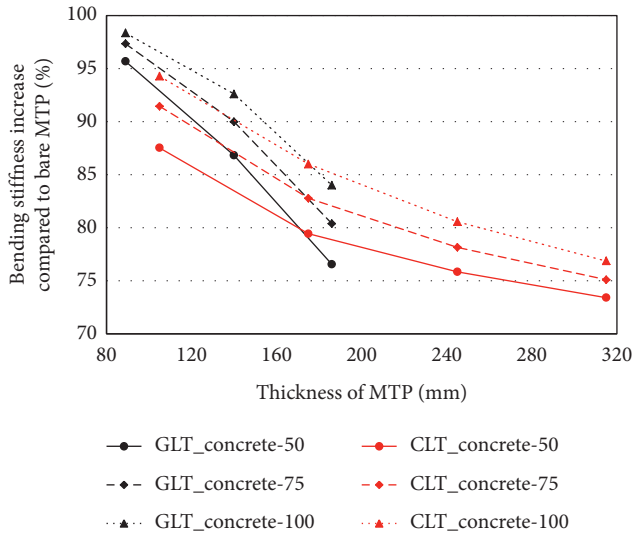

Figure 4: Effective bending stiffness increase compared to bare MTP versus thickness of MTP in TCC system.

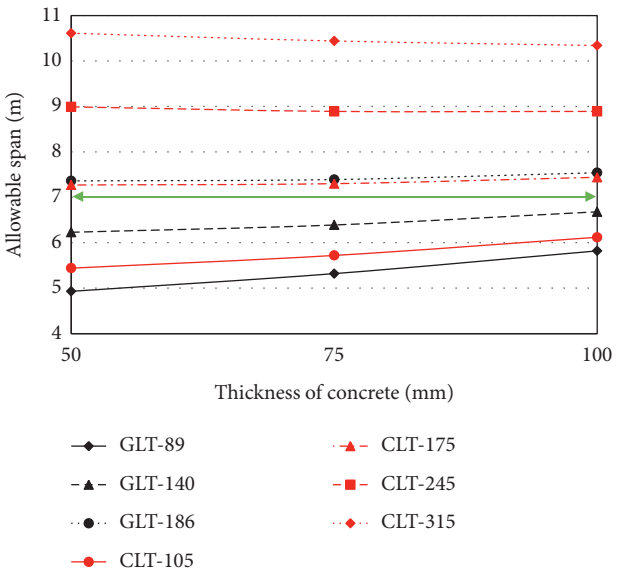

Figure 5: Allowable span versus thickness of concrete in TCC system.

choice of connection between the timber and concrete elements has only a minor impact on the design beyond a threshold level (moderately partial composite) [35] and the thickness of concrete required for acceptable vibration performance for a given span and timber element is more strongly determined by the anchorage requirements of the connectors.

Table 4: Influence of connection properties on TCC floor allowable spans.

Timber	Timber thickness (mm)	Insulation thickness (mm)	Concrete thickness (mm) / Connector spacing (mm)					
			50	50	75	75	100	100
			250	500	250	500	250	500
GLT	89	0	4.98 (+)	4.75 (+)	5.39 (++)	5.16 (++)	5.92 (+++)	5.71 (+++)
	89	5	4.76 (+++)	4.54 (+++)	5.14 (+++)	4.93 (+++)	5.67 (+++)	5.48 (+++)
	140	0	6.26 (+)	6.00 (+)	6.44 (++)	6.15 (++)	6.75 (+++)	6.46 (+++)
	140	5	5.97 (+++)	5.75 (+++)	6.10 (+++)	5.87 (+++)	6.40 (+++)	6.17 (+++)
	186	0	7.39 (+)	7.13 (+)	7.43 (++)	7.13 (++)	7.60 (+++)	7.28 (+++)
	186	5	7.07 (+++)	6.86 (+++)	7.06 (+++)	6.83 (+++)	7.20 (+++)	6.96 (+++)
CLT	105	0	5.47 (+)	5.23 (+)	5.78 (++)	5.52 (++)	6.21 (+++)	5.95 (+++)
	105	5	5.23 (+++)	5.02 (+++)	5.50 (+++)	5.28 (+++)	5.93 (+++)	5.72 (+++)
	175	0	7.29 (+)	7.05 (+)	7.33 (++)	7.05 (++)	7.50 (+++)	7.20 (+++)
	175	5	7.02 (+++)	6.82 (+++)	7.01 (+++)	6.79 (+++)	7.15 (+++)	6.92 (+++)
	245	0	9.01 (+)	8.78 (+)	8.92 (++)	8.64 (++)	8.93 (+++)	8.62 (+++)
	245	5	8.74 (+++)	8.56 (+++)	8.59 (+++)	8.39 (+++)	8.56 (+++)	8.35 (+++)
	315	0	10.63 (+)	10.41 (+)	10.46 (++)	10.20 (++)	10.37 (+++)	10.08 (+++)
	315	5	10.36 (+++)	10.20 (+++)	10.14 (+++)	9.96 (+++)	10.02 (+++)	9.82 (+++)

Remarks: "+" represents the STC is the first level of the acoustic performance or at least 45 dB. "++" represents the STC is the second level of the acoustic performance or at least 50 dB. "+++" represents the STC is the third level of the acoustic performance or at least 55 dB.

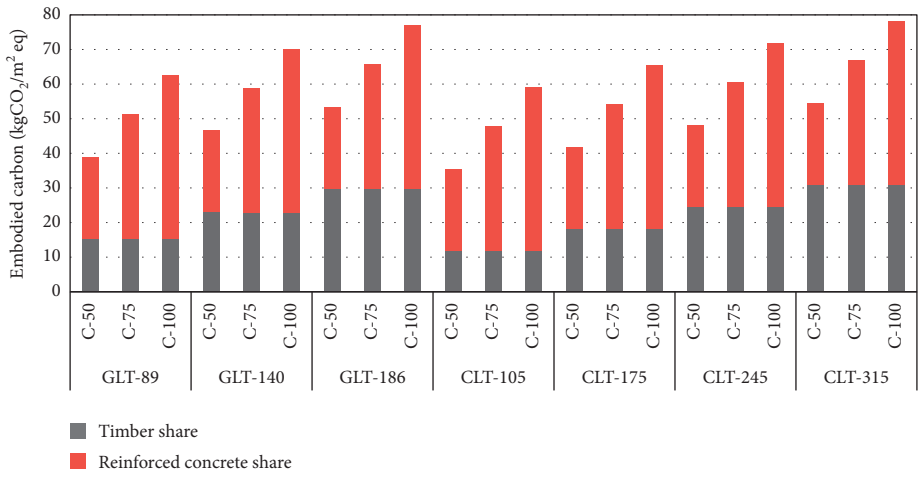

Figure 6: Embodied carbon versus thickness of concrete and MTP in TCC system.

3.5. Design Decision Based on Acoustic Performance. The sound transmission class value for each span is also presented in Table 4 along with the span for an additional 5 mm acoustic layer. Although an increase in concrete thickness can improve the acoustic performance of the composite floor, as stated above, the addition of concrete may cause a reduction in allowable span due to vibration requirements. To mitigate this issue, an acoustic layer can be placed between MTP and concrete, which will enhance sound insulation without a potential negative impact on vibration-controlled floor span. It was found that, by providing a 5 mm acoustic layer, the TCC floor span only reduces by only approximately 300 mm. Therefore, acoustic layers can provide designers with a chance to achieve higher STC values and nearly similar spans (compromising around 300 mm) without increasing the concrete thickness and therefore embodied carbon for sustainable design.

3.6. Design Decision Based on Embodied Carbon. The embodied carbon will obviously increase once concrete topping is added to MTP to form TCC. Figure 6 shows how the increase in timber and concrete thickness can lead to an increase in embodied carbon based on the share of timber and reinforced concrete. For each MTP type, the largest increase in embodied carbon happens when a 50 mm thick concrete topping is added to bare MTP. Thereafter, the rate of increase in embodied carbon decreases as the concrete thickness increases by 25 mm increment to a total of 100 mm. Figure 7 was plotted to assist designers in the selection of TCC system by taking into consideration the amount of embodied carbon for specific span requirements. For instance, for a span length of 6 m, a design engineer has options of CLT-105_Concrete-100 (105 mm thick CLT with 100 mm thick concrete) and GLT-140_Concrete-50. Comparing their embodied carbon content per square meter, the

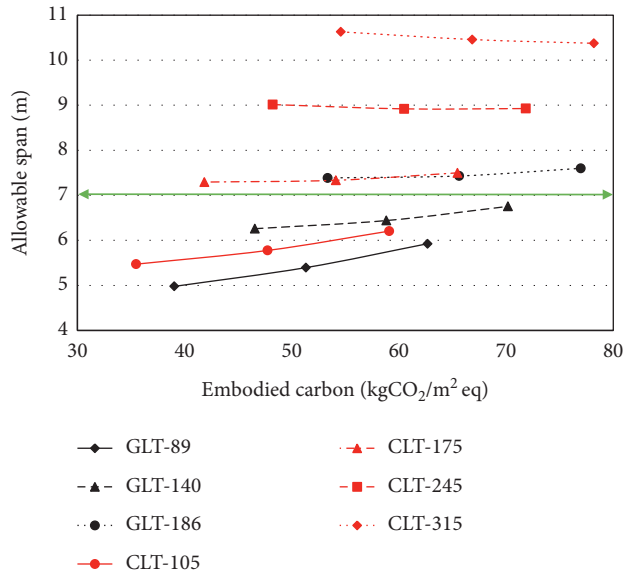

Figure 7: Allowable span versus embodied carbon of TCC system (the three points on each curve represent from left to right 50 mm, 75 mm, and 100 mm thick concrete).

GLT-140_Concrete-50 is more environmentally friendly, comparing to the other option. Similarly, one can observe that two systems, GLT-186_Concrete-75 and CLT-175_Concrete-100, provide almost identical spans and embodied carbon and the same applies to GLT-186_Concrete-50 and CLT-175_Concrete-75. Based on these observations, it is generally beneficial from a sustainability perspective to increase the thickness of MTP in an attempt to reach a longer span than to increase concrete thickness.

4. Conclusions

By using a new analysis approach [20] to investigate the influence of concrete topping on the structural and sustainability performance of the TCC system, the following conclusions can be drawn:

(1) The increase in concrete thickness to achieve a longer span is only effective for TCC floor systems with spans shorter than about 7 m, due to vibration performance being the controlling design parameter. This is because the addition of concrete beyond this span has the counteracting effect of increasing bending stiffness but reducing the natural frequency.

(2) Following from 1 above, it is generally true that it is beneficial to increase MTP thickness instead of concrete thickness to achieve a longer span, especially for a floor span shorter than 7 m, from a sustainability perspective. This is due to the substantially larger carbon footprint of concrete than timber on a per-volume basis.

(3) If self-tapping screws are used, there is evidence to suggest that the connection parameters, such as spacing, have a minor influence on the allowable floor span when these parameters are above certain threshold levels. Other connector systems may provide more sensitivity, but further studies are required.

This research focused on embodied carbon as a single metric and did not account for cost or other environmental impacts from the material selection, for example, eutrophication or acidification potential and on-site construction. Further analysis including these effects and accounting for the relationship between embodied carbon and life cycle cost is recommended.

Data Availability

All the data, models, and code generated or used during the study appear in the submitted article.

Conflicts of Interest

The authors declare that they have no conflicts of interest.

Acknowledgments

The authors would like to thank the Natural Sciences and Engineering Research Council of Canada (NSERC) for the financial support through the Industrial Research Chair (IRC) in Engineered Wood and Building System Program.

References

[1] A. Gosselin, P. Blanchet, N. Lehoux, and Y. Cimon, "Main motivations and barriers for using wood in multi-story and non-residential construction projects," *BioResources*, vol. 12, no. 1, pp. 546–570, 2017.

[2] R. F. Falk, "Wood as a sustainable building material," *Forest Products Journal*, vol. 59, no. 9, pp. 6–12, 2009.

[3] L. F. Cabeza, C. Barreneche, L. Miró, J. M. Morera, E. Bartolí, and A. Inés Fernández, "Low carbon and low embodied energy materials in buildings: a review," *Renewable and Sustainable Energy Reviews*, vol. 23, pp. 536–542, 2013.

[4] H. Reid, S. Huq, A. Inkinen et al., *Using Wood Products to Mitigate Climate Change: A Review of Evidence and Key Issues for Sustainable Development*, International Institute for Environment and Development, Scotland, UK, 2004.

[5] P. Kremor and M. Symmons, "Mass-timber construction as an alternative to concrete and steel in the Australian building industry: a PESTL evaluation of the potential," *International Wood Products Journal*, vol. 6, no. 3, pp. 138–147, 2015.

[6] D. Yeoh, M. Fragiacomo, M. De Franceschi, and K. Heng Boon, "State of the art on timber-concrete composite structures: literature review," *Journal of Structural Engineering*, vol. 137, no. 10, pp. 1085–1095, 2011.

[7] M. A. H. Mirdad and Y. H. Chui, "Behaviour of mass timber panel-concrete connections with inclined self-tapping screws and insulation layer," in *Proceedings of the World Conference on Timber Engineering (WCTE)*, Seoul, Republic of Korea, August 2018.

[8] F. Moar, S. Vanzo, M. A. H. Mirdad, Y. H. Chui, and Y. Steige, "Influence of self-tapping screw inclination and soundproofing resilient interlayer on timber-concrete composite slab," in *Proceedings of the 5th International Conference on Structural Health Assessment of Timber Structures*, Guimarães, Portugal, 2019.

[9] A. Dias, J. Schänzlin, and P. Dietsch, "Design of timber-concrete composite structures," *Action FP1402/WG 4*, COST, European Cooperation in Science and Technology, Aachen, Germany, 2018.

[10] M. A. H. Mirdad and Y. H. Chui, "Load-slip performance of Mass Timber Panel-Concrete (MTPC) composite connection with self-tapping screws and insulation layer," *Construction and Building Materials*, vol. 213, pp. 696–708, 2019.

[11] A. Ceccotti, "Composite concrete-timber structures," *Progress in Structural Engineering and Materials*, vol. 4, no. 3, pp. 264–275, 2002.

[12] A. Dias, J. Skinner, K. Crews, and T. Tannert, "Timber-concrete-composites increasing the use of timber in construction," *European Journal of Wood and Wood Products*, vol. 74, no. 3, pp. 443–451, 2016.

[13] R. Zizzo, J. Kyriazis, and H. Goodland, *Embodied Carbon of Buildings and Infrastructure: International Policy Review*, Forestry Innovation Investment Ltd., Vancouver, British Columbia, 2017.

[14] C. Cao, "21-Sustainability and life assessment of high strength natural fibre composites in construction," *Advanced High Strength Natural Fibre Composites in Construction*, Elsevier, Amsterdam, Netherlands, pp. 529–544, 2017.

[15] L. Ben-Alon, V. Loftness, K. A. Harries, G. DiPietro, and E. C. Hameen, "Cradle to site Life Cycle Assessment (LCA) of natural vs conventional building materials: a case study on cob earthen material," *Building and Environment*, vol. 160, Article ID 106150, 2019.

[16] Mantle314, "Mass timber's carbon impact," 2020, https://mantle314.com/insights/mass-timber-carbon-impact.

[17] S. Shaked and O. Jolliet, "Global life cycle impacts of consumer products," *Encyclopedia of Environmental Health*, Elsevier, Amsterdam, Netherlands, pp. 1002–1014, 2011.

[18] EN 1995-1-1, *Eurocode 5: Design of Timber Structures Part 1-1: General-Common Rules and Rules for Buildings*, CEN European Committee for Standardization, Brussels, Belgium, 2009.

[19] S. Cuerrier-Auclair, *Design Guide for Timber-Concrete Composite Floors in Canada*, Special Publication SP-540E, FPInnovations, Pointe-Claire, QC, Canada, 2020.

[20] M. A. H. Mirdad, *Structural performance of Mass Timber Panel-Concrete (MTPC) composite floor system with inclined self-tapping screws and an insulation layer*, Ph.D. thesis, Department of Civil & Environmental Engineering, University of Alberta, Edmonton, AB, Canada, 2020.

[21] M. A. H. Mirdad, Y. H. Chui, and D. Tomlinson, "Capacity and failure mode prediction of mass timber panel-concrete composite floor system with mechanical connectors," *Journal of Structural Engineering*, vol. 147, no. 2, Article ID 04020338, 2020.

[22] M. A. H. Mirdad, Y. H. Chui, D. Tomlinson, and Y. Chen, "Bending stiffness and load-deflection response prediction of mass timber panel-concrete composite floor system with mechanical connectors," *Journal of Performance of Constructed Facilities*, 2021.

[23] C. Zhang and P. Gauvreau, "Timber-concrete composite systems with ductile connections," *Journal of Structural Engineering*, vol. 141, no. 7, Article ID 04014179, 2015.

[24] M. A. H. Mirdad and Y. H. Chui, "Strength prediction of mass-timber panel-concrete composite connection with inclined screws and a gap," *Journal of Structural Engineering*, vol. 146, no. 8, Article ID 04020140, 2020.

[25] M. A. H. Mirdad and Y. H. Chui, "Stiffness prediction of Mass Timber Panel-Concrete (MTPC) composite connection with inclined screws and a gap," *Engineering Structures*, vol. 207, Article ID 110215, 2020.

[26] S. R. S. Monteiro, A. M. P. G. Dias, and S. M. R. Lopes, "Transverse distribution of internal forces in timber-concrete floors under external point and line loads," *Construction and Building Materials*, vol. 102, pp. 1049–1059, 2016.

[27] C. Higgins, A. R. Barbosa, and C. Blank, "Structural tests of concrete composite-cross-laminated timber floors," Report 17-01, Oregon State University, Corvallis, OR, USA, 2017.

[28] K. Holschemacher, S. Klotz, and D. Weisse, "Application of steel fibre reinforced concrete for timber-concrete composite constructions," *Lacer*, vol. 7, pp. 161–170, 2002.

[29] J. Skinner, R. Harris, K. Paine, P. Walker, and J. Bregulla, "Ultra-thin topping upgrades for improved serviceability performance," *Advanced Materials Research*, vol. 778, pp. 673–681, 2013.

[30] A. M. P. G. Dias, S. M. R. Lopes, J. W. G. Van de Kuilen, and H. M. P. Cruz, "Load-carrying capacity of timber-concrete joints with dowel-type fasteners," *Journal of Structural Engineering*, vol. 133, no. 5, pp. 720–727, 2007.

[31] A. M. P. G. Dias, H. M. P. Cruz, S. M. R. Lopes, and J. W. van de Kuilen, "Stiffness of dowel-type fasteners in timber-concrete joints," *Proceedings of the Institution of Civil Engineers - Structures and Buildings*, vol. 163, no. 4, pp. 257–266, 2010.

[32] P. Hamm, A. Richter, and S. Winter, "Floor vibrations – new results," in *Proceedings of the World Conference on Timber Engineering (WCTE)*, Riva del Garda, Italy, 2010.

[33] L. Hu, S. Cuerrier-Audair, Y. H. Chui et al., "Design method for controlling vibrations of wood-concrete composite floor systems," in *Proceedings of the World Conference on Timber Engineering (WCTE)*, Vienna, Austria, 2016.

[34] CSA O86-19, *Engineering Design in Wood*, Canadian Standards Association, Mississauga, Canada, 2019.

[35] T. Joyce, H. Daneshvar, Y. H. Chui, and L. Zhang, "Optimizing mass timber-concrete composite floor systems with respect to embodied carbon," in *Proceedings of the 2nd International Conference on New Horizons in Green Civil Engineering (NHICE-02)*, Victoria, British Columbia, 2020.

[36] L. Hu, Y. H. Chui, P. Hamm, T. Toratti, and T. Orskaug, "Development of ISO baseline vibration design method for timber floors," in *Proceedings of the World Conference on Timber Engineering (WCTE)*, Seoul, Republic of Korea, 2018.

[37] NBCC, *National Building Code of Canada*, National Research Council, Ottawa, Canada, 2015.

[38] M. Schmid, "Acoustic performance of timber concrete composite floors," in *Proceedings of the International Congress and Exposition on Noise Control Engineering 2005 (INTER-NOISE 2005)*, Rio de Janeiro, Brazil, August 2005.

[39] Rothoblaas, "Silent floor-resilient underscreed foil made of bitumen and polyester felt," 2021, https://www.rothoblaas.com/products/soundproofing/soundproofing-layers/silent-floor.

[40] Athena, *Athena Impact Estimator for Buildings v5.4 Software and Database*, Athena Sustainable Materials Institute, Ontario, Canada, 2019.

[41] A.-B. Laurent, S. Gaboury, J.-R. Wells et al., "Cradle-to-gate life-cycle assessment of a glued-laminated wood product from Quebec's Boreal forest," *Forest Products Journal*, vol. 63, no. 5-6, pp. 190–198, 2013.

[42] A.-B. Laurent, J.-F. Menard, P. Lesage, and R. Beauregard, "Cradle-to-gate environmental life cycle assessment of the portfolio of an innovative forest products manufacturing unit," *BioResources*, vol. 11, no. 4, pp. 8981–9001, 2016.

[43] Structurlam, "Environmental product declaration: CrossLam CLT by Structurlam," 2021, https://www.astm.org/CERTIFICATION/DOCS/480.EPD_FOR_Structurlam_CLT_20200113.pdf.
[44] Nordic structures, "Environmental Product Declaration: Nordic X-LamTM," August 2018, https://www.nordic.ca/data/files/datasheet/file/EPD_Nordic_X-Lam.pdf.

Hindawi
Advances in Civil Engineering
Volume 2021, Article ID 6612886, 16 pages
https://doi.org/10.1155/2021/6612886

Research Article

Cyclic Behavior and Modeling of Bolted Glulam Joint with Cracks Loaded Parallel to Grain

Jing Zhang,[1] **Zhi-Fang Liu**,[2] **Yong Xu**,[1] **Mai-Li Zhang**,[1] **and Liu-Cheng Mo**[1]

[1]*Department of Structural Engineering, Guangzhou University, Guangzhou 510006, China*
[2]*Guangdong Architectural Design & Research Institute Co., Ltd., Guangzhou 510006, China*

Correspondence should be addressed to Jing Zhang; zhangjinggz@163.com

Received 19 November 2020; Revised 2 December 2020; Accepted 2 March 2021; Published 13 March 2021

Academic Editor: Arnaud Perrot

Under varying humidity and temperature conditions, with the constraint of metal fasteners to wood shrinkage, cracks along the bolt lines are generally observed in bolted glulam joints. A three-dimensional (3D) numerical model was established in software package ANSYS to investigate the cyclic behavior of bolted glulam joints with local cracks. A reversed cyclic loading was applied in the parallel-to-grain direction. The accuracy of numerical simulation was proved by comparison with full-scale experimental results. Typical failure modes were reproduced in the numerical analysis with the application of wood foundation zone material model and cohesive zone material model. The effect of crack number and length on the hysteretic behavior of bolted glulam joints was quantified by a parametric study. It was found that initial cracks impair the peak capacity and elastic stiffness of bolted glulam joints significantly. More decrease in capacity was observed in joints with more cracks, and longer cracks affect elastic stiffness more dramatically. Moreover, with the existence of initial cracks, the energy dissipated and equivalent viscous damping ratio of bolted joints are reduced by 24% and 13.3%, respectively.

1. Introduction

Connections are always recognized as the weakest part of timber structures. It was reported that nearly 80% of structural collapses arise from connections [1]. The mechanical behavior of joints significantly affects resistance, durability, and energy dissipation of timber structures. Dowel-type joints, an effective fastening technique extensively applied in actual engineering, have attracted tremendous research interest. Extensive experimental and numerical studies on the static [2–5] and cyclic behavior [6–8] of dowel-type joints have been conducted and available in the literature. The load-carrying capacity and failure modes of bolted joints are related to material behavior, geometry, and loading type. Relatively large energy dissipation and ductile behavior could be achieved with small diameter bolts, and slender bolts are preferred in the bolted glulam joints in order to avoid brittle failure modes [9].

In terms of modeling the mechanical behavior of bolted glulam joints, several methods have been proposed by previous researchers. An analytical method named Beam-on-Foundation model was first applied [10] and modified [11] to predict the monotonic strength and hysteretic behavior of nailed and bolted wood connections. To represent the dynamic response of timber connections, hysteresis models such as Bouc-Wen-Baber-Noori model [12], Florence model [13], and Pinching4 [14] were employed in structural analysis. A three-dimensional (3D) finite-element-based model is a recent and efficient approach to estimate the behavior of bolted glulam joint. Complete strain and stress distributions can be obtained and observed from numerical analysis. In the numerical modeling, a reasonable definition of material behavior is particularly important to achieve relatively accurate numerical results. To take into account the localized crushing behavior of wood underneath the fasteners, a foundation zone around the fasteners with weakened material properties was defined in a two-dimensional numerical model [15], and it was extended to 3D FE models by Hong [16]. To consider the progressive failure of wood in bolted glulam joints, several failure criteria were proposed by previous researchers. In the

3D numerical model of a single-bolt connection developed by Moses and Prion [17], anisotropic plasticity material model was defined for wood in compression and Weibull Weakest Link Theory was applied to consider brittle failure. It was indicated that the force-displacement relationship was predicted well, while the ultimate loads were underestimated. Hill yield criterion and maximum stress failure criterion were selected by Kharouf [18] when establishing a numerical model of timber joints, and it was found that failure modes and deformation predicted by numerical analysis fit well with experimental results. Hoffman failure criterion was applied by Xu et al. [19] to take into account the damage evolution of wood. Tsai-Wu failure criterion is able to consider the difference between tension and compression strengths of wood [20], while stress interaction coefficients defined in the criterion are difficult to determine [21]. The application of cohesive zone material model into bolted glulam joints has been attempted by several researchers [22–24]. With the definition of mixed mode damage onset and propagation criteria, it was proved to be a powerful tool to simulate splitting and row shear commonly observed in bolted joints.

Extensive researches have been conducted on mechanical behavior and strength enhancement of bolted glulam joints as above. However, little attention was paid to the mechanical behavior of bolted glulam joints with local cracks. Shrinkage cracks are generally observed in bolted glulam joints due to their sensitivity to varying relative humidity of the environment. Shrinkage and swelling strains of wood are restrained with the existence of steel fasteners in the joint area, and cracking of wood is easily caused by perpendicular-to-grain restrained stress [25]. Previous researches have proved that the capacity, stiffness, and ductility of bolted glulam joints are decreased by initial cracks under monotonic loading, and failure modes of bolted glulam joints switched from ductile failure with bolt yielding to brittle failure of wood [26, 27]. It is essential to further investigate the influence of initial cracks on the cyclic behavior of bolted glulam joints. In respect of numerical modeling, the complexity of contact problems and material behavior provides challenges of convergence. Even though some 3D numerical analysis has been conducted on the monotonic behavior of bolted glulam joints, few attempts have been conducted to model the cyclic behavior of timber joints by 3D numerical analysis.

To reveal the influence law of cracks on the cyclic behavior of bolted glulam joints intuitively, a 3D numerical model was established in this paper. Hill yield criterion and wood foundation model were applied to simulate the behavior of wood in compression and wood around fasteners, respectively. Brittle failure of wood and propagation of initial cracks were modeled with the application of cohesive zone material model. Several contact pairs were defined to model the interaction between different parts in the joint, and reversed cyclic loading was applied in the parallel-to-grain direction. The experimentally observed failure modes and hysteretic curves were used to verify the numerical results, and the influence of different crack patterns was explored by a parametric study.

2. Development of Finite-Element-Based Model

2.1. Material Modeling. To model the mechanical behavior of wood in compression, the transversely isotropic plastic material model was defined with the application of the Hill yield criterion, which had been incorporated in business software ANSYS. To take into account the embedment behavior of wood underneath bolts, a foundation zone was set around bolts with a radius of 1.8-time bolt diameter. The generalized Hill plasticity model with anisotropic hardening rule was applied to represent the mechanical behavior of wood foundation. 1% of initial modulus was taken as tangent modulus of hardening segment. With embedment tests loaded in perpendicular- and parallel-to-grain directions, a bilinear relationship between load per unit length and deformation was obtained, as shown in Figure 1, and nominal yield stress and strain of foundation zone were calculated by

$$\varepsilon_{\text{nom.}} = \frac{W_y}{d},$$
$$\sigma_{\text{nom.}} = \frac{P_y}{d}, \tag{1}$$
$$K = \frac{P_y}{W_y},$$

where $\varepsilon_{\text{nom.}}$ and $\sigma_{\text{nom.}}$ are the nominal yield strain and stress (MPa) of wood foundation, respectively; W_y and P_y are the deformation (mm) and yield load (N/mm) in Figure 1. Further calibration was conducted to derive effective foundation parameters. Shear modulus and yield strain were calculated according to a theoretical formula given in [28], as presented in

$$G_{ij} = G_{ji} = \frac{\sqrt{E_i \cdot E_j}}{2 \cdot \left(1 + \sqrt{\nu_{ij} \cdot \nu_{ji}}\right)},$$
$$\left(\gamma_y\right)_{ij} = \left(\gamma_y\right)_{ji} = \frac{\left(\sigma_{\text{int.}}\right)_i}{1.98 \cdot E_i} \cdot \sqrt{\frac{E_i}{G_{ij}}}, \tag{2}$$

where G is the initial shear modulus; E is the effective modulus of wood foundation; ν is Poisson's ratio; γ_y is the shear yield strain; and $\sigma_{\text{int.}}$ is the intercept of the second linear portion in the bilinear stress-strain relationship. For bolts and steel plate existing in bolted glulam joints, elastic modulus and Poisson's ratio were taken as 210,000 MPa and 0.3, respectively. The isotropic plastic material model with a bilinear constitutive relationship was defined, as shown in Figure 2.

To simulate the propagation of initial cracks and brittle failure (i.e., splitting and row shear) of wood in bolted glulam joints, surface-to-surface contact pairs with elements CONTA174 and TARGE170 were defined on the predicted cracking path. To characterize the constitutive relationship of the interface, the cohesive zone material model with damage initiation and growth criteria was implemented in the numerical model. As shown in Figure 3, a bilinear traction separation law was defined, and mode I and II

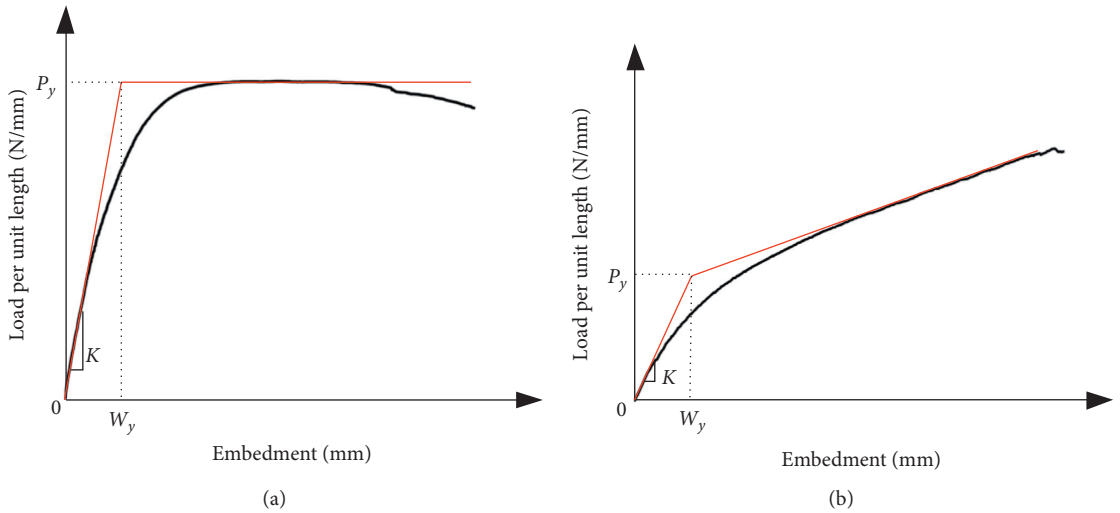

Figure 1: Load-embedment curves obtained from embedment tests and corresponding bilinear relationships. (a) Parallel to grain. (b) Perpendicular to grain.

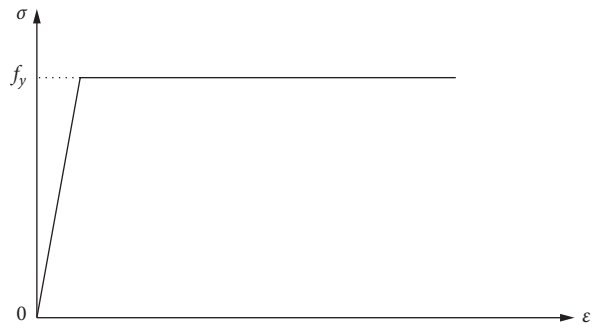

Figure 2: Bilinear stress-strain relationship for steel material.

fractures caused by perpendicular-to-grain tensile stress and longitudinal shear stress were taken into account. In Figure 3, K_n and K_t represent normal and tangential contact stiffness, respectively. A linear softening segment was observed after peak point corresponding to material strengths $f_{t,90}$ and f_s, and complete debonding occurs when reaching critical values of relative displacement u_n^c or u_t^c. Mixed mode fracture was considered in the analysis with a combined energy criterion, expressed as follows:

$$\frac{G_{\mathrm{I}}}{G_c^{\mathrm{I}}} + \frac{G_{\mathrm{II}}}{G_c^{\mathrm{II}}} = 1, \tag{3}$$

where G_{I} and G_{II} indicate fracture energies in modes I and II and G_c^{I} and G_c^{II} represent respective critical values, which are obtained from Double Cantilever Beam (DCB) test and End Notched Flexure (ENF) test, respectively, with the application of compliance combination method. In this numerical model, a small fictitious viscosity is introduced to avoid convergence difficulties.

2.2. Finite-Element Model. A 3D finite-element model of bolted glulam joints was established in FE-software ANSYS. Eight-node solid element SOLID185 was applied to embody the joints. To model the interaction between bolts and steel plate, timber and bolts, timber and steel plate, and timber and steel gasket, surface-to-surface contact pairs were defined with CONTA174 and TARGE170 elements. For bolt-to-steel plate and wood-to-steel contacts, coefficients of friction were taken as 0.001 and 0.3, respectively [29]. An example of the distribution zone of different material models was presented in Figure 4. The transversely isotropic plastic material model with the Hill yield criterion was induced to represent the compressive behavior of wood in the joint. Wood foundation zone material model was applied to simulate the embedment behavior of wooden parts surrounding the bolts, and the radius of the cylinder was set to be 1.8 d, where d indicates the bolt diameter. The mechanical behavior of bolts and steel plate was modeled with a bilinear isotropic plastic constitutive relationship. To simulate the splitting and plug shear failure of wood in the joint area, crack growth paths along the bolt lines were predicted based on experimental observations [23], as shown in Figure 5. The width of wooden parts plugged out by bolt load was assumed to be $dsin\phi$, and $\phi = 30^\circ$ was determined based on the friction between bolt and wood as given in [30]. For bolted glulam joints with initial cracks, hard contact conditions were defined to simulate the opening and closure of initial cracks. All the material constants applied in the analysis were listed in Table 1.

To study the cyclic behavior of bolted glulam joints, a gap of 30 mm was set between the top surface of steel plates and the slot, as presented in the side view of Figure 4. The bottom surface of the slotted-in steel plate was fixed, and a reversed cyclic loading was applied on the top end of glulam specimens. The loading protocol recommended in EN 12512 standard [31] was applied, as presented in Figure 6. The parameter V_y required for cyclic loading protocol was determined as yield displacement under monotonic loading. The amplitudes of loading cycles ranged from $0.25V_y$ to $6.0V_y$, the single cycle was considered for the amplitudes $0.25V_y$ and $6.0V_y$, and three cycles were repeated for other amplitude levels.

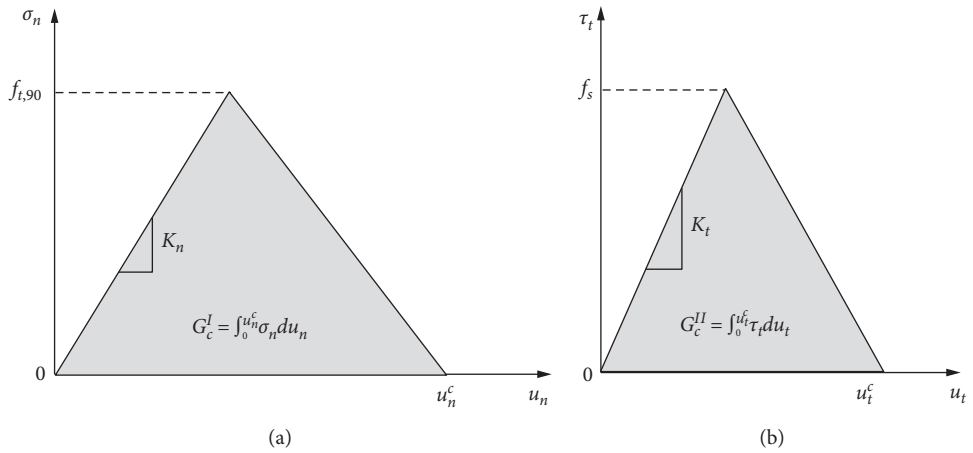

Figure 3: Cohesive zone material behavior. (a) Fracture mode I. (b) Fracture mode II.

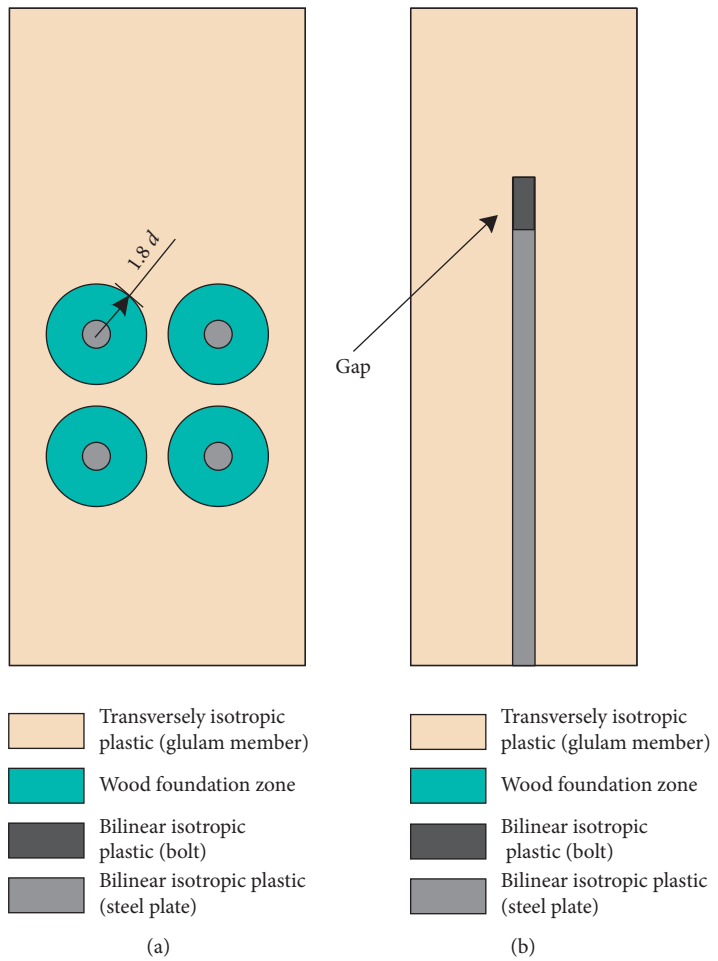

Figure 4: An example of the distribution zones of different material models. (a) Front view. (b) Side view.

3. Model Verification

To validate the feasibility of the numerical model, a bolted glulam joint with five replicates was manufactured and tested. The configuration of tested joints is presented in Figure 7. The width and thickness of glulam members are 200 mm and 100 mm, respectively. The slotted-in steel plates are 8 mm in thickness with a nominal yield stress of 235 MPa. Two bolts with a strength grade of 8.8 and a diameter of 12 mm are included in the joint, which has a nominal yield strength of

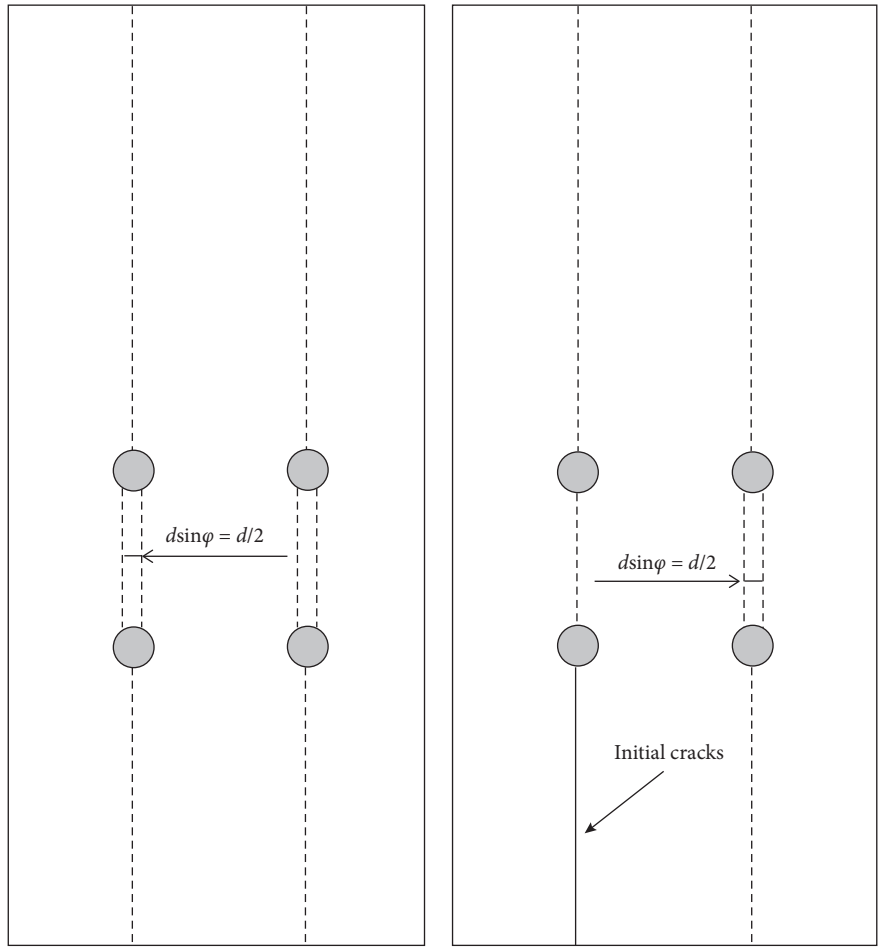

Figure 5: Fictitious fracture layers set in joints with four bolts. (a) Without initial cracks. (b) With initial cracks.

Table 1: Material constants applied in this model.

Component	Bolt	Steel plate	Wood	Wood foundation
Modulus of elasticity (N/mm^2)	$E = 2.1e5$	$E = 2.1e5$	$E_L = 1.02e4$ $E_{R;T} = 510$	$E_L = 1.04e3$ $E_{R;T} = 103$
Modulus of rigidity (N/mm^2)	—	—	$G_{LT;LR} = 845$ $G_{RT} = 80$	$G_{LT;LR} = 273$ $G_{RT} = 76$
Poisson ratio	$\nu = 0.3$	$\nu = 0.3$	$\nu_{LT;LR} = 0.37$ $\nu_{RT} = 0.44$	$\nu_{LT;LR} = 0.37$ $\nu_{RT} = 0.44$
Yield stress (N/mm^2)	$f_y = 640$	$f_y = 235$	$\sigma_L = 23.50$ $\sigma_{R;T} = 3.68$	$\sigma_L = 20.58$ $\sigma_{R;T} = 5.09$
Strengths (N/mm^2)	—	—	$f_{t;90} = 2.7$ $f_s = 5.7$	$f_{t;90} = 2.7$ $f_s = 5.7$
Fracture energies (N/mm)	—	—	$G_c^{\mathrm{I}} = 0.24$ $G_c^{\mathrm{II}} = 0.55$	$G_c^{\mathrm{I}} = 0.24$ $G_c^{\mathrm{II}} = 0.55$

640 MPa according to Chinese code [32]. As can be seen from Figure 8, under the cyclic loading, obvious bending deformation of bolts was observed in the bolted glulam joints.

The numerical model of the tested joint was established and the results obtained from numerical analysis were compared to experimental findings for verification purposes. The failure modes of bolted joints predicted by numerical

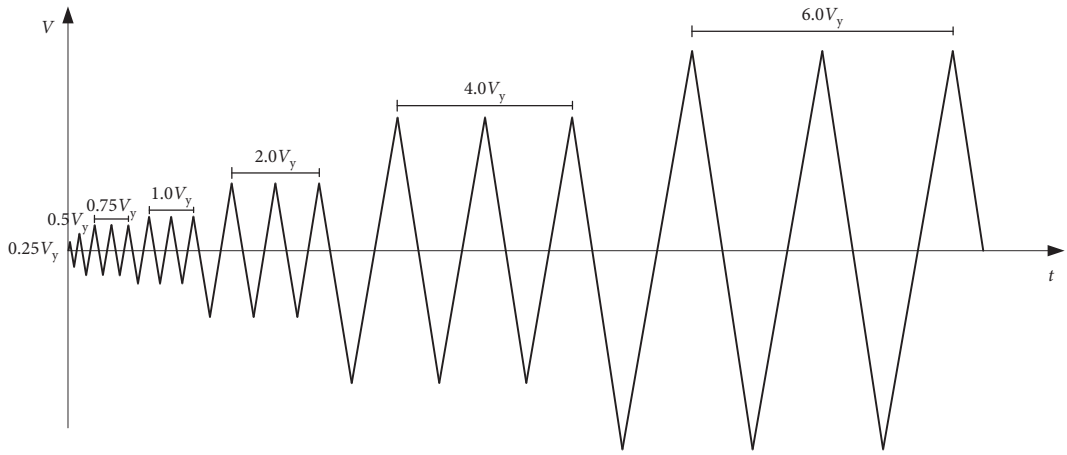

Figure 6: Loading protocol recommended in EN 12512 (2001).

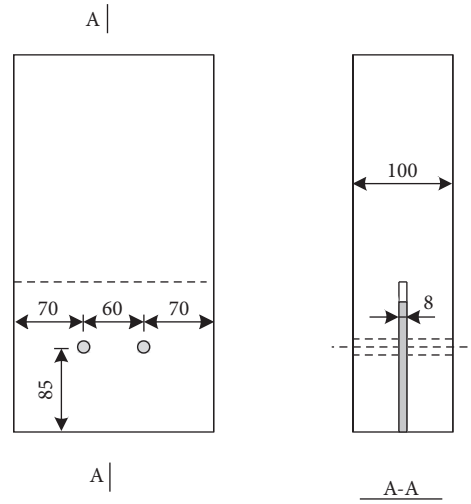

Figure 7: Detailed configurations of test bolted joint.

analysis are shown in Figure 8. Bolt bending deformation and embedment deformation of wood observed in the joint are quite similar to the experimental phenomenon. The comparison between the test obtained and the numerical predicted hysteretic curves was conducted and presented in Figure 9. As can be seen from the figure, the shape of the force-displacement hysteretic loops predicted by numerical analysis fit well with the test results. The deviation in displacement levels is caused by the difference between experimental obtained and numerical predicted yield displacement V_y under monotonic loading, which was related to the variability in wood properties and bolt clearance existing in test specimens. The mechanical parameters such as elastic stiffness and peak loading capacity are calculated and listed in Table 2. It can be seen that elastic stiffness obtained from the test is lower than the numerical results due to wood properties variation in the tested specimens. The experimentally obtained peak load-bearing capacity is slightly larger than the numerically predicted values, which is believed to relate to the discrepancy between the nominal and actual yield strength of bolts. The enclosed area of hysteretic loops was calculated to obtain the accumulative energy dissipation of the joints under reversed cyclic loading. As listed in Table 2, the numerical predicted energy dissipation is 1766.4 J, which is only 7% larger than the test value. It validates the reasonability of applying the numerical model to simulate the cyclic behavior of bolted glulam joints.

4. Parametric Study

To investigate the effects of crack patterns on the cyclic behavior of bolted glulam joints, a parametric study was conducted with the consideration of different bolt configurations. A single-bolt line with two bolts was included in Joint 1, as shown in Figure 10(a). The cross-sectional size of the glulam member is 120 x 90 mm, and the bolts are 12 mm in diameter with a nominal yield strength of 480 MPa. The geometric size of the glulam member in Joint 2 is identical to the tested joint, and the bolts are 16 mm in diameter with a nominal yield strength of 640 MPa, as presented in Figure 10(b). Different crack numbers and locations were considered in the analysis. The detailed information of crack patterns is shown in Figure 11. For crack patterns SB and ST in Joint 1, different crack lengths are considered and initial crack is cut through the bottom and top bolt, respectively. Initial cracks set on both sides of the steel plate are included in Joint 1 with crack patterns DB and DT. For crack patterns LS and LD in Joint 2, initial cracks along the left bolt line are set on single and both sides of the slotted-in steel plate, respectively. Initial cracks along both right and left bolt lines are included in the joints with crack patterns RLS and RLD.

4.1. Failure Modes and Hysteretic Curves. For initially perfect Joint 1, splitting failure of wood is observed under positive loading (i.e., tension load), as shown in Figure 12(a). Bolt yielding occurred under negative loading, as can be seen from the von Mises stress distribution of the middle cross section in Figure 12(b). In terms of the hysteretic curve, an obvious pinch phenomenon is observed from Figure 13(a), which is caused by the brittle failure of wood and plastic deformation of bolts. Under positive loading, a sudden drop of load-carrying capacity occurred at a loading amplitude level of 2.0 mm due to the splitting failure of wood.

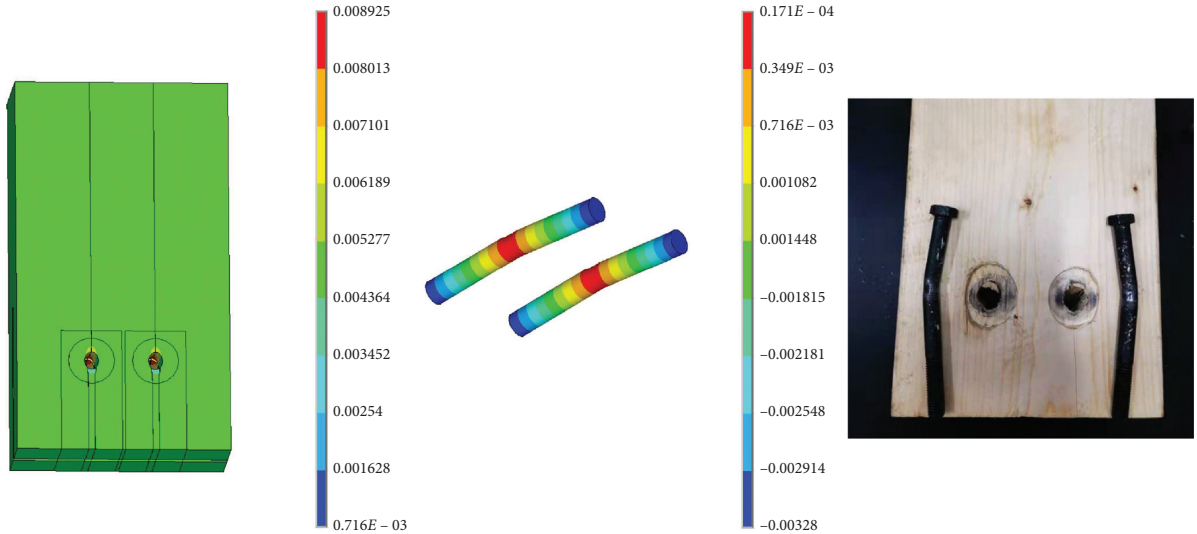

Figure 8: Failure modes of bolted glulam joint obtained from numerical analysis and experiment.

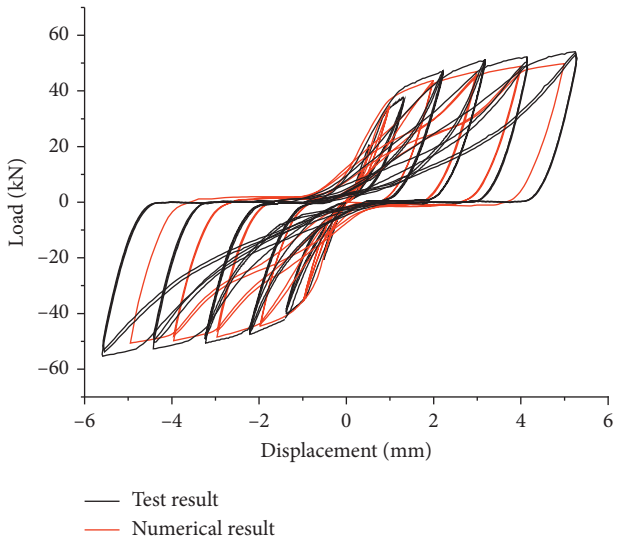

Figure 9: Comparison between experimentally obtained and numerical predicted hysteretic curves.

Compared to the mechanical behavior of the joint under positive loading, a more ductile performance is observed under negative loading. The joint with crack pattern DT exhibited a more pitched hysteretic behavior when compared with the initially perfect joint, as shown in Figure 13(b). The peak loading capacity and elastic stiffness are reduced by initial cracks. Under positive loading, a small decrease in capacity occurred when the displacement reaches 2 mm, which is caused by the propagation of initial cracks.

To investigate the effect of different numbers of cracks on the hysteretic behavior of bolted glulam joints, a comparison is conducted between Joint 1 with crack patterns SB and DB as presented in Figure 13(c). As can be seen from the figure, for Joint 1-SB with a single crack on one side of the steel plate, the brittle failure of wooden parts on the other side leads to the decrease of the load-carrying capacity from 30.7 kN to 19.2 kN. Compared to Joint 1-SB, a relatively lower peak capacity on the positive side is observed in Joint 1-DB with two initial cracks. Different crack lengths are considered in Figure 13(d), and the hysteretic curve of Joint 1-DB is compared to that of 1-DT. As can be seen from the figure, crack lengths only affect the elastic stiffness of bolted joints under positive loading. The initial crack in Joint 1-DB propagates from bottom bolt to top bolt at the displacement of 1 mm, and a slight decrease of capacity is observed in the figure. After this crack propagation, the same cracking conditions are obtained in these two joints, and thus the hysteretic curve of Joint 1-DB coincides with Joint 1-DT under further application of displacement load.

The main failure modes of initially perfect Joint 2 include the embedment failure of wooden parts around bolt holes and brittle failure of wood in the joint area, as shown in Figure 14. Obvious embedment deformation is observed before the occurrence of splitting failure of wood, as presented in Figure 14(a), while the bolts remain stiff and straight, and no significant bolt bending deformation is observed. The von Mises stress distribution of the middle section is given in Figure 14(c). It is indicated that only a slight portion of the bolts reaches the yield strength and the rest performs an elastic behavior.

Compared to Joint 1, a more significant pinch phenomenon is observed in the hysteretic curve of Joint 2, as shown in Figure 15(a), which is caused by the unrecoverable embedment deformation and splitting failure of wood. When the relative displacement of the initially perfect joint reaches 3.1 mm, splitting failure occurred along the bolt lines, and the capacity of the joint under positive loading decreases from 71 kN to 46 kN. In the loading cycle with an amplitude level of 6.0 mm, the peak capacity of the joint under positive loading is close to 60 kN. The capacity drops quickly in the unloading process, and the residual plastic deformation is around 4.3 mm. Nearly zero capacity is observed when the displacement declines from 4.3 mm to −2.5 mm under reversed loading due to the significant

Table 2: Mechanical parameters obtained from experimental and numerical results.

	Elastic stiffness (kN/mm)	Peak load (kN)	Accumulated energy dissipation (J)
Test result	38.0	52.9	1650.8
Numerical result	49.5	50.7	1766.4

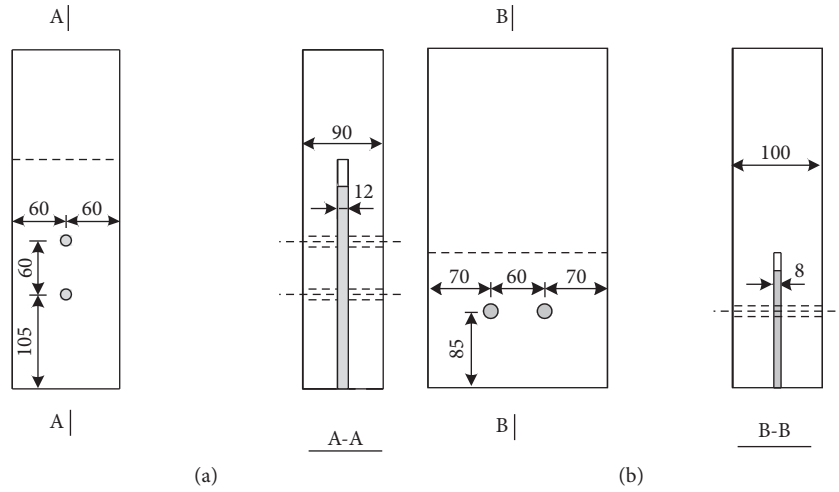

Figure 10: Two bolted glulam joints considered in the parametric study. (a) Joint 1. (b) Joint 2.

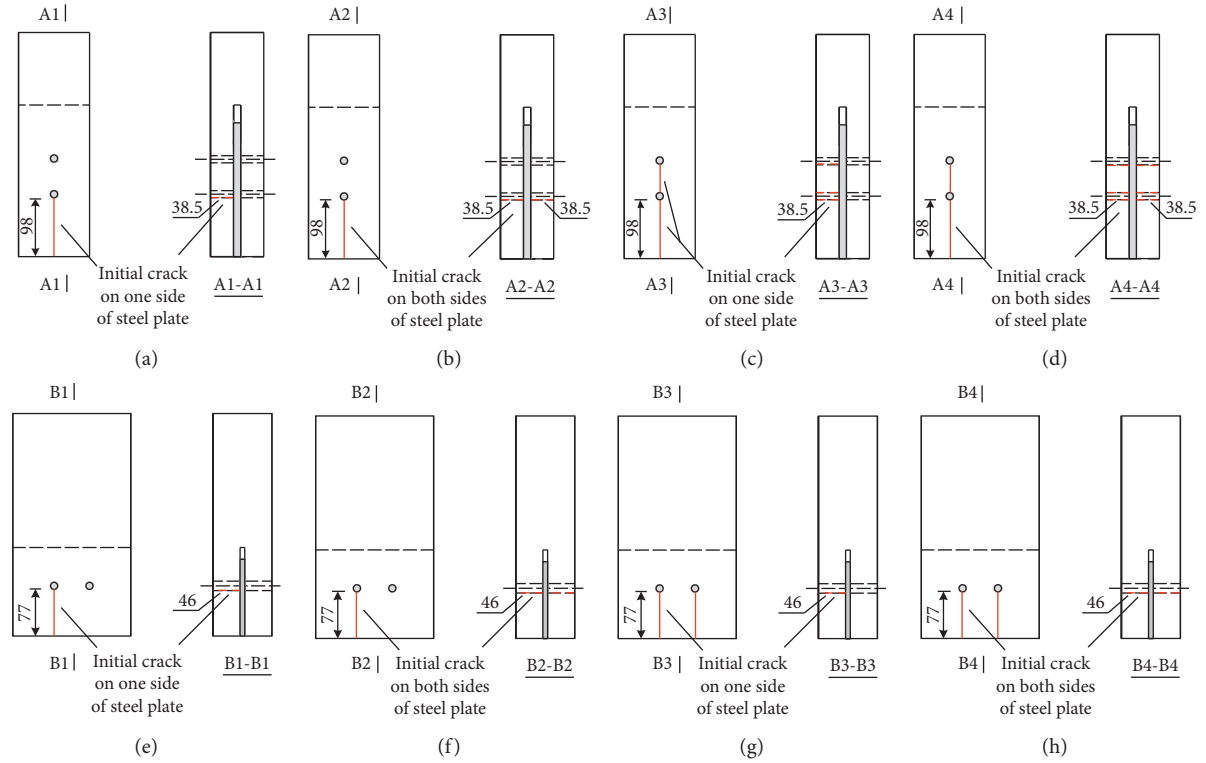

Figure 11: Different crack patterns considered in Joint 1 and Joint 2. (a) Joint 1-SB. (b) Joint 1-DB. (c) Joint 1-ST. (d) Joint 1-DT. (e) Joint 2-LS. (f) Joint 2-LD. (g) Joint 2-RLS. (h) Joint 2-RLD.

embedment deformation. By comparison with the initially perfect joint, the peak loading capacity and elastic stiffness of the joint with crack pattern RLD are impaired by initial cracks, as can be observed from the positive side of Figure 15(a). The propagation of cracks occurred at the displacement of 2.9 mm. In Figure 15(b), a comparison is

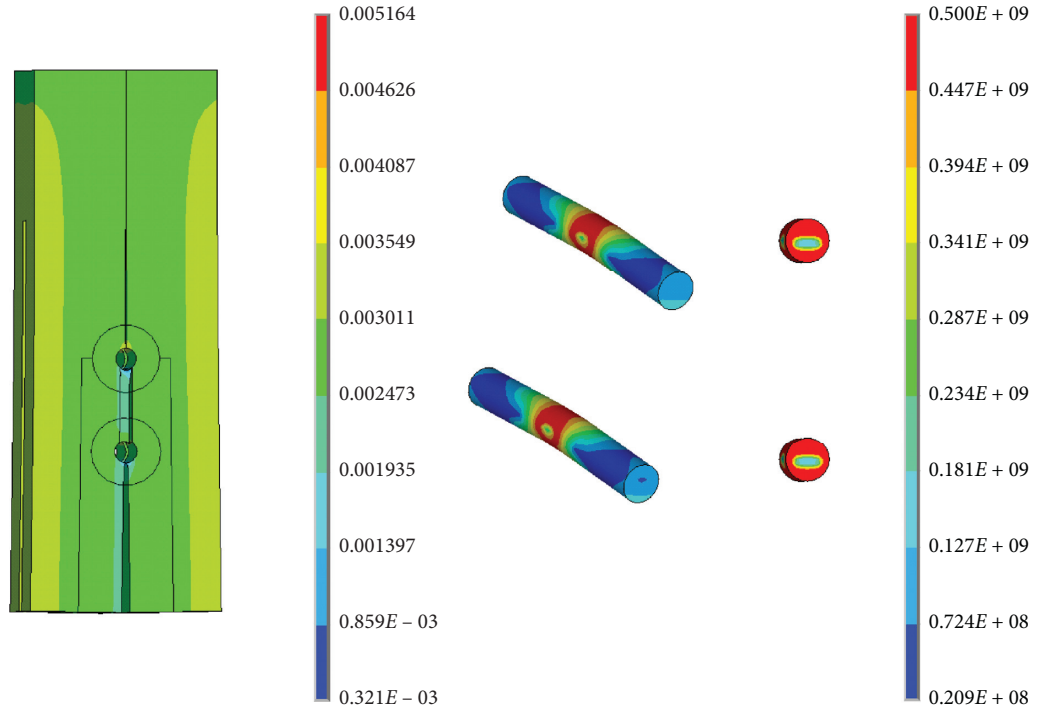

Figure 12: Failure mode of initially perfect Joint 1: (a) splitting failure of wooden parts; (b) von Mises stress distribution of bolts.

conducted between Joint 2 with crack patterns LD and RLD to explore the influence of different numbers of cracks. It can be seen that when compared with Joint 2-RLD including four cracks, a larger peak capacity is observed in Joint 2-LD with two cracks along the left bolt line. A drop of capacity in Joint 2-LD is observed at the displacement of 4.2 mm due to the splitting failure of wood along the right bolt line.

4.2. Skeleton Curves. The skeleton curves of Joint 1 are presented in Figure 16, which are obtained by connecting peak points of each primary loading cycle in the force-displacement hysteretic loops. Different numbers and lengths of initial cracks are considered in the comparison. As can be seen from Figure 16, the positive and negative sides of skeleton curves can be divided into three segments, respectively. A linear load-displacement relationship is observed in the first segment. Under positive loading, the stiffness of the linear segment is reduced by initial cracks when compared with the initially perfect joint, which is caused by the influence of crack opening on the interaction between bolts and wooden parts. The second segment is nonlinear, and stiffness attenuation is observed due to the occurrence of bolt yielding. After the peak point, a significant decrease in load-bearing capacity is observed from skeleton curves, which is caused by a brittle failure of wood in the joint area.

Mechanical parameters of Joint 1 under positive and negative loading were calculated and listed in Table 3, including elastic stiffness, yield force, yield displacement, peak capacity, ultimate displacement, and ductility ratio. The yield point was estimated based on ASTM D5764 [33], as shown in Figure 17. A straight line is drawn parallel to the linear segment and the offset is set as 5% of bolt diameter. The intersection point between the line and the skeleton curve is determined as the yield point. For envelope curves with the declining branch, the ultimate displacement is defined as the deformation corresponding to 80% of peak strength and the ductility ratio is calculated as ultimate displacement divided by yield displacement.

As can be seen from Figure 16 and Table 3, the peak loading capacity and initial stiffness of Joint 1 under positive loading are impaired by initial cracks, while negligible influence is observed on the mechanical performance under negative loading. Under positive loading, the peak capacity of Joint 1-SB and Joint 1-DB is 31.4 kN and 29.4 kN, respectively. Compared to the initially perfect joint, the decreasing ratio of capacity can be up to 21.8%, which is calculated by dividing the decrease by the corresponding value of the initially perfect joint. Further, it is indicated that more cracks lead to a more significant reduction in peak loading capacity. In terms of elastic stiffness, when compared to Joint 1-SB, lower stiffness is observed in Joint 1-DB with two initial cracks.

Different crack lengths are considered in Joint 1-DB and Joint 1-DT. As can be seen from Table 3, a similar peak capacity is found for these two joints, which indicated that crack lengths have little influence on the peak capacity of bolted joints. The elastic stiffness of Joint 1-DB and Joint 1-DT is 24.5 kN/mm and 17.2 kN/mm, respectively. Under positive loading, a longer crack reduces the elastic stiffness of bolted joint more significantly. When compared with an

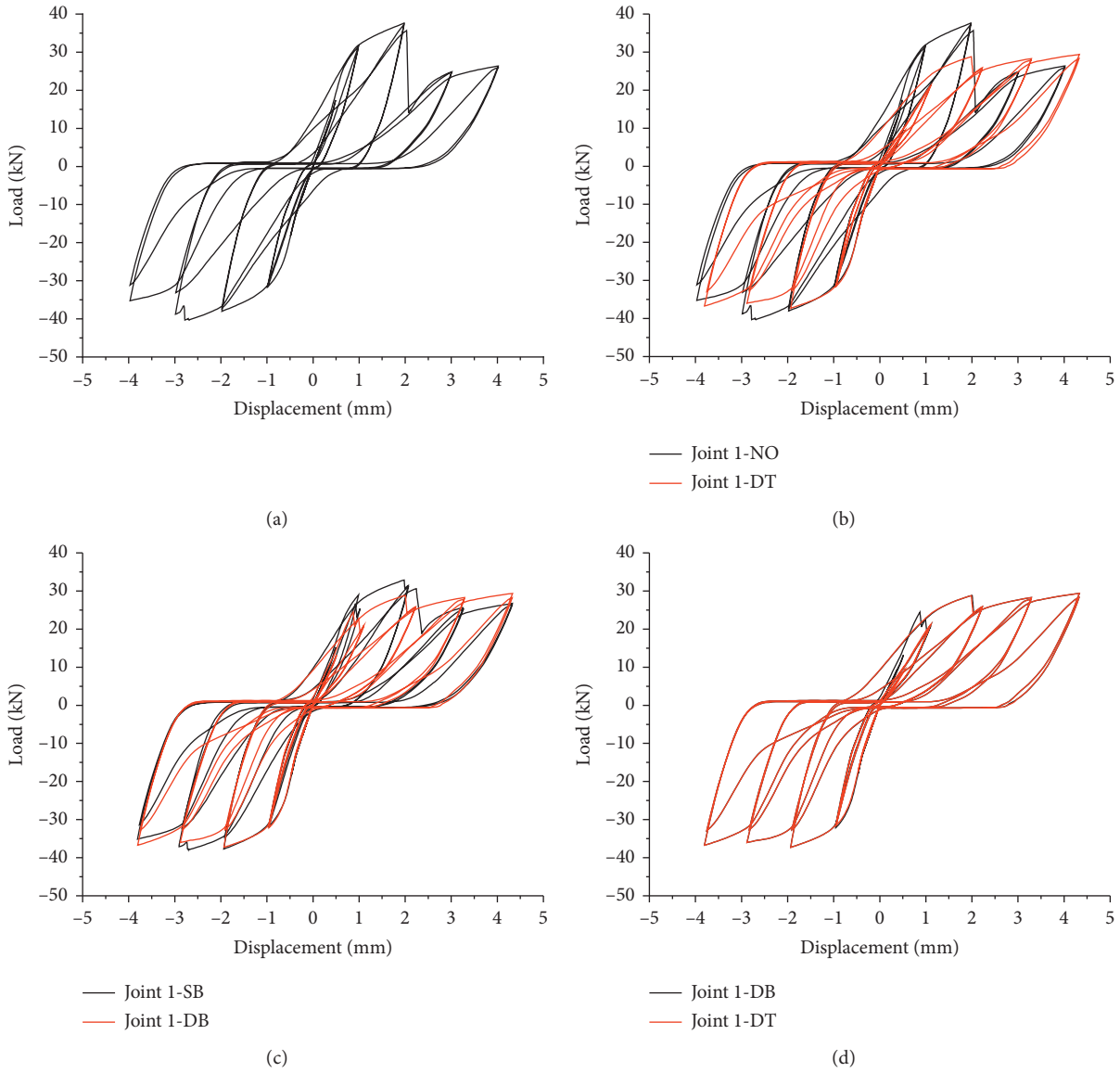

Figure 13: Hysteretic curves of Joint 1: (a) initially perfect Joint 1; (b) comparison between initially perfect Joint 1 and Joint 1-DT; (c) comparison between Joint 1-SB and Joint 1-DB; (d) comparison between Joint 1-DB and Joint 1-DT.

initially perfect joint, the decreasing ratio of elastic stiffness can be up to 47.4% with the existence of two cracks through the top bolt. In terms of ductility ratio, it can be found from Table 3 that the ductility ratio of the initially perfect joint is lower than the joints with initial cracks. Brittle failure of wood under external load leads to a sudden drop of capacity in the initially perfect joint, while a smoothing skeleton curve is realized in Joint 1-DB and Joint 1-DT with the occurrence of crack propagation instead of brittle failure of wood. The ductility ratio of Joint 1-DB and Joint 1-DT is 2.85 and 2.32, respectively.

The skeleton curves and mechanical parameters of Joint 2 are presented in Figure 18 and Table 4, respectively. Similar to Joint 1, the reduction in the peak loading capacity and elastic stiffness is observed with the existence of initial cracks. As can be seen from the table, the peak capacity of Joint 1-LS and Joint 1-RLD under positive loading is 68.4 kN and 60.1 kN, respectively. Compared to an initially perfect joint with a capacity of 71.4 kN, the decreasing ratio of capacity can be up to 15.8%. With initial cracks on both bolt lines, the elastic stiffness of bolted joints declines from 49.6 kN/mm to 40.2 kN/mm with a decreasing ratio of 19.0%. Compared to Joint 1, the influence of initial cracks is less significant on the peak capacity and elastic stiffness of Joint 2, while initial cracks impair the ductility behavior of Joint 2, contrary to the observed trend in Joint 1. Similar ultimate displacement is observed in the joints with or without initial cracks, as shown in Table 4.

4.3. Stiffness Degradation. Under reversed cyclic loading, the stiffness of bolted glulam joints declined gradually with increased loading amplitudes with wood crushing or bolting yielding. The secant stiffness of primary loading cycles was calculated as follows:

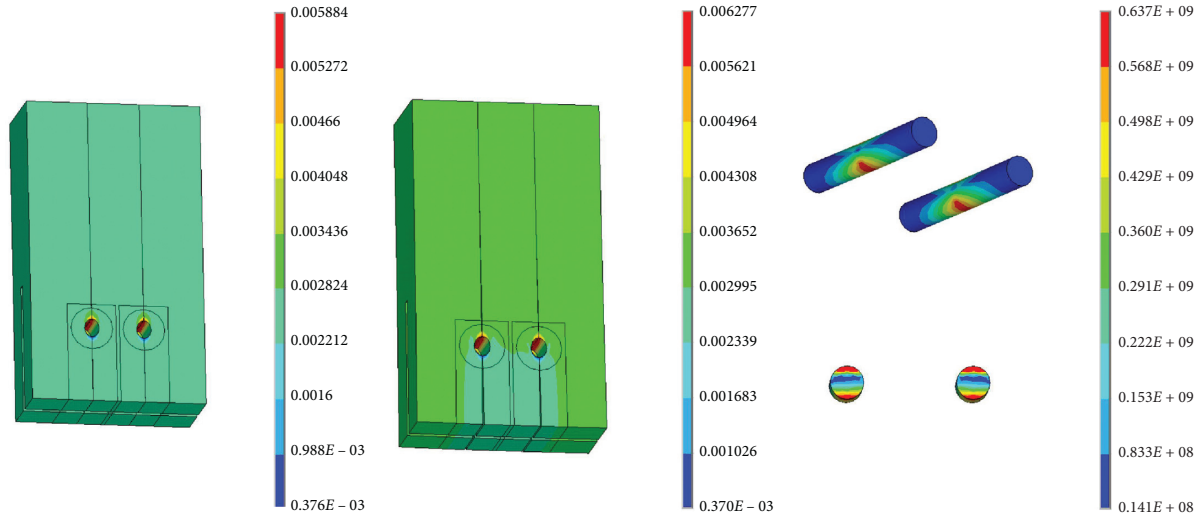

Figure 14: Failure mode of initially perfect Joint 2: (a) embedment deformation of wood; (b) splitting failure in the joint area; (c) von Mises stress distribution of bolts.

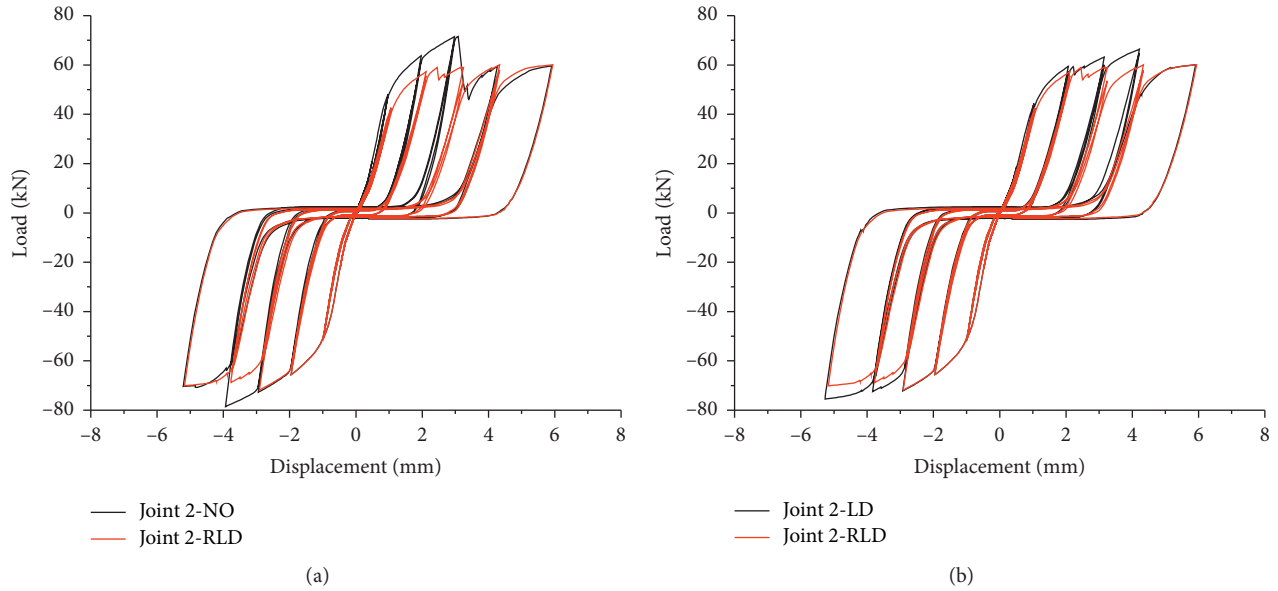

Figure 15: Hysteretic curves of Joint 2: (a) comparison between initially perfect Joint 2 and Joint 2-RDT; (b) comparison between Joint 2-LD and Joint 2-RLD.

$$K_i = \frac{|F_{ip}| + |F_{in}|}{|\Delta_{ip}| + |\Delta_{in}|}, \quad (4)$$

where F_{ip} and Δ_{ip} represent the maximum positive load and corresponding displacement of loading cycle i; F_{in} and Δ_{in} indicate the maximum negative force and corresponding displacement of cycle i. The change of secant stiffness with the increase of displacement is presented in Figure 19. It can be seen that the secant stiffness of the initially perfect joint is the largest in the same loading cycle compared to joints with initial cracks. Also, more numbers of cracks and longer cracks lead to more decrease in the secant stiffness of joints.

At the early loading stage, the gradual growth of secant stiffness is observed with full contact interaction. For initially perfect Joint 1, the largest secant stiffness of 36.5 kN/mm is obtained at the displacement of 0.5 mm, as shown in Figure 19(a). It decreases to 32 kN/mm when the amplitude of the loading cycle rises to 1.0 mm, which is caused by the development of bolt yielding. A deep decrease of secant stiffness is observed with the amplitude level growing to 2 mm due to the occurrence of brittle failure of wood. For Joint 1 with crack pattern DT, the peak secant stiffness is around 26 kN/mm, which is 28.8% lower than the initially perfect joint. A relatively flat segment was observed after the peak point, and a little decrease of secant stiffness occurs

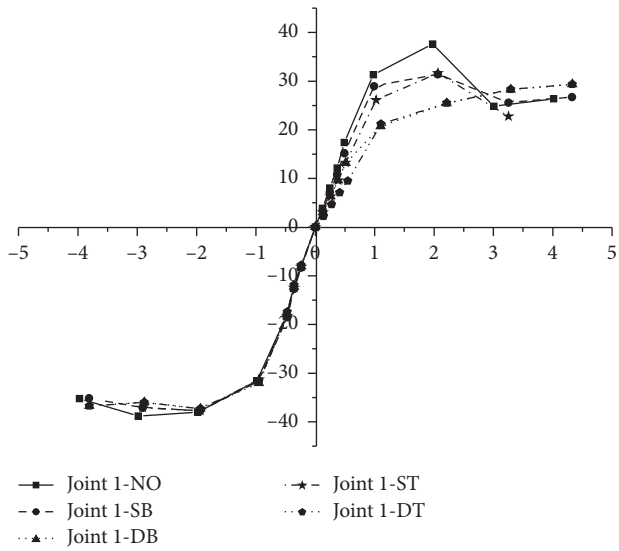

Figure 16: Comparisons of skeleton curves for Joint 1.

Table 3: Summary of the mechanical parameters of Joint 1.

	Joint 1-NO	Joint 1-SB	Joint 1-DB	Joint 1-ST	Joint 1-DT
Elastic stiffness (kN/mm)	32.7/33.6	28.9/33.5	24.5/33.6	24.6/33.5	17.2/33.0
Yield force (kN)	35.8/−36.0	30.5/−35.8	22.4/−35.7	30.3/−35.9	24.1/−35.6
Yield displacement (mm)	1.7/−1.68	1.65/−1.62	1.52/−1.64	1.85/−1.63	1.87/−1.68
Peak load (kN)	37.6/−38.8	31.4/−37.7	29.4/−37.3	31.6/−37.7	29.4/−37.3
Ultimate displacement (mm)	2.55/−3.97	3.27/−3.82	4.33/−3.80	3.02/−3.82	4.33/−3.80
Ductility ratio	1.50/2.36	1.98/2.36	2.85/2.32	1.63/2.34	2.32/2.26

Note. Mechanical parameters are calculated from the positive and negative sides of skeleton curves, respectively.

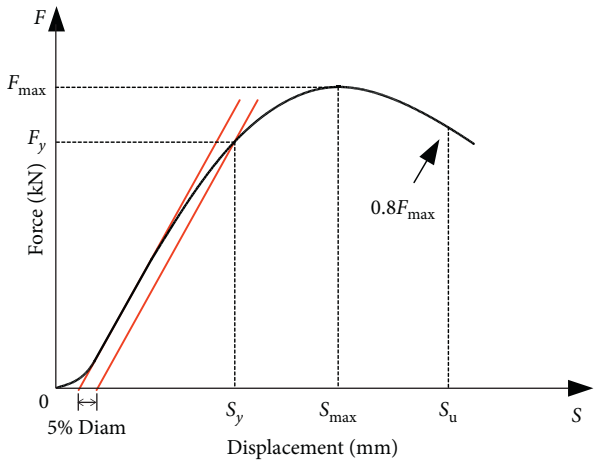

Figure 17: The method of 5% diameter used to determine the yield point.

when the amplitude increases from 0.5 mm to 1.0 mm. It is indicated that the damage accumulation such as bolt yielding and wood locally compression is not significant at the loading stage.

Similar to Joint 1, a first growing tendency of secant stiffness is observed in Joint 2, as shown in Figure 19(b). The largest secant stiffness of the initially perfect joint is 50.9 kN/mm obtained at the displacement of around 1 mm. The peak value of Joint 2-RLD is 45.9 kN/mm, which is decreased by 9.8% with the existence of initial cracks. A rapid drop of secant stiffness is observed after the peak point due to the occurrence of embedment failure of wood. Compared to Figure 19(a), it can be found that the decrease of peak secant stiffness in Joint 2 is much lower than that observed in Joint 1, which indicates that initial cracks have a less dramatic effect on the secant stiffness of bolted joints with embedment failure mode.

4.4. Energy Dissipation. To estimate the accumulative energy dissipation of the joint under reversed cyclic loading, the enclosed area of the hysteretic loop was calculated for each loading cycle based on numerical integration, and the accumulative energy dissipation was presented in Figure 20. As can be seen from Figure 20(a), the energy dissipated in Joint 1 is negligible during the loading cycles with a magnitude lower than 0.5 mm, which indicated that the materials behave elastically at this deformation level. With the displacement increasing from 1.0 mm to 4.0 mm, bolt yielding and obvious bolt bending deformation are observed in the joint, and the energy dissipated grows rapidly. The total energy dissipated in initially perfect Joint 1 is around 677 J. Compared to joints with crack pattern DB and DT, the joints with single crack dissipated more energy at the displacement lower than 4 mm, while similar total energy dissipated of around 514 J is obtained at the end of the loading process.

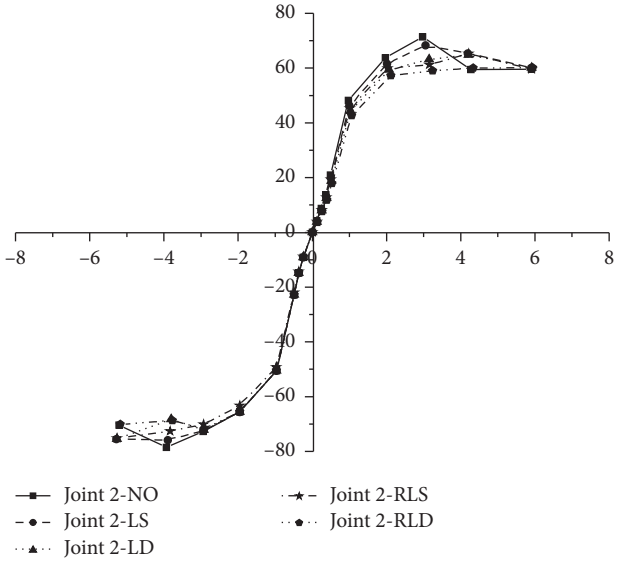

Figure 18: Comparisons of skeleton curves for Joint 2.

Table 4: Summary of the mechanical parameters of Joint 2.

	Joint 2-NO	Joint 2-LS	Joint 2-LD	Joint 2-LRS	Joint 2-LRD
Elastic stiffness (kN/mm)	49.6/52.2	46.2/52.2	42.9/52.2	44.8/50.7	40.2/52.1
Yield force (kN)	61.7/−63.3	60.3/−63.2	57.6/−62.6	59.6/−60.9	56.0/−63.0
Yield displacement (mm)	1.85/−1.79	1.92/−1.79	1.96/−1.81	1.92/−1.79	2.0/−1.82
Peak load (kN)	71.4/−78.6	68.4/−75.8	64.8/−75.5	65.3/−75.1	60.1/−71.8
Ultimate displacement (mm)	5.91/−5.21	5.90/−5.28	5.91/−5.27	5.91/−5.27	5.94/−5.17
Ductility ratio	3.19/2.91	3.08/2.95	3.02/2.91	3.08/2.94	2.94/2.84

Note. Mechanical parameters are calculated from the positive and negative sides of skeleton curves, respectively.

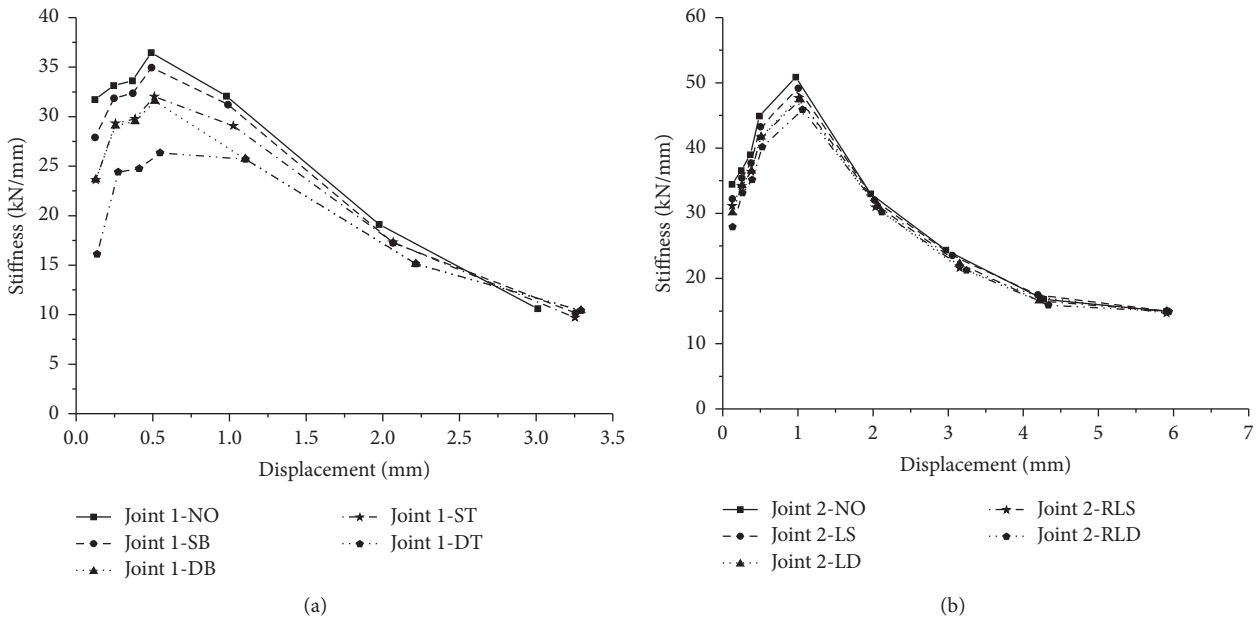

Figure 19: Stiffness degradation observed in bolted glulam joints: (a) Joint 1; (b) Joint 2.

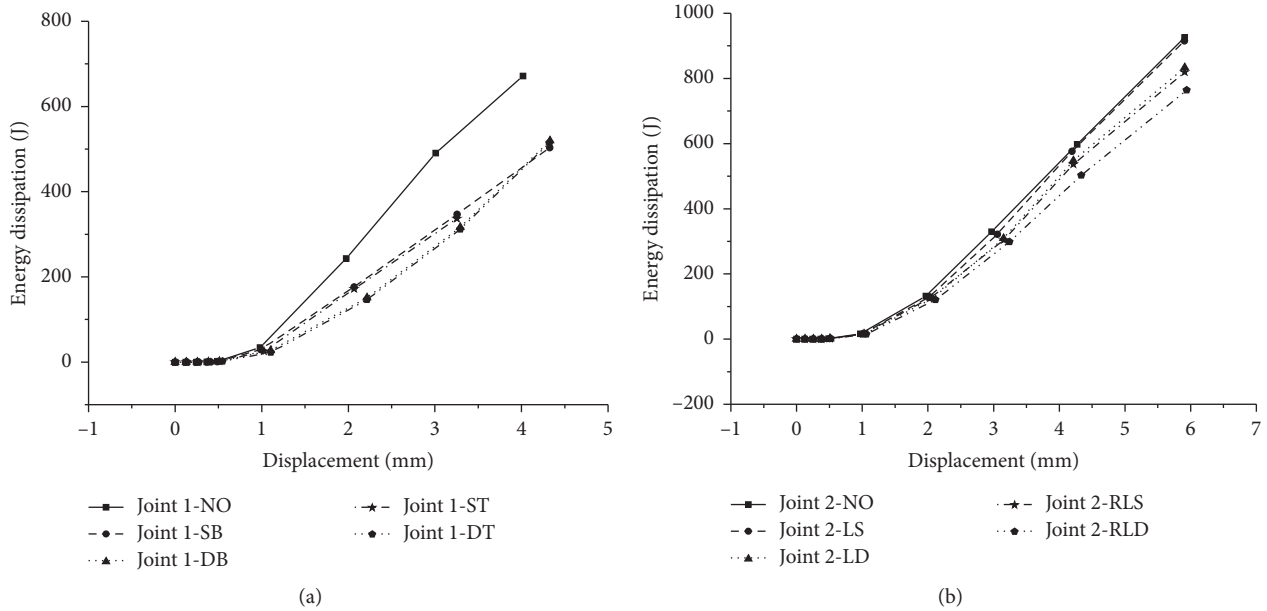

Figure 20: Comparisons of energy dissipation curves: (a) Joint 1; (b) Joint 2.

The energy dissipated of bolted glulam joints with initial cracks is only 76% of the initially perfect joint.

For initially perfect Joint 2, a similar increasing tendency is observed and the total energy dissipated is 932 J. As can be found from Figure 20(b), lower energy dissipated is observed in the joints with more cracks. The total energy dissipated of Joint 2-RLD is 764 J, and the decreasing ratio is 18% compared to the initially perfect joint.

Equivalent viscous damping ratios have been calculated at different amplitude levels as follows:

$$\xi = \frac{1}{2\pi} \cdot \frac{E_p}{E_d}, \tag{5}$$

where E_p represents the enclosed area of the hysteretic loop for each primary loading cycle and E_d equals the area of two triangles ($S_{\Delta OAB} + S_{\Delta OCD}$), as shown in Figure 21. The relationships between equivalent viscous damping ratios and the displacement are presented in Figure 22.

It can be seen from Figure 22(a) that the equivalent viscous damping ratios of Joint 1 are quite low at displacement of 0.5 mm. With the displacement rising from 0.5 mm to 2.0 mm, the damping ratio of the initially perfect joint increases to 0.18 linearly with damage accumulation, and a damping ratio of 0.196 is achieved at the displacement of 3.0 mm. For Joint 1 with initial cracks, the damping ratios increase as the displacement grows from 0.5 mm to 2.0 mm, and a damping ratio of around 0.17 is obtained. The damping ratio is reduced by 13.3% with the existence of initial cracks. After the peak point, a drop of equivalent viscous damping ratio is observed with further application of displacement loading.

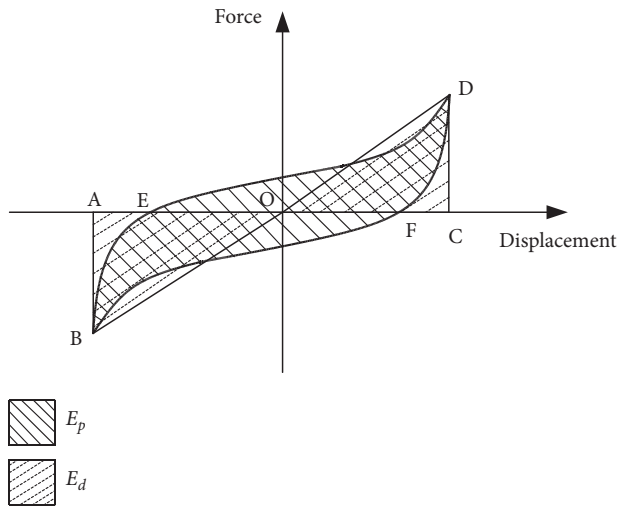

Figure 21: Determination of energy dissipation.

As can be seen from Figure 22(b), a similar changing tendency of equivalent viscous damping ratio is observed in Joint 2 before the displacement reaches 2.0 mm. The equivalent viscous damping ratio of initially perfect Joint 2 is lower than that of Joint 1. A peak damping ratio of 0.114 is obtained at the displacement of 2.0 mm and the damping ratio decreases with further increase in loading amplitude. The damping ratio of Joint 2-LS and Joint 2-RLD is 0.112 and 0.109, respectively. Less significant influence of initial cracks on equivalent viscous damping ratio is observed in Joint 2 when compared to Joint 1.

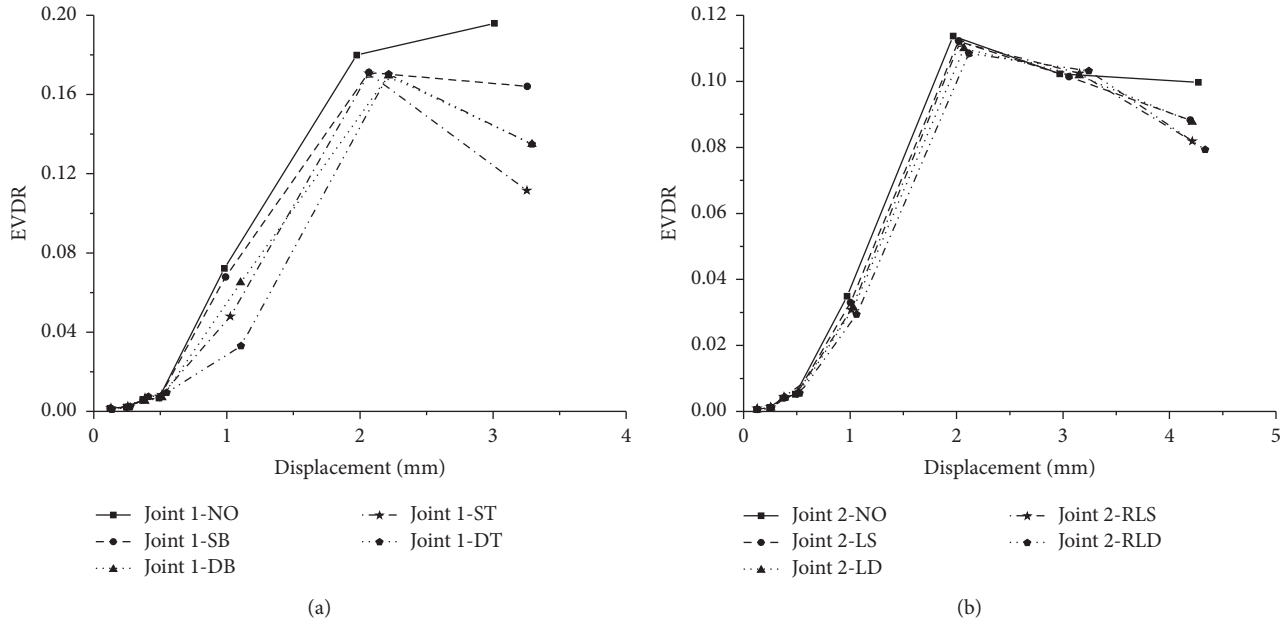

Figure 22: Relationships between equivalent viscous damping ratio and displacement: (a) Joint 1; (b) Joint 2.

5. Conclusion

In the paper, a 3D numerical model was developed to investigate the influence of initial cracks on the cyclic behavior of bolted glulam joints under parallel-to-grain loading. Cohesive zone material law was applied to simulate the propagation of initial cracks and brittle failure of wood. With the application of the Hill yield criterion and wood foundation zone model, the local crushing behavior of wood was reproduced by numerical results. The feasibility of the numerical model was verified by comparison with full-scale experimental results, and different crack patterns and bolt configurations were further considered in a parametric study.

It was found that peak capacity and elastic stiffness of bolted glulam joints were reduced with the existence of initial cracks. More decrease in capacity was observed in joints with more cracks, and longer cracks affect elastic stiffness more dramatically. For Joint 1 with splitting failure occurring under positive loading, the decreasing ratios can be up to 21.8% and 47.4%, respectively. The ductility behavior of Joint 2 with controlled failure mode of wood embedment is impaired by initial cracks. Moreover, under reversed cyclic loading, less energy dissipated is observed in bolted glulam joints with initial cracks, which is only 76% of energy dissipated in the initially perfect joint. Further, the equivalent viscous damping ratio of bolted glulam joint is reduced by 13.3% with the existence of initial cracks.

Data Availability

The data used to support the findings of this study are included within the article and available from the corresponding author upon request.

Conflicts of Interest

The authors declare that they have no conflicts of interest.

Acknowledgments

The authors gratefully acknowledge the National Natural Science Foundation of China (Grant no. 51908147) for supporting this research.

References

[1] R. Y. Itani and K. F. Faherty, *Structural Wood Research: State-of-The-Art and Research Needs*, ASCE, Reston, VA, USA, 1984.

[2] T. V. P. Caldeira, N. Dourado, A. M. P. De Jesus, M. F. S. F. De Moura, and J. J. L. Morais, "Quasi-static behavior of moment-carrying steel-wood doweled joints," *Construction and Building Materials*, vol. 53, pp. 439–447, 2014.

[3] E.-M. Meghlat, M. Oudjene, H. Ait-Aider, and J.-L. Batoz, "A new approach to model nailed and screwed timber joints using the finite element method," *Construction and Building Materials*, vol. 41, pp. 263–269, 2013.

[4] C. L. Santos, A. M. P. De Jesus, J. J. L. Morais, and B. F. C. Fontoura, "An experimental comparison of strengthening solutions for dowel-type wood connections," *Construction and Building Materials*, vol. 46, pp. 114–127, 2013.

[5] P. Zarnani and P. Quenneville, "Strength of timber connections under potential failure modes: an improved design procedure," *Construction and Building Materials*, vol. 60, no. 16, pp. 81–90, 2014.

[6] I. Gavric, M. Fragiacomo, and A. Ceccotti, "Cyclic behaviour of typical metal connectors for cross-laminated (CLT) structures," *Materials and Structures*, vol. 48, no. 6, pp. 1841–1857, 2015.

[7] A. Jorissen and M. Fragiacomo, "General notes on ductility in timber structures," *Engineering Structures*, vol. 33, no. 11, pp. 2987–2997, 2011.

[8] A. Lokaj and K. Klajmonová, "Dowel type joints of round timber exposed to static and cyclic tension forces," *Procedia Engineering*, vol. 114, pp. 240–247, 2015.

[9] M. Popovski, "Seismic performance of braced timber frames," Doctoral dissertation, University of British Columbia, Vancouver, Canada, 2000.

[10] T. L. Wilkinson, "Analysis of nailed joints with dissimilar members," *Journal of the Structural Division*, vol. 98, no. 9, pp. 2005–2013, 1972.

[11] R. O. Foschi and H. Prion, "Behaviour of heavy timber connections under cyclic loads," Thesis, Report, University of British Columbia, Vancouver, B.C., Canada, 1996.

[12] J. Xu and J. D. Dolan, "Development of nailed wood joint element in ABAQUS," *Journal of Structural Engineering*, vol. 135, no. 8, pp. 968–976, 2009.

[13] Y.-L. Shen, J. Schneider, S. Tesfamariam, S. F. Stiemer, and Z.-G. Mu, "Hysteresis behavior of bracket connection in cross-laminated-timber shear walls," *Construction and Building Materials*, vol. 48, pp. 980–991, 2013.

[14] Z. Shu, Z. Li, M. He, X. Zheng, and T. Wu, "Seismic design and performance evaluation of self-centering timber moment resisting frames," *Soil Dynamics and Earthquake Engineering*, vol. 119, pp. 346–357, 2019.

[15] R. O. Foschi, "Load-slip characteristic of nails," *Wood Science*, vol. 7, pp. 69–76, 1974.

[16] J. P. Hong, "Three-dimensional nonlinear finite element model for singe and multiple dowel-type wood connections," Doctoral Dissertation, University of British Columbia, Vancouver, B.C., Canada, 2007.

[17] D. M. Moses and H. G. L. Prion, "Stress and failure analysis of wood composites: a new model," *Composites Part B: Engineering*, vol. 35, no. 3, pp. 251–261, 2004.

[18] N. Kharoufa, G. McClure, and I. Smith, "Elasto-plastic modelling of wood bolted connections," *Computers and Structures*, vol. 81, no. 8-11, pp. 747–754, 2003.

[19] B. H. Xu, A. Bouchaïr, M. Taazount, and E. J. Vega, "Numerical and experimental analyses of multiple-dowel steel-to-timber joints in tension perpendicular to grain," *Engineering Structures*, vol. 31, no. 10, pp. 2357–2367, 2009.

[20] M. Patton-Mallory, P. Pellicane, and F. Smith, "Qualitative assessment of failure in bolted connections: tsai-Wu criterion," *Journal of Testing and Evaluation*, vol. 26, no. 5, pp. 497–505, 1998.

[21] M. Patton-Mallory, P. J. Pellicane, and F. W. Smith, "Modeling bolted connections in wood: review," *Journal of Structural Engineering*, vol. 123, no. 8, pp. 1054–1062, 1997.

[22] N. Dourado, F. G. A. Silva, and M. F. S. F. De Moura, "Fracture behavior of wood-steel dowel joints under quasi-static loading," *Construction and Building Materials*, vol. 176, pp. 14–23, 2018.

[23] J. Zhang, M.-J. He, and Z. Li, "Numerical analysis on tensile performance of bolted glulam joints with initial local cracks," *Journal of Wood Science*, vol. 64, no. 4, pp. 364–376, 2018.

[24] C. L. Santos, A. M. P. De Jesus, J. J. L. Morais, and J. L. P. C. Lousada, "Quasi-static mechanical behaviour of a double-shear single dowel wood connection," *Construction and Building Materials*, vol. 23, no. 1, pp. 171–182, 2009.

[25] J. Sjödin and C.-J. Johansson, "Influence of initial moisture induced stresses in multiple steel-to-timber dowel joints," *Holz als Roh- und Werkstoff*, vol. 65, no. 1, pp. 71–77, 2006.

[26] M. He, J. Zhang, and Z. Li, "Influence of cracks on the mechanical performance of dowel type glulam bolted joints," *Construction and Building Materials*, vol. 153, pp. 445–458, 2017.

[27] J. Zhang, M. He, and Z. Li, "Mechanical performance assessment of bolted glulam joints with local cracks," *Journal of Materials in Civil Engineering*, vol. 30, no. 6, 2018.

[28] E. P. Saliklis, T. J. Urbanik, and B. Tokyay, "Bilinear modelling of cellulosic orthotropic nonlinear materials," *Journal of Pulp and Paper Science*, vol. 29, no. 12, pp. 407–411, 2003.

[29] B. H. Xu, M. Taazount, A. Bouchaïr, and P. Racher, "Numerical 3D finite element modelling and experimental tests for dowel-type timber joints," *Construction and Building Materials*, vol. 23, no. 9, pp. 3043–3052, 2009.

[30] J. L. Jensen and P. Quenneville, "Fracture mechanics analysis of row shear failure in dowelled timber connections," *Wood Science and Technology*, vol. 44, no. 4, pp. 639–653, 2009.

[31] BSI, *Timber Structures-Test Methods-Cyclic Testing of Joints Made with Mechanical Fasteners*, BSI, London, UK, 2001.

[32] BSI, *Mechanical Properties of Fasteners Bolts, Screws and Studs*, BSI, London, UK, 2000.

[33] ASTM, *Standard Test Method for Evaluating Dowel-Bearing Strength of Wood and Woodbase Products*, ASTM, West Conshohocken, PA, USA, 2013.

Hindawi
Advances in Civil Engineering
Volume 2021, Article ID 6677450, 8 pages
https://doi.org/10.1155/2021/6677450

Research Article

An Inelastic Theoretical Model regarding the Load-Carrying Capacity of PSL Bending Component

Baolu Sheng,[1,2] **Yuling Bian**,[3] **Dong He**,[4] **and Aiping Zhou**[1,2]

[1]*National Engineering Research Center of Biomaterials, Nanjing Forestry University, 159 Longpan Rd., Nanjing 210037, China*
[2]*School of Civil Engineering, Nanjing Forestry University, Nanjing 210037, China*
[3]*Wuxi Vocational Institute of Commerce, 809 Qianhu Rd., Wuxi 214153, China*
[4]*Dongfang Turbine Co.,Ltd., 666 Jinshajiang Rd., Deyang City, Sichuan Province 618000, China*

Correspondence should be addressed to Baolu Sheng; baolu52520@163.com

Received 13 November 2020; Revised 2 December 2020; Accepted 27 February 2021; Published 11 March 2021

Academic Editor: Musa Adamu

Parallel strand lumber (PSL) is an attractive structural wood composite which may have prospective use in building constructions. Conducting nonlinear analysis for the bending of PSL beams is a critical step in the determination of ultimate strength and deflection of them, which is an essential requirement of the building design philosophy based on probability of ultimate state. For the purposes of this article, an inelastic theoretical model regarding the load-carrying capacity of the PSL bending component has been developed. Based on the uniaxial loading tests, the stress-strain behaviors of PSL composite in the grain direction were measured. 4-point bending experiments were also performed in this study to investigate the failure mechanism of the PSL components. The results show that the tensile stress-strain relationship of PSL materials in the grain direction remains linear until breaking, while the compressive stress-strain relationship exhibits nonlinear characteristics once the compressive stress exceeds the proportional limit, which can be expressed by a quadratic polynomial. The failure mode of the PSL beam can be summarized that the fibres in the top of the broken section were buckling and those in the bottom of the section were broken when failure occurred. Significant nonlinear behavior was exhibited based on the load-deflection curves of the PSL beams. To predict the nonlinear bending performance of the PSL beams, a theoretical model that could consider the nonlinear stress-strain relations of PSL and predict the damage modes of the PSL beams was developed. Well agreements can be observed between the results of calculations and experiments.

1. Introduction

PSL is a wood-based composite material with outstanding mechanical properties for construction. It is fabricated by gluing raw wood strands together along the grain direction under high pressure and microwave heat, which are often a by-product during the plywood manufacturing process [1]. After this industrial production process, the defects of raw wood will be eliminated. The consistent properties and fire resistance of PSL are superior to those of raw wood [2]. Thus, PSL has sufficient strength and rigidity [3] that makes PSL material very well suitable as beams and columns for cross- and large-span building structure and for high-rise buildings [2]. In addition, due to the development of the energy-efficient building and green building initiatives, PSL has been becoming an extensively potential prospective structural material for building constructions.

It is a vital work for safeguard design to precisely evaluate the strength and deflection of the structural members in the condition of strength limit state. However, the structure and mechanical properties of PSL have a strong orientation. As a matter of fact, PSL is a natural oriented fiber-reinforced composite. The approach of strength theory and mechanical model proposed by classical theories to analyze the behaviors of the component made of homogeneous or isotropic materials cannot be suitable to conduct the inelastic analysis for PSL structural members. Additionally, linear principles are currently employed in design code for wood

buildings to predict the load-carrying capacity and deflection in the strength limit state as the nonlinear behaviors of wood or wood composites have not been well modelled [2]. Unfortunately, considerable researchers have found that almost all engineered wood composites or raw wood materials, including PSL, have strong nonlinear characteristics in the stress-strain relationship under compression parallel to grain [4–6]. Wood-based structure members are actually displaying strong nonlinear performances when approaching the strength limit state. Accordingly, there are certain errors in the results inevitably in the calculation of the ultimate bearing capacity and the ultimate deformations of structure members by the use of the linear elastic principle. Therefore, to well understand the engineering behaviors of PSL composite, such as inelastic analysis and failure mechanisms, is the cornerstone of the development of wooden construction.

Some analytical or numerical models have been proposed to evaluate the nonlinear performances of wood or wood composite structure members. Naghipour et al. [7] developed a theoretical model to investigate the nonlinear behaviors of reinforced wood-plastic composite (WPC) beams wrapped with glass and carbon fiber-reinforced polymers. Nonlinear characteristics of WPC composite in the direction of tension and compression were considered by using an exponential function. Borri et al. [8] proposed a numerical procedure to study the performances of wood beams reinforced by using CFRP sheets. The bilinear model was adopted to simulate the elastic-plastic behavior in compression of wood material and linear elastic one in tension. Another model to investigate the flexural performances of CFRP retrofit wood beams was reported by Li et al. [9]. A quadratic curve was adopted to model the compressive nonlinearity of wood materials, and the function of the curve was obtained by data fitting for experiments. Actually, it is commonly accepted that the stress-strain relationship of raw wood materials in the grain direction is linear for tensile stress and nonlinear for compressive stress. Some mathematical models have been proposed for simulating this nonlinearity [6, 10–12]. Huang et al. [13] proposed an inelastic model of engineered bamboo bending components by considering the difference between tensile moduli and compressive moduli. The theoretical model, of which the nonlinearity of stress-strain relationships was considered, to predict the deflection, stress and strain, and ultimate bearing capacity of wood-based composite structural components in the strength limit state, however, is not available up to now.

In this paper, considering nonlinear behaviors of material, a theoretical model to predict the bending bearing capacity of PSL beams was developed and the ultimate deformation of the beam in midspan was also given by assuming a fictitious plastic hinge at the critical cross section. Firstly, mathematical formulas for describing the stress-strain relationships of PSL composite along the grain were proposed based on tests. Secondly, to investigate the failure mode and the failure mechanism of PSL beams, four-point bending tests were performed. A novel model, which takes the nonlinear stress-strain relationship of PSL composite into account, to predict the responses during all service periods from loading to failure for PSL bending members was developed at last. Well agreements can be observed between the results of calculations and experiments.

2. Stress-Strain Relationship along Parallel to Grain Direction

The stress-strain curve was obtained by experiments. Test materials were offered by FPInnovations, Vancouver, Canada. Tests were carried out in the laboratory of FPInnovations, Vancouver, Canada. Compressive test along the grain direction was referred to ASTM D143-09 [14]. Prisms with dimensions of 50 mm × 50 mm × 200 mm were adopted as specimens for tests. 22 specimens were tested. The loading direction should be perpendicular to both ends of the compressive specimen and parallel to fiber orientation. An axial compression test can use spherical hinge bearing to reallocate load traverse distribution so that the load could be evenly acted on the whole cross section passing through the roller. The loading procedure is controlled by the displacement method at a rate of motion of a movable crosshead of 0.6 mm/min. Longitudinal strain at the middle of the specimen was measured by strainometer. Specimens for the tensile test were also designed referring to ASTM 143-09 [13], and the dimensions of them (30 samples) are shown in Figure 1. Two ends of the tensile specimen are, respectively, clamped in the upper clamping head and the lower clamping head. The axis of the two clamping heads tends towards the same direction of the grain. The loading procedure is controlled by the displacement method at a rate of motion of a movable crosshead of 1 mm/min. A strainometer was fastened in the middle of the specimen to measure the strain over 50 mm length there. It was found that the curve of stress-strain relationships remains linear from loading to breaking when it was tensile failure. For the compressive properties, however, the stress varies linearly with the strain before the proportional point while becomes nonlinear when the stress exceeds the point.

The curve of uniaxial stress-strain relationships of PSL composites along the grain can be divided into three stages, i.e., first, the linear elasticity in tension, the linear elasticity in compression, and the nonlinear in compression, as shown in Figure 2. The nonlinear segment can be simulated via a second-order polynomial. Hence, the uniaxial longitudinal stress-strain relationships of the PSB composites can be represented as a piecewise function as shown in the following equation:

$$\sigma(\varepsilon) = \begin{cases} l_1(\varepsilon + l_2)^2 + l_3, & \varepsilon_{ce} \le \varepsilon \le \varepsilon_{cu}, \\ E\varepsilon, & -\varepsilon_{tu} \le \varepsilon \le \varepsilon_{ce}, \end{cases} \quad (1)$$

where E is the elastic modulus of PSL material along parallel to grain direction (MPa). σ_{cu}, σ_{ce}, and σ_{tu} are the stress at maximum compressive loading, proportional compressive limit, and ultimate tensile limit, respectively. ε_{tu} and ε_{cu} are the maximum strain in the tensile and compressive loading, respectively ($\mu\varepsilon$), and ε_{ce} is the compressive strain at the point of proportional limit ($\mu\varepsilon$). l_1, l_2, and l_3 are coefficients.

Considering the continuum and compatible conditions of the stress-strain curves, the coefficients can be expressed as follows:

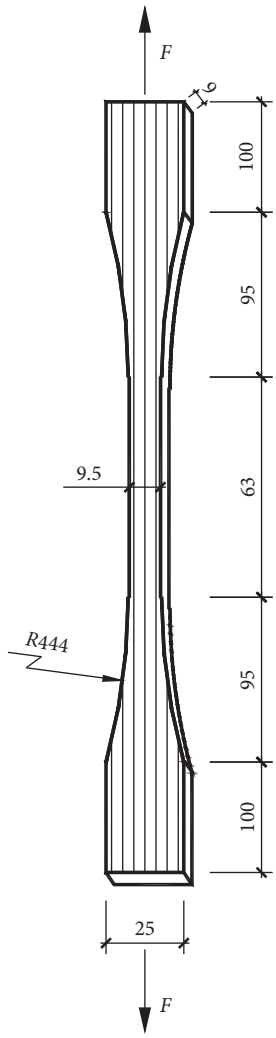

Figure 1: Dimension of tensile specimens (unit: mm).

$$\sigma\left(\varepsilon_{ce}\right) = l_1\left(\varepsilon_{ce}^2 + 2l_2\varepsilon_{ce} + l_2^2\right) + l_3 = \sigma_{ce}, \tag{2a}$$

$$\sigma\left(\varepsilon_{cu}\right) = l_1\left(\varepsilon_{cu}^2 + 2l_2\varepsilon_{cu} + l_2^2\right) + l_3 = \sigma_{cu}, \tag{2b}$$

$$\frac{\mathrm{d}\sigma\left(\varepsilon_{cu}\right)}{\mathrm{d}\varepsilon} = 2l_1\left(\varepsilon_{cu} + l_2\right) = 0. \tag{2c}$$

According to equations (2a)–(2c), the coefficients can be obtained as follows:

$$l_1 = -\frac{\sigma_{cu} - \sigma_{ce}}{\left(\varepsilon_{cu} - \varepsilon_{ce}\right)^2}, \tag{3a}$$

$$l_2 = -\varepsilon_{cu}, \tag{3b}$$

$$l_3 = \sigma_{cu}, \tag{3c}$$

Figure 2 illustrates the stress-strain relationships obtained by analyzing the test results. Table 1 gives the test results.

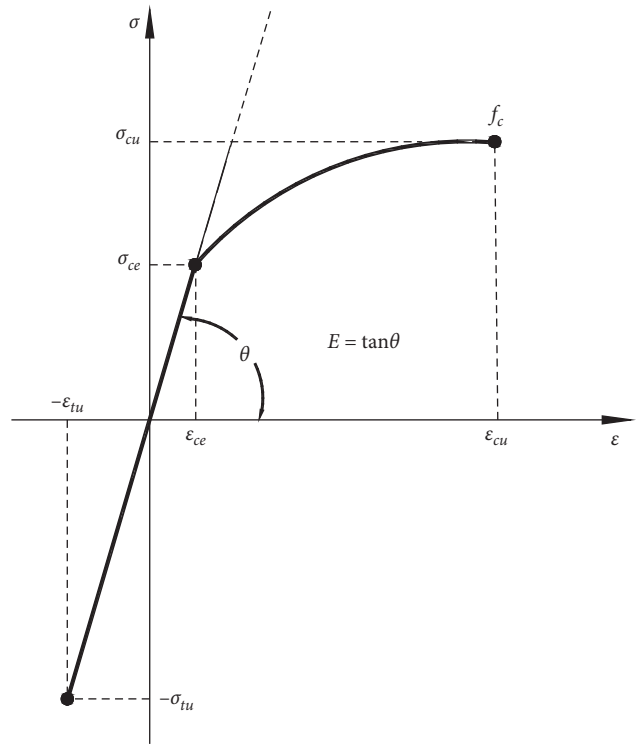

Figure 2: Uniaxial stress-strain relationships.

3. Analytical Model

3.1. Load-Carrying Capacity. The methodology for analyzing the nonlinear bending of the PSL beam in this research is based on Euler's beam theory and Huang's method [13, 15–17]. Fibres above and under the neutral axis were longitudinally compressed and tensioned, respectively, in case the beam was bent. The following assumptions were adopted: (1) cross section of the PSL beam above and under the neutral axis remains linear plane before and after loading; (2) the fibres in the top of the section reached maximum compressive stress and those in the bottom of the section reached ultimate tensile stress when the beam failed. Based on the above assumptions, the strain and stress diagram over the damage section shows a linear relationship; however, the distribution of compressive stress possessed nonlinear characteristics when stresses are beyond the compressive proportional limit, as shown in Figure 3. Thus, the stress distribution of the critical cross section of beam in moment span may be divided into three zones along the height of the PSL beam, i.e., plastic compressive zone (PCZ), elastic compressive zone (ECZ), and tensile zone (TZ). The upper part of the beam cross section is the PCZ, in which the stresses of the fibres in the upper outmost surface are equal to the ultimate compressive strength, σ_{cu}, when the beam fails. The area between the PCZ and the neutral axis is ECZ, in which the stresses and the strains of the fibres are equal to the compressive proportional limit, σ_{ce} and ε_{ce}, respectively, in the interface surface between PCZ and TCZ. The area under the neutral axis is the TZ, in which the stresses and strains of the fibres in the lower outmost surface are equal to

Table 1: Mechanical parameters of the PSL specimen.

Parameters	Proportional limit		Ultimate limit		Modulus (MPa)
	Strain ($\mu\varepsilon$)	Stress (MPa)	Strain ($\mu\varepsilon$)	Stress (MPa)	
Tension	—	—	1200	80.0	1650
Compression	2800	55.0	5700	62.5	

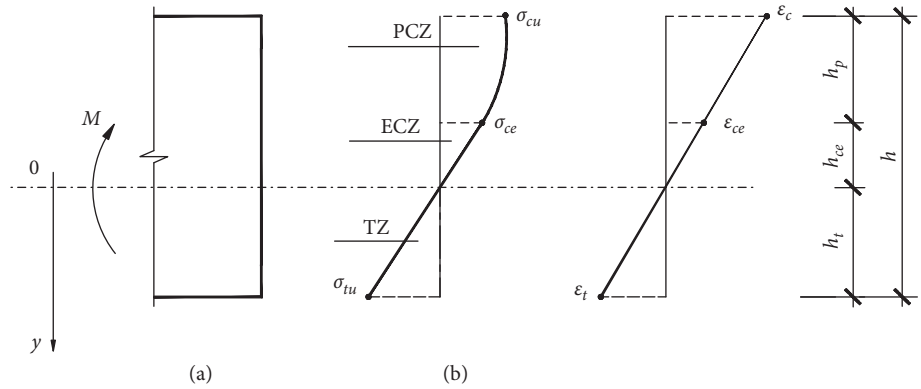

Figure 3: Diagrams of the stress and strain over the moment section. (a) stress diagram and (b) strain diagram.

the ultimate tensile strength, σ_{tu} and ε_{tu}, respectively, when the beam broken. Thus, the force equilibrium in the longitudinal direction of the beam over the section yields

$$b\int_{-(h_p+h_{ce})}^{h_t}\sigma(y)\mathrm{d}y = 0. \tag{4}$$

where b is the width of the section. Because the compressive damage mechanism is very complex, it is impossible to functionally describe the actual stress distribution over the depth of the plastic zone.

Therefore, to exactly calculate the actual nonlinear stress distribution by using equation (4) is not practical. However, the actual nonlinear stress distribution may be approximately evaluated via equation (4) since the stress distribution over the depth of the plastic zone may be prescribed in accordance with the first term of equation (1) and the stress of outside fiber of the plastic zone is ε_{cu}. Thus, the stress with respect to the coordinate, y, over the depth of the plastic zone may be expressed as

$$\varepsilon(y) = -\frac{\varepsilon_{cu}-\varepsilon_{ce}}{h_p}y, \tag{5}$$

in which $-(h_{ce}+h_p) \le y \le -h_{ce}$ should be satisfied. Substituting for $\varepsilon(y)$ from equation (5) and for coefficients l_1, l_2, and l_3 from equations (3a)–(3c) into the first term of equation (1), the stress with respect to coordinate, y, over the depth of plastic zone, the actual nonlinear stress distribution can be obtained.

Therefore, the stress distribution with respect to the coordinate y over the damaged cross section can be expressed as

$$\sigma(y) = \begin{cases} l_1(sy+l_2)^2 + l_3, & -(h_{ce}+h_p) \le y \le -h_{ce}, \\ Es|y|, & -h_{ce} \le y \le h_t, \end{cases} \tag{6}$$

in which s is the curvature of the beam at moment section. h_p, h_{ce}, and h_t are the depths of plastic, compressive, and tensile zones, respectively. Referring to Figure 3(b) and taking the geometrical relationships into account lead to

$$\begin{aligned} h_t\varepsilon_{ce} &= \varepsilon_t h_{ce}, \\ \sigma_t = E\varepsilon_t \text{ and } \sigma_{ce} &= E\varepsilon_{ce}, \end{aligned} \tag{7}$$

where σ_t is the tensile stress of the fibres in the outside of the tensile zone. Substituting for $\sigma(y)$ from equation (6) gives

$$\int_{-(h_p+h_{ce})}^{-h_{ce}}\left[l_1(sy+l_2)^2+l_3\right]\mathrm{d}y + \int_{-h_{ce}}^{h_t}Es|y|\mathrm{d}y = 0, \tag{8}$$

where

$$s = -\frac{\varepsilon_{cu}-\varepsilon_{ce}}{h_p}. \tag{9}$$

Also, taking the geometric relations of the zones over the section into account and referring to Figure 3(b) lead to

$$h_p + h_{ce} + h_t = h, \tag{10}$$

where h is the depth of the section. From equations (7), (8), and (10), each depth of plastic, elastic compressive, and tensile zones can be obtained as follows:

$$h_p = \left(\sigma_{ce}^2 - \sigma_t^2\right)h\beta, \tag{11a}$$

$$h_{ce} = 2\sigma_{ce}h\left[\frac{l_1}{3}\left(\varepsilon_{cu}^2+\varepsilon_{cu}\varepsilon_{ce}+\varepsilon_{ce}^2\right)+\frac{l_2}{2}\left(\varepsilon_{cu}+\varepsilon_{ce}\right)+l_3\right]\beta, \tag{11b}$$

$$h_t = 2\sigma_t h\left[\frac{l_1}{3}\left(\varepsilon_{cu}^2+\varepsilon_{cu}\varepsilon_{ce}+\varepsilon_{ce}^2\right)+\frac{l_2}{2}\left(\varepsilon_{cu}+\varepsilon_{ce}\right)+l_3\right]\beta, \tag{11c}$$

where

$$\beta = \frac{1}{\left\{\sigma_{ce}^2 + (2/\sigma_{ce})\left[(l_1/3)\left(\varepsilon_{cu}^2 + \varepsilon_{cu}\varepsilon_{ce} + \varepsilon_{ce}^2\right) + (l_2/2)(\varepsilon_{cu} + \varepsilon_{ce}) + l_3\right]\left(\sigma_{ce}^2 + \sigma_{ce}\sigma_t\right) - \sigma_t^2\right\}}. \tag{12}$$

The moment at the section can be calculated by

$$M = b\int_{-(h_p+h_{ce})}^{h_t} \sigma(y)y\mathrm{d}y. \tag{13}$$

According to the plane assumption over the bending section cut, the strain at any point with respect to the coordinate, y, can be expressed as $\varepsilon(y) = sy$. Substituting $\varepsilon(y)$ into the first term of equation (6), the strain variation with respect to the coordinate, y, can be analytically obtained. Consequently, substituting for $\sigma(y)$ from equation (6) yields

$$M = b\left\{\int_{-(h_p+h_{ce})}^{-h_{ce}} \left[l_1(sy + l_2)^2 + l_3\right]y\mathrm{d}y + \int_{-h_{ce}}^{h_t} Es|y|^2\mathrm{d}y\right\}. \tag{14}$$

Finally, the function of the moment yielded by compressive force in the plastic zone can be expressed as

$$M = \frac{1}{4}bl_1s^2\left[\left(h_p + h_{ce}\right)^4 - h_{ce}^4\right] + \frac{1}{3}bl_2s\left[\left(h_p + h_{ce}\right)^3 - h_{ce}^3\right] + \frac{1}{2}bl_3\left[\left(h_p + h_{ce}\right)^2 - h_{ce}^2\right] + \frac{bEs}{3}\left(h_{ce}^3 + h_t^3\right), \tag{15}$$

where s represents the curvature of the beam working in the nonlinear state. Considering the geometric relations between the strain, ε, and the curvature over the moment section, it can be obtained that $\sigma_{ce} = Esh_{ce}$. Deriving h_{ce} from this equation and substituting h_{ce} into equation (11b) yield

$$s = \frac{1}{\left\{2Eh\left[(l_1/3)\left(\varepsilon_{cu}^2 + \varepsilon_{cu}\varepsilon_{ce} + \varepsilon_{ce}^2\right) + (l_2/2)(\varepsilon_{cu} + \varepsilon_{ce}) + l_3\right]\beta\right\}}. \tag{16}$$

In the case of critical condition, on which the stress on the top surface of the beam is just reached the proportional limit, σ_{ce}, and the whole section remains in the elastic state, the depth of the plastic zone of the section, $h_p = 0$, and the plastic moment are zero. Therefore, it can be obtained from equation (11a) that

$$\sigma_t^2 - \sigma_{ce}^2 = 0. \tag{17}$$

Deriving σ_t from this equation and substituting σ_t into equations (11b) and (11c) yield the depths of compressive and tension zones on the critical condition, respectively, which are expressed as follows:

$$h_{ce} = h_t = \frac{h}{2}. \tag{18}$$

Let s_c denote the curvature of the critical state, and the geometric relation between the strains and the curvature of the section leads to $\sigma_{ce} = Es_ch_{ce}$. Substituting h_{ce} from equation (18) into this equation gives the curvature s_c, on the critical condition:

$$s_c = \frac{2\sigma_{ce}}{Eh}. \tag{19}$$

Let the plastic moment be zero, and substituting for h_{ce} and h_t from equation (18) into (13) and then replacing s in equation (13) by s_c from equation (19), the moment of the elastic limit of the beam, M_c, can be obtained:

$$M_c = \frac{\sigma_{ce}bh^2}{6}. \tag{20}$$

3.2. Deformation. Referring to Figure 4, the deflection analysis of the beam can be implemented by using the symmetrical half structure. Assume that the moment span is in nonlinear state and the curvature of it is s, while the shear span remains in the elastic state and the curvature of it is s_c. Hence, the differential equation governing the deformation of the beam can be expressed as

$$\frac{\mathrm{d}^2y}{\mathrm{d}x^2} = \begin{cases} -\dfrac{Fx}{2\mathrm{EI}}, & 0 \le x \le m, \\ -s, & m \le x \le \dfrac{l}{2}. \end{cases} \tag{21}$$

The boundary and continuum conditions can be expressed as

$$y(0) = 0, \quad y^+(m) = y^-(m), \quad \frac{\mathrm{d}y^+(m)}{\mathrm{d}x} = \frac{\mathrm{d}y^-(m)}{\mathrm{d}x} \text{ and } \frac{\mathrm{d}y(l/2)}{\mathrm{d}x} = 0. \tag{22}$$

From equations (21) and (22), the deformation equations of the beam with respect to the coordinate x can be obtained, which were expressed as follows:

$$y = \begin{cases} -\dfrac{F}{4\mathrm{EI}}\left[\dfrac{1}{3}x^3 + (m - l)mx\right], & 0 \le x \le m, \\ -\dfrac{1}{2}s\left(x^2 - lx + \dfrac{1}{3}m^2\right), & m \le x \le \dfrac{l}{2}. \end{cases} \tag{23}$$

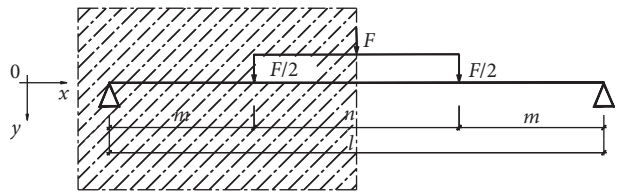

Figure 4: Deflection analysis model.

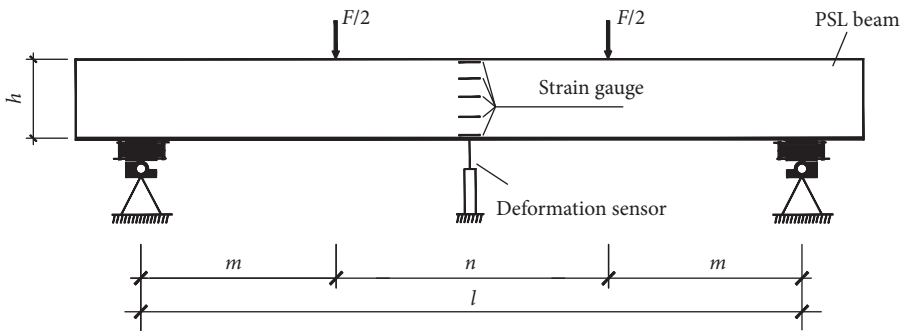

Figure 5: 4-point bending test.

where $I = (bh^3/12)$. If the moment span works in the elastic state, considering the continuum condition at the section $x = m$ yields the curvature of this segment

$$s_m = \frac{Fm}{2EI}. \tag{24}$$

Replacing s in equation (23) with s_m in equation (24) gives the curvature equation of the beam

$$y = \begin{cases} -\dfrac{F}{4EI}\left[\dfrac{1}{3}x^3 + (m-l)mx\right], & 0 \le x \le m, \\ -\dfrac{Fm}{4EI}\left(x^2 - lx + \dfrac{1}{3}m^2\right), & m \le x \le \dfrac{l}{2}. \end{cases} \tag{25}$$

According to Huang's method [18], the deformation at midspan of the PSL beam can be expressed as

$$v = -\frac{Fm}{4EI}\left(\frac{1}{3}m^2 - \frac{1}{4}l^2\right) + \frac{1}{4}\varepsilon_t h\left(\frac{1}{h_t} - \frac{2}{h}\right), \tag{26}$$

where $v$is the deformation at midspan of the PSL beam.

4. Test Validation

In order to validate the analytical model developed above, load-carrying capacities and deformations of three PSL beams were analyzed by the model above and by experiments. 4-point bending test was adopted to investigate the bending performances of the PSL beam. Test method was referred to ASTM D198-09 [19]. The section dimensions of the samples are 60 mm in width and 90 mm in depth. The test span is 1660 mm. Beams were supported by a pair of metal roller which has sufficient stiffness and provides unrestricted longitudinal deformation and rotation of beam at reactions due to loading. The total load on the beam was symmetrically and monotonously applied at two points equidistant from the reactions through a pair of blocks, which are extending entirely across the beam width and may rotate the axis perpendicular to the span without restraint. The test setup is shown in Figure 5. A deformation sensor was installed under the middle span of the beam to measure the vertical displacement there. The total load of the beam and the vertical displacement in the middle span were simultaneously recorded. The failure mode is shown in Figure 6. Local buckling at the top and tensile broken at the bottom of the beam can be observed. This is in agreement with the assumption in Section 3. Figure 7 compares the load-deflection curves between experimental results and calculations using the theoretical model, of which the mechanical parameters of PSL were taken from Table 1. Well agreement can be observed. This implies that the model developed in this paper for analyzing the bending of PSL beams is feasible.

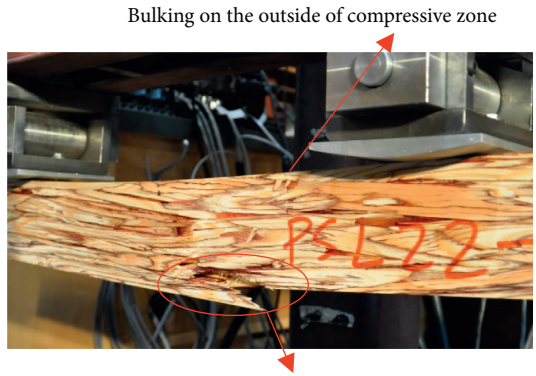

Figure 6: Damage mode of the PSL beam.

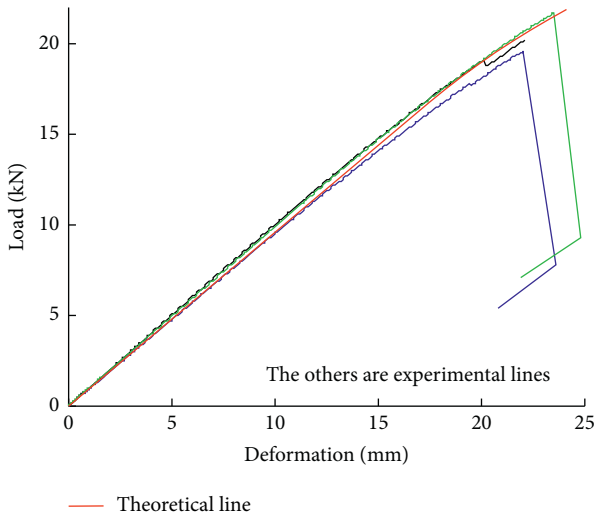

Figure 7: Comparison of the load-deflection curves of PSL beams obtained by test and analysis.

5. Conclusions

Based on the theories of mechanics of composite, PSL was treated as a transversely isotropic composite, and this paper aimed at studying the stress-strain relationships, the failure mechanism, and the nonlinear flexural of PSL beams through the experiments and theoretical analysis. The main contents and results can be concluded as follows:

(1) The uniaxial tensile and compressive properties in parallel to grain direction were studied by experiments. Failure mechanisms and the stress-strain relationship of each stress state were investigated. It was found that the tensile failure of PSL in parallel to grain direction presents the progressive process and higher strength, and the tensile stress-strain relationship exhibits linear behavior. The compressive strength of the material shows lower strength and brittle behavior, and then the compressive stress-strain relationship exhibits nonlinear characteristics.

(2) 4-point bending tests for PSL beams were carried out to investigate the flexural behaviors and the damage mechanism of them. 3 stages of bending failure of PSL beams under pure bending loading can be observed. The first is the perfect elastic bending stage, and the beams were in the elastic state when the loading is less than the proportional limit. The second is the nonlinear hardening stage, i.e., when the loading exceeded the proportional limit, part of fibres in the compressive zone in the critical section came into a nonlinear state, the inelastic compressive zone was gradually expanding towards the neutral axis, and the stiffness of PSL beams was continuously degraded with the augment of loading. The last one is the failure stage, i.e., when the depth of the inelastic compressive zone reached the ultimate value, the fibres in the outer surface of the compressive zone were bulking and those in the outer surface of the tensile zone were broken. Hence, the PSL beam was failed.

(3) A theoretical model to evaluate the loading capacity and the deflection of PSL beams was proposed based on experimental studies and theoretical analysis. Well agreements were achieved between the results obtained by using the proposed model and those obtained by experiments.

Data Availability

The data used to support the findings of this study are available from the corresponding author upon request.

Conflicts of Interest

The authors declare that there are no conflicts of interest regarding the publication of this paper.

Acknowledgments

The research was supported by the National Science Fund of China (no. 51978338), the Priority Academic Program Development of Jiangsu Higher Education Institutions (PAPD), and the Doctorate Fellowship Foundation of Nanjing Forestry University.

References

[1] P. Sukontasukkul, F. Lam, and S. Mindess, "Fracture of parallel strand lumber (PSL) under impact loading," *Materials and Structures*, vol. 33, pp. 445–449, 2000.

[2] Canadian Wood Council, *Wood Design Manual*, Canadian Wood Council, Ottawa, Canada, 2010.

[3] S. R. Arwade, R. Winans, and P. L. Clouston, "Variability of the compressive strength of parallel strand lumber," *Journal of Engineering Mechanics*, vol. 136, no. 4, pp. 405–412, 2010.

[4] V. Yadama, M. P. Wolcott, and L. V. Smith, "Elastic properties of wood-strand composites with undulating strands," *Composites Part A: Applied Science and Manufacturing*, vol. 37, no. 3, pp. 385–392, 2006.

[5] P. L. Clouston and F. Lam, "A stochastic plasticity approach to strength modeling of strand-based wood composites," *Composites Science and Technology*, vol. 62, no. 10-11, pp. 1381–1395, 2002.

[6] X. Song and F. Lam, "Laterally braced wood beam-columns subjected to biaxial eccentric loading," *Computers & Structures*, vol. 87, no. 17-18, pp. 1058–1066, 2009.

[7] M. Naghipour, M. Nematzadeh, and Q. Yahyazadeh, "Analytical and experimental study on flexural performance of WPC-FRP beams," *Construction and Building Materials*, vol. 25, no. 2, pp. 829–837, 2011.

[8] A. Borri, M. Corradi, and A. Grazini, "A method for flexural reinforcement of old wood beams with CFRP materials," *Composites Part B: Engineering*, vol. 36, no. 2, pp. 143–153, 2005.

[9] Y.-F. Li, Y.-M. Xie, and M.-J. Tsai, "Enhancement of the flexural performance of retrofitted wood beams using CFRP composite sheets," *Construction and Building Materials*, vol. 23, no. 1, pp. 411–422, 2009.

[10] I. M. M. Bazan, "Ultimate bending strength of timber beams," Doctoral dissertation, Thesis presented to Nova Scotia Technological College, Halifax, Canada, 1980.
[11] M. R. O'Halloran, "Curvilinear stress strain relationship for wood in compression," Doctoral dissertation, Thesis presented to Colorado State University, Fort Collins, Colorado, 1973.
[12] A. Ylinen, "A method of determining the buckling stress and the required cross sectional area for centrally loaded straight columns in elastic and inelastic range," *IABSA Publications*, vol. 16, pp. 529–549, 1956.
[13] D. Huang, A. Zhou, and Y. Bian, "Experimental and analytical study on the nonlinear bending of parallel strand bamboo beams," *Construction and Building Materials*, vol. 44, pp. 585–592, 2013.
[14] American Society for Testing and Materials (ASTM), *Standard Test Method for Small Clear Specimens for Timber: D143-09*, American Society for Testing and Materials, West Conshohocken, PA, USA, 2009.
[15] A. Zhou, D. Huang, H. Li, and Y. Su, "Hybrid approach to determine the mechanical parameters of fibers and matrixes of bamboo," *Construction and Building Materials*, vol. 35, pp. 191–196, 2012.
[16] D. Huang, Y. Bian, A. Zhou, and B. Sheng, "Experimental study on stress-strain relationships and failure mechanisms of parallel strand bamboo made from phyllostachys," *Construction and Building Materials*, vol. 77, pp. 130–138, 2015.
[17] B. D. Zakic, "Inelastic bending of wood beams," in *Proceedings of ASCE*, vol. 99, no. ST10, pp. 2079–2095, 1974.
[18] Z. Huang, Z. Chen, D. Huang, and A. Zhou, "The ultimate load-carrying capacity and deformation of laminated bamboo hollow decks: experimental investigation and inelastic analysis," *Construction and Building Materials*, vol. 117, pp. 190–197, 2016.
[19] American Society for Testing and Materials (ASTM), *Standard Test Method of Static Texts of Lumber in Structural Size: D198-09*, American Society for Testing and Materials, West Conshohocken, PA, USA, 2009.

Hindawi
Advances in Civil Engineering
Volume 2021, Article ID 6683589, 10 pages
https://doi.org/10.1155/2021/6683589

Research Article

Experimental Investigation on the Load-Carrying Capacity of Steel-to-Laminated Bamboo Dowel Connection I: Single Fastener with Slotted-In Steel Plate under Tension

Zhaoyan Cui,[1] **Liuhui Tu**,[2] **Ming Xu**,[2] **Zhongfan Chen**,[2] **and Qingfeng Xu**[3]

[1]*National Engineering Research Center of Biomaterials, Nanjing Forestry University, Nanjing 210037, China*
[2]*Key Laboratory of Concrete and Prestressed Concrete Structures of Ministry of Education, Southeast University, 02, Southeast University Road, Nanjing 211189, China*
[3]*Shanghai Key Laboratory of Engineering Structure Safety, SRIBS, Shanghai 200032, China*

Correspondence should be addressed to Ming Xu; xuming@seu.edu.cn

Received 2 November 2020; Revised 22 December 2020; Accepted 31 January 2021; Published 16 February 2021

Academic Editor: Filippo Ubertini

The dowel-type connection is widely applied in timber and bamboo structures. It is ambiguous regarding the calculation method of engineered bamboo connections completely referred to the timber design codes. The steel-to-laminated bamboo dowel connections with slotted-in steel plate tests were conducted to investigate the mechanical performance under tension based on the ASTM-D5652-15. The effects of the thickness, dowel diameter, and end distance on the yield load, ultimate load, initial stiffness, and ductility of the connections were studied. The difference in the yield load for different end distance is negligible. With the same thickness of the connections, the lower the thickness to dowel diameter, the larger the load-carrying capacity. The three typical yield modes and corresponding load-displacement curves of the connections are observed. By considering the rigid-plastic model, the theoretical equation for the connections is proposed and proven to fit well with the experimental results. It presents a better prediction for the load-carrying capacity of steel-to-laminated bamboo dowel connections with slotted-in steel plate.

1. Introduction

Due to the advantages of a simple manufacturing process, low adhesive content, and beautiful surface, laminated bamboo has a broad prospect as an engineered material in the construction industry [1, 2]. Compared with other biological structural materials, the laminated bamboo has higher tensile strength and stiffness with less variability [1], meaning that, for construction purposes, it would be a better choice than the others.

For the engineered structures, the reliability of the connections is the key to the structural design. The connection performance of laminated bamboo could directly affect the strength, life expectations, and robustness of the structure, making the relevant research extremely important. The dowel connection of the timber and bamboo structure can be divided into single-shear connection and double-shear connection from the number of shears faces of each dowel. The multishear connections can be divided into a wood-to-wood connection and a steel-to-wood connection from the different materials of the connected main and side materials, and the steel-to-wood connection includes a steel splint connection and a steel filler connection. The simple form and reliable transmission of force make the steel-to-wood connection the most important form of connections in the modern timber structures, especially those dowel-type connections with slotted-in steel plates for having no steel plate coverage and good aesthetics; and the occurrence of cracks can be easily observed to avoid potential safety hazards [3].

Researchers have explored the calculation theories and methods of wood bolt connection for years. The European yield theory was originated from Johansen [4] theory of timber connection, which set the foundation for Eurocode 5

[5]. In the United States, the design method has been changed from empirical design to method based on the yield theory since 1991. Several factors, such as the dowel diameter, the thickness to diameter ratio, and the end distance have been investigated to study the possible effect on the load-carrying capacity of the connection. Daudeville et al. [6] carried out the dowel-bearing test on the wood, indicating that the dowel diameter has an influence on the bearing strength. In a certain range, it has a positive correlation with the dowel-bearing strength, and the result is consistent with the European wood structure design specification. Solitis et al. [7] proposed the concept of thickness-to-diameter ratio in 1987 and believed that, with the same dowel diameter, the greater the thickness of the bolted joint of wood, the better the ductility. Cesar [8] pointed out in the study that when the dowel end distance to diameter ratio is less than 4, the brittle fracture is easy to occur. Doyle [9] found that an increase in the spacing of the bolts within a certain range helps to enhance the bearing capacity of the joints. The requirements on these bolted constructions directly affect the form of damage to the joints. The loading direction has also been found to have a significant effect on the performance of the connection. The failure modes of the timber loaded parallel and perpendicular to the grain are significantly different. Patel and Hindman [10] studied the bearing properties of the bolted joints in the transverse direction and found that the failure mode is related to the fracture toughness of the wood. In addition, moisture content [11] and temperature can affect the load-carrying capacity.

At present, the existing equations of the steel-to-wood connection in the national design codes and standards focus on different failure modes: Eurocode 5: design of timber structures evaluates the bearing capacity of the connection with the thickness of the side members, the dowel-bearing capacity of the material, and the diameter of the dowel. The minimum value of predictions under each failure mode is taken as the calculation result to predict the bearing capacity of the connection. Similar methods have been applied in the National Design Specification for Wood Construction in the US [12] and the Canadian Standard [13].

Although the bamboo material shares great similarities with wood at the aspect of physical and mechanical properties, the difference between the two materials is not negligible. There are relatively few studies on the engineered bamboo material. Cui et al. [14] tested the bearing capacity of bolted steel-bamboo scrimber-steel connections and found that Eurocode 5 had better prediction accuracy. Hover [15] conducted an experimental study on the bolt connection of the laminated bamboo loaded parallel to the grain and analyzed its failure mechanism and bearing capacity. In general, the research on the bearing performance of laminated bamboo connections is still scarce at home and abroad, and further exploration is urgently needed.

The purpose of the study is to analyze the load-carrying capacity of the steel-to-laminated bamboo connection loaded parallel to the grain. The dowel diameter, the thickness, and the end distance of the connections have been taken into consideration. The experimental results have been compared with the existing equations, and a more accurate equation for laminated bamboo has been developed based on the analysis in the paper.

2. Materials and Test Methods

2.1. Materials. The fabrication process of the raw laminated bamboo material has been described specifically in previous research [16]. Based on the Chinese standard [17], ASTM D143-14 [18], and ASTM D5764-97a [19], the physical and mechanical properties of the laminated bamboo have been tested. The mean values of its air-dry and oven-dry density are 609 kg/m^3 and 592 kg/m^3 with a moisture content of 5.9%. The compressive strength is 59.63 MPa parallel to the grain with the MOE of 12087 MPa. The corresponding tensile strength is 104.16 MPa with the MOE of 10820, and the shear strength is 17.26 MPa. The tensile strength of laminated bamboo perpendicular to grain is 3.35 MPa. The yield strength of the dowel is 480 MPa and the tensile strength is 600 MPa. The length of the unthreaded area in the middle of the screw was not less than 120 mm. The steel plate is Q345 grade steel with a thickness of 10 mm; and the thickness of the groove is 12 mm.

2.2. The Test Specimens and Method. As mentioned before, many factors may influence the bearing capacity of the connections. In this study, the dowel diameter, the thickness, and end distance are selected as reference factors. The test set-up and front and lateral views of the connections are shown in Figure 1. The length of laminated bamboo specimen is 900 mm, and the width is 120 mm. It is noted that the end distances of the connections are 5*D*, 6*D*, 7*D*, and 8*D* except that the control group is 7*D*. The detailed parameters of different groups are shown in Table 1. Each test was repeated 3 times. The test method was based on ASTM-D5652-15 [20] and was appropriately adjusted in combination with the test conditions. The test was carried out with a 100-ton MTS Fatigue testing machine. As shown in Figures 1(b) and 1(c), 1 denotes the MTS actuator, 2 the fixed device for the steel plate, 3 the steel plate, 4 the displacement transducer support, 5 the dowel, 6 the displacement transducer roof, 7 the fixed device for the specimens, and 8 the MTS ground anchor. After preloading to eliminate the effect of the initial gap and deformation, the specimens were subjected to monotonic uniform loading in the tension direction with displacement control. The loading rate was 1 mm/min. The loading process stopped when significant damage appeared or the bearing capacity dropped below 80% of the maximum load. The load of the connections was measured by the test set-up. The displacement was measured by two displacement transducers on both sides.

The average value measured by the two displacement meters was chosen as the relative displacement between the dowel and the laminated bamboo, and the load data are combined to generate the load-displacement curves. A straight line was fit to the initial linear portion of the load-deformation curve. The line was offset by a deformation equal to 5% of the fastener diameter. The load at which the

offset line intersects the load-deformation curve was selected as the yield load, F_y. The elastic stiffness, K_1, is calculated by the slope of the initial linear portion of the load-deformation curve. The postyield stiffness, K_2, is calculated by the tangent of the load-displacement curve through the intersection of the initial linear portion of the load-deformation curve and the horizontal line through the yield load.

3. Results and Analysis

3.1. The Failure Modes and Load-Displacement Curves of the Connections. According to the Eurocode yield theory, there are three yield modes for double-shear connections in Figure 2. Mode I represents the case where fasteners do not bend, and wood fibers crushing occurres beneath the dowel without through cracks. Mode II represents the case where fasteners yield in bending at one plastic hinge point per shear plane, with bearing-dominated yield of wood fibers in contact with the fasteners in side member(s), respectively. Mode III represents the case where fasteners yield in bending at two plastic hinge points per shear plane, with the limited localized crushing of wood fibers near the shear plane(s).

As shown in Figure 3, all of the three yield modes of the dowels occur in the connections. When the thickness of side members is small and the thickness to diameter ratio is also small, Mode I is prone to occur, for example, T2-D1-L1. It is mainly because the bending strength of the dowel is larger and the shear strength of the laminated bamboo parallel to grain is lower. But when the thickness to diameter ratio is large enough, Mode III occurs, specimen T1-D2-L1. It is because the bearing zones become larger and dowel bending is restrained. For the other connections, the failure modes belong to Mode II.

The failure modes of side members under the yield mode of one plastic hinge (Mode II) are mainly shear failure and splitting failure and they are accompanied by embedding failure. When the thickness of side members is small, the ductility is lower and the specimen exhibits splitting failure. As the thickness increases, the plastic displacement increases, and the dowel hole is elongated. The specimens exhibit splitting failure and embedding failure. But when the dowel diameter is larger, for example, M14 and M16, the specimens exhibit shear failure and embedding failure. When the end distance of the connections is in the range of $6D$–$8D$, the connections exhibit better ductility and embedding failure. Therefore, the sufficient end distance of the connections is essential in the design of the laminated bamboo connections.

The typical load-displacement curves of the connections are shown in Figure 4. The curves can be divided into a linear branch, a nonlinear branch within and beyond the proportional limit, and falling branch rapidly. The influences of the dowel diameter, thickness, and end distance on the mechanical properties of the connections parallel to grain were analyzed in the paper. As shown in Figure 4(a), with the dowel diameter increasing from 10 mm to 16 mm, the ultimate load, yield load, and initial stiffness increase gradually. When the dowel diameter is 10 mm, the ultimate displacement is about 20 mm and it exhibits better ductility. As the thickness increases, the ultimate load and displacement increase in Figure 4(b). When the thickness is 30 mm, the ultimate load and displacement are too small, just 27.15 kN and 2.49 mm. The ultimate displacement is close in the range of 90–120 mm. The connections have good ductility and the curve change is similar to the same diameter and thickness when the end distance is above $6D$ as shown in Figure 4(c). Therefore, an end distance of 6 to 8 dowel diameters and a thickness equal to or greater than 7 dowel diameters will provide reasonable results for laminated bamboo connections.

3.2. The Effect of Different Factors. The test results are shown in Table 2. The mean values of a series of measurements of different groups have been collected. The initial stiffness of the connections, K_1, yield displacement, Δ_y, and yield load, F_y, were obtained by the 5% diameter offset method. μ is the ductility ratio, $\mu = \Delta_u/\Delta_y$. and COV is the coefficient of variation of F_u. If the displacement at the point of intersection is larger than the ultimate displacement, the ultimate load is defined as the yield load. The ultimate load, F_u, was obtained as the load-carrying capacity of the connections.

The influences of the dowel diameter, thickness, and end distance on the yield and ultimate load, initial stiffness, and ductility ratio are compared and analyzed in Figure 5. For T1-D1-L1 as the control group, the corresponding yield and ultimate load are 32.33 kN and 50.56 kN; and the initial stiffness and ductility ratio are 43.56 kN/mm and 10.26. For the dowel diameter, with the diameter increasing from 10 mm to 16 mm, the yield and ultimate load and the initial stiffness increase gradually in Figure 5(a). But the ductility ratio slightly reduces. It is because the dowel diameter determines the bearing area between the dowel and the bamboo material but the increase of the diameter of the connections could cause the failure mode to change from combined embedding failure and splitting failure to shear failure.

As for the thickness factor, it has the most significant effect on the initial stiffness, ductility ratio, and ultimate load of the connections in Figure 5(b). As the specimen increases from 30 mm to 120 mm, the ultimate load increases rapidly from 27.15 kN to 50.56 kN and the ductility ratio increases from 1.98 to 10.26. But when the thickness of side members is in the range of 90–120 mm, the thickness variation has no significant effect on yield load. It is mainly because the failure modes are similar, and the yield mode is determined by the compressing buckling of the bamboo fiber, which belongs to the local material property and is independent of the overall size of the specimens.

When the end distance of the connections increases from $5D$ to $8D$, the shear area of side members enlarges as well, leading to the ultimate load increasing slightly. There is no obvious correlation between end distance with the yield load and initial stiffness because the yield mode depends on the material properties of the laminated bamboo. The initial stiffness is around 38–45 kN/mm. It is noted that when the end distance is 60 mm, the ductility ratio is very small, just 3.7. It should be avoided in the design of engineered bamboo

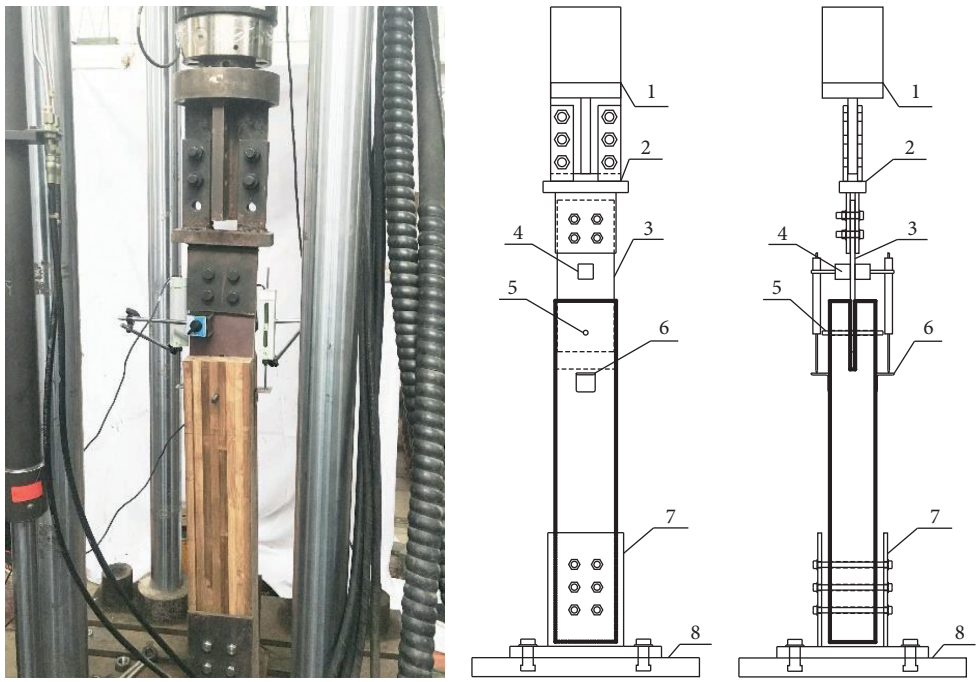

Figure 1: Test method of the connections. (a) Test set-up. (b) Front view. (c) Lateral view.

Table 1: Detailed parameters of different groups parallel to grain.

No.	t (mm)	t_s (mm)	D (mm)	l_e (mm)	γ
T1-D1-L1	120	54	12	84	4.50
T2-D1-L1	30	14	12	84	1.17
T3-D1-L1	60	29	12	84	2.42
T4-D1-L1	90	44	12	84	3.67
T1-D2-L1	120	54	10	70	5.40
T1-D3-L1	120	54	14	98	3.86
T1-D4-L1	120	54	16	112	3.38
T1-D1-L2	120	54	12	60	4.50
T1-D1-L3	120	54	12	72	4.50
T1-D1-L4	120	54	12	96	4.50

D denotes the dowel diameter, t denotes the thickness of the specimens, t_s denotes the thickness of the side members, l_e denotes the end distance, and γ denotes the thickness to diameter ratio.

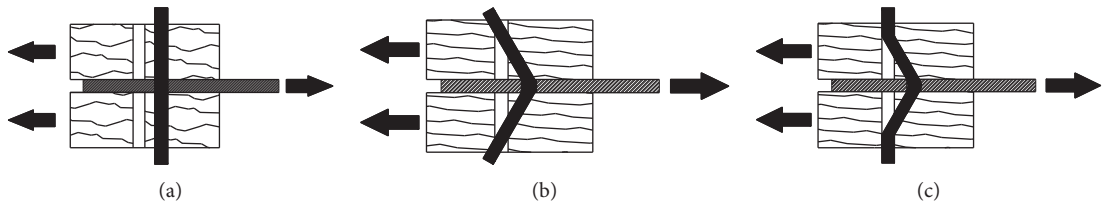

Figure 2: The yield modes of dowel-type fasteners in timber connections. (a) Mode I. (b) Mode II. (c) Mode III.

Figure 3: The yield and failure modes of the connections parallel to the grain. (a) Dowel diameter. (b) The thickness. (c) End distance.

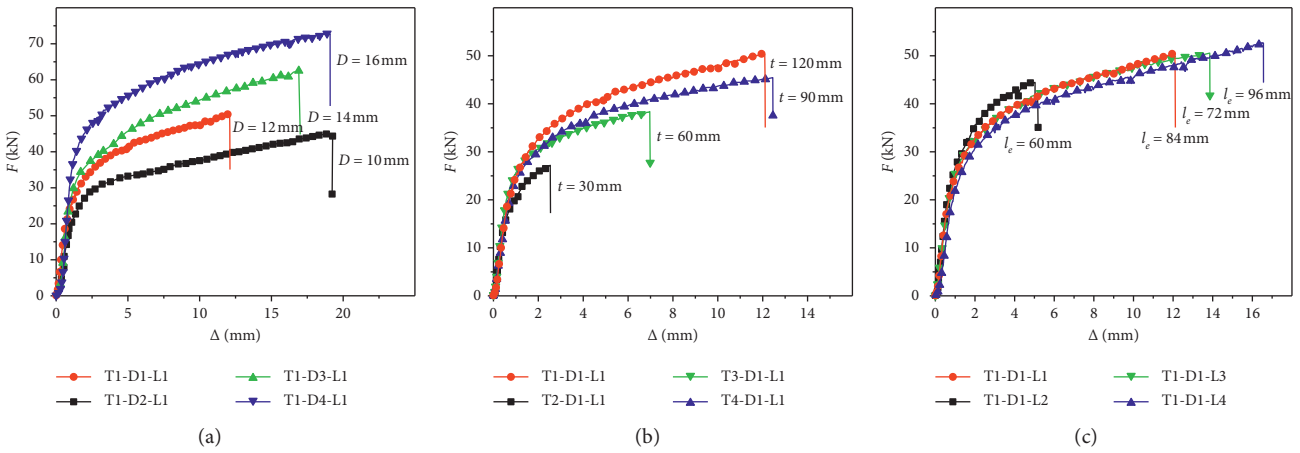

Figure 4: The load-displacement curves of the connections. (a) Dowel diameter. (b) The thickness. (c) End distance.

Table 2: The test results of the connections in different groups.

No.	γ	F_y (kN)	Δ_y (mm)	K_1(kN/mm)	F_u (kN)	Δ_u (mm)	K_2 (kN/mm)	μ
T1-D1-L1	4.50	32.33	1.17	43.56	50.56	12.05	4.77	10.30
T2-D1-L1	1.17	23.40	1.26	28.78	27.15	2.49	2.65	1.98
T3-D1-L1	2.42	25.66	1.40	34.45	38.33	6.96	3.42	4.97
T4-D1-L1	3.67	30.15	1.44	38.76	45.48	12.46	5.16	8.65
T1-D2-L1	5.40	28.89	1.98	29.56	45.08	19.00	3.95	9.60
T1-D3-L1	3.86	39.56	1.86	44.42	62.49	16.90	2.80	9.09
T1-D4-L1	3.38	48.56	2.54	53.28	72.98	18.98	3.09	7.47
T1-D1-L2	4.50	30.26	1.36	38.14	44.45	5.03	3.21	3.70
T1-D1-L3	4.50	32.16	1.26	45.56	50.83	13.32	4.81	10.57
T1-D1-L4	4.50	33.88	1.39	44.28	52.82	16.53	5.23	11.89

structures. This phenomenon proved that connections with sufficient end distance could guarantee the ductility of the connections.

4. Calculation

4.1. The Existing Calculation Methods. Regarding the load-carrying capacity and yield resistance of the connections, different national standards of timber structure have different calculation methods. In Eurocode 5 [5], the three different equations were used to calculate the corresponding failure modes based on the Eurocode yield theory; and the characteristic load-carrying capacity of the connections can be obtained as the minimum value of the three equations. It can be expressed as follows:

$$F_u = \min\begin{cases} f_{h,1,k} t_1 d, & \text{I}, \\ f_{h,1,k} t_1 d\left[\sqrt{2 + \dfrac{4M_{y,RK}}{f_{h,1,k} d t_1^2}} - 1\right], & \text{II}, \\ 2.3\sqrt{M_{y,RK} f_{h,1,k} d}, & \text{III}, \end{cases} \tag{1}$$

where F_u is the characteristic load-carrying capacity per shear plane per fastener, kN, $f_{h,1,k}$ is the embedding strength of timber members, MPa, t_1 is the thickness of side member, mm, d is the dowel diameter, mm, and $M_{y,Rk}$ is the yield moment of the dowel, N·mm.

In Canadian engineering design in the wood [13], the yield resistance of the connections rather than bearing capacity was calculated according to different failure modes. Like Eurocode 5, the minimum value of the connections was obtained to calculate the yield resistance. It can be expressed as follows:

$$F_y = \min\begin{cases} \phi_y f_1 \mathrm{d} t_1, & \text{I}, \\ \phi_y f_1 d^2\left(\sqrt{\left(f_2 f_y / 6(f_1 + f_2) f_1\right) + (t1/5\ d)}\right), & \text{II}, \\ \phi_y f_1 d^2 \sqrt{\dfrac{2 f_2 f_y}{3(f_1 + f_2) f_1}}, & \text{III}, \end{cases} \tag{2}$$

where F_y is yield resistance per shear plane per fastener, kN, f_1 is the embedding strength of the side member, MPa, f_2 is the embedding strength of the main member, MPa, t_1 is the thickness of side member, mm, d is the dowel diameter, mm, f_y is the yield strength of the dowel, MPa, and ϕ_y is resistance factor for yielding failure, 0.8. For the connection with slotted-in steel plate, f_2 can be calculated as

$$f_2 = K_{sp}\left(\frac{\phi_{\text{steel}}}{\phi_Y}\right) f_u, \tag{3}$$

where K_{sp} is the parameter, and the value of 3.0 is taken for mild steel; ϕ_{steel} is the resistance factor for steel plates in connections with dowels, 0.8 for mild steel, and f_u is the specific tensile strength of steel, MPa.

4.2. The Equation for the Laminated Bamboo. The Eurocode yield theory is originated from Johansen theory of timber connection, which set the foundation for national standards of timber structure above. The basic assumptions of the theory are as follows: the failure mode of the connections is ductile and the embedding stress-strain relationship is the ideal rigid-plastic model. Then, based on the equilibrium condition of forces and three yield modes of fasteners, the equations to express the load-carrying capacity of the connections can be determined. The stress distributions under three different yield modes in the rigid-plastic model are shown in Figure 6. The red circle denotes plastic hinge, R is the load-carrying capacity per shear plane per fastener, kN, f_e is the embedding strength of timber members, MPa, t is the thickness of side member, mm, and M_y is the yield moment of the dowel, N·mm.

The following equations of the connections under three yield modes can be developed to calculate the load-carrying capacity:

$$R_{\text{I}} = f_e \mathrm{d} t, \tag{4}$$

$$R_{\text{II}} = f_e \mathrm{d} t\left(\sqrt{2 + \frac{4M_Y}{f_e \mathrm{d} t^2}} - 1\right), \tag{5}$$

$$R_{\text{III}} = 2\sqrt{M_y f_c d}. \tag{6}$$

Regarding the yield moment of the dowel, the calculation method is different in national standards of the timber structure. In Chinese timber structure design code [21], the yield moment of the dowel is related to the yield strength and the equation can be expressed as

$$M_y = k_w W f_y, \tag{7}$$

where k_w is the ratio of the plastic section modulus to the elastic section modulus, when the plastic behavior of the dowel is fully developed, 1.7, if not, 1.4. W is the moment of section resistance in mm^3. F_y is the yield strength of the dowel in MPa.

In American design specification for wood construction, the yield moment is related to bending strength of the dowel. It can be determined based on the yield load of 5% diameter deviation method or the average of the tensile strength and yield strength. Generally, it is taken as 1.3 times of yield strength. The equation can be expressed as

$$M_y = 0.22 f_y d^3. \tag{8}$$

In Eurocode 5, the yield moment is related to tensile strength, and the equation can be expressed as

$$M_y = 0.22 f_t d^{2.6}, \tag{9}$$

where f_t is the tensile strength of the bolt in MPa.

As mentioned before, M10, M12, M14, and M16 are tested and the yield moments are 72.30 kN mm, 167.70 kN mm, 271.80 kN mm, and 394.80 kN mm, respectively. By comparison with different national standards, the results calculated in American code are the closest with experimental results; and the relative difference is less than 15%. Next, equation (8) can be substituted into equations (5) and (6) to calculate the single-

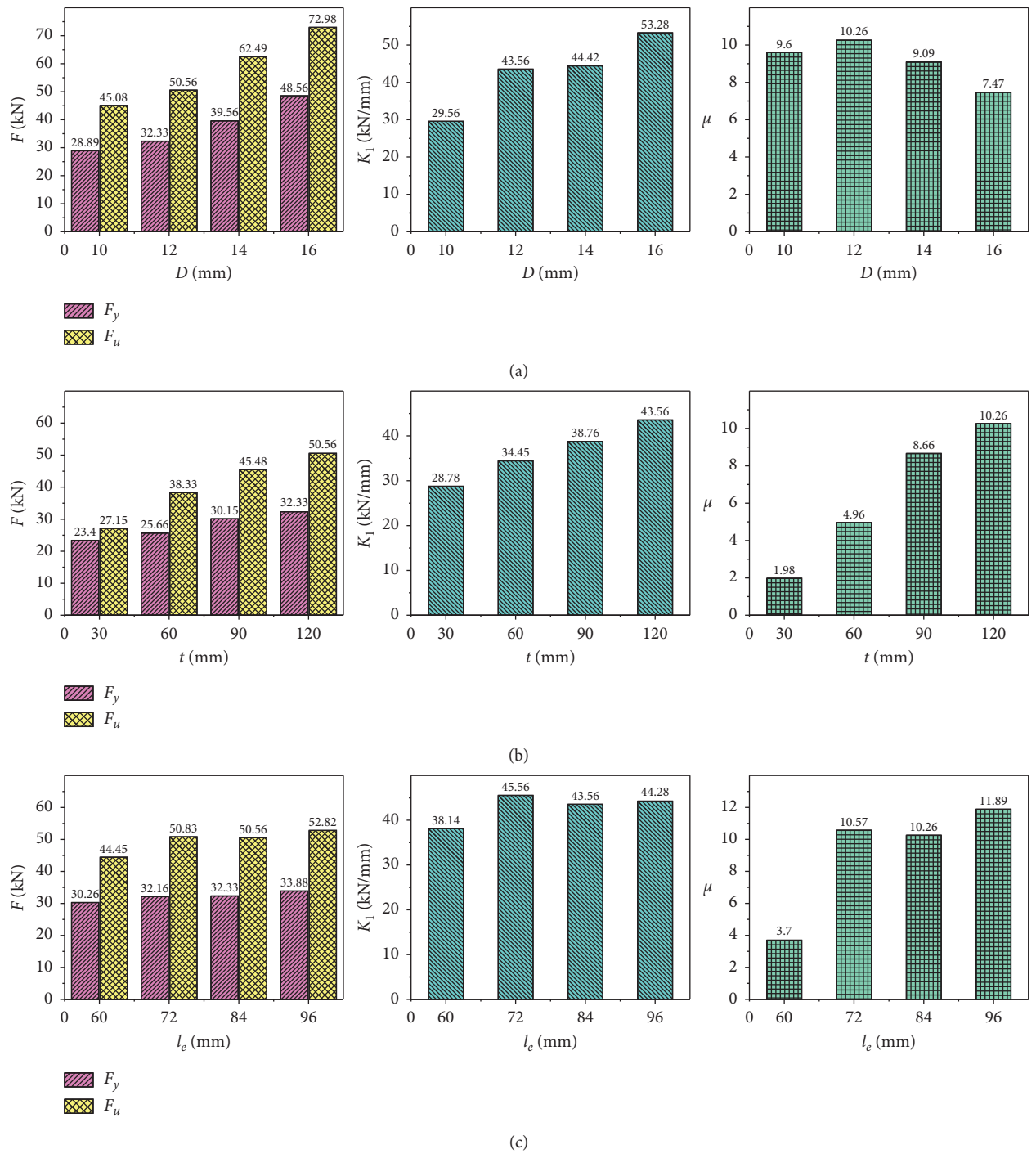

Figure 5: The effect of different factors on the mechanical parameters of the connections. (a) Dowel diameter. (b) The thickness. (c) End distance.

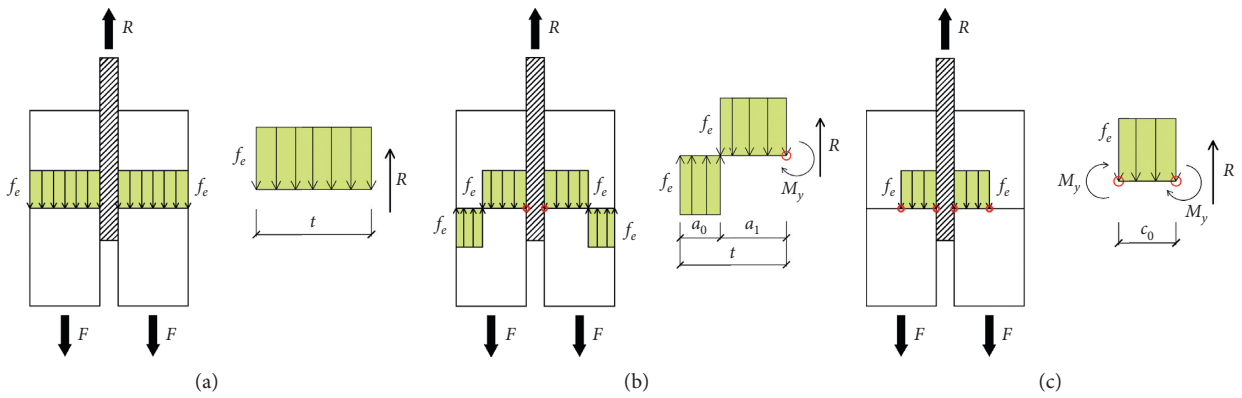

Figure 6: The stress distributions under three different yield modes. (a) Mode I. (b) Mode II. (c) Mode III.

shear bearing capacity of the connections. So, the equation can be expressed as

$$R = \min\begin{cases} f_e dt, \\ f_c dt\left(\sqrt{2+\dfrac{0.88 f_y d^2}{f_e t^2}}-1\right), \\ 0.94 d^2\sqrt{f_y f_e}. \end{cases} \tag{10}$$

According to three yield modes of boundary conditions, equation (10) can be further solved, which includes the thickness to diameter ratio interval. It can be shown in Figure 7. So, the upper and lower limits of Mode II are determined, and the equation can be expressed as

$$R = \begin{cases} f_e dt, & \dfrac{t}{d} \le 0.66\sqrt{\dfrac{f_Y}{f_e}}, \\ f_e dt\left(\sqrt{2+\dfrac{0.88 f_Y d^2}{f_e t^2}}-1\right), & 0.66\sqrt{\dfrac{f_Y}{f_e}} \le \dfrac{t}{d} \le 1.88\sqrt{\dfrac{f_Y}{f_c}}, \\ 0.94 d^2\sqrt{f_Y f_c}, & \dfrac{t}{d} \ge 1.88\sqrt{\dfrac{f_Y}{f_e}}. \end{cases} \tag{11}$$

The dowel-bearing capacity of laminated bamboo is an essential parameter to evaluate the load-carrying capacity of this kind of connection. Previous tests and researches [22, 23] suggest that the dowel-bearing capacity of the laminated bamboo parallel to grain can be expressed as

$$f_{e,\mathrm{par}} = (-0.0236\ D + 1.471) f_{c,o}, \tag{12}$$

where $f_{e,\ \mathrm{par}}$ and $f_{c,\ 0}$ stand for embedding strength and compressive strength of the laminated bamboo parallel to grain in MPa, respectively.

Based on the above equations, the theoretical and experimental results of load-carrying capacity and failure modes are shown in Table 3. Compared with the ultimate load, the theoretical results are conservative but the predicted failure modes are accurate. In order to obtain an accurate solution of the load-carrying capacity of steel-to-laminated bamboo dowel connections with slotted-in steel plate, the formulas would need further discussion and optimized analysis. The modified coefficient C_g can be introduced and combined with equation (11) to predict the load-carrying capacity of the connections. For further analysis, the modified coefficient C_g is obtained to evaluate three yield modes. The corresponding values are 1.14 in Mode I, 1.08 in Mode II, and 1.50 in Mode III. When the connection occurs, Mode III, the modified coefficient is the largest. Through the previous analysis, when the end distance of the connections is 6 to 8 dowel diameters, they exhibit better ductility and bearing capacity. Plus, the effect of end distance on the bearing capacity of the connections is not considered in the calculation method. The sufficient end distance could guarantee the accuracy of the results and structural safety. It is noted that, considering the limited number of the connections, the modified coefficient

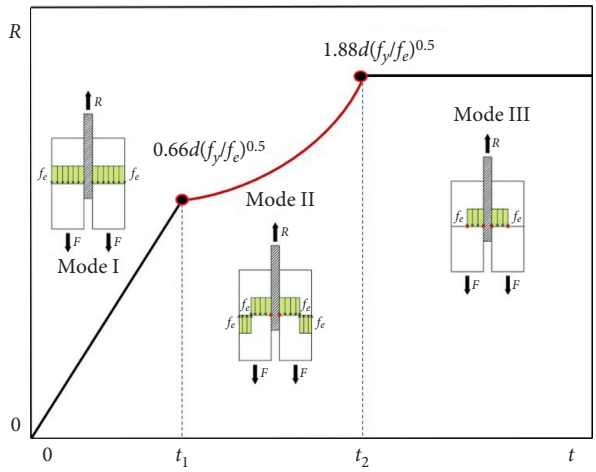

Figure 7: The boundary conditions of the load-carrying capacity of the connections.

Table 3: The comparison of the load-carrying capacity of the connections.

No.	Experimental results		Theoretical results		C_g
	F_u (kN)	Yield mode	R (kN)	Yield mode	
T1-D1-L1	58.59	II	46.95	II	1.08
T2-D1-L1	21.15	I	23.80	I	1.14
T3-D1-L1	30.33	II	35.90	II	1.07
T4-D1-L1	40.45	II	41.77	II	1.09
T1-D2-L1	48.08	III	29.97	III	1.50
T1-D3-L1	62.49	II	56.54	II	1.11
T1-D4-L1	72.98	II	67.32	II	1.08

suggested in the paper needs to be further verified. To sum up, the modified equation has better prediction and safety for the steel-to-laminated bamboo dowel connection with slotted-in steel plate.

5. Conclusion

The study investigated the load-carrying performance of one dowel-type steel-to-bamboo connection with a slotted-in steel plate. The effects of dowel diameter, thickness, and end distance on the yield load, the elastic stiffness, the ultimate load, the plastic stiffness, and the ductility rate of the connections have been studied. The following conclusions can be drawn:

(1) The typical load-displacement curves and yield modes of the connections parallel to the grain have been studied. The failure modes of side members are mainly shear failure and splitting failure, and they are accompanied by embedding failure. As for the dowel, the one-hinge yield mode has been witnessed the most.

(2) The influence of different factors on the load-carrying capacity of the connections has been analyzed as well. The dowel diameter significantly influences the yield and ultimate load and the initial stiffness. When the thickness of side members is in the range of 90–120 mm, the thickness variation has no significant effect on yield load. As for the end distance, when it is in the range of $6D$–$8D$, the connections exhibit better ductility and embedding failure.

(3) Compared with experimental results, the theoretical results are conservative but the predicted failure modes are accurate. Further, the modified coefficient is introduced and combined with the theoretical equation to predict the load-carrying capacity of the connections, which has better prediction and safety for the steel-to-laminated bamboo dowel connection with slotted-in steel plate.

Data Availability

The data used to support the findings of this study are available from the corresponding author upon request.

Conflicts of Interest

The authors declare that they have no conflicts of interest.

Acknowledgments

This research was supported by the National Natural Science Foundation of China (NSFC) (51778299) and Open Fund of Shanghai Key Laboratory of Engineering Structure Safety (2019-KF05).

References

[1] A. Sinha, D. Way, and S. Mlasko, "Structural performance of glued laminated bamboo beams," *Journal of Structural Engineering*, vol. 140, no. 1, Article ID 04013021, 2013.

[2] Y. Xiao and J. Ma, "Fire simulation test and analysis of laminated bamboo frame building," *Construction and Building Materials*, vol. 34, no. 34, pp. 257–266, 2012.

[3] J. Fueyo, M. Dominguez, J. A. Cabezas et al., "Design of connections with metal dowel-type fasteners in double shear," *Materials and Structures*, vol. 42, no. 3, pp. 385–397, 2009.

[4] K. Johanson, "Theory of timber connections," *International Association for Bridge and Structural Engineering*, vol. 9, pp. 249–262, 1949.

[5] The European Standard EN 1995-1-1: 2004 (E), Eurocode 5: Design of Timber Structures-Part 1-1: General-Common Rules and Rules for Buildings, 2004.

[6] L. Daudeville, L. Davenne, and M. Yasumura, "Prediction of the load carrying capacity of bolted timber joints," *Wood Science and Technology*, vol. 33, no. 1, pp. 15–29, 1999.

[7] L. A. Soltis, F. K. Hubbard, and T. L. Wilkinson, "Bearing strength of bolted timber joints," *Journal of Structural Engineering*, vol. 112, no. 9, pp. 2141–2154, 1986.

[8] E. César, "Capacity Predictions for Bolted Timber Joints Failing by split-ting," *The 10th World Connection Timber Engineering*, Miyazaki, Tokyo, Japan, 2008.

[9] L. Doyle, *Performance of Joints with Eight Bolts in Laminated Douglas-Fir (No. FSRN-FPL-10)*, Forest Products Lab Madison Wis., Madison, WI, USA, 1964.

[10] M. Patel and D. Hindman, "Comparison of single-and two-bolted LVL perpendicular-to-grain connections. II: fracture

models," *Journal of Materials in Civil Engineering*, vol. 24, no. 4, pp. 347–355, 2011.

[11] W. Mengjie, "Effect of humidity change on the performance of bolted joints of wood structural steel fillings," Master's thesis, Harbin Industrial University, Harbin, China, 2013.

[12] American Forest & Paper Association, *ANSI/AF&PA NDS-2012 National Design Specification for Wood Construction*, AF&PA, Washington, D.C., USA, 2012.

[13] Canadian Standard Association, *O86-01, Engineering Design in Wood*, Canadian Standard Association, Toronto, Canada, 2001.

[14] Z. Cui, M. Xu, Z. Chen et al., "Experimental study on bearing capacity of bolted steel-PSB-steel connections," *Engineering Mechanics*, vol. 36, no. 1, pp. 96–103, 2019, (In Chinese).

[15] J. H. P. Hover, "Load carrying capacity of multiple fastener steel to bamboo joints loaded parallel to the fibre direction," 2017.

[16] M. Xu, Z. Cui, L. Tu, Q. Xia, and Z. Chen, "The effect of elevated temperatures on the mechanical properties of laminated bamboo," *Construction and Building Materials*, vol. 226, pp. 32–43, 2019.

[17] Jg/T 199-2007, *Testing Methods for Physical and Mechanical Properties of Bamboo Used in Building*, Standards Press of China, Beijing, China, 2007.

[18] American Society for Testing and Materials, *Standard Test Methods for Small Clear Specimens of Timber*, American Society for Testing and Materials, West Conshohocken, PA, USA, 2014.

[19] American Society for Testing and Materials, *Standard Test Method for Evaluating Dowel-Bearing Strength of Wood and Wood-Based Products*, American Society for Testing and Materials, West Conshohocken, PA, USA, 2013.

[20] American Society for Testing and Materials, *Standard Test Method for Single-Bolt Connections in Wood and Wood-Based Products*, American Society for Testing and Materials, West Conshohocken, PA, USA, 2015.

[21] China Architecture Industry Press G. B. 50005—2003, *Timber Structures Design Code*, China Architecture Industry Press, Beijing, China, 2017.

[22] Z. Cui, L. Tu, M. Xu, Z. Chen, and C. Wang, "The evaluation of dowel-bearing properties of laminated bamboo parallel to grain," *Structures*, vol. 25, pp. 956–964, 2020.

[23] Z. Cui, M. Xu, L. Tu, Z. Chen, and B. Hui, "Determination of dowel-bearing strength of laminated bamboo at elevated temperatures," *Journal of Building Engineering*, vol. 30, Article ID 101258, 2020.

Hindawi
Advances in Civil Engineering
Volume 2021, Article ID 6637853, 15 pages
https://doi.org/10.1155/2021/6637853

Research Article

Bamboo/Wood Composites and Structures Shear and Normal Strain Distributions in Multilayer Composite Laminated Panels under Out-of-Plane Bending

Jan Niederwestberg,[1] **Jianhui Zhou**,[2] **Ying Hei Chui**,[1] **and Dongsheng Huang**[3]

[1]*Department of Civil & Environmental Engineering, University of Alberta, Edmonton T6G 1H9, Canada*
[2]*School of Engineering, University of Northern British Columbia, Prince George V2N 4Z9, Canada*
[3]*National Engineering Research Center of Biomaterials, Nanjing Forestry University, Nanjing 210037, China*

Correspondence should be addressed to Jan Niederwestberg; jan.niederwestberg@ualberta.ca

Received 11 November 2020; Revised 6 January 2021; Accepted 9 January 2021; Published 31 January 2021

Academic Editor: Hui Yao

Innovative mass timber panels, known as composite laminated panels (CLP), have been developed using lumber and laminated strand lumber (LSL) laminates. In this study, strain distributions of various 5-layer CLP and cross-laminated timber (CLT) were investigated by experimental and two modelling methods. Seven (7) different panel types were tested in third-point bending and short-span shear tests. During the tests, the digital imaging correlation (DIC) technique was used to measure the normal and shear strain in areas of interest. Evaluated component properties were used to determine strain distributions based on the shear analogy method and finite element (FE) modelling. The calculated theoretical strain distributions were compared with the DIC test results to evaluate the validity of strain distributions predicted by the analytical model (shear analogy) and numerical model (FE analysis). In addition, the influence of the test setup on the shear strain distribution was investigated. Results showed that the DIC strain distributions agreed well with the ones calculated by the shear analogy method and FE analysis. Both theoretical methods agree well with the test results in terms of strain distribution shape and magnitude. While the shear analogy method shows limitations when it comes to local strain close to the supports or gaps, the FE analysis reflects these strain shifts well. The findings support that the shear analogy is generally applicable for the stress and strain determination of CLP and CLT for structural design, while an FE analysis can be beneficial when it comes to the evaluation of localized stresses and strains. Due to the influence of compression at a support, the shear strain distribution near the support location is not symmetric. This is confirmed by the FE method.

1. Introduction

Cross laminated timber (CLT) and other mass timber panels like glue-, nail-, or dowel-laminated timber have become increasingly popular in the last decades. The increase in popularity can be a tribute to their large dimensions and cross sections, which allow for high levels of prefabrication and fast construction. Glue-, nail-, and dowel-laminated timber panels are manufactured from parallel lumber pieces connected to each other by either glue or nails of wooden dowels. Due to the parallel members, these panel types behave like beam elements in out-of-plane loading situations and can be considered as one-way elements. On the other hand, CLT panels are made from the commonly orthogonally arrangement of layers consisting of graded sawn lumber pieces that are glued to each other. The orthogonal arrangement of the layers lets CLT panels behave more like plates under out-of-plane loading, where loads can be transferred in both panel directions. Based on this, CLT panels can be considered two-way elements. However, the orthogonal arrangement of the layers leads to layers with radial-tangential cross section, which provide low shear modulus and strength. Due to this, CLT under out-of-plane loading is prone to high shear deformations and the so-called rolling shear failures when exposed to shear stresses perpendicular to the grain. Besides the low shear properties

of these cross-layers, gaps between the lumber pieces within these layers further promote shear deformation and rolling shear failures. Edge-gluing between adjacent laminates within a layer is beneficial but is not mandatory in the production of CLT [1].

Hybrid CLT with 3 layers made from European spruce and a European beech centre layer was tested in out-of-plane loading by [2]. Four-point bending tests and planar shear tests were used to determine the rolling shear properties of the beech core layer. Deflection measurements and strain gauges were used to determine the shear modulus of the beech. It was found that beech cross-layers improve the global shear behaviour of CLT significantly; both, shear modulus and strength improved; and the failure was shifted towards a longitudinal shear failure within the outer layers. In addition, the improved shear performance potentially allows for a simplified approach in design, treating the section as a rigid composite.

The bending and shear behaviour of 3-layer CLP and CLT formed from spruce-pine-fir (SPF) and laminated strand lumber (LSL) materials were investigated by [3]. Four (4) different lay-ups were evaluated in the program through bending and shear tests. The results showed that specimens with a LSL core layer and SPF outer layers had a 23% higher bending strength while reaching similar bending stiffness and a significant increase in shear stiffness compared to regular CLT. In addition, the bending failure was shifted from a rolling shear failure towards a flexural tensile failure. The short-span shear tests showed that the shear strength of specimens with a LSL core layer and SPF outer layers increased by 46% compared to regular CLT.

The use of oriented strand board (OSB) and spruce-pine-fir lumber in 3- and 5-layer CLP and CLT panels was evaluated by [4]. Ten different lay-ups were tested in the major and minor strength direction. The shear resistance and stress of the lay-ups were determined by experiments, shear analogy method, and finite element (FE) analysis. The results showed that the OSB provided higher mechanical properties compared to the lumber in the minor strength direction of the panels. Various failure modes were observed during bending tests. All hybrid CLT panels showed higher shear resistance compared to regular CLT. Furthermore, it was observed that the difference in shear resistance between the major and minor strength directions of hybrid CLT panels decreased with an increasing number of layers.

Three-layer CLP was investigated in [5]. The outer layers were made from Acacia lumber, while the core layer was formed from bamboo boards. Bending and shear tests were performed based on [6]. The tested CLP panels showed 176% higher bending stiffness and 37% higher bending strength compared to regular spruce-pine-fir CLT. The shear strength of the tested CLP was found to be 20% lower than the shear strength of spruce-pine-fir CLT. It was stated that the shear performance can potentially be improved if bamboo boards with higher strength are used.

Different analytical models were used by [7] to investigate the influence of shear deformation and the so-called rolling shear phenomenon in CLT in out-of-plane loading. The research compared results from the shear analogy method, the so-called Gamma method, and FE analysis with theoretical results assuming infinitely rigid transverse layers. The results showed that the influence of shear deformation can usually be neglected for most construction relevant cases (span-to-thickness ratio >30). For shorter panels, the influence of shear deformation should be considered. All of the utilized methods were capable of addressing the shear deformation and showed good agreement if appropriate input properties are used.

The influence of regular gaps between laminates within CLT layers was investigated by [8]. Laboratory test results were compared with results from FE analysis. The results from FE analysis showed good agreement with the laboratory tests. The work shows that the influence of small gaps can generally be neglected when determining the bending stiffness and that the influence of larger gaps can be addressed using a volume fraction approach. It was found that the influence of gaps between laminates on the in- and out-of-plane shear and torsional stiffness does not follow a volume fraction approach and that even narrow gaps lead to a significant reduction in stiffness.

The bending and shear properties of seven (7) different 5-layer CLP and CLT panel lay-ups were investigated in [9]. The bending properties were evaluated in third-point bending tests as well as modal tests while the shear properties were determined in short-span three-point bending tests. Compared to regular CLT, the CLP tests showed an increase of up to 43% of the bending stiffness, 87% of the bending strength, and up to 143% of the shear strength. The results were compared with the results calculated based on the shear analogy method. Similar to the findings in [3], the observed failure modes suggest that the use of structural composite lumber materials could avoid potential rolling shear failures. The digital imaging correlation (DIC) technique was employed to measure the strain developments in the thickness direction during bending and shear tests. The DIC results were briefly presented in [10].

All the research presented above addresses different structural CLP or CLT elements, but only some of it measures the strain behaviour of these elements during loading. While the work by [2, 4] evaluated local strain behaviour using strain gauges, only [10] utilized the DIC technique to evaluate strain distributions over the full height of the sections. Strain gauges are commonly used to evaluate the strain in the cross-layers of CLT and CLP elements. Due to the local nature of strain gauges, strain gauges located on these cross-layers cannot usually detect the influence of support conditions on the strain distribution, which is addressed in this research. The research [4, 7, 8] shows that FE analysis is well suited for determining strain, stress, and deflection of CLT and CLP panels. Nevertheless, the works do not address the effects of rapid local changes in loading.

Both the shear analogy method and FE modelling are currently adopted for the structural design of CLT building. The shear analogy method is a user-friendly analytical method, which is applicable for both CLT and CLP panels with the advantages in computational efficiency. FE modelling is well known to handle complicated geometry and load cases. The tests conducted in [9, 10] provided the

experimental data for the work presented herein, which aims to compare the shear and normal strains between DIC measurements and predictions by shear analogy method and FE modelling. The results will provide insights into the structural design of CLT members under out-of-plane loads.

2. Materials and Methods

As mentioned above, some of the materials, specimen preparation, test procedures, and test results were previously presented in [10]. Therefore, the used materials, the specimen preparation, and test procedures are only described here briefly as more detailed information can be found in [10]. In addition to the brief descriptions related to the laboratory tests and the analysis based on the shear analogy method, this section contains detailed information about the determination of the stress distributions and the modelling details in FE analysis.

2.1. Component Properties and Specimen Fabrication. Spruce-pine-fir (SPF) lumber of No. 2 grade and laminated strand lumber (LSL) were used to form the seven (7) symmetrically lay-up CLP and CLT panels. Before the CLP and CLT panels were formed, the moduli of elasticity (MOE) of the materials parallel to the grain were evaluated based on [6]. For the MOE values perpendicular to the grain and the shear moduli of the lumber, assumptions were made. The MOE perpendicular to the grain and the shear modulus parallel to the grain were estimated based on ratios of 1/16 and 1/30 of the MOE parallel to the grain of the lumber as suggested by [11]. The shear modulus perpendicular to the grain was assumed based on test results published in [12]. The MOE perpendicular to the grain of the LSL was assumed based on a ratio of 1/8 of the MOE parallel to the grain of the LSL [13]. The planar shear properties of the LSL were evaluated based on [14]. Table 1 presents the material properties of the lumber and LSL.

Seven (7) different CLP and CLT lay-ups were formed from the lumber and LSL. The panels were manufactured using a one-component polyurethane adhesive applied to one face only at a spread rate of 220 g/m^2. Due to the low moisture content of the LSL, the LSL surfaces were misted with water (32 g/m^2) before the gluing process to facilitate the curing of the adhesive. A bonding pressure of 1.38 N/mm^2 was applied to the assemblies. The panels were stored after gluing for at least 24 h before cutting the panels into test specimens. Two lay-ups were formed with but joints within LSL layers. Like the edges of the lumber pieces within a layer, these butt joints were formed without the application of adhesive. Figure 1 shows a butt joint within LSL layers. From the panels, which were about 2750 mm long, 1219 mm wide, and 184 mm thick, shear and bending specimens were cut. Shear specimens were cut to dimensions of 200 mm width and 1200 mm length. Test specimens for lay-ups with butt joints were cut in a way that the butt joints were located at the centre of the specimen. The bending specimens were cut to a width of 200 mm. Table 2 presents the different lay-ups,

Table 1: Component properties of lumber and LSL materials.

Material	Index	MC (%)	Density (kg/m^3)	MOE (N/mm^2)		Shear modulus (N/mm^2)	
				//	⊥	//	⊥
Lumber	Count	18	36	36	—	—	—
	Mean	7.4	470	10494	350*	656*	120*
	SE	0.05	5.0	243	—	—	—
LSL	Count	22	44	44	—	6	6
	Mean	3.4	644	9520	1190*	463	200
	SE	0.03	3.0	130	—	26.7	7.6

*Values based on assumptions.

Figure 1: Butt joints in the 2nd and 4th layer of a 5-layer A1a specimen.

Table 2: Five-layer CLP and CLT lay-ups ("T" = timber, "L" = LSL).

ID	Lay-up	Layer orientation	Shear tests	Bending tests
A1	T-L-L-L-T	//-//-//-//-//	8	13
A1a	T-L*-L-L*-T	//-//*-//-//*-//	8	16
A1b	T-L-L*-L-T	//-//-//*-//-//	8	14
B1	L-T-L-T-L	//-⊥-//-⊥-//	6	12
B2	L-T-L-T-L	//-//-//-//-//	6	14
C1	T-T-T-T-T	//-⊥-//-⊥-//	2	4
C2	T-T-T-T-T	⊥-//-⊥-//-⊥	2	4

*Layer contained a centred butt joint in LSL layer.

indicates the layer orientations, and provides the number of test specimens tested.

Before the shear and bending tests were performed, high contrast speckle patterns were applied onto the specimens. These speckle patterns allowed the digital imaging correlation (DIC) software to track the displacement of recognizable shapes and patterns based on photos taken during the loading process. By comparing the location of the recognizable patterns and shapes within the consecutively taken pictures with a reference picture taken before loading, the DIC software is capable of measuring displacement and strain of the laminate materials. Further information about DIC technique can be found in [15]. The shear test specimens were prepared with one speckle area, located over a support to measure the shear strain with minimum interference from bending strain. Two speckle areas were applied to the bending test specimens: one to evaluate maximum normal strain in the shear-free zone at the centre of the span and the other on one side halfway between a support and the

nearest loading point to evaluate the shear strain unaffected by the supports. Figure 2 shows a picture of the shear test setup and the speckle pattern as well as a shear force diagram. The shear speckle area is indicated by a red rectangle. Figure 3 shows a picture of the third-point bending tests and the applied speckle areas as well as a shear force and bending moment diagram. The shear speckle area is indicated by a red square while the bending speckle area is indicated by a green square.

2.2. Test Procedures. The shear and bending tests were performed based on [6] in test setups recommended in [16]. The shear tests were performed as short-span centre-point load shear tests at a span of 1000 mm (span-to-depth ratio = 5.5) and at a displacement rate of 2 mm/min. A total of 40 shear tests were performed. For the bending tests, a third-point bending test setup was employed at a test span of 2500 mm (span-to-depth ratio = 13.6), and tests were performed at a displacement rate of 4 mm/min. A total of 77 bending tests were undertaken. During the shear and bending tests, the applied load was recorded. In addition, two DIC cameras were focused on each speckle area and pictures were taken every two seconds and the recorded load was automatically correlated to the taken pictures.

2.3. Digital Imaging Correlation Analysis. The commercial DIC software VIC-3D [17] was used to analyse the DIC data. In the analysis, the relative displacements of the speckles within the DIC pictures are used to determine the strain across the speckled area. The software allows the user to define a specific path for which the strain values can be extracted, which are then plotted with respect to the location along the defined path. Here, the strain data extracted from the DIC data is directly used, only minor recalibrations were undertaken to centre the strain data over the cross section height. In addition, it should be noted that since VIC-3D uses the Lagrange strain tensors to calculate the shear strain, which is half of the engineering shear strain, the shear strain values were converted into engineering shear strain values. Shear and bending stress distributions can be determined based on the measured strain distributions using equations (1) and (2), respectively:

$$\tau_{(z)} = G_{(z)}\gamma_{(z)}, \tag{1}$$

where $\tau_{(z)}$ is the shear stress at location z in N/mm^2, $G_{(z)}$ is shear modulus at location z in N/mm^2, $\gamma_{(z)}$ is the shear strain at location z, and z is the distance of the location of interest to the neutral axis in mm:

$$\sigma_{(z)} = E_{(z)}\varepsilon_{(z)}, \tag{2}$$

where $\sigma_{(z)}$ is the bending stress at location z in N/mm^2, $E_{(z)}$ is the MOE at location z in N/mm^2, and $\varepsilon_{(z)}$ is the normal strain at location z.

To ensure that the strain data was taken from within the elastic range of the lay-ups, the strain data was determined at a load of approximately 40% of the average failure load of the corresponding test group. The approximate 40% loading of the average failure loads are presented in Table 3, where F_u is the failure load. For the bending tests, F_u represents the total load, not the individual loads.

While the DIC technique provides useful information on the shear and normal strain distributions, a direct conversion to stress distributions was not attempted in this research. In order to determine stress distributions, not only are the material properties required, but the layer boundaries need to be established precisely. Due to the measurement process with the speckle pattern on a white painted surface, the layer boundaries are hard to determine in some cases. While the boundaries could be estimated based on the known layer thicknesses, the location component of the strain distributions of the DIC measurements has to be considered less precise. The DIC strain is determined based on local averaging processes, which leads to uncertainty and missing values close to the specimen boundaries. This makes it difficult to precisely reference the strain to the layer boundaries. For specimens with lumber cross-layers, the large differences in the moduli of elasticity of the adjacent layers can lead to significant and unrealistic stress spikes in the associated stress distribution.

2.4. Shear Analogy Analysis. The shear analogy method is based on [18] and has been adopted in the CLT product standard [16] as well as in the Canadian timber design code CSA O86 [11] to determine the effective bending stiffness and shear stiffness of CLT. In order to determine the stress and strain distributions, the effective bending stiffness EI_{eff} of the cross section needs to be known. Here, the effective bending stiffness was determined for a shear-rigid equivalent system as described in [19]. The effective bending stiffness EI_{eff} of a rectangular cross section is determined based on fd3

$$EI_{\text{eff}} = \sum_{i}^{n} E_i \frac{b_i h_i^3}{12} + \sum_{i}^{n} E_i A_i z_{c,i}^2, \tag{3}$$

where EI_{eff} is the effective bending stiffness in Nmm^2, E_i is the MOE of layer i in N/mm^2, b_i and h_i are the width and thickness, respectively, of layer i in mm, A_i is the cross section area of layer i in mm^2, and $z_{c,i}$ is the distance of the centre of layer i to the neutral axis in mm.

While the strain distributions in the DIC tests can be directly extracted from the DIC software and then could be used to determine the stress distributions, the approach based on the shear analogy goes the opposite way. Here, the stress distributions are determined first and the strain distributions are then determined by transforming equations (1) and (2) towards $\gamma_{(z)}$ and $\varepsilon_{(z)}$, respectively. The shear stress distribution for an inhomogeneous cross section can be determined based on equation (4). Equation (5) presents an equation for the determination of the bending stress distribution of an inhomogeneous cross section:

$$\tau_{(z)} = \frac{V \sum E_{(z)} S_{(z)}}{EI_{\text{eff}} b_{(z)}}, \tag{4}$$

where V is the shear force in N, $\sum E_{(z)} S_{(z)}$ is the MOE weighted static moment at location z in Nmm, and $b_{(z)}$ is the width of the element at location z in mm:

Figure 2: DIC area in shear test and related shear diagram.

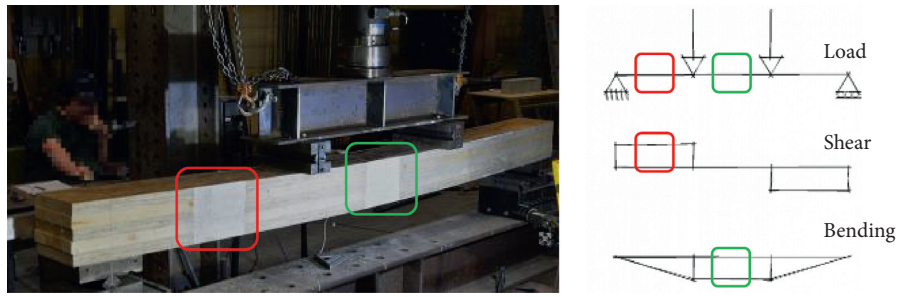

Figure 3: DIC areas in bending test and related shear and bending diagrams.

Table 3: Failure loads and loads for strain evaluation of lay-ups.

ID	Lay-up	Layer orientation	Shear tests		Bending tests	
			F_u (kN)	$0.4F_u$ (kN)	F_u (kN)	$0.4F_u$ (kN)
A1	T-L-L-L-T	//-//-//-//-//	138.7	55.5	86.0	34.4
A1a	T-L*-L-L*-T	//-//*-//-//*-//	136.5	54.6	75.6	30.2
A1b	T-L-L*-L-T	//-//-//*-//-//	148.9	59.5	79.8	31.9
B1	L-T-L-T-L	//-⊥-//-⊥-//	77.7	31.1	55.9	22.3
B2	L-T-L-T-L	//-//-//-//-//	178.1	71.2	108.1	43.2
C1	T-T-T-T-T	//-⊥-//-⊥-//	73.4	29.4	57.7	23.1
C2	T-T-T-T-T	⊥-//-⊥-//-⊥	37.4	15.0	28.5	11.4

F_u is the total failure load measured by a load cell attached to the cross-head.

$$\sigma_{(z)} = \frac{M}{EI_{\text{eff}}} E_{(z)} z, \tag{5}$$

where M is the bending moment in Nmm.

It should be noted that effective bending stiffness (EI_{eff}) was used for the determination of the strain values, while the relatively small span-to-thickness ratio of the bending tests suggests that the use of the apparent bending stiffness (EI_{app}), which includes the effects of shear deformation, might be more appropriate. Here, the effective bending stiffness (EI_{eff}) was used since it is a common published design parameter for mass timber panels and the general shape of the strain distributions would not be altered significantly, although there would be a slight difference in numerical values if EI_{app} was used instead.

The shear and bending stresses were determined based on a load of approximately 40% of the average failure load of the corresponding test group (see Table 3).

2.5. Finite Element Analysis. The FE analysis allows the direct extraction of strain and stress distributions. For the FE analysis, the commercial software Abaqus was employed [20]. The software allows creating three-dimensional models which can present the desired structure. Here, the CLP and CLT specimens were modelled by 3D deformable elements. It was assumed that the influence of gaps between adjacent pieces of lumber within layers running parallel to the test span can be neglected; each parallel layer was modelled by a single element. Layers that included gaps between pieces running perpendicular to the test span (A1a, A1b, B1, C1, and C2) were modelled with physical gaps (1 mm). The material properties used in the FE model were generally based on the properties evaluated in the component tests. Assumptions were made for the missing property characteristics. The properties were assigned direction based on the property orientations within the lay-ups. It should be noted that the lumber cross-layer elements were assigned the property "Lumber ⊥." Here, the properties of the lumber were converted to the global directions of the FE model in order to be able to present FE colour contour plots, which are based on global local systems. Therefore, the property directions of the lumber cross-layers needed to be changed

to match the other materials. Table 4 presents the material properties used in the FE models.

The bond between layers was assumed to be rigid; therefore, the layers were tied together in the FE models. In order to allow the extraction of the strain and stress data at similar locations as used in the laboratory tests, partitions were created in the model at the locations of interest. The general mesh size was chosen to be about half the layer thickness. Only in the areas of interest, the mesh size was redefined to 1/9 of the layer thickness to increase the data resolution. It should be noted that the redefined mesh was chosen for the purpose of resolution and that no convergence tests were conducted for the peak strain values. The boundary conditions were applied to reflect the boundary conditions of the laboratory tests. In order to simulate the influence of the support and loading plates, steel plates were added to the model, to which the boundary conditions and loads were applied. Similar to the laboratory shear tests, the supports in the FE shear model were not free to rotate, while the supports in the bending tests FE model were not restrained and were allowed to rotate freely. The contacts between all elements were defined as hard contacts in the normal direction of the surfaces other than the tied surfaces between layers and a friction coefficient of 0.3 was assigned of the tangential behaviour. The applied load level used in the analysis was 40% of the average failure load of the corresponding test group (see Table 3). Figure 4 shows the FE models for the CLT shear and bending test specimen C1. The locations of the shear related results are shown by red lines and the location of the bending strain results is indicated by a yellow line.

3. Results and Discussion

In the following, the results from the digital imaging correlation (DIC) strain measurements, the shear analogy (SA), and the FE analysis are presented. All results were obtained at a load of about 40% of the failure loads of the respective specimens in the related test setups as indicated in Table 3. The following graphs show colour contour plots from the DIC and FE evaluations, as well as strain diagrams presenting data evaluated based on DIC, shear analogy (SA) method, and finite element (FE) analysis. The locations of the strain evaluations in the DIC and FE contour plots tests are indicated by black dashed lines. The associated strain distributions were evaluated based on a chosen reference line within the software. It should be noted that the legends associated with the DIC colour contour plots are based in the full contour plot areas. The FE strain distributions were measured at the outer surface of the models. The colours within the DIC and FE contour plots might not match, and the plots are presented in order to show the strain distributions over the sections.

3.1. Shear Strain in Shear Tests. As shown in Figures 2 and 4, the shear strain measurements from the shear tests were evaluated close to the support areas. Figure 5 presents the data for the lay-ups A1, A1a, and A1b. Here, contour plots are shown from A1 only since all three lay-ups are almost identical, which reflects in the contour plots as well as the diagrams. Figures 6–9 show the information for lay-ups B1, B2, C1, and C2, respectively.

In general, it can be said that the DIC and FE colour contour plots match each other fairly well for all specimens. It should be noted that the shear strain in the DIC contour plot is presented as Lagrange strain tensors and therefore the strain values in the DIC contour plot legends are about half of the FE strain at the corresponding locations. High strain zones are located in similar areas of the contour plots. It can be seen that gaps between laminates (B1, C1, and C2) show high strain areas within the DIC contour plots, while the gaps show less significantly in the FE contour plots. The reason for this is likely the DIC evaluation method. As mentioned earlier, DIC determines the strain based on averaged relative movements. In the DIC analysis, the two boundaries and the related speckles are optically connected as they are used as reference points for each other. When gaps widen during loading, the speckles on the two boundaries of the gaps lead to high measured strain in the DIC. In the FE analysis, the boundaries of the gaps are not used as reference points for the determination of the strain values and thereby the strain values show less pronounce in the contour plots. In all diagrams, it can be observed that both DIC and FE data show asymmetrical strain distributions with respect to the centre of the cross sections ($z = 0$ mm) with higher strain towards the bottom lumber-to-LVL glueline followed by a step in strain. The asymmetric shape of the shear strain distributions from the shear tests was due to nearby reaction force. A locally induced load has a similar effect, leading to an asymmetrical shaped strain distribution with higher shear strain values on the side (z = positive or negative) of the induced load. Here, this was amplified since the boundary conditions were not free to rotate. The specimen rotates on the inner edges of the support, leading to a rapid decrease in internal forces within the cross section. While the FE distributions generally show similar characteristics as the DIC distributions, the SA distributions show a symmetrical shape, while still showing similar characteristics such as stepwise and parabolic characteristics. For A1, A1a, and A1b (Figure 5), it can be seen that the three specimens show similar strain distributions. It can be seen that the measured strain based on DIC exceeds both SA and FE calculated strains, but similar characteristics between DIC and FE strain distributions can be observed. For specimens B1, B2, C1, and C2 (Figures 6–9), the main characteristic of the shear strain distributions can be described as stepwise. Specimens with lumber cross-layers (B1, C1, and C2), especially, show strong steps, while the distribution specimen B2 shows both strong stepwise and parabolic characteristics.

3.2. Shear Strain in Bending Tests. As shown in Figures 3 and 4, the shear strain measurements from the bending tests were evaluated halfway between a support and the closest loading point. Figure 10 presents the data for the lay-ups A1, A1a, and A1b. Here, contour plots are shown from A1 only

Table 4: Material properties in finite element models.

Material	MOE (N/mm^2)			Shear modulus (N/mm^2)			Poisson ratio (—)		
	E_{11}	E_{22}	E_{33}	G_{12}	G_{13}	G_{23}	ν_{12}	ν_{13}	ν_{23}
Lumber	10494	350*	350*	656*	656*	120*	0.32*	0.35*	0.43*
Lumber ⊥	350*	10494	350*	656*	120*	656*	0.11*	0.43*	0.12*
LSL	9520	1904*	1904*	463	463	200	0.21*	0.13*	0.38*

*Values based on assumptions.

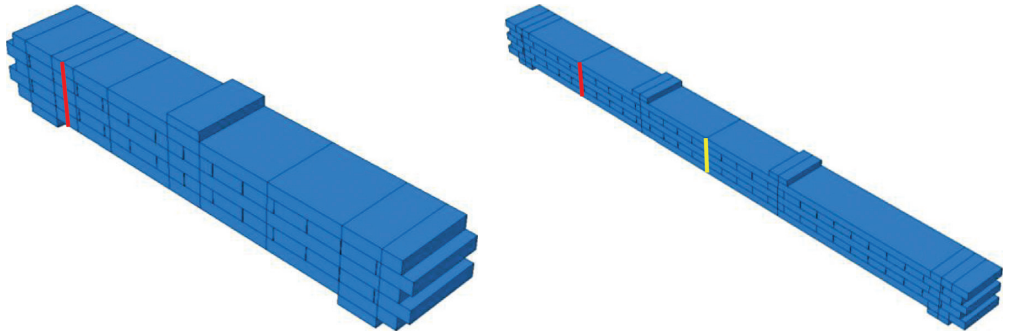

(a) (b)

Figure 4: Finite element models for shear and bending of CLT C1 (shear strain location = red lines, bending strain location = yellow line).

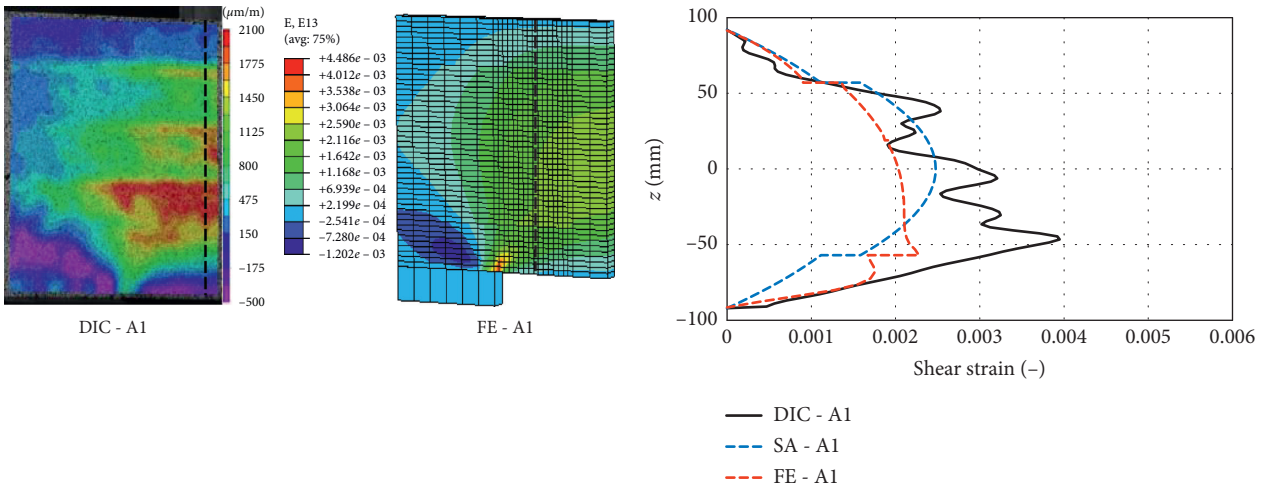

(a) (b)

Figure 5: Continued.

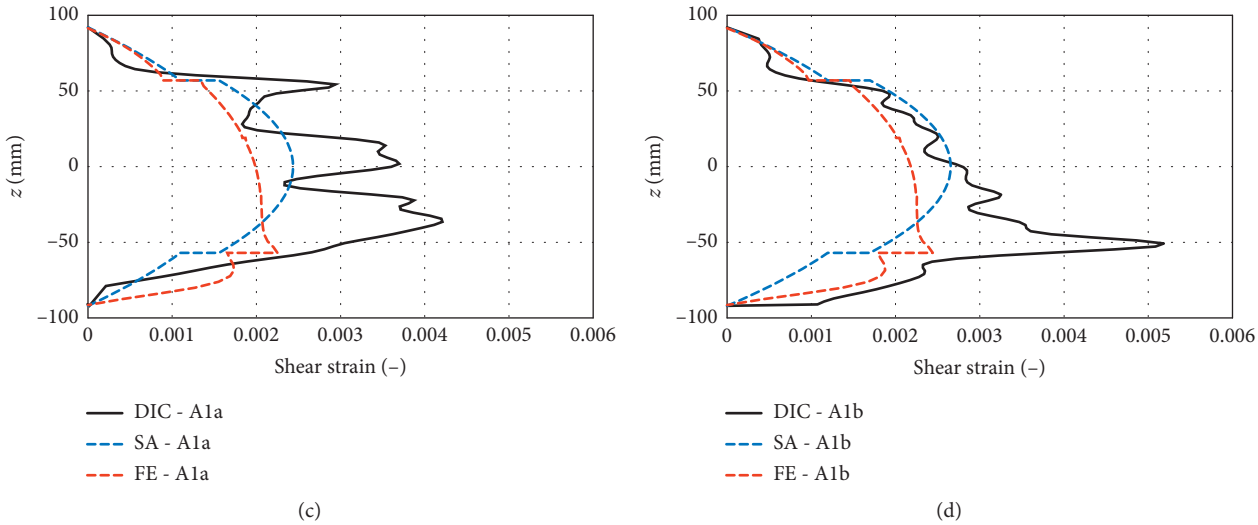

(c) (d)

Figure 5: Colour contour plots of A1 and shear strain distribution from shear tests for A1, A1a, and A1b.

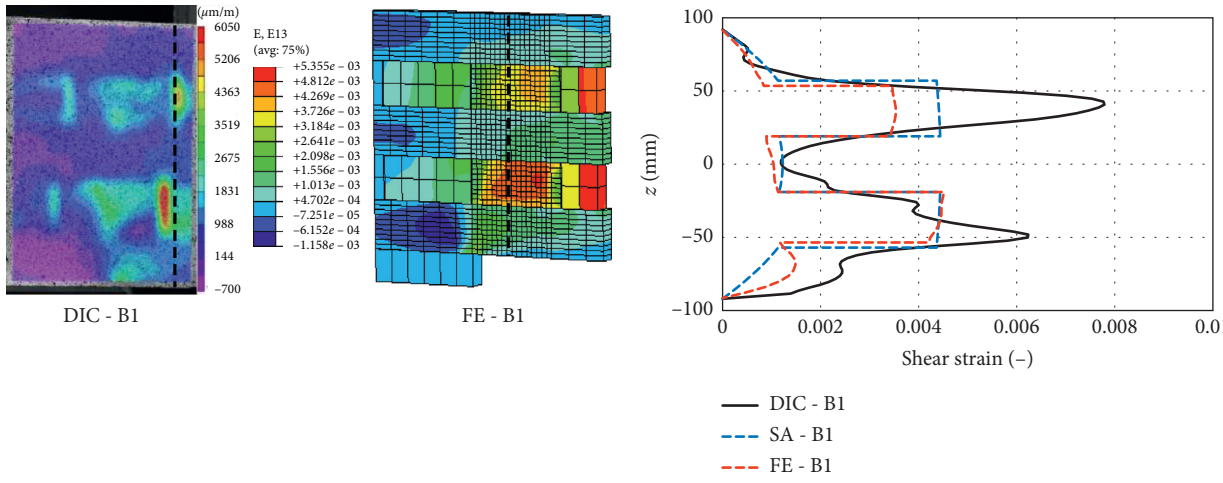

(a) (b)

Figure 6: Colour contour plots and shear strain distribution from shear tests for B1.

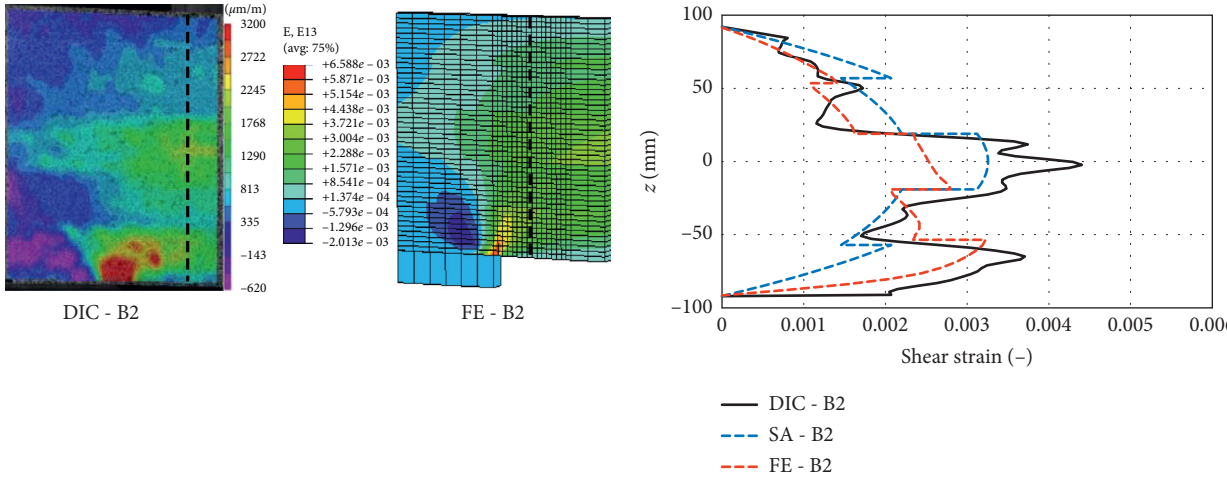

(a) (b)

Figure 7: Colour contour plots and shear strain distribution from shear tests for B2.

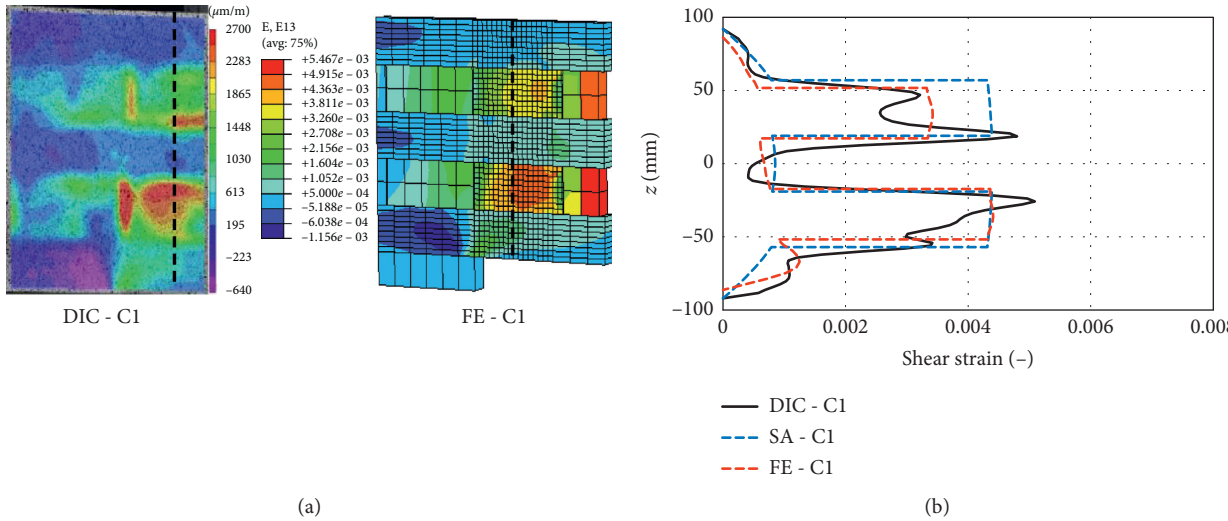

Figure 8: Colour contour plots and shear strain distribution from shear tests for C1.

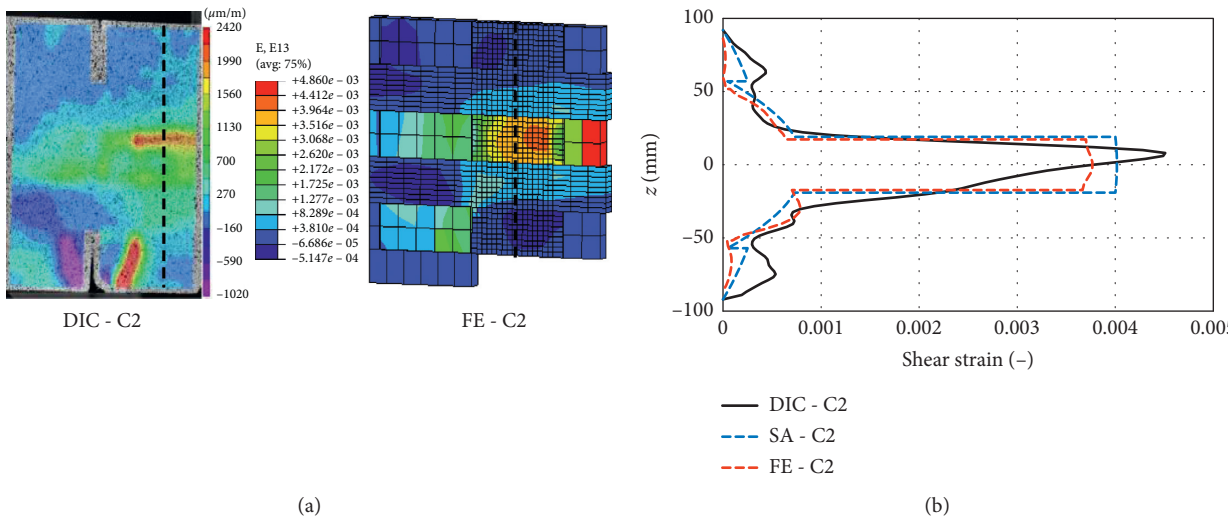

Figure 9: Colour contour plots and shear strain distribution from shear tests for C2.

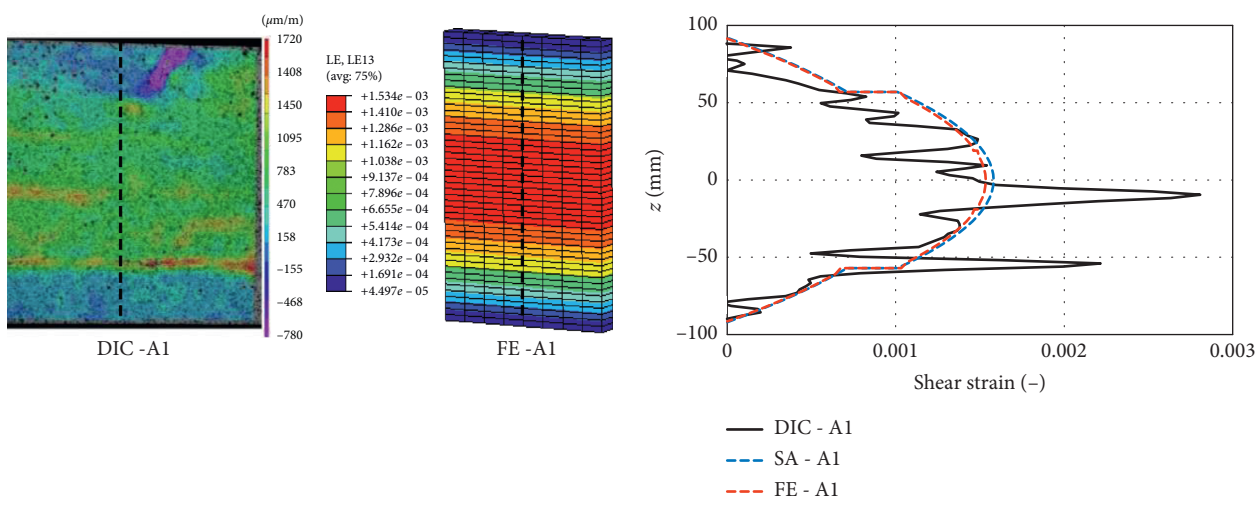

Figure 10: Continued.

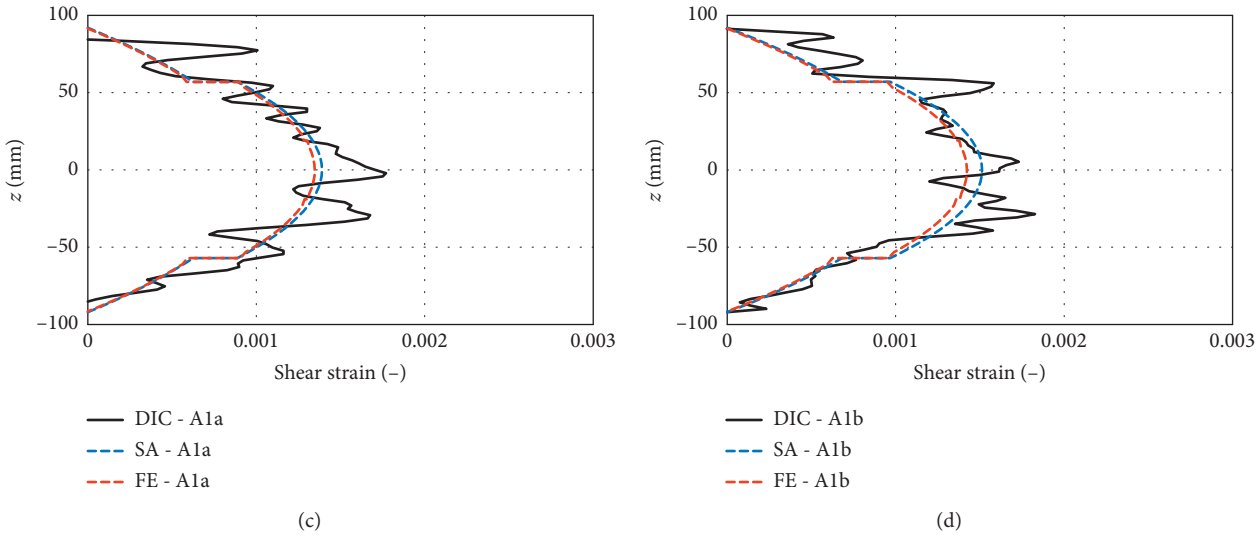

Figure 10: Colour contour plots of A1 and shear strain distribution from bending tests for A1, A1a, and A1b.

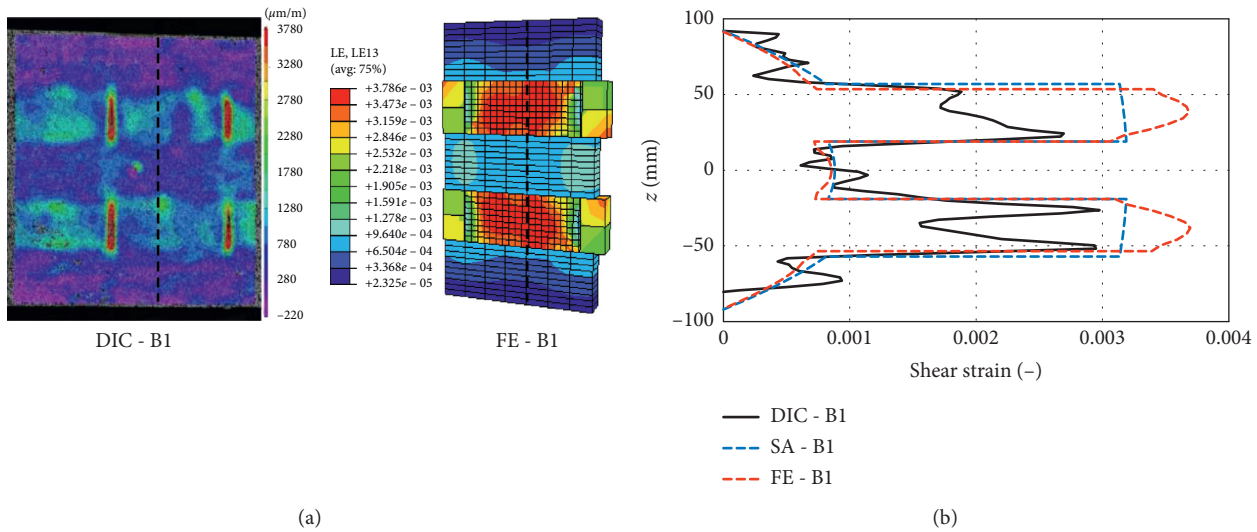

Figure 11: Colour contour plots and shear strain distribution from bending tests for B1.

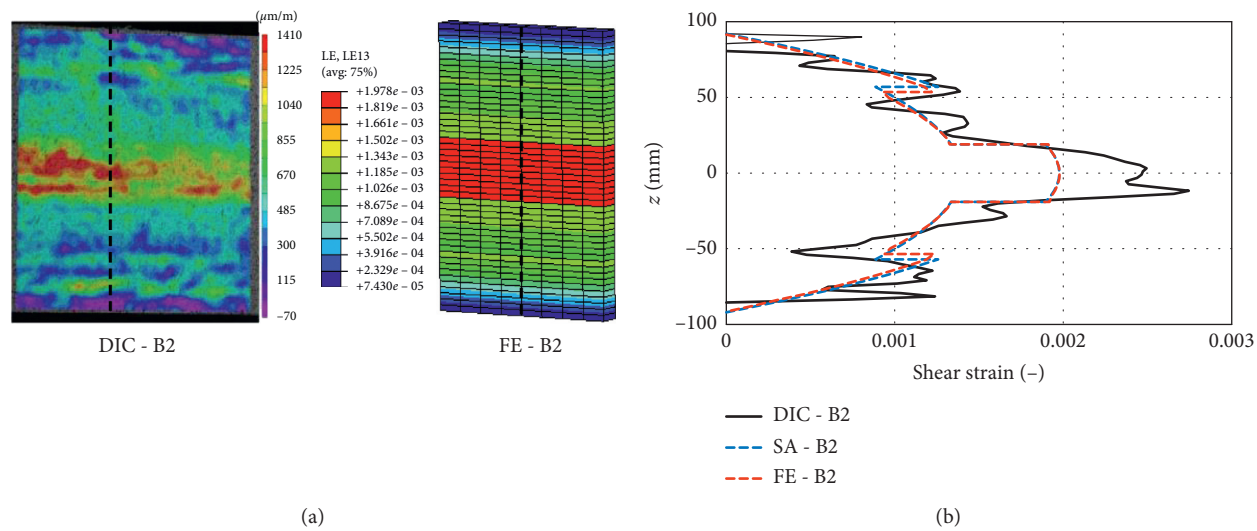

Figure 12: Colour contour plots and shear strain distribution from bending tests for B2.

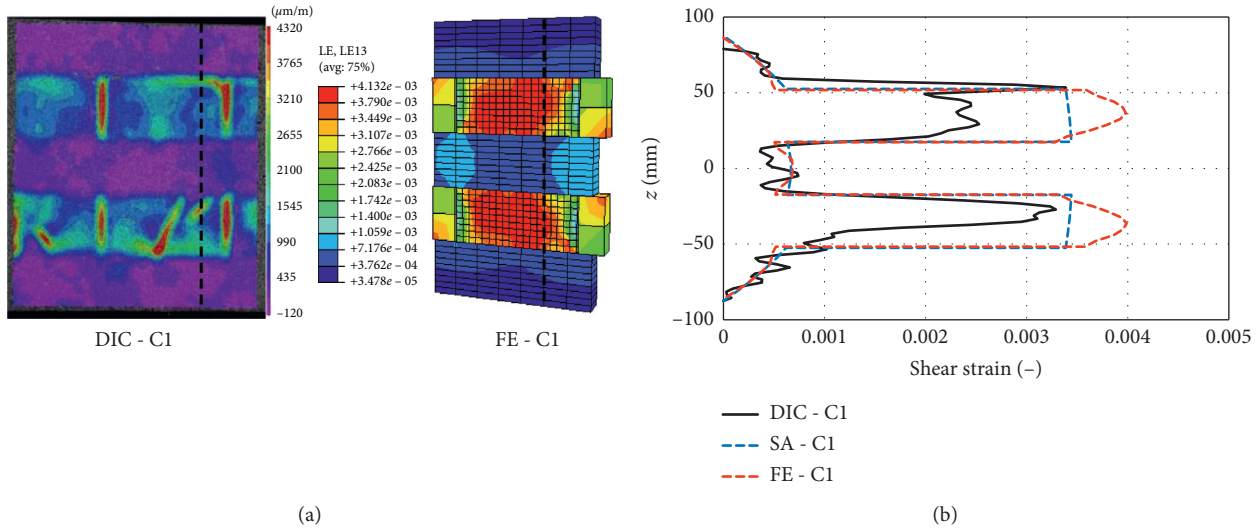

Figure 13: Colour contour plots and shear strain distribution from bending tests for C1.

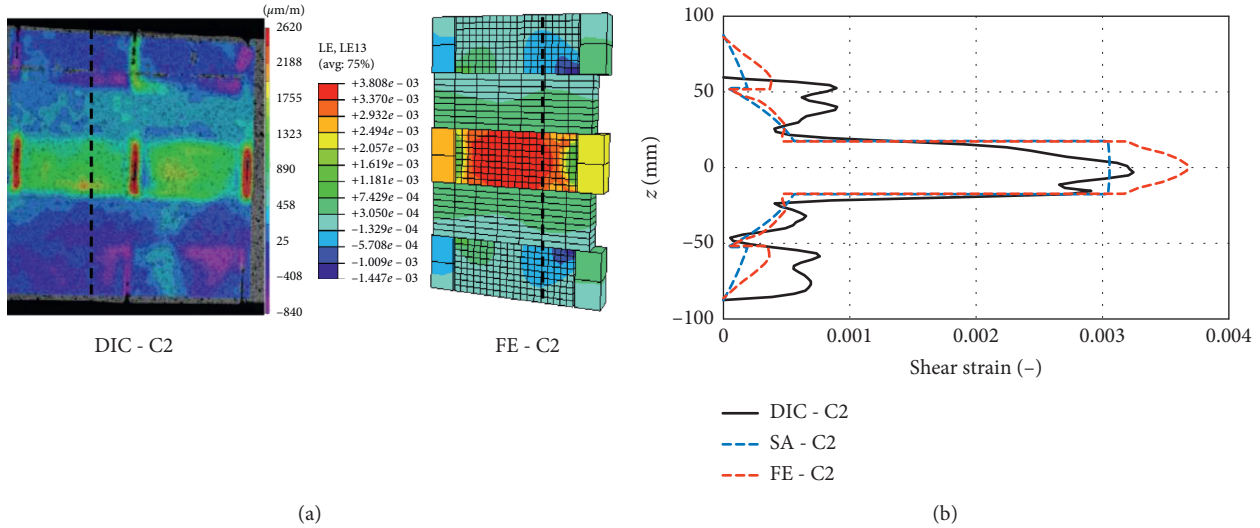

Figure 14: Colour contour plots and shear strain distribution from bending tests for C2.

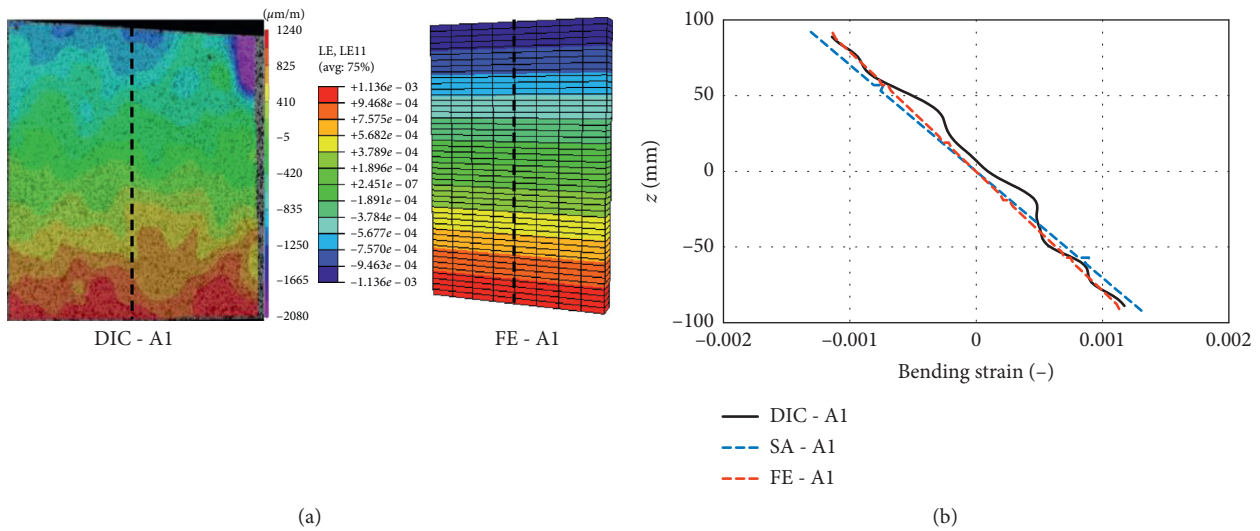

Figure 15: Colour contour plots and normal strain distribution from bending tests for A1.

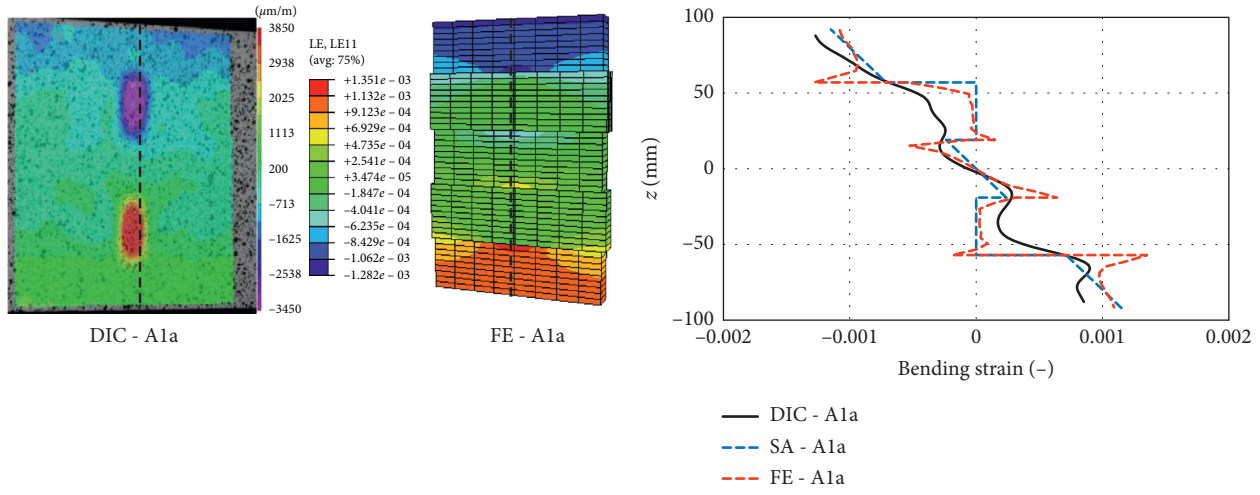

Figure 16: Colour contour plots and normal strain distribution from bending tests for A1a.

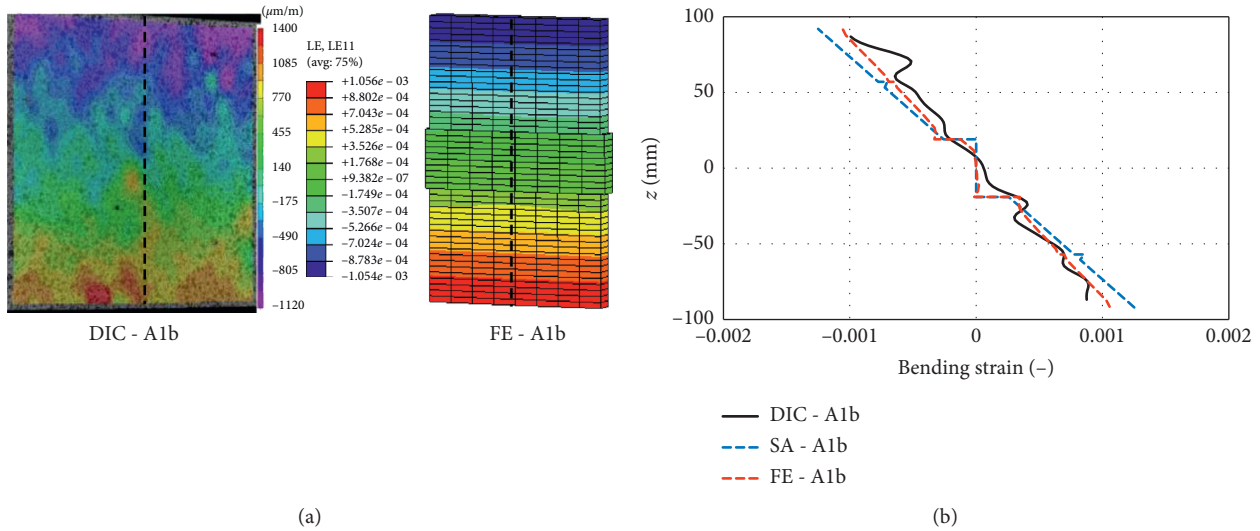

Figure 17: Colour contour plots and normal strain distribution from bending tests for A1b.

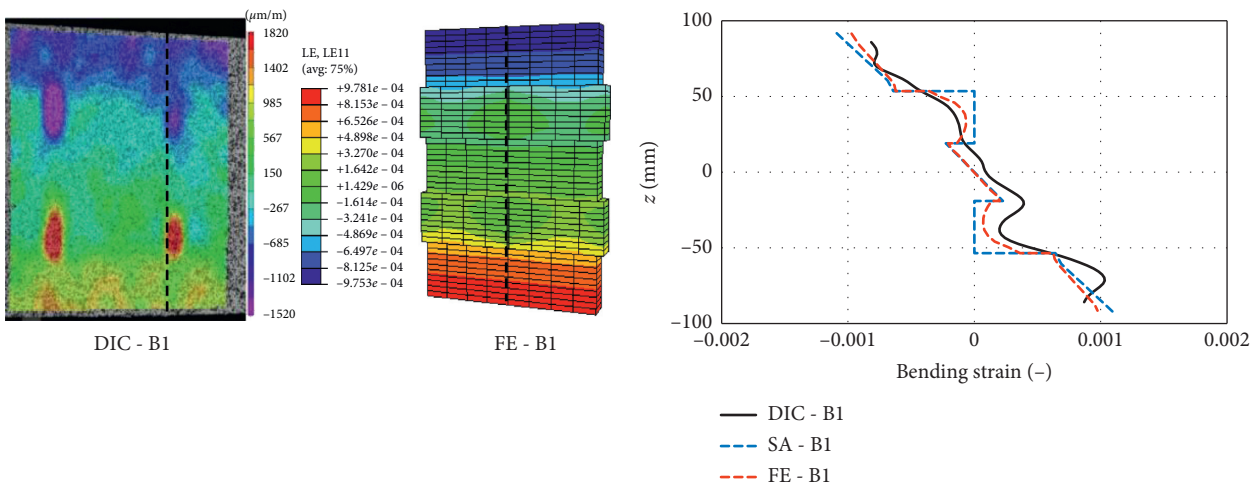

Figure 18: Colour contour plots and normal strain distribution from bending tests for B1.

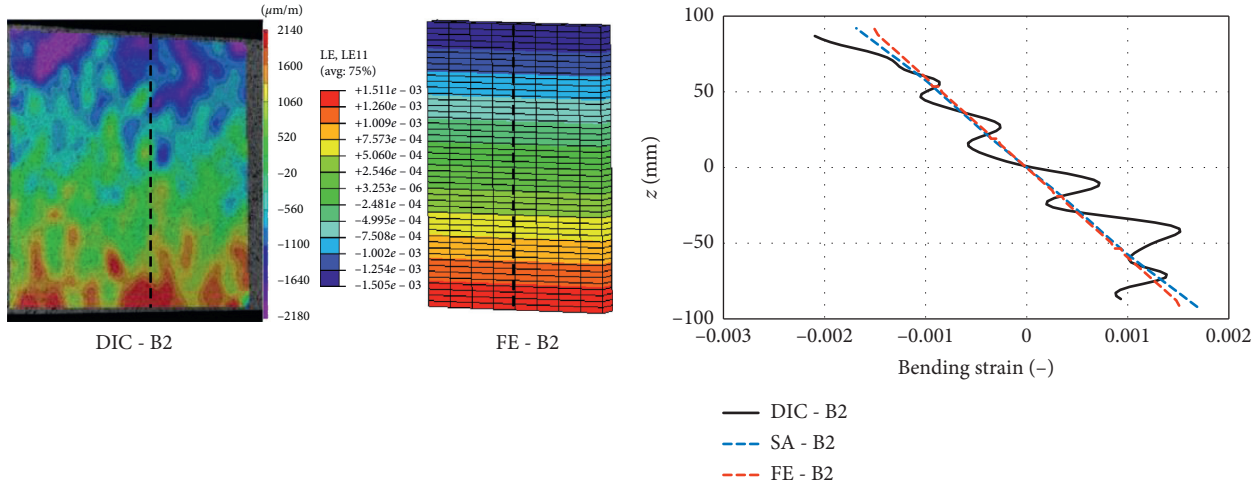

Figure 19: Colour contour plots and normal strain distribution from bending tests for B2.

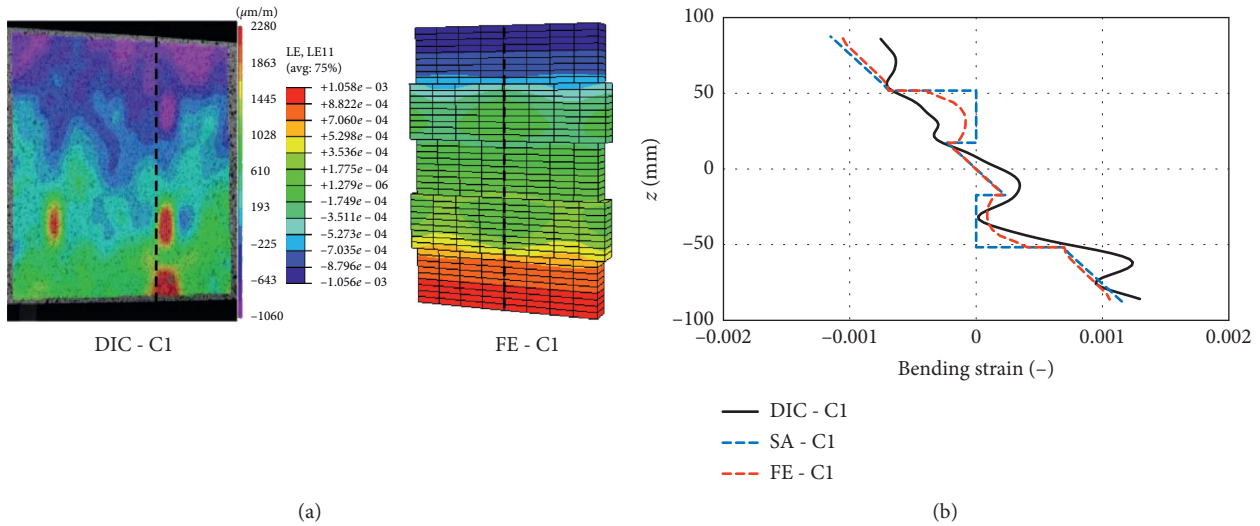

Figure 20: Colour contour plots and normal strain distribution from bending tests for C1.

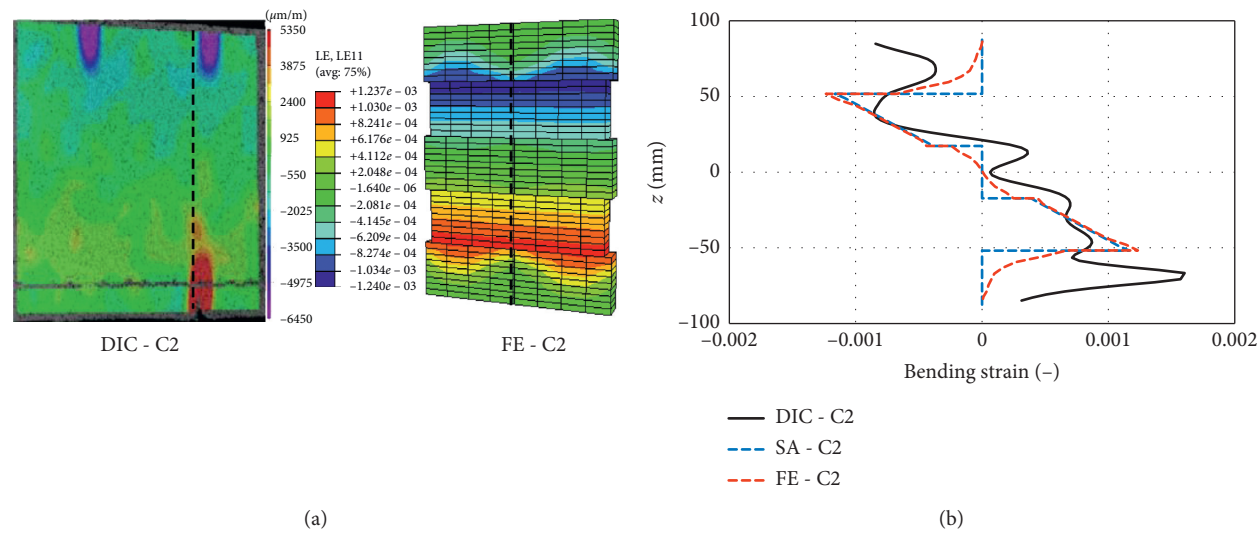

Figure 21: Colour contour plots and normal strain distribution from bending tests for C2.

since all three lay-ups are almost identical, which reflects in the contour plots as well as the diagrams. Figures 11–14 show the information for lay-ups B1, B2, C1, and C2, respectively.

As before, for the shear test related strain evaluations, it can be seen that the colour contour plots of DIC and FE match well. As previously described, the shear strain in the DIC contour plot is presented as Lagrange strain tensors and is therefore about half of the corresponding FE values. Similar to the shear strain DIC contour plots from the shear tests, gaps between laminates (B1, C1, and C2) show high strain areas. As before, this is likely due to the strain evaluation process of the DIC method. Compared to the shear test related shear strain distributions, the shear strain from the bending tests shows a higher level of symmetry with respect to the centre of the cross section ($z = 0$ mm). This has to do with the location of the strain determination. Here, the absence of a nearby induced load or a reaction force leads to a symmetrical strain distribution shape. Besides the missing higher strain towards the bottom lumber-to-LVL glueline, all specimens show the same characteristics that were observed in the shear test related strain distributions.

3.3. Normal Strain in Bending Tests. As shown in Figures 3 and 4, the normal strain measurements from the bending tests were evaluated about halfway between loading points. Figures 15–21 present the data for the lay-ups A1, A1a, A1b, B1, B2, C1, and C2, respectively. It should be noted that all FE results were taken slightly off centre in order to obtain strain values from the edge of the gaps between lamina, while the SA related data was determined within the gaps. This was done since the SA approach only distinguishes between two cases, a solid cross section or a cross section with gaps, but cannot address the strain at the boundaries. This is the case for lay-ups A1a, A1b, B1, C1, and C2.

Similar to the shear strain evaluations, the colour contour plots of DIC and FE show good agreement for the normal strain. Due to the DIC strain evaluation process, gaps between laminates (A1a, A1b, B1, C1, and C2) show as high strain areas. Here, specimens A1, A1a, and A1b are presented separately since the gaps in A1a and A1b are located close to the areas of interest. Based on the distribution of the modulus of elasticity (MOE), specimens A1 and B2 (Figures 15 and 19, respectively) are almost homogeneous. This reflects in the normal strain distributions, where these two specimens show linear behaviour in all three methods. The DIC data of A1, especially, shows good agreement, while the DIC data of B2 shows some deviation from the calculated strain distributions. These variations could have occurred due to the rough surface of the LVL and associated inaccuracies in the DIC measurement. Another reason could be the local variations in MOE. Similar to A1, A1b (Figure 17) shows almost linear behaviour since the installed gap is located close to the neutral axis and therefore the influence of the gap is rather small. For all other specimens with gaps, namely, A1a, B1, C1, and C2 (Figures 16, 18, 20, and 21, respectively), the influence of the gaps is more obvious. It can be seen that both SA and FE show good agreement with the measured DIC data, with the FE distributions generally reflecting the DIC data better in the area of the gaps where the DIC distributions follow a more rounded trend compared to the defined steps of the SA method. It can be seen that the rounded steps of the DIC distributions in the areas of the gaps are larger within the tension zone (bottom half of the cross sections). A reason could be that the gaps in the compression zone (top half of the cross sections) close, thereby transferring forces in contact. Another reason could be different MOE values in compression and tension within the materials [21].

4. Conclusions

Seven (7) different 5-layer composite laminated panels (CLP) and cross-laminated timber (CLT) panels were manufactured and tested as beams in short-span shear tests and third-point bending tests. Shear and normal strain measurements were taken during the tests using the digital imaging correlation (DIC) technique. The strain distributions were compared with distributions calculated based on the shear analogy (SA) method and finite element (FE) analysis.

The results show that the shear analogy method is capable of estimating shear and normal strain distributions in CLP and CLT and therefore the shear and normal stress distributions. In situations where loads are introduced locally or supports induce a rapid change in internal forces due to geometrical constraints, the shear analogy method underestimates local shear strain, which could lead to potential premature failure of the structural element. This is not surprising since the shear analogy method was not developed to determine internal stresses and strains close to local loadings or supports. Here, a determination of the shear strain and stress based on FE analysis might be advisable as the FE results show better agreement with the measured DIC strain in the areas of the supports. In addition, the FE analysis generally shows a closer agreement with the measured strain around gaps within layers as the shear analogy can only distinguish between the gap and no-gap cases, but not the gap boundary case. Furthermore, FE analysis has the potential to include the effects of local reinforcement measures on strain distributions. It should be noted that the accuracy of both shear analogy and FE analysis is highly dependent on the assumed material properties.

Data Availability

The data used to support the findings of this study are available from the corresponding author upon request.

Conflicts of Interest

The authors declare that there are no conflicts of interest regarding the publication of this paper.

Acknowledgments

Funding for the research was provided by the Natural Sciences and Engineering Research Council of Canada (NSERC)

through the Engage Program and Alberta Innovates through its Alberta Bio Future Research and Innovation Program.

References

[1] R. Brandner, G. Flatscher, A. Ringhofer, G. Schickhofer, and A. Thiel, "Cross laminated timber (CLT): overview and development," *European Journal of Wood and Wood Products*, vol. 74, no. 3, pp. 331–351, 2016.

[2] S. Aicher, M. Hirsch, and Z. Christian, "Hybrid cross-laminated timber plates with beech wood cross-layers," *Construction and Building Materials*, vol. 124, pp. 1007–1018, 2016.

[3] W. G. Davids, N. Willey, R. Lopez-Anido et al., "Structural performance of hybrid SPFs-LSL cross-laminated timber panels," *Construction and Building Materials*, vol. 149, pp. 156–163, 2017.

[4] Q. Li, Z. Wang, Z. Liang, L. Li, M. Gong, and J. Zhou, "Shear properties of hybrid CLT fabricated with lumber and OSB," *Construction and Building Materials*, vol. 261, 2020.

[5] N. M. Galih, S. M. Yang, and S. G. Kang, "Study on the mechanical properties of tropical hybrid cross laminated timber using bamboo laminated board as core layer," *Journal of the Korean Wood Science and Technology*, vol. 48, no. 2, pp. 245–252, 2020.

[6] ASTM International, *ASTM D198-15: Standard Test Methods of Static Tests of Lumber in Structural Sizes*, ASTM International, West Conshohocken, PA, USA, 2015.

[7] A. Sandoli and B. Calderoni, "The rolling shear influence on the out-of-plane behavior of CLT panels: a comparative analysis," *Buildings*, vol. 10, no. 3, 2020.

[8] L. Franzoni, A. Lebée, F. Lyon, and G. Forêt, "Elastic behavior of cross laminated timber and timber panels with regular gaps: thick-plate modeling and experimental validation," *Engineering Structures*, vol. 141, pp. 402–416, 2017.

[9] J. Niederwestberg, J. Zhou, and Y. H. Chui, "Mechanical properties of innovative, multi-layer composite laminated panels," *Buildings*, vol. 8, no. 10, 2018.

[10] J. Niederwestberg, J. Zhou, and Y. H. Chui, "Strain distribution of 5-layer composite laminated panels using digital imaging correlation technique," in *Proceedings of the World Conference of Timber Engineering 2018*, Seoul, South Korea, August 2018.

[11] Canadian Standards Association, *CSA O86-19 Engineering Design in Wood*, Canadian Standards Association, Toronto, Canada, 2019.

[12] M. Gong and Y. H. Chui, *Evaluation of Planar Shear Properties of Cross Layer in Massive Timber Panel. Final Report #: WSTC2014-038*, Wood Science and Technology Centre, The University of New Brunswick, Fredericton, Canada, 2015.

[13] Y. H. Chui, M. Gong, and J. Niederwestberg, *"Development of a Lumber-SCL Massive Timber Panel Product, Final Report #: WSTC2014-038*, Wood Science and Technology Centre, The University of New Brunswick, Fredericton, Canada, 2015.

[14] ASTM International, *ASTM D2718-00: Standard Test Methods for Structural Panels in Planar Shear (Rolling Shear)*, ASTM International, West Conshohocken, PA, USA, 2006.

[15] M. A. Sutton, "Digital image correlation for shape and deformation measurements," in *Springer Handbook of Experimental Solid Mechanics*, pp. 565–600, Springer, Berlin, Germany, 2008.

[16] APA-The Engineered Wood Association, *Standard for Performance-Rated Cross-Laminated Timber: ANSI/APA PRG 320*, APA-The Engineered Wood Association, Tacoma, WA, USA, 2017.

[17] Correlated Solutions Incorporated, *Correlated Solutions Homepage*, Correlated Solutions Incorporated, Irmo, SC, USA, 2020, http://www.correlatedsolutions.com.

[18] H. Kreuzinger, "Platten, Scheiben und Schalen–ein Berechnungsmodell für gängige Statikprogramme," *Bauen mit Holz*, vol. 1, pp. 34–39, 1999.

[19] S. Winter, H. Kreuzinger, and P. Mestek, "Flächen aus brettstapeln, brettsperrholz und verbundkonstruktionen," 2008, https://mediatum.ub.tum.de/doc/739585/739585.pdf.

[20] Dassault Systemes, "ABAQUS 6.22 [Computer Software]," 2019.

[21] M. H. Schneider and J. G. Phillips, "Elasticity of wood and wood polymer composites in tension compression and bending," *Wood Science and Technology*, vol. 25, no. 5, pp. 361–364, 1991.

Hindawi
Advances in Civil Engineering
Volume 2020, Article ID 6621333, 8 pages
https://doi.org/10.1155/2020/6621333

Research Article

FE Modeling for Bolted Wood Connection Using a Porous Constitutive Model

Huazhang Zhou[1,2] **and Xiaoqiang Zhou**[2]

[1]*Key Lab of Structures Dynamic Behaviour and Control (Harbin Institute of Technology), Ministry of Education, Harbin 150090, China*
[2]*School of Civil Engineering, Harbin Institute of Technology, Harbin 150090, China*

Correspondence should be addressed to Huazhang Zhou; huazhang.zhou@hit.edu.cn

Received 4 October 2020; Revised 18 November 2020; Accepted 12 December 2020; Published 28 December 2020

Academic Editor: Min-Juan He

According to the facts of localized crushing failure of bolt groove in wood connection with enough end distance and the three-phase composites of wood with solid (wood substance), water, and gas, a confined compression test for the wood cylinder was conducted for achieving constitutive relation under the complex stress state in wood groove. A porous constitutive model was developed according to the confined compression experiments. Then, the constitutive model was implemented in a finite element modeling of mental dowel-type fasters in wood-to-wood connections to analyse the load-carrying capacity parallel to the grain. Through changing the thicknesses of centre members and side members of wood connections made of a similar wood species, *Pinus Sylvestris* var. *Mongolica*, the effects of thickness combinations of centre members and side members on the failure modes and load-carrying capacity of bolted wood connection including numerical simulations and experiments were compared. The failure modes, including the yielding of centre member, the yielding of side member, and the yielding of the bolt, as well as the rigid rotation of the bolt, all reappeared by the finite element modeling with the porous constitutive model. The predicted deformation shapes and load-displacement relations of bolted wood connections were compared with experimental ones, and good correlations were observed. This paper presents a new approach to simulate the local embedment crushing of bolt groove in wood connections.

1. Introduction

Finite element (FE) numerical simulation of the localized problem in wood structure is always a difficult issue due to the inevitable differences between FE results and experiment results. The reasons causing the differences involve the high variable mechanical properties of wood, differences between clear wood and structural wood, size effect, defects of wood, effect of moisture content, duration of load, and even the test method for material parameters for the localized compression wood. Hence, to reduce the differences between FE simulation and experiment, some hypotheses were adopted in FE modeling to calibrate the mechanical parameters. For example, Moses reduced the initial modulus to cover the work-hardening behaviour of wood, and a multiplier 0.01 was used in the modeling [1]. Guan adopted a modification factor of the empirical modulus to simulate the stiffness of the flat nail embedment test, where a multiplier 0.25 was used [2]. Barrett developed a FE modeling using a foundation material model and limit foundation zone around bolt hole of 4.5 times of diameter of the bolt to simulate the localized problem of nailed connections in wood [3]. Sandhaas developed a continuum damage mechanics model including eight types of failure modes to simulate the performance of timber joints with the slotted-in steel plate, where the size effect for fracture energy was taken into consideration by means of the characteristic element length [4]. By utilizing the modification factors, the simulation results were consistent with those of corresponding experiments. However, the modification factors are always

empirical coefficients which are dependent on the experiences of sophisticated engineers.

Difference induced by the test method for mechanical parameter is also one source for the differences between simulation results and experiment results. The mechanical parameters for the constitutive model in FE modeling were usually determined through uniaxial compression or tension tests. However, in bolted wood connection, the stress state in wood groove is not uniaxial one. Localized wood groove is restrained by lateral wood, which usually deforms along the direction parallel to the grain including shear deformation and crushing deformation components. However, a stress-strain relation from the uniaxial test cannot descript accurately the stress state in wood groove. On the other hand, the dowel-bearing strength test specified in ASTM D5764-97a only specifies the average embedment strength of groove [5]. The embedment strength is also different with the strength from the uniaxial test due to different stress states. Hence, a confined compression test of the wood cylinder was conducted to obtain the real deformation-compression relation in wood groove. A new approach to simulate the localized issue of wood groove in bolted connection by applying the porous constitutive model for wood groove was established to mitigate the dependency on the experiences.

A three-dimensional (3D) FE modeling developed in this paper is based on the phenomena of failure process and failure model of wood groove in bolted connection. During the contacting between bolt and wood groove, localized wood groove is compressed and wood void becomes less and less. If without enough end distance (7d) for the connection, wood groove will crack along the direction of load and shear failure will happen. However, for the connection with enough end distance, only localized wood will be crushed and then plastic hinge may appear in the bolt. In the process of groove crushing, the embedment stiffness of connection changes with the changing of the contact state. At the beginning of contact, embedment stiffness is small. Then, it becomes bigger and nearly keeps a constant. When groove crush is happening, embedment stiffness increases steeply which means that groove becomes compact and the wood void becomes small. In the numerical modeling, the effect of embedment stiffness and strength will be reflected in the porous constitutive by the corresponding relationship between void ratio of wood and pressure on the porous medium.

2. Porous Constitutive Model for Wood

Wood can be seemed as a three-phase medium which is composed of wood solid, liquid, and gas. The wood substance components of wood are the product of wood parenchyma. The liquid component is usually water, and the gas component is usually air. The gaps between the wood substance are called voids. The voids may contain air, water, or both. The void ratio e is the proportion of the volume of voids with respect to the volume of wood substance [6]. Volume of wood changes due to the water expelled from the voids. Mechanical behaviour of wood is also largely dependent on the proportion of wood solids versus voids. When wood is localized compressed, crushing failure is one of typical failure modes and its void ratio becomes less and less. In the elastic stage, the relationship between void ratio and compression stress can be described by a differential equation, the change of the void ratio and the change of logarithm of the equivalent pressure stress [7], shown in the following equation:

$$\mathrm{d}e = -k\,\mathrm{d}\left[\ln\left(p + p_{\mathrm{t}}^{\mathrm{el}}\right)\right], \tag{1}$$

$$p = -\frac{1}{3}\left(\sigma_{\mathrm{R}} + \sigma_{\mathrm{T}} + \sigma_{\mathrm{L}}\right), \tag{2}$$

where e is the void ratio of wood; p is the equivalent pressure stress; σ_{R}, σ_{T}, and σ_{L} are stress components in the directions of radius, tangent, and longitude, respectively; k is the value of the logarithmic bulk modulus, a dimensionless material parameter, which is the slope of the curve between void ratio and the logarithm of the equivalent pressure stress when wood is confined compressed, and it describes the detailed shape of void ratio vs. stress; and $p_{\mathrm{t}}^{\mathrm{el}}$ is the tensile strength of wood.

After using the equivalent pressure stress, the total stress and deviator stress have the following relationships [7]:

$$\begin{aligned} \boldsymbol{\sigma} &= \mathbf{S} - p\mathbf{I}, \\ \mathbf{S} &= 2G\mathbf{e}, \end{aligned} \tag{3}$$

where $\boldsymbol{\sigma}$ is the total stress; $\mathbf{S}$ is the deviator stress; $\mathbf{I}$ is a unit matrix; G is the shear modulus; and $\mathbf{e}$ is the deviator strain [7], which can be expressed as

$$\mathbf{e} = \boldsymbol{\varepsilon} - \frac{1}{3}\varepsilon_{\mathrm{vol}}\mathbf{I}, \tag{4}$$

where $\boldsymbol{\varepsilon}$ is the total strain and $\varepsilon_{\mathrm{vol}}$ is the logarithmic volumetric strain; and $\varepsilon_{\mathrm{vol}} = \ln\left(\mathrm{d}V/\mathrm{d}V_0\right)$, where V is the volume of wood and V_0 is the initial volume of wood. Then, the stress and strain can be solved by the above equations.

3. Confined Compression Test of Wood

A setup for the confined compression test was devised to conduct the experiments for obtaining the relationship between void ratio of wood and equivalent pressure in the direction of parallel to grain, shown as in Figure 1(a). A wood cylinder made of the species of *Pinus Sylvestris* var. *mongolica* was inserted into the steel block through a round hole bored in the block. Then, the wood cylinder was compressed by a steel cylinder which was fit to the hole. The diameters of the wood cylinder and the hole are both 20 mm. After sanded by the sand paper, the wood cylinder was inserted in the hole. During the test, the compression velocity of the cylinder was controlled at a rate of 0.5 mm/min [5, 8] and the compression load and displacement were recorded. The information for wood cylinders is shown in Table 1.

Seven wood cylinders with different initial density and different initial void ratio were compressed parallel to grain. Figure 1(b) shows the typical crushing failure mode of the cylinder. The wood cylinders were shortened, and diagonal

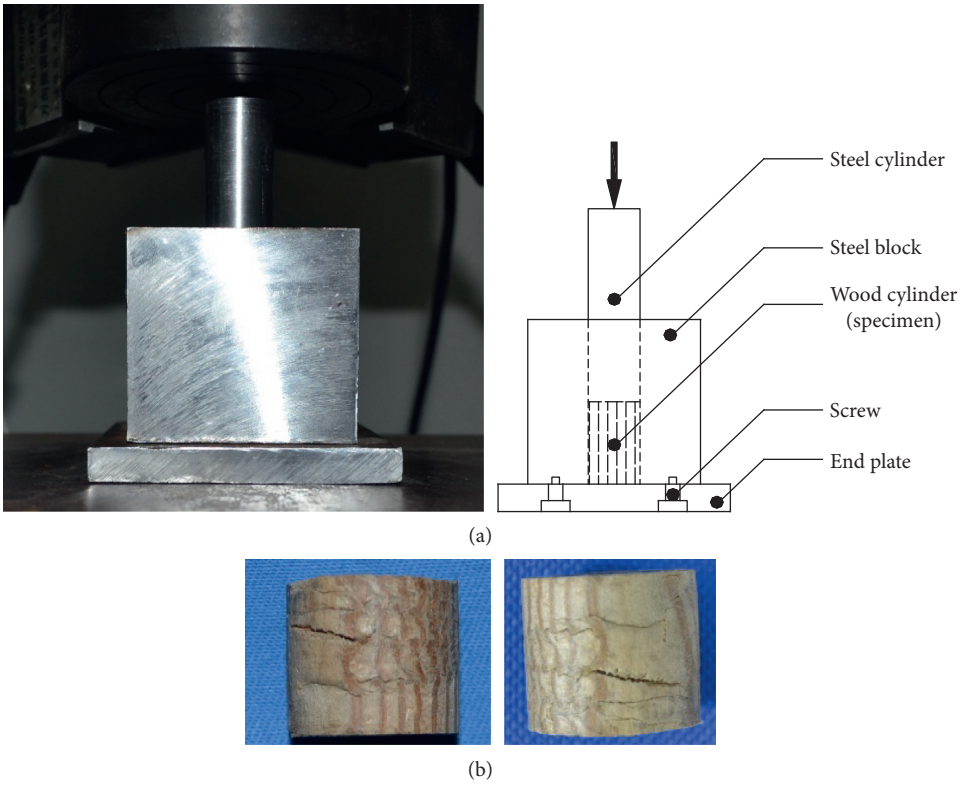

Figure 1: Confined compression test of the wood cylinder parallel to grain: (a) test setup for confined compression experiment; (b) typical crushing failure mode of wood cylinders.

Table 1: The information of wood cylinder specimens for confined compression tests.

Specimen no.	Mass (g)	Initial length (mm)	Initial void ratio
S1	4.317	33.10	3.03
S2	3.863	29.92	2.98
S3	4.638	32.94	2.74
S4	5.272	38.82	2.87
S5	5.768	41.90	2.82
S6	5.459	43.44	3.19
S7	4.188	31.74	2.99

cracks appeared. Figure 2 shows the curves of stress versus elongation parallel to grain from the confined compression tests of wood cylinders.

Based on the relationship among three components including wood substance, water, and void [9], the initial void ratio of wood can be expressed by

$$e_0 = \frac{(1+w)\rho_{wp}}{\rho_0} - 1 = \frac{(1+w)\rho_{wp} S l_0}{m_0} - 1, \quad (5)$$

where e_0, w, and ρ_0 are initial void ratio, moisture content, and density of wood, respectively; ρ_{wp} is the density of the wood solids, for different wood species, $\rho_{wp} = 1.50 - 1.56\,\mathrm{g/cm^3}$, and here an average value [6] was applied; and S, l_0, and m_0 are the cross-section area, initial length, and mass of wood cylinder specimens, respectively. The initial void for wood cylinder specimens is shown in Table 1.

For the confined compression test, the longitudinal strain is not zero, while the tangent strain and radial strain are both zero, which can be derived by the following equation:

$$\begin{bmatrix} \frac{1}{E_L} & -\frac{\nu_{RL}}{E_R} & -\frac{\nu_{TL}}{E_T} \\ -\frac{\nu_{LR}}{E_L} & \frac{1}{E_R} & -\frac{\nu_{TR}}{E_T} \\ -\frac{\nu_{LT}}{E_L} & -\frac{\nu_{RT}}{E_R} & \frac{1}{E_T} \end{bmatrix} \begin{bmatrix} \sigma_L \\ \sigma_R \\ \sigma_T \end{bmatrix} = \begin{bmatrix} \varepsilon_L \\ 0 \\ 0 \end{bmatrix}. \quad (6)$$

Then, the radial stress and tangent stress can be expressed by the longitudinal stress, shown in the following equations:

$$\sigma_R = \frac{\nu_{LR} + \nu_{LT}\nu_{TR}}{1 - \nu_{RT}\nu_{TR}} \frac{E_R}{E_L} \sigma_L, \quad (7)$$

$$\sigma_T = \frac{\nu_{LT} + \nu_{LR}\nu_{RT}}{1 - \nu_{TR}\nu_{RT}} \frac{E_T}{E_L} \sigma_L. \quad (8)$$

For the tested wood species, the elastic ratio and Poisson's ratio [10] are shown in Table 2. After applying the elastic ratio and Poisson's ratio, the equivalent stress of the confined compression wood cylinder can be solved, $\sigma_R = 0.041\sigma_L$, $\sigma_T = 0.031\sigma_L$, and $p = -0.357\sigma_L$, respectively.

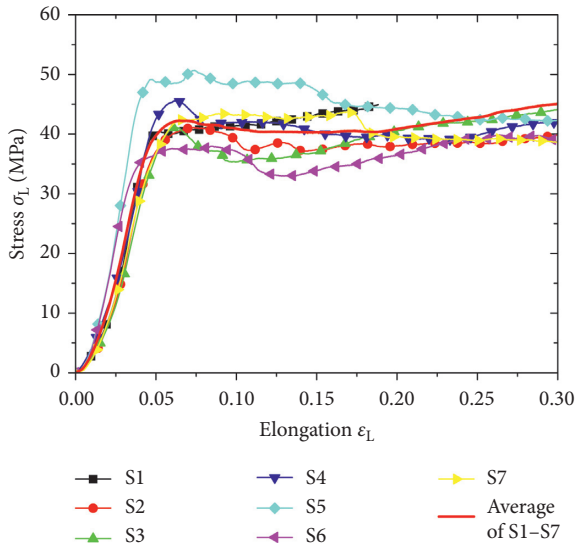

Figure 2: Compression curves of confined compression tests of wood cylinders parallel to the grain.

Table 2: Elastic ratio and Poisson's ratio of wood.

ν_{LR}	ν_{LT}	ν_{RT}	E_T/E_L	E_R/E_L	G_{LR}/E_L	G_{LT}/E_L	G_{RT}/E_L
0.347	0.315	0.408	0.044	0.088	0.096	0.081	0.011

The change of void ratio of the wood cylinder during compressing can be solved by the compression deformation, and its initial void ratio and height can be expressed as

$$\Delta e = e_0 - e = \frac{\Delta h}{h_0}(1 + e_0), \tag{9}$$

where Δe is the change of void ratio of wood, h_0 is the initial length of the wood cylinder, and Δh is the compressive deformation of the wood cylinder. After calculating the equivalent stress p and Δe, curves of the equivalent stress versus the change of void ratio can be obtained, shown as in Figure 3.

Comparing the curves from the experiments of seven wood cylinders in Figure 3(a), the curves of different cylinders with different initial void ratios are close to each other except the specimen S5. However, an average curve of equivalent stress versus change of void ratio can reflect the compression behaviour of wood with the boundary condition of confined restrain. Based on equation (1), the logarithmic bulk modulus of wood was calculated by the average curve. From the average curve shown in Figure 3(b), it can be found that the logarithmic bulk modulus k is not a constant, which reflects three stages of the contact between wood groove and bolt. At the beginning of compression, the logarithmic bulk modulus decreases rapidly until bolt and wood groove contact closely. Then, it nearly keeps a constant. Finally, it climbs rapidly at the same time plasticity is yielded in wood groove. Here, a regressed relationship between the logarithmic bulk modulus k and the change of void ratio Δe was expressed by equation (10) using a polynomial based on the average curve:

$$\begin{aligned} k = {} & 17.910 - 1.279 \times 10^3 \Delta e + 4.116 \times 10^4 \Delta e^2 - 6.850 \times 10^5 \Delta e^3 + 6.343 \times 10^6 \Delta e^4 \\ & - 3.298 \times 10^7 \Delta e^5 + 9.000 \times 10^7 \Delta e^6 - 9.980 \times 10^7 \Delta e^7. \end{aligned} \tag{10}$$

4. FE Modeling and Validation of Embedment Crushing of Wood Groove

4.1. 3D FE Modeling for Bolted Wood Connection. A 3D FE modeling for bolted connection in wood was created using C3D8 solid elements in ABAQUS [7]. Surface contact between wood groove and steel bolt was taken into consideration with the coefficient of friction of 0.15 [11]. The material property of perfect porous elasto-plasticity was assigned to the wood groove zone around the three times of bolt diameter according to crushing deformation in experiment results and FE calculation. A Drucker–Prager plasticity was assigned to wood in the groove zone. The material angle of friction of wood was set as 11°, and dilation angle was zero [4]. An orthotropic elasticity property was assigned to other zones of wood. A perfect elasto-plasticity property was assigned to the steel bolt. The requisite material properties used in FE modeling are listed in Table 3. Here, the properties of clear wood were assigned to the pin groove due to the fact that the wood without defects was usually chosen to make joints and only localized crushing occurred at the joint zone with enough end distance (7d). The dependent relationship of the logarithmic bulk modulus on change of void ratio was implemented in a user defined subroutine UFIELD in which a user defined field variable was defined as the void ratio of each integrate point in the FE software ABAQUS [7].

4.2. Test of Single Bolted Wood Connection. To validate the FE modeling with the perfect elasto-plastic porous constitutive model, 12 lateral resistance tests of single bolt connection of wood made of the species of *Pinus sylvestris* var. *mongolica* were conducted in the direction of parallel to grain according to ASTM D5652 [8]. The dimensions of centre member and side member of connections are all 150 mm in the direction of parallel to grain and 80 mm in the direction of perpendicular to grain, shown as in Figure 4. The diameters of the bolt and groove are 10.5 mm and 13 mm, respectively. The side distance is 40 mm and end distance is 100 mm for every connections. Four groups of thickness combinations for connection specimens, three samples per

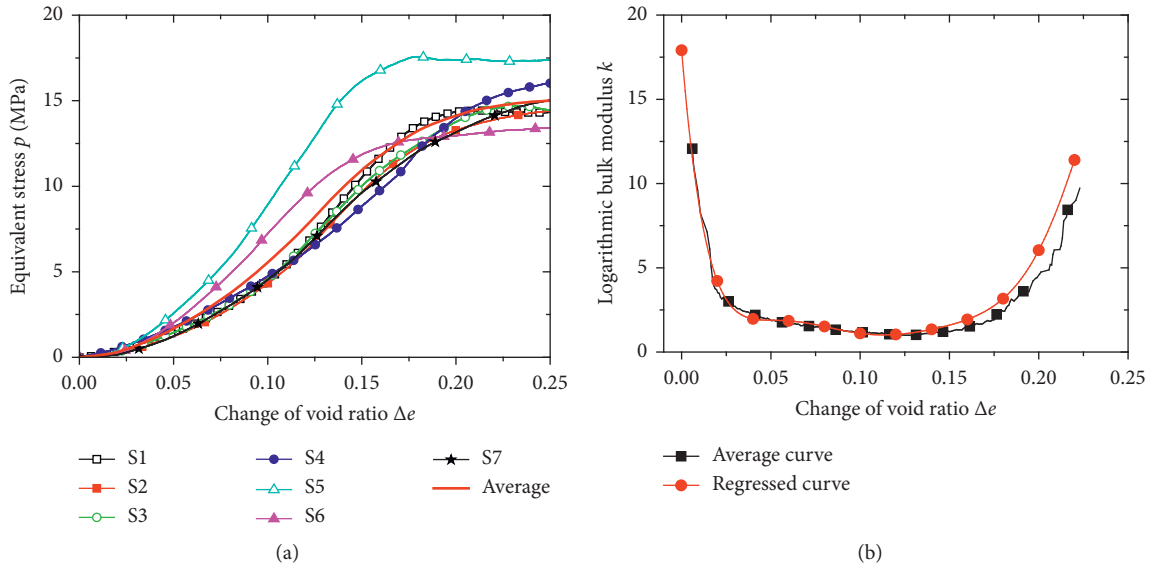

Figure 3: Compression curves of confined compressed wood cylinders parallel to the grain: (a) equivalent stress versus change of void ratio; (b) the logarithmic bulk modulus versus change of void ratio.

Table 3: The material properties for FE modeling.

Requisite constants	Value
Elastic modulus of wood parallel to grain	9000 N/mm^2
Yield stress of wood crushing parallel to grain of wood	40.0 N/mm^2
Tension strength parallel to grain of clear wood	112.9 N/mm^2
Average initial void ratio of wood cylinders	2.944
Elastic modulus of steel bolt	2.06×10^5 N/mm^2
Poisson's ratio of steel bolt	0.3
Yield stress of steel bolt	235 N/mm^2

*The data are from experiments.

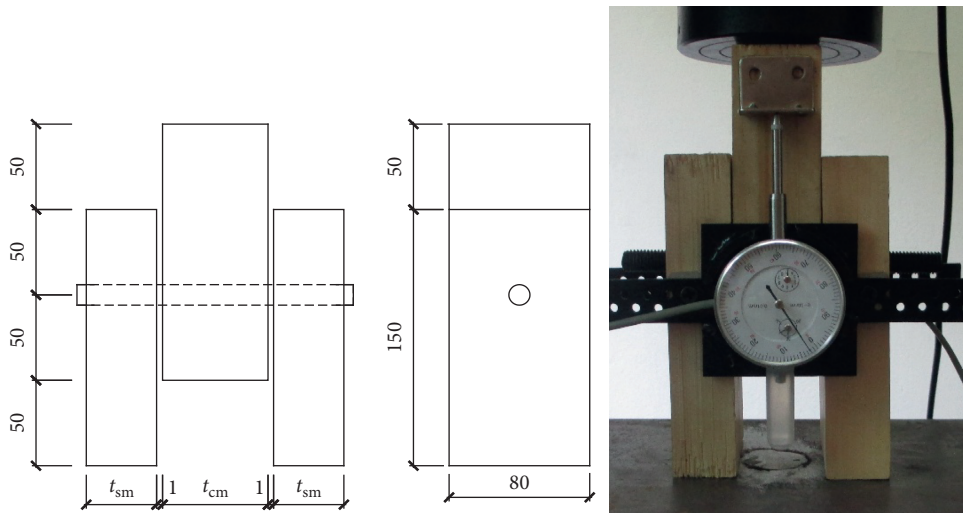

Figure 4: Bolted wood connection.

Table 4: Thickness combinations for bolted wood connections.

	Combination 1	Combination 2	Combination 3	Combination 4
Thickness of centre member, t_{cm} (mm)	40	40	60	60
Thickness of side member, t_{sm} (mm)	30	10	30	60

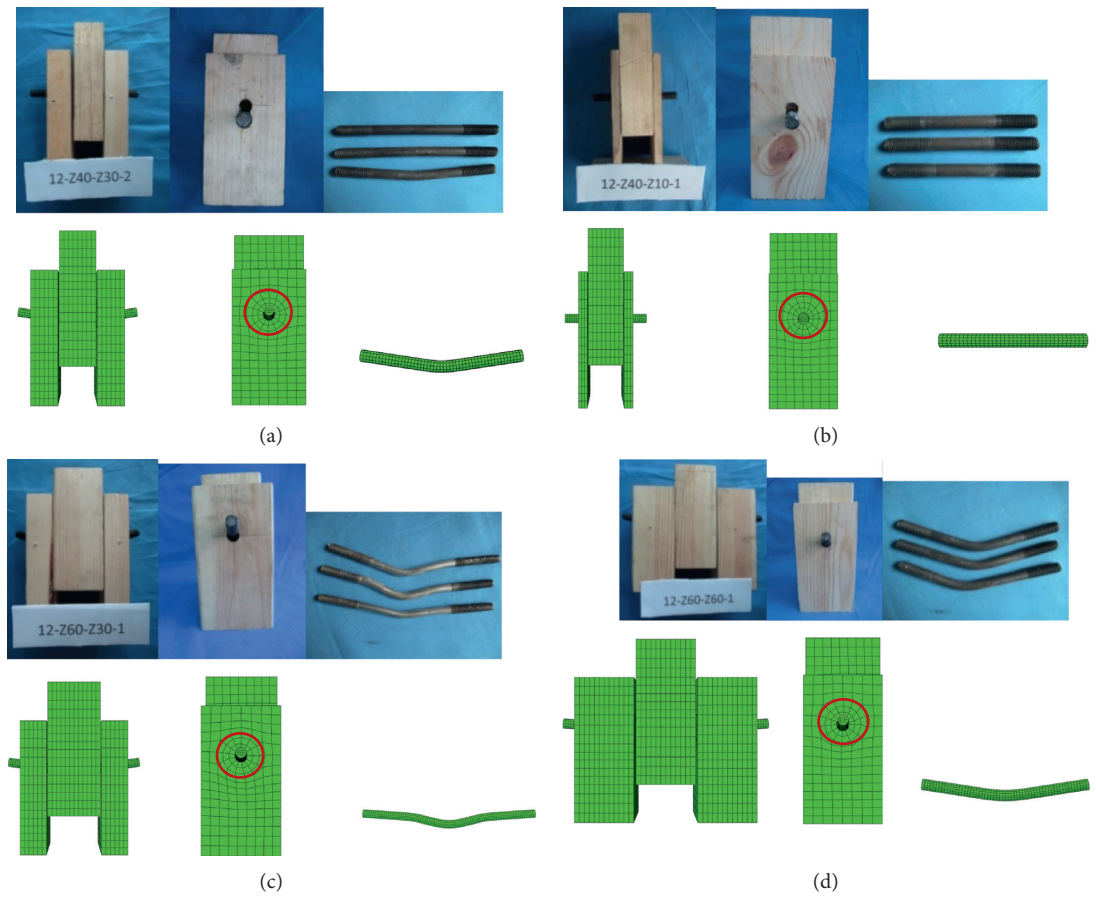

FIGURE 5: Typical failure models of bolt connection with different thickness combinations both in tests and FE simulations: (a) combination 1: $t_{cm} = 40$ mm and $t_{sm} = 30$ mm; (b) combination 2: $t_{cm} = 40$ mm and $t_{sm} = 10$ mm; (c) combination 3: $t_{cm} = 60$ mm and $t_{sm} = 30$ mm; (d) combination 4: $t_{cm} = 60$ mm and $t_{sm} = 60$ mm.

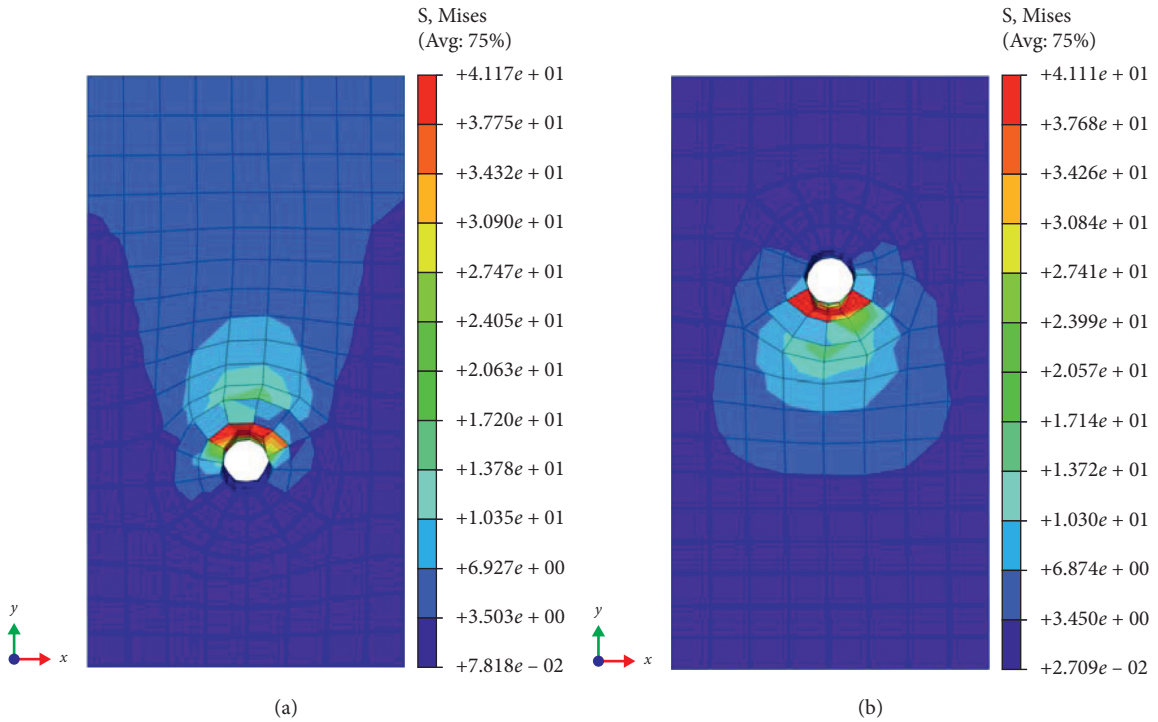

FIGURE 6: Stress contours for wood grooves in (a) centre member and (b) side member (combination 1).

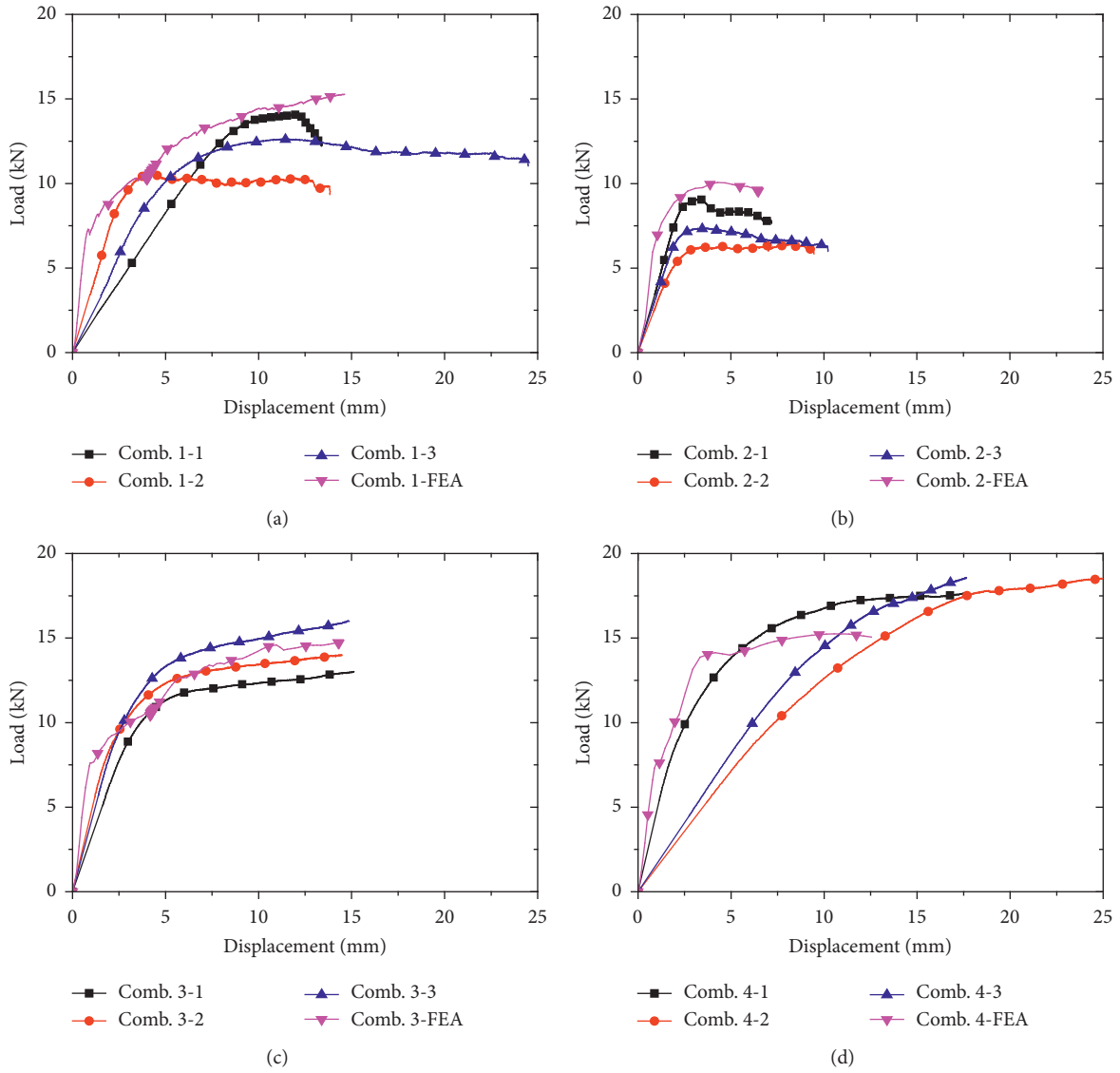

FIGURE 7: The load-displacement curves of single bolt connections: (a) combination 1: $t_{cm} = 40$ mm and $t_{sm} = 30$ mm; (b) combination 2: $t_{cm} = 40$ mm and $t_{sm} = 10$ mm; (c) combination 3: $t_{cm} = 60$ mm and $t_{sm} = 30$ mm; (d) combination 4: $t_{cm} = 60$ mm and $t_{sm} = 60$ mm.

combination, were prepared, whose detail thicknesses are shown in Table 4.

4.3. Validation of FE Modeling. The deformations of all tested connections from different thickness combinations are shown in Figure 5. For each combination, one typical deformed connection and all three deformed bolts are exhibited in the same figure, including these from the tested connection and numerical modeling. The deformation of FE modeling shows good agreement with the experiment observation. Localized crushing failure of pin groove and plastic hinges in the steel bolts appears in different connections. It is obvious that crushing failure did appear at the compressive pin groove, and stress contours for combination 1 are shown in Figure 6. The stress concentration phenomenon and local crushing deformation occur under the contact surface between bolt and groove. The number of plastic hinges in bolts depends on the thickness ratio between the centre member and side member. For the combination 2, the thickness of side member is the thinnest among the four combinations, crushing failure appeared in side member, and the rigid body deformation happened in the bolt. Hence, there was no plastic hinge in the bolt in combination 2. Meanwhile, in combination 4, there were three plastic hinges in the bolt and two hinges in each shear plane. The FE modeling with perfect elasto-plastic porous constitutive exhibits the practicability to simulate the deformation of wood connection including localized deformation of groove and bolt's deformation.

The load-displacement curves for all tested connections and FE simulations are shown in Figure 7. All curves showed the changes of stiffness of bolted connection. The stiffness becomes less and less with the increase in deformation when the localized wood and steel bolt come into plasticity. The

ultimate load from FE results was very close to the maximum loads among three experiment results. While the diameter of the bolt is large and wood members are thin, the yield of groove also can be simulated. The six yield modes for single shear and four yield modes for double shear can all be modeled by the FE modeling. Comparing the deformations of experiments and FE simulations, although the initial stiffness by FE modeling is a little bigger than those of experiments, the overall simulated curves are general accordant with those of experiment curves. The possible reason is that the contact gap between bolt and wood groove brings additional deformation. Hence, the initial stiffness in simulation is more than that of experiment.

5. Conclusions

A method to simulate the localized crushing failure of wood groove in bolted wood connection applying a perfect elastoplasticity porous constitutive model was developed. According to the three-phase composites of wood with solid, water, and gas, wood void ratio expression was derived. A confined compression of the wood cylinder was conducted for void ratio versus stress relationship. The tests can simulate the real stress state in wood groove and provide the FE parameter of wood species for numerical simulation. A relationship between wood void ratio and compression stress was established. The empirical constitutive model for localized crushing wood was validated by the good agreement between experiments and numerical simulations for bolted wood connection with enough end distance (7d). The FE modeling also can predict the load bearing capacity of the all yield modes for single shear and double shear. Its application may be expanded to simulate complex bolted connection in wood structures, such as multiple fastener connections.

Data Availability

The data used to support the findings of this study are available from the corresponding author upon request.

Conflicts of Interest

The authors declare that they have no conflicts of interest.

Acknowledgments

The authors thank the financial support of National Key Research and Development Program of China (no. 2019YFD1101001).

References

[1] D. M. Moses, *Constitutive and analytical models for structural composite lumber with applications to bolted connections*, Ph.D. Dissertation, University of British Columbia, Vancouver, Canada, 2000.

[2] T. Zhou and Z. W. Guan, "A new approach to obtain flat nail embedding strength of double-sided nail plate joints," *Construction and Building Materials*, vol. 25, no. 2, pp. 598–607, 2011.

[3] H. Jung-Pyo and D. Barrett, "Three-dimensional finite-element modelling of nailed connections in wood," *Journal of Structural Engineering*, vol. 136, no. 6, pp. 715–722, 2010.

[4] S. Carmen, *Mechanical behaviour of timber joints with slotted-in steel plates*, Ph.D. Dissertation, Technology University Delft, Delfts, Netherlands, 2012.

[5] ASTM D 5764-97a, *Standard Test Method for Evaluating Dowel-Bearing Strength of Wood and Wood-Based Products*, American Society for Testing and Materials, West Conshohocken, PA, USA, 2002.

[6] F. F. P. Kollmann, A. Wilfred, and J. R. Cote, *Principles of Wood Science and Technology, 1 Solid Wood*, Springer-Verlag New Yourk Inc, New York, NY, USA, 1968.

[7] D. S. Simulia, *ABAQUS 6.14. ABAQUS Theory Guide*, Dassault Systèmes Simulia Corp., Johnston, RI, USA, 2014.

[8] ASTM D 5652-95, *Standard Test Methods for Bolted Connections in Wood and Wood–Based Products*, American Society for Testing and Materials, West Conshohocken, PA, USA, 2002.

[9] M. D. Wood, *Soil Behaviour and Critical State Soil Mechanics*, Cambridge University Press, Cambridge, UK, 1990.

[10] D. W. Green, E. Winandy Jerrold, and E. Kretschmann David, *Mechanical Properties of Wood, Wood as an Engineering Material*, Forest Products Laboratory, Madison, WI, USA, 1999.

[11] W. Simpson and T. W. Anton, *Physical Properties and Moisture Relations of Wood: Wood Handbook, Wood as an Engineering Material*, Forest Products Laboratory, Madison, WI, USA, 1999.

Hindawi
Advances in Civil Engineering
Volume 2020, Article ID 6639789, 10 pages
https://doi.org/10.1155/2020/6639789

Research Article

Flexural Properties of Steel-Bamboo Composite Slabs in Different Connection Methods

Hui Zhong[1], **Qifeng Shan**[1], **Jialiang Zhang**[1], **Xiaocun Zhang**[1] and **Yushun Li**[2]

[1]*School of Civil and Environmental Engineering, Ningbo University, Ningbo 315211, China*
[2]*College of Civil Engineering and Architecture, Qingdao Agricultural University, Qingdao 266109, China*

Correspondence should be addressed to Yushun Li; lys0451@163.com

Received 5 October 2020; Revised 20 November 2020; Accepted 13 December 2020; Published 23 December 2020

Academic Editor: Dongsheng Huang

This paper presents a study aimed to estimate the flexural performance of profiled steel sheet-bamboo plywood composite slabs as a first step to evaluate its potential application as structural components. Nine specimens were tested to investigate the stability of steel-bamboo composite structure. According to different connection methods, three types of composite slabs were discussed, including pure bonding slabs (PBSs), composite bonding slabs (CBSs), and reinforced composite bonding slabs (RCBS). The result showed that specimens employed multiple composite methods (RCBS) exhibited excellent flexural bearing capacity and stiffness compared with PBS. The increase of bamboo plywood thickness could improve bearing capacity and flexural stiffness of composite slabs, while the reduction of screw spacing could enhance the bearing capacity and ductility of composite slabs. The RCBS, which can provide higher bearing capacity and stiffness and possess excellent deformation capability, are well worth of research and practical application.

1. Introduction

Today, environmental issues are receiving increasing attention because human activities have caused abnormal weather in many parts of the world. Construction industry, which is a huge source of carbon emissions and energy consumption, is facing the challenge of environmental protection. In order to maintain sustainable development of human society, it is essential to employ environment-friendly materials as construction materials [1, 2]. Bamboo has long been known for its fast growth, lightweight, high strength, and biodegradable properties. It is a kind of natural building material with the advantages of a large strength ratio and convenience of processing. However, the rigidity of bamboo plywood is insufficient and large deformation will occur when the load is applied [3, 4].

To have a better application of bamboo plywood in building structures, a new structural system named bamboo-steel composite structure was developed. This kind of structure consists of various composite members such as composite slab, composite wall, composite beam and composite column, with semirigid connection or other reliable connection methods [5–7]. Those structures combine the high strength of steel with the environmental amity of bamboo. Two materials are complementary to each other and bamboo plywood can avoid the weakness of easy buckling for profiled steel sheets. Buildings with those components are environmental friendly, light weight, and earthquake-resistant [8–11].

However, as a new structure system, researches on the steel-bamboo composite structure are rarely involved. Domestic and foreign researches focus on the composite structures like steel-concrete composite floor [12], steel-wood structure [13], bamboo-concrete composite beams [14], CFRP, and wood structure [15]. Therefore, it is essential to investigate the properties of the steel-bamboo composite slabs.

In this study, a new type of bamboo-steel composite slab which consisted of four pieces of bamboo plywood and one piece of profiled steel sheet (Figure 1) was proposed. Adhesive bonding and adhesive-screw hybrid connection were utilized to form a whole component [16, 17]. According to

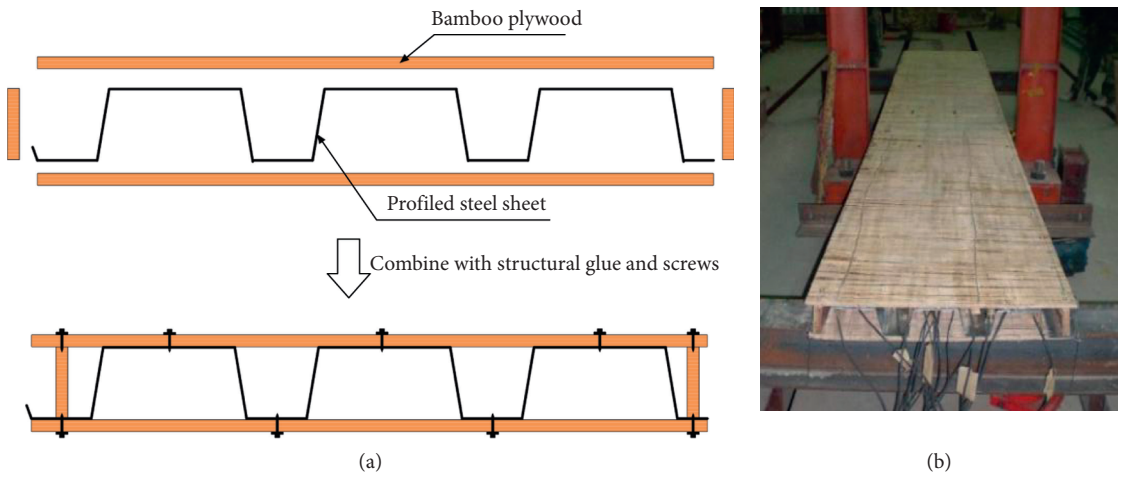

Figure 1: (a) Section form of composite slabs. (b) Photograph.

different connection methods, nine slab specimens were tested to investigate the mechanical properties of composite slabs and to discuss their application prospects.

2. Specimens and Loading

2.1. Specimens. Nine large-scale specimens were tested to investigate the mechanical properties of composite slabs. The dimension of these slab specimens is 0.65 m × 3.3 m and the span is 3.0 m. Three connection methods were adopted (Figure 2). One connection method named PBS was connected by simple adhesive bonding (Figure 2 (PBS)), and CBS was strengthened with the self-tapping screw on the basis of PBS (Figure 2 (CBS)). The last method is RCBS which improved capacity with bamboo laths nailed on both sides of the composite slab (Figure 2 (RCBS)). The first group, namely PBS, is designed as the control group. The difference between specimens in PBS is the thickness of bamboo plywood. The second group, CBS, is designed to investigate the function of screw and thickness of bamboo plywood as well. In the last group, RCBS, bamboo laths were utilized to compare with PBS and CBS. All parameters of these specimens are shown in Table 1. In addition, the section of a composite slab is hollow where it can be filled with various insulating piping, and the quality of this kind of composite floor is relatively light. In order to meet the requirements of practical applications, fine aggregate concrete of corresponding thickness can be laid on the floor to meet the seismic conditions. Thus, the vibration problem of composite slabs is not considered here.

2.2. Material Properties

2.2.1. Bamboo Plywood. As a new type of bamboo-based material, bamboo-based panel possess the advantages of high strength, low cost, and large dimensions with natural texture. The type of bamboo-based panel which is chosen for the composite slab is bamboo plywood. Raw bamboos are processed into a bamboo mat or bamboo curtain, and these crisscross group bamboo mats and curtains will be as the core material; after several processes including drying, dipping, lay-up and hot-press gluing, and the bamboo plywood was finally made. Typical thickness of bamboo plywood varies from 10 mm to 25 mm, and this kind of bamboo plywood is massively produced and mainly used as concrete formwork in China and other Southeast Asian countries. In this experiment, the bamboo plywood is used as a component to prevent the profiled steel sheet from buckling. And in order to be used in practical engineering, the thickness of slabs should be thinner. Therefore, the thickness of bamboo plywood for composite specimens can be appropriately reduced and was chosen as 5 mm, 6 mm, and 7 mm, respectively.

The average Young's modulus of bamboo plywood (E_b) is shown in Table 2, which were obtained by conducting amounts of typical tests according to conventional testing methods for timber material. The detailed dimensions of the specimen are calculated by the following formula: $L = 20 \times t + 5\,(\text{mm})$. L is the length of bamboo plywood; t is the thickness of bamboo plywood. The width of specimens is 50 mm. And these tests were following the standard used in the U.S. (ASTM Standards: D4761). Figure 3(a) shows the typical tests to measure the modulus of elasticity (MOE) and modulus of rupture (MOR) of bamboo plywood. The load-deflection curve of a typical specimen is shown in Figure 3(b). This curve showed a linear relationship to 0.8 kN, approximately 50% of the ultimate load. The result indicated that bamboo plywood has a strong deformation capacity.

2.2.2. Profiled Steel Sheet. The profiled steel sheet used cold-rolled carbon constructional steel strip with a Young' modulus (E_s) of 206 GPa, a yield strength (f_y) of 235 MPa, a tensile strength (f_t) of 375 MPa, and the thickness of the steel sheet adopted here is 0.75 mm. It is a common cold-formed thin-walled steel application to construction, such as concrete-steel composite structures (composite deck slabs) or light-weight steel construction (light-weight walls). The dimension details of profiled steel sheets are shown in Figure 4.

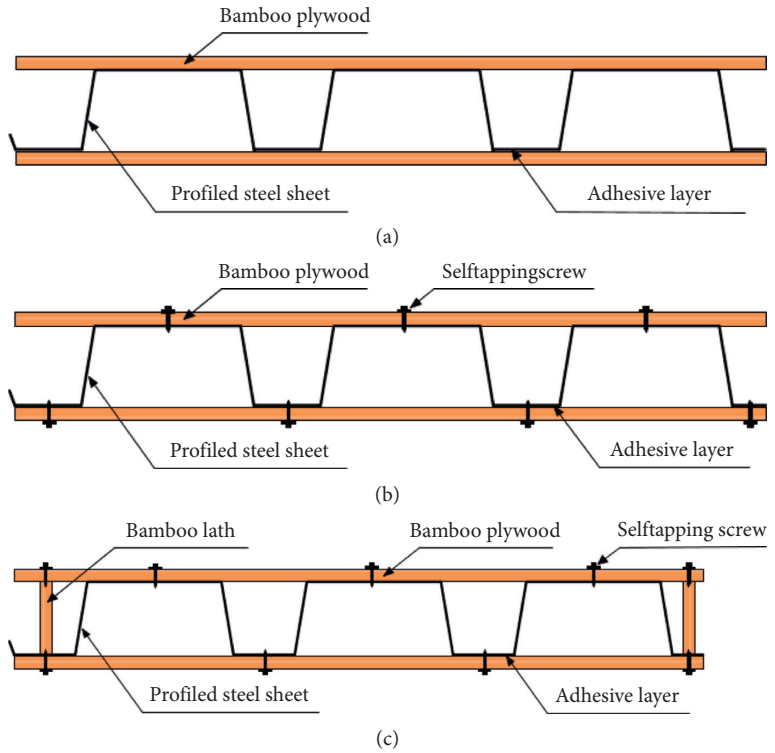

Figure 2: Methods of connection. (a) PBS. (b) CBS. (c) RCBS.

Table 1: Detail of test specimens.

Specimens	t_b (mm)	t_s (mm)	h_a (mm)	Screws spacing (mm)	Span (m)
PBS-5	5.0	0.75	85.4	—	3.0
PBS-6	6.0	0.75	87.4	—	3.0
PBS-7	7.0	0.75	89.4	—	3.0
CBS-5	5.0	0.75	86.0	200, 200	3.0
CBS-6	6.0	0.75	87.8	200, 200	3.0
CBS-7	7.0	0.75	89.2	200, 200	3.0
RCBS-7-1	7.0	0.75	89.4	200, 400	3.0
RCBS-7-2	7.0	0.75	89.4	200, 200	3.0
RCBS-7-3	7.0	0.75	89.4	200/100, 200	3.0

Note. The height of profiled steel sheet is 75 mm. t_b is the thickness of bamboo plywood; t_s is the thickness of profiled steel sheet; h_a is the height of composite slab; selftapping screws spacing, A, B, and C: A is the uniform spacing on top bamboo plywood, B is the close-set spacing on top bamboo plywood in dense zone, and C is the uniform spacing on bottom bamboo plywood. The screw spacing of a lateral plate is the same as the bamboo plywood.

Table 2: Material properties.

Parameter	Value (MPa)
E_b	5885
E_s	206
f_y	235
f_t	375

Note. E_b is the Young's modulus of bamboo plywood; E_s is the Young' modulus of profiled steel sheet; f_y is the yield strength of profiled steel sheet; f_t is the tensile strength profiled steel sheet.

2.2.3. Adhesive Bonding and Selftapping Screw. In the experiment, two connection methods were adopted: adhesive bonding and selftapping screw. Among them, adhesive bonding is used to connect the surface between the bamboo plywood and the profiled steel sheet while selftapping screw is used for local reinforcement. The adhesive bonding used is called National Adhesives, which are produced and supplied by Henkel [18]. This adhesive is a common structural epoxy used for bonding metal, wood, glass, concrete, and others, with the advantage of rapid curing and high strength. And the selftapping screw used is common and efficient for cold-formed steel structures with a nominal diameter of 4.5 mm. The mechanical properties of this kind of adhesive and selftapping screw had been tested in previous experiments, and the shear strength and shear modulus of this structural adhesive were 5.1 MPa and 0.25 GPa. [19].

2.3. Specimens Preparation. The specimens processing can be divided into four steps in total: (1) wiring and gluing. (2) Assembling. (3) Screwing. (4) Heavy object compaction (Figure 5). Before processing and preparing these composite

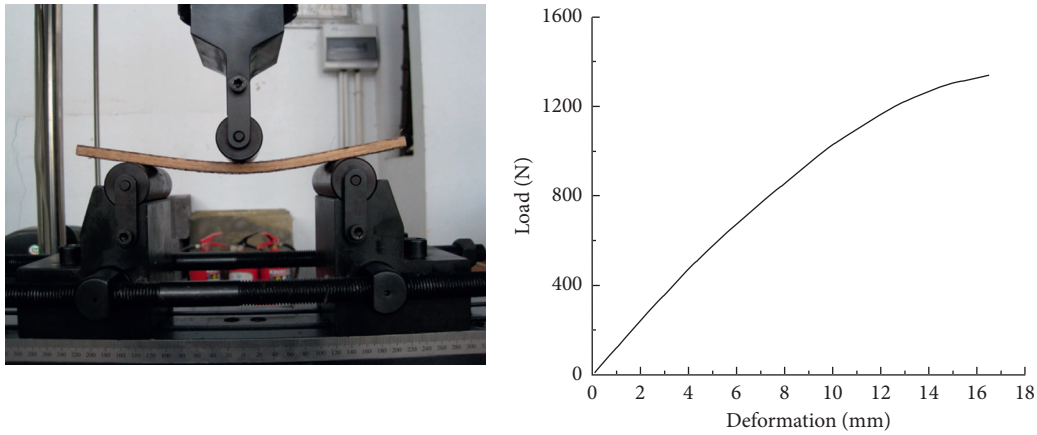

(a) (b)

Figure 3: (a) Typical test for bamboo plywood. (b) Load-deformation curve of specimens.

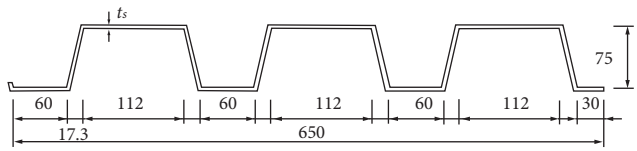

Figure 4: Dimension details of profiled steel sheet.

(a) (b) (c) (d)

Figure 5: Specimens processing. (a) Wiring and gluing. (b) Assembling. (c) Screwing. (d) Compaction.

slabs, it is necessary to do surface treatments for the bamboo plywood and profiled steel sheet, which could remove impurities on the surface of the material and guarantee their connection effect. These specimens which used structure adhesive need pressure and curing, and the pressure period is two days, and the curing period is a week.

2.4. Test Specimens and Set-Up. All the tests were carried out in the Civil Engineering laboratories at Ningbo University and Northeast Forestry University. A Jack was used to control load and simulate the uniformly distributed load by means of eight points with four concentrated force. The width of the load application engaged the entire width of bamboo plywood. And strain gauges with a sampling frequency of 2 Hz were used to detect the stress-strain distribution of profiled steel sheet and bamboo plywood in the middle and a quarter of the slabs, respectively. Several displacement sensors were arranged to record the deformation of these specimens. Figure 6 shows the positions of strain gauges. Figure 7 shows the schematic representation of eight-point bending test.

3. Experimental Result

3.1. Failure Modes and Test Observations. Typical failure processes of composite slabs are shown in Figure 8, respectively.

Those bamboo-steel composite slabs have similar failure processes during the experiment, and all of the failure processes can be divided into three stages. Among them, the failure process of PBS is typical. During the first stage, the sound of crack can be heard and the initial crack can be observed on the connection surface of the slab. In the second

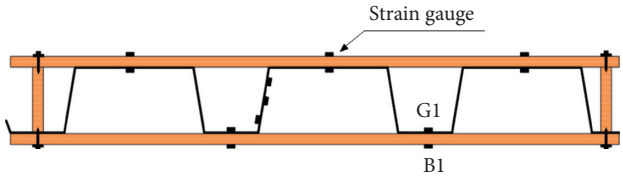

Figure 6: The positions of strain gauges.

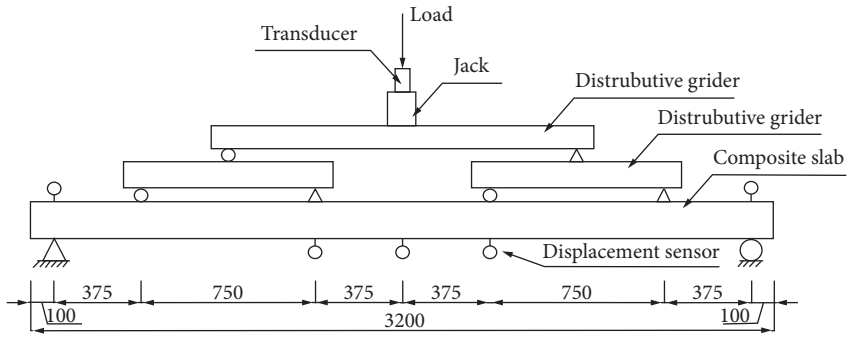

(a)

(b)

Figure 7: Eight points bending test. (a) Diagrammatic view. (b) Photograph.

(a) (b) (c)

Figure 8: Failure mode of composite slabs. (a) Failure mode of PBS. (b) Failure mode of CBS. (c) Failure mode of RCBS.

stage, new cracks continued to exist and original cracks gradually widened. Most of the cracks were located at the upper surface of the slabs where they are close to the loading point. When the structural adhesive was fully damaged, the last stage had reached. Two materials were obviously separated, and the profiled steel sheet was locally buckled in the compression zones of the midspan section.

CBS and RCBS had the same failure processes as PBS during the first stage and second stage. In the last stage, in addition to the failure characteristics of PBS, a different phenomenon was visible as well. Screws of CBS were loosed, and the profiled steel sheet was locally buckled after the bamboo plywood between the screws gradually bulged. As for RCBS, the lateral slab was significantly deformed and the

bamboo plywood at the screw connection was turn off before the profiled steel sheet was locally buckled. At the end of the test, local buckling as well as bending failure of longitudinal slab were observed.

3.2. Load-Deflection Curves and Bearing Capacity. The load vs. midspan deflection curves of specimens are shown in Figure 8, which are divided into three types according to different connection methods.

The curves of CBS were mainly linear up to the peak load, and then, the curves dropped suddenly. By looking at the curve shape of PBS and RCBS, it can be found that both have gone through the elastic stage, the plastic stage, and the descending stage. This suggests that they have similar ductility. However, it is evident that RCBS had a significant increase in bearing capacity. For example, the ultimate capacity of RCBS-7-2 was about four times higher than PBS-7. All of the RCBS was linear up to 21 kN, which were approximately 88%, 70%, and 74% of their peak load, respectively. Meanwhile, the deformation of this type specimen was considerably large. The maximum midspan deflection of RCBS-7-2 reached 59 mm measured by displacement sensor (Figure 9(c)). However, for those composite slabs, the maximum loads on serviceability limit states (q_n) were much less than the ultimate ones (q_u). For example, q_n of RCBS-7-3 (10 kN) was much smaller than q_u (28.35 kN). By comparing the theoretical bearing capacity with the experimental results, it can be concluded that the bearing capacity (q_n) mainly depends on the original material properties of the bamboo plywood or profiled steel plate, not the reinforcement method. Of course, it is no doubt that these reinforced ways can improve the whole stability of composite slabs.

A summary of the experimental results is presented in Table 3.

4. Experimental Analysis

4.1. Result Analysis. From the above, PBS, which used adhesive bonding only, is easy to cause adhesive failures. Once the profiled steel sheet and the bamboo plywood are separated, the bamboo plywood will produce a larger deflection which breaks the connection of steel and bamboo, resulting in the local buckling of the profiled steel sheet finally. Therefore, PBS is not suitable to exert the bearing capacity of the composite structure. CBS can avoid large-scale adhesive failure, but the stiffness of them (S_w) are significantly larger than PBS and RCBS. Destruction of these specimens began with the debonding of the bamboo plywood between the screws, then the screw connection failed quickly, and finally led to the buckle of the profiled steel sheet. As for RCBS, their ultimate bearing capacity and overall stability are significantly enhanced. In the failure experiment, the bamboo plywood cracked before the nails was pulled out, then the bamboo board came unglued, and eventually the whole board failed. Therefore, we can draw the conclusion that the property of bamboo plywood has been brought into full play. Comparing with the former two methods, RCBS can effectively improve the ductility of the composite slabs and is more conducive to the application of engineering.

4.2. Parametric Study. We adopted three connection modes to analyze the reliability and practicability of the bamboo-steel composite slabs. The results indicated that the mechanical properties of RCBS were better than PBS and CBS. Meanwhile, parameters such as the thickness of bamboo plywood and the spacing of self-tapping screws may also cause differences in the ultimate bearing capacity.

4.2.1. Effect of Bamboo Plywood Thickness. A variety of different thickness of bamboo plywood were used in this experiment. In general, as the thickness of bamboo plywood increased, the ultimate bearing capacity of the composite slab improved. In the first group, with the increasing of the bamboo plywood thickness, the maximum load of the composite slab has been increased (Figure 9(a)). However, in the second group, under the effect of the screws, the variation in the thickness of the bamboo slab has little effect on mechanical performance.

4.2.2. Effect of Selftapping Screw Spacing. The specimens with selftapping screws can enhance the integrity of composite plates. For RCBS-7-1, its screw spacing is 200/400 mm and ultimate bearing capacity is 23.81 kN. The screw spacing of RCBS-7-2 is 200 mm, and its ultimate bearing capacity is 29.82 kN. By changing the screw spacing of the bottom bamboo plywood, the ultimate bearing capacity is increased by 25%. On the other hand, the connections between the steel sheet and bamboo plywood have also been improved. Taking RCBS-7-2 as an example, two strain gauges G1 and B1 were arranged at the bottom of its midspan slab (Figure 6) to draw its load-strain curve. By observing the curve (Figure 10), it can be found that the strain changes of the two strain gauges have high consistency, indicating that the combination effect between the steel sheet and bamboo plywood is obvious. Therefore, after adding screws, the connection between the bamboo plywood and the profiled steel sheet is much more stable, and the toughness and overall bearing capacity of the specimens are improved. Moreover, in the steel-bamboo structure, bamboo plywood was often more easily broken than screw joint when they are strengthened with screws, so it can be known that adding screws can thoroughly play the performance of bamboo plywood. In the experiment, screws arranged with a spacing of 200 mm can satisfy the strengthening of steel-bamboo structure. If the more denser spacing is adopted, local stiffness will be too large, thus reducing the overall strength and ductility.

4.2.3. Bamboo Lateral Slab. It is very effective to use lateral slabs to improve the ultimate bearing capacity and overall stability of bamboo-steel composite slabs. RCBS-7-2 attained ultimate bearing capacities of 29.82 kN, which are much higher than that of other specimens (Figure 11). Meanwhile,

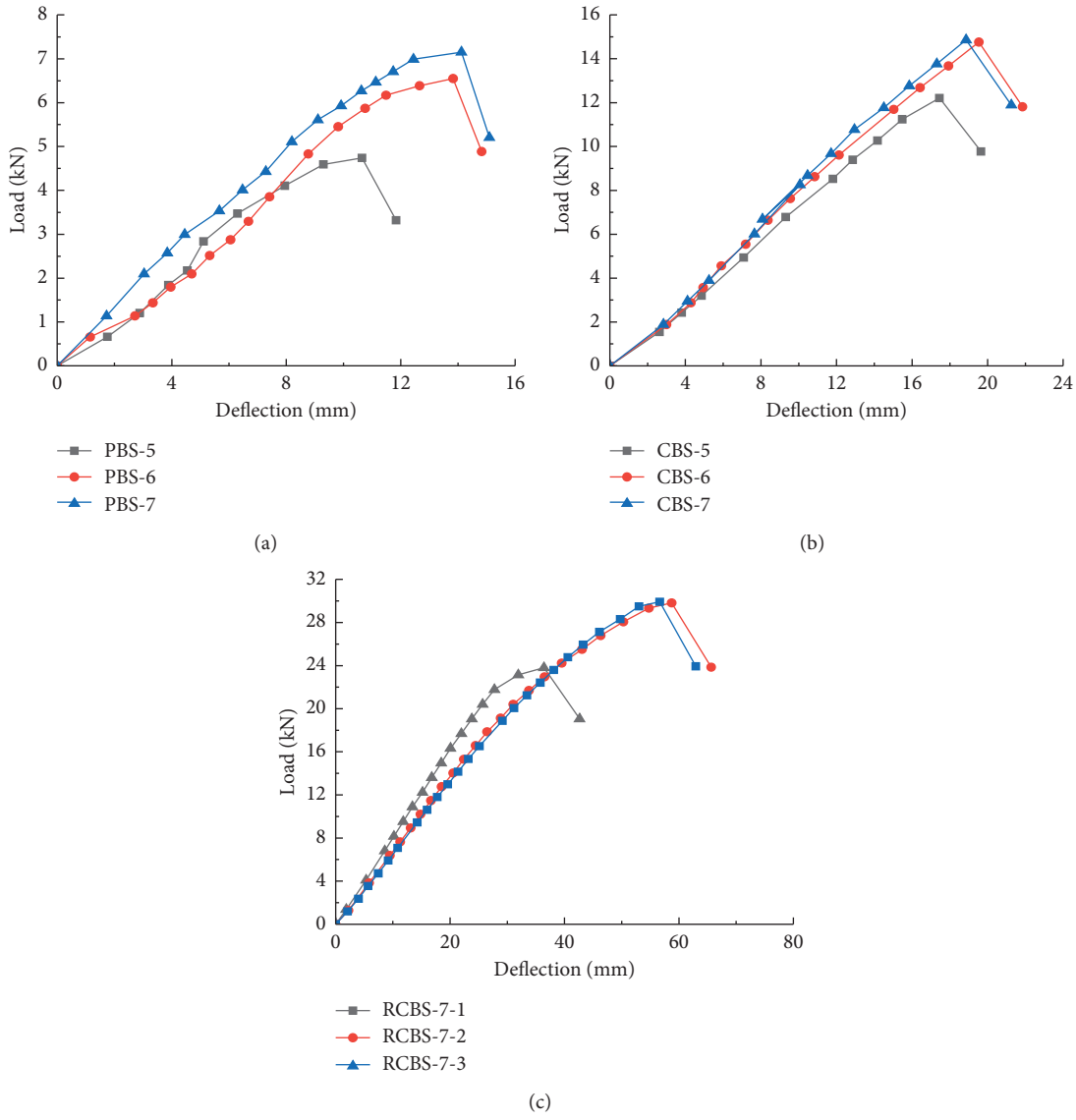

Figure 9: Load-deflection curves for bamboo-steel composite slabs. (a) Load-deflection curves for PBS. (b) Load-deflection curves for CBS. (c) Load-deflection curves for RCBS.

Table 3: Test results of large-scale specimens.

Specimens	Screws spacing (mm)	q_u (kN)	$f_{c\max}$ (mm)	S_w (kN/mm)
PBS-5	—	4.74	10.65	0.44
PBS-6	—	6.55	13.83	0.47
PBS-7	—	7.16	14.12	0.51
CBS-5	200, 200	12.21	17.48	0.70
CBS-6	200, 200	14.76	19.54	0.76
CBS-7	200, 200	14.86	18.86	0.79
RCBS-7-1	200, 400	23.81	36.41	0.65
RCBS-7-2	200, 200	29.82	58.74	0.51
RCBS-7-3	200/100, 200	28.35	56.65	0.50

Note. q_u is the ultimate load on bamboo-steel composite slab; $f_{c\max}$ is the maximum midspan deflection of bamboo-steel composite slab; S_w is stiffness per unit.

the maximum deformation capacity of these specimens has been greatly improved. Taking RCBS-7-2 as an example, it has a maximum deformation of 58.74 mm, which is much larger than the other specimens (Figure 12(a)). Therefore, the bamboo lath used can help these composite slabs to play better ductility and have good seismic performance as well.

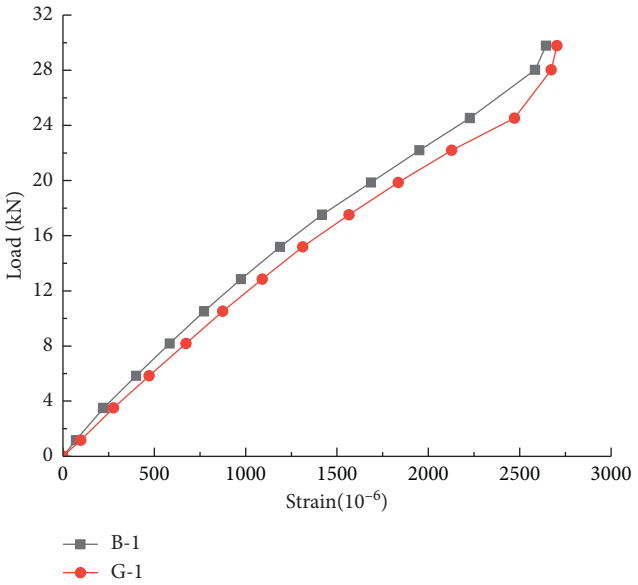

Figure 10: Load-strain curve of B-1 and G-1.

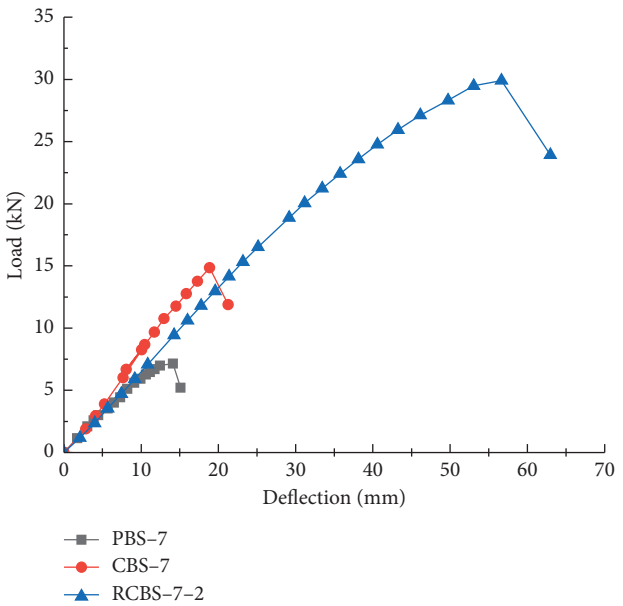

Figure 11: Comparison of composite slabs with different reinforcement methods.

(a) (b)

Figure 12: Deformation changes of RCBS. (a) Large deformation failure. (b) Recoverable deformation.

What's more, by comparing the picture before and after deformation (Figure 12(b)), we can draw the conclusion that RCBS have a better ability to recover deformation. This is because the deformation of those specimens is mainly elastic deformation, which can be recovered quickly after unloading. Meanwhile, the residual deformation was very small which ensures that the composite floor can withstand repeated loads without any damage in actual work.

5. Conclusion

The present study is an attempt to investigate the possibility of combination between bamboo-based panels and profiled steel sheets with adhesives or adhesive-screw mixing connections to be slab floor. Based on the experimental results of nine composite slab specimens, the following can be concluded:

(1) The failure of composite floor is caused due to the invalidation of steel and bamboo connection. PBS and CBS are prone to connection failure because once they enter the plastic stage, their connections will quickly fail. Pure adhesive bonding is hard to provide good connection ability to the interface of bamboo plywood and profiled steel sheet. Even though CBS is enhanced with selftapping screws, the connection is not stable enough to prevent the separation of the whole component.

(2) The bearing capacity of RCBS is much better and they are ductile in the plastic deformation stage which is essential in practical application. This kind of composite slabs, with the advantage of simplicity, effectiveness, and economy, can make it the most industrially viable. The bamboo plywood side plate can effectively enhance the integrity of the composite floor and make the composite floor show ductility. Therefore, it is suggested that the composite floor should adopt the section form which is strengthened with a bamboo lateral slab.

(3) With the thickness of bamboo plywood increasing, the ultimate bearing capacity of composite slab improves obviously. In order to improve the performance of composite slab, it is important to choose a suitable thickness of bamboo plywood. Although adopting thicker bamboo plywood or steel sheets is beneficial for composite structure, its contribution to the whole bearing capacity is limited comparing with the connection method. Therefore, the thickness requirements can be met by using bamboo plywood and steel plates produced by ordinary processing.

(4) The screw spacing had an obvious influence on the bearing capacity and ductility of the composite structure. In the case of RCBS, the ultimate bearing capacities improve significantly when the screw spacing ranges between 200 mm and 400 mm. However, as for CBS, the ultimate bearing capacities do not enhance markedly when the screw spacing ranges between 100 mm and 200 mm. But the ductility of the specimen can be improved to some extent.

Data Availability

The data used to support the findings of this study are available from the corresponding author upon request.

Conflicts of Interest

The authors declare that there are no conflicts of interest regarding the publication of this paper.

Acknowledgments

The authors gratefully acknowledge the financial support provided by the National Natural Science Foundation of China (NSFC) (51678310 and 51978345), Ningbo Science and Technology Project (202002N3090), and Ningbo Natural Science Foundation (2018A610349). The acknowledgment is also extended to technical support of Civil Engineering Laboratories of Ningbo University and Northeast Forestry University.

References

[1] A. T. Balasbaneh, A. K. B. Marsono, and E. K. Kermanshahi, "Balancing of life cycle carbon and cost appraisal on alternative wall and roof design verification for residential building," *Construction Innovation*, vol. 18, no. 3, pp. 274–300, 2018.

[2] S. Paudel, S. Couturier, P. H. Nguyen, R. Kamphuis, B. Lacarrière, and O. Le Corre, "A relevant data selection method for energy consumption prediction of low energy building based on support vector machine," *Energy and Buildings*, vol. 138, pp. 240–256, 2017.

[3] M. Mahdavi, P. L. Clouston, and S. R. Arwade, "Development of laminated bamboo lumber: review of processing, performance, and economical considerations," *Journal of Materials in Civil Engineering*, vol. 23, no. 7, pp. 1036–1042, 2011.

[4] H. T. Li, Q. s. Zhang, D. S. Huang, and A. J. Deeks, "Compressive performance of laminated bamboo," *Composites Part B: Engineering*, vol. 54, pp. 319–328, 2013.

[5] S. Wei, Y. Li, H. Shen, and T. Jiang, "Tests and analysis on flexural strength of lightweight bamboo-steel composite floor slab," in *Proceedings of the International Conference on Electric Technology & Civil Engineering*, Lushan, China, April 2011.

[6] Y. Li, S. Wei, Z. Huang, B. Ge, and W. Yan, "Experimental study on mechanical behavior of profiled steel sheet-bamboo plywood composite slabs," *Jianzhu Jiegou Xuebao/Journal of Building Structures*, vol. 29, no. 1, pp. 96–102, 2008.

[7] Y. Xiao, B. Shan, R. Z. Yang, Z. Li, and J. Chen, "Glue laminated bamboo (GluBam) for structural applications," *Materials and Joints in Timber Structures*, vol. 9, no. 1, pp. 589–601, 2014.

[8] J. Guo, Y. Li, B. Yang, and Y. Fei, "Study on the design of steel-bamboo composite member," *Applied Mechanics and Materials*, vol. 204–208, pp. 4047–4050, 2012.

[9] Y. Wei, M. Q. Zhou, and D. J. Chen, "Flexural behaviour of glulam bamboo beams reinforced with near-surface mounted steel bars," *Materials Research Innovations*, vol. 19, no. 1, pp. 98–103, 2015.

[10] P. Lacki, P. Kasza, and K. Adamus, "Optimization of composite dowels shape in steel-concrete composite floor," *Composite Structures*, vol. 222, Article ID 110902, 2019.

[11] T. V. P. Caldeira, N. Dourado, M. F. S. F. de Moura, and J. J. L. Morais, "Quasi-static behavior of moment-carrying steel-wood doweled joints," *Construction and Building Materials*, vol. 53, pp. 439–447, 2014.

[12] X. Zhou, Y. He, Z. Jia, and S. Nie, "Experimental study on vibration behavior of cold-form steel concrete composite floor," *Advanced Steel Construction*, vol. 7, no. 3, pp. 302–312, 2011.

[13] L. Zheng, M. He, F. Lam, R. Zhou, and M. Li, "Seismic reliability evaluation of steel-timber hybrid shear wall systems," *Earthquakes and Structures*, vol. 13, no. 3, pp. 289–297, 2017.

[14] B. Liu, W. L. S. Zhang, and Y. Xiao, "Mechanical behavior of connections for glubam-concrete composite beams," *Construction and Building Materials*, vol. 143, pp. 158–168, 2017.

[15] Q. F. Xie, J. Y. Xue, H. T. Zhao, and J. F. Hu, "Experimental study on bond behavior between CFRP sheet and wood," *Advanced Materials Research*, vol. 368–373, pp. 2314–2318, 2011.

[16] Y. S. Yu, W. L. He, and L. J. Li, "Optimal design of the mechanical properties of bamboo plywood form based on response surface model," *Beijing Linye Daxue Xuebao/Journal of Beijing Forestry University*, vol. 31, no. 7, p. 103, 2009.

[17] H. Y. Shen, Y. S. Li, W. L. Zhang, J. Xu, and B. Lü, "Experimental study on flexural behavior of cold-formed thin-wall steel-bamboo plywood composite beams," *Jianzhu Jiegou Xuebao/Journal of Building Structures*, vol. 30, no. 5, p. 171, 2009.

[18] M. North, "Sticking to composites," *Reinforced Plastics*, vol. 51, no. 4, p. 32, 2007.

[19] J. Zhang, Z. Zhang, K. Tong, J. M. Wang, and Y. Li, "Bond performance of adhesively bonding interface of steel-bamboo composite structure," *Journal of Renewable Materials*, vol. 8, no. 6, pp. 687–702, 2020.

Hindawi
Advances in Civil Engineering
Volume 2020, Article ID 8869935, 12 pages
https://doi.org/10.1155/2020/8869935

Research Article

Application and Analyzation of the Vision-Based Structure Model Displacement Measuring Method in Cassette Structure Shaking Table Experiment

Wang Yanhua,[1,2] **Wang Cheng**,[1,2] **Feng Yan**,[1,2] **Dai Bowen**,[1,2] **and Wu Gang**[1,2]

[1]*Key Laboratory of Concrete and Prestressed Concrete Structures of Ministry of Education, Southeast University, Nanjing 210096, China*
[2]*School of Civil Engineering, Southeast University, Nanjing 211189, China*

Correspondence should be addressed to Wang Yanhua; 101010371@seu.edu.cn and Wang Cheng; wangchengkyrie@outlook.com

Received 17 September 2020; Revised 28 October 2020; Accepted 9 November 2020; Published 30 November 2020

Academic Editor: Dongsheng Huang

In the shaking table test of large cassette structure, story drift is an essential set of experimental data. The traditional method of displacement measurement is limited to problems such as necessary full contact with the structure model for installation of sensors, large work of installation, and easily interfered by environment. The noncontact displacement measurement method, such as optical measuring technology, can solve the above problems and serve as an effective supplementary method for traditional displacement measuring in the shaking table test. This paper proposed a vison-based displacement measuring method. Predesigned artificial targets which act as sensors are installed on each floor of the cassette structure model. A high-speed industrial camera is used to acquire the series of the images of the artificial targets on the structure model during the shaking table test. A Python-OpenCV-based structural calculation program combining computer vision and machine vision is developed to extract and calculate the displacement of the artificial targets from the series of the images acquired. The proposed method is applied in a shaking table test of a reduced-scale fifteen-floor reinforced concrete cassette structure model, in which the laser displacement meter and the seismic geophone are also applied as a comparison. The experimental results acquired by the proposed method are compared with the results acquired by the laser displacement meter and the seismic geophone. The average error of the story drift obtained by the proposed vision-based measurement method is within 5% and is in good agreement with the laser displacement meter and the seismic geophone, which confirms the effectiveness of the proposed method.

1. Introduction

Cassette structure is a new type of the space structure system, which is independently developed in China. There is a growing study interest in the composition, characteristic, and performance of reinforced concrete cassette structure in high-rise structures under earthquake action. The shaking table test is a good method to analyse the seismic behaviour and the performance of the cassette structure in the high-rise structure. In the shaking table test, the displacement measurement technology is one of the most important research fields of engineering detection. The displacement measurement methods can be roughly divided into two types, contact and noncontact [1]. The contact measurement method is mainly realized by using classic traditional sensors which mainly include the LVDT (linear variable differential transformer), inertial sensor, and wire-type displacement gauge. The noncontact measurement method includes using various traditional noncontact displacement sensors or optical principle-based displacement measuring methods which mainly includes holographic interferometry [2], speckle interferometry [3], laser distance measurement, and vision-based measurement methods [4, 5]. The measurement results of these contact methods are easily affected by the structure model, especially cracks and other damages of the structure under large earthquake action, which means that the displacement measurement requirements are more stringent and the reliability of the contact point connection is particularly important. In addition, the installation workload of the displacement gauge, seismic geophone, or

other instrument with contacts becomes huge when the measuring points are too many. On the contrary, the vision-based method, as a kind of the noncontact measurement method, has no contact to the structure model and not interferes with the movement of the specimen, which is more reliable [6]. Compared to other optical-based methods such as holographic and speckle interference, version-based measurement method has the advantages of simpler equipment needed, lower requirements for the measurement environment, and a wider measurement range [7], which can replace traditional measurement methods in some situations or be an effective supplement to traditional measurement methods.

Many researchers have tried to apply the vision-based measurement method in the shaking table test. Ji [8], based on the principle of computer vision, using camera parameter calibration, image tracking, and three-dimensional point reconstruction technology, established a structural dynamic displacement test method using a consumer camera. Wang Xiaoguang et al. [9] gave a robust landmark matching algorithm and developed a three-dimensional full-field displacement measurement system for shaking table experiments based on the VS2010 development environment. Hyungchul Yoon et al. [10], using a consumer-grade camera, proposed a visual measurement method, in which the measurement mark points are selected manually. Zhou Ying et al. [11] used a consumer-grade camera as the acquisition device and adopted the characteristic optical flow technology based on point matching to realize the motion tracking of the target and obtain the displacement time course of the target. Han Jianping [12] compiled noncontact displacement measurement programs by MATLAB based on computer vision and performed displacement measurement in the shaking table test of a four-story reinforced concrete frame-filled wall structure model. Even though, the vision-based method has seldom been applied in the shaking table test of the huge structure model, especially in the large cassette structure.

In the shaking table test of the large cassette structure, due to the complicated background of the artificial target, the recognition and location of the artificial target become exceedingly difficult. Therefore, for the shaking table test of the fifteen-floor reduced-scale structure model, this paper proposed a noncontact measurement method. A designed artificial target is installed on the structure as a "sensor," and a single high-speed industrial camera is applied to acquiring the series of the target's image during the shaking table test. A calculation program is developed to extract the target from the complicated background and calculate the displacement of the artificial target. The measurement program is compiled by Python, and the OpenCV module is applied. The proposed method is applied in the measurement of story drift in the shaking table test, while the traditional displacement sensor is also applied as a comparison. The experimental results acquired by the proposed method and the traditional displacement sensor are compared to verify the effectiveness and precision of the proposed method.

2. Vision-Based Displacement Measurement Method

The technical route of the proposed vision-based displacement measurement method is shown in Figure 1.

2.1. Image Acquisition. In this paper, the high-speed industrial camera hk-a4000-tc500 is applied, and fixed focus lens (80 mm) are used for image collection. The camera is connected to a calculation server equipped with a large-capacity solid-state hard disk through the optical fiber and control box, as shown in Figure 2. To ensure the quality and speed of the acquired images, the camera directly outputs grayscale pictures, which is convenient for later image processing and avoid the errors due to grayscale conversion.

2.2. Camera Calibration. To locate the artificial target in real world coordinate, the corresponding relationship between the real world coordinate system and the two-dimensional image coordinate system has to be determined. Therefore, a geometric model of the camera imaging must be established, the model parameters of which are camera parameters. Camera calibration is the procedure of determining camera parameters through experiments and calculations. In this test, considering that the high-resolution industry camera is applied and only the middle area of the artificial target image is used for calculation, the effect of optical distortion can be ignored [13]. Only the scaling factor is needed to be determined in the camera calibration.

SF (scaling factor) is the relationship between the image space and physical space, and the scaling factor calculation formula is given as follows [14].

$$\mathrm{SF} = \frac{D_{\mathrm{mm}}}{D_{\mathrm{pixel}}}. \tag{1}$$

The edge length D_{pixel} of the artificial target in the image is acquired by performing subpixel corner point recognition on the images of the high-precision artificial target. The real size of the artificial target is known as D_{mm}, as shown in Figure 3. In this paper, the value of D_{pixel} and D_{mm} is separately $D_{\mathrm{pixel}} = 61.82118944$ pixel and $D_{\mathrm{mm}} = 220\sqrt{2}$ mm. Therefore, the conversion coefficient can be obtained by using Formula (1), which is $\mathrm{SF} = 220\sqrt{2}/61.82118944 = 5.032691648$ mm/pixel.

2.3. Computer Version-Based Artificial Target Recognition. In this paper, the computer vision-based artificial target identification method is applied to extracting the image area of the artificial targets, which is fundamental to the subsequent machine vision-based positioning of the artificial target point. The extraction procedure is shown in Figure 1, mainly including image filtering, edge detection, contour detection, and mask generation. The whole procedure is shown in Figure 4.

2.3.1. Image Filtering. The image filter will only be used in the computer vision-based artificial target extracting procedure. Some key information of the edge will be lost in the filtering procedure, such as Gaussian filtering [15] and median filtering, which will cause errors to the measurement results. To preserve the edge information, the edge preservation filtering (EPF) method is adopted in this paper.

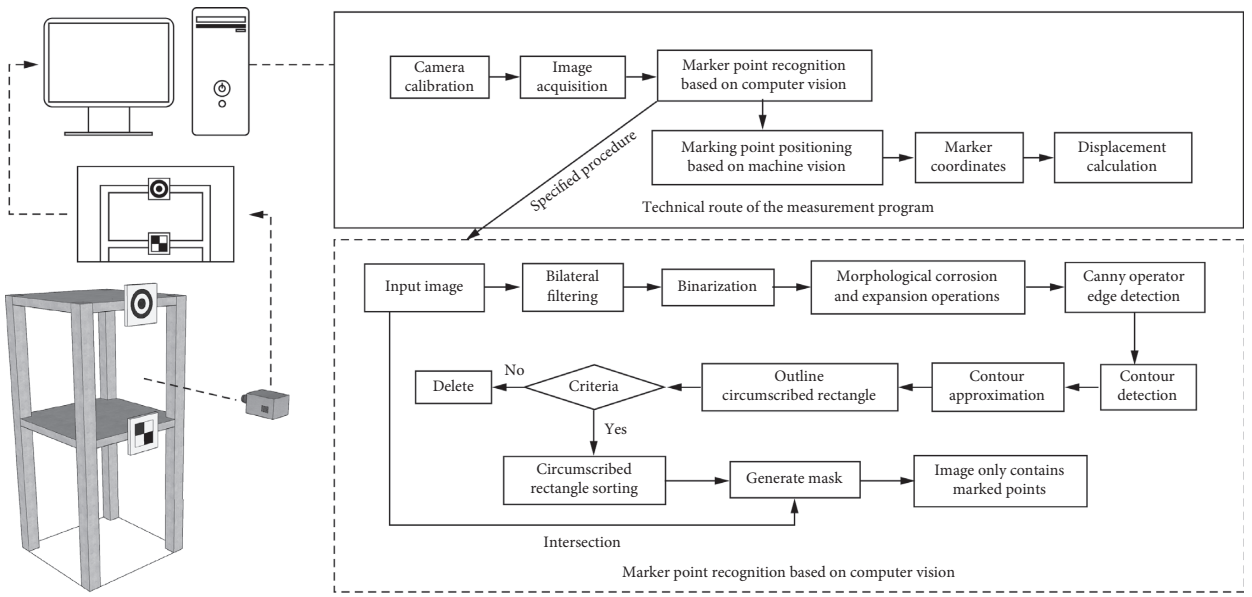

Figure 1: Technical route of them easurement program.

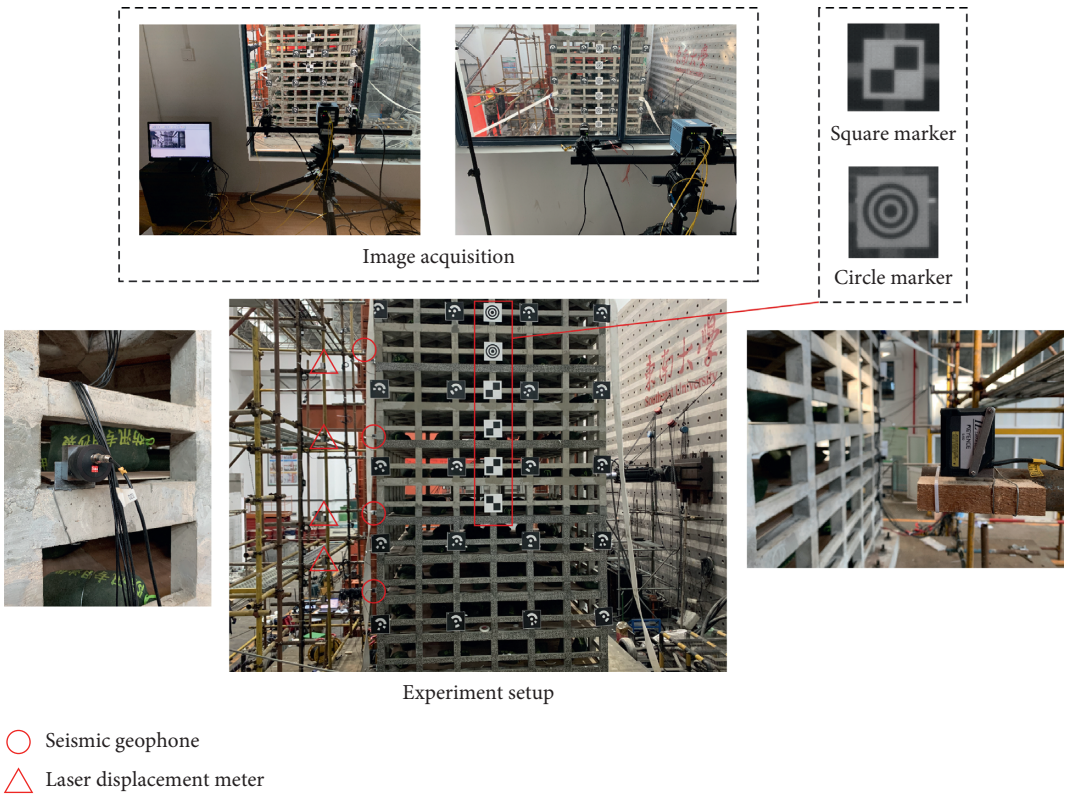

Figure 2: Experiment setup.

2.3.2. Morphological Operations. After binarization, there are some burrs and interference information on the edge of the image, and some interference information can be removed by multiple morphological dilation and corrosion calculation, as shown in Figure 4.

2.3.3. Edge Detection. The improved canny edge detection method is used to detect the edge of the image after the morphological operation, which is the foundation of the contour extraction in the next step. The improved canny edge detection method is to calculate the gradient and

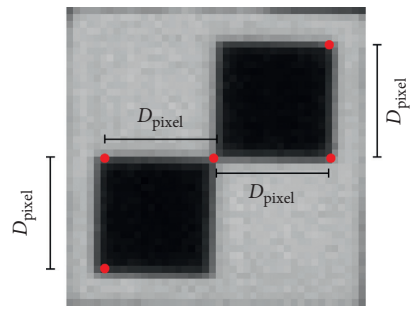

Figure 3: Schematic diagram of scaling factor solution.

Figure 4: Computer vision-based maker recognition.

direction of each pixel in the image, as shown in equations (2) and (3), and performs threshold filtering on the results to obtain the image edge. Then, through the nonmaximum suppression of the double threshold method, as shown in Figure 5, the unnecessary edges are filtered; thereby, a more realistic image edge is obtained.

$$G = \sqrt{G_x^2 + G_y^2}, \tag{2}$$

$$\theta = \arctan\left(\frac{G_y}{G_x}\right), \tag{3}$$

where G_x and G_y are the gradients of one pixel in x and y directions; θ is the direction of the gradient.

2.3.4. Contour Detection-Based Target Extraction. Contour is a set of contour points of a connected region, as shown in Figure 6. The procedure of the contour-based target extraction is to first obtain the contour of the picture

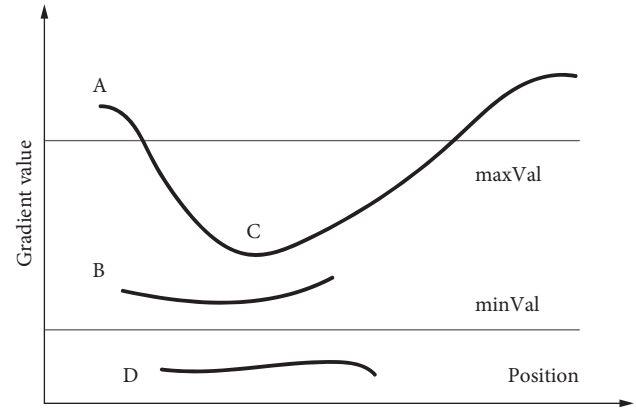

A Gradient value > maxVal: boundary
C minVal < Gradient value < maxVal: with boundaries reserved
B minVal < Gradient value < maxVal: without boundaries removed
D Gradient value < minVal: removed

Figure 5: Nonmaximum suppression.

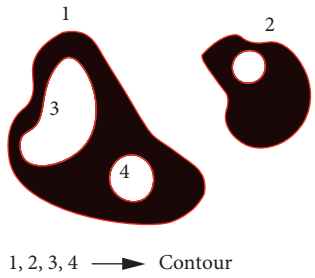

Figure 6: Contour schematic diagram.

by performing contour detection on the edge-detected image, and the detected contour is then approximated according to the principle of the minimum distance, through which some redundant contour is filtered out. Finally, the circumscribed rectangle of the obtained contour is calculated.

The edge of the artificial target is a connected region, by performing contour detection on the edge-detected artificial target image, the contour of the artificial target, and other redundant information can all be detected. Because the contour of the artificial target is already an approximate square, its bounding rectangle is also an square and satisfies certain conditions, while other irregular bounding rectangles cannot meet these features. Filter conditions can be set according to this difference to remove the unwanted bounding rectangle and obtain the bounding rectangle that only contains the artificial target.

Finally, the bounding rectangle of the artificial targets are separated from the original image. According to the vertex coordinates and the width of the bounding rectangle, a mask can be made. The size of mask is the same as the original image, but the inside of the rectangular area is set to 1, while the outside is set to 0. The images that only contain the artificial targets can be extracted by performing the intersection operation of the mask and the original image, as shown in Figure 4.

2.4. Machine Version-Based Artificial Target Locating. Two methods of artificial target locating are applied in this paper, which are the corner detection method and template-based grayscale centroid method, respectively.

2.4.1. Pixel Level Corner Detection. After the above-mentioned computer vision-based processing, the image of the artificial target is successfully separated from the background. The subpixel corner detection is then used to calculate the center coordinates of the marked points. The main procedure is as follows: first, pixel level corner detection [16] and then corner detection on the subpixel level near the desired corner.

The pixel level corner detection uses the Harris corner detection method, that is, a local window $W(x, y)$ centered by (x, y) on the image slides $(\Delta x, \Delta y)$ on the image. The eigenvalues of the matrix M corresponding to each pixel is solved, where the matrix M is

$$M(x, y) = \begin{bmatrix} \sum_w I_x(x, y)^2 & \sum_w I_x(x, y) I_y(x, y) \\ \sum_w I_x(x, y) I_y(x, y) & \sum_w I_y(x, y)^2 \end{bmatrix}, \tag{4}$$

where $I(x, y)$ is the grayscale value of point (x, y), I_x, I_y is the partial derivative of x, y to $I(x, y)$.

When the eigenvalues λ_1, λ_2 satisfy the condition: (1) λ_1, λ_1 are large; (2) $\lambda_1 \approx \lambda_2$, the corresponding pixel is the corner point.

2.4.2. Subpixel Level Corner Detection. The subpixel level corner detection is to search the real corner point around the pixel level corner detection point, as shown in Figure 7.

The subpixel corner detection is to solve the equation set under the conditions of the situation shown in Figure 6, which is as follows:

(a) The image area near point p is uniform, the gradient of which is 0

(b) The gradient of the edge is orthogonal to the $q - p$ vector along the edge direction

Assuming that the starting point q is near the actual subpixel corner, all $q - p$ vectors which satisfy the above conditions are detected, and equation (5) is satisfied. Many sets of gradients and related vectors $q - p$ can be found around the p point, and the inner product of the $q - p$ vector and the gradient of p is 0; the system of equations can be solved. The solution of the equation set is the subpixel accuracy coordinates of the actual corner point q.

$$\langle \nabla I(p), q - p \rangle = 0, \tag{5}$$

where $\nabla I(p)$ is the gradient of p; $q - p$ is the vector of points q and p.

2.4.3. Grayscale Centroid Method Based on Template Matching. If the extracted images of the circle-shaped artificial targets are directly calculated by the grayscale centroid method, the centroid position of the same artificial target will be different due to the selected boundary of the artificial target, which will cause errors to the displacement measurement results as shown in Figure 8.

Moreover, because the percentage of the artificial target in the whole picture is exceedingly small, it is impossible to directly perform the positioning calculation. To solve this problem, in this paper, the images of the artificial target area obtained by the computer vision method are further subjected to template matching to achieve more accurate segmentation. Then, the following equation is used to calculate the centroid coordinate of each artificial target.

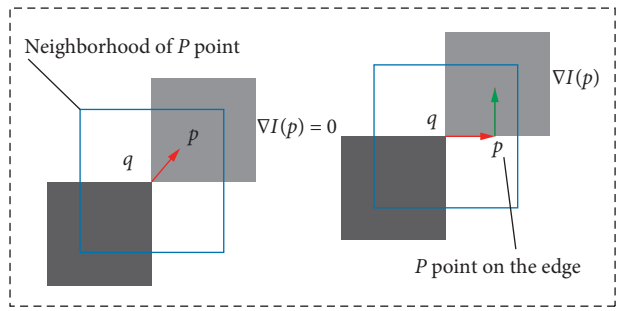

Figure 7: Subpixel corner detection.

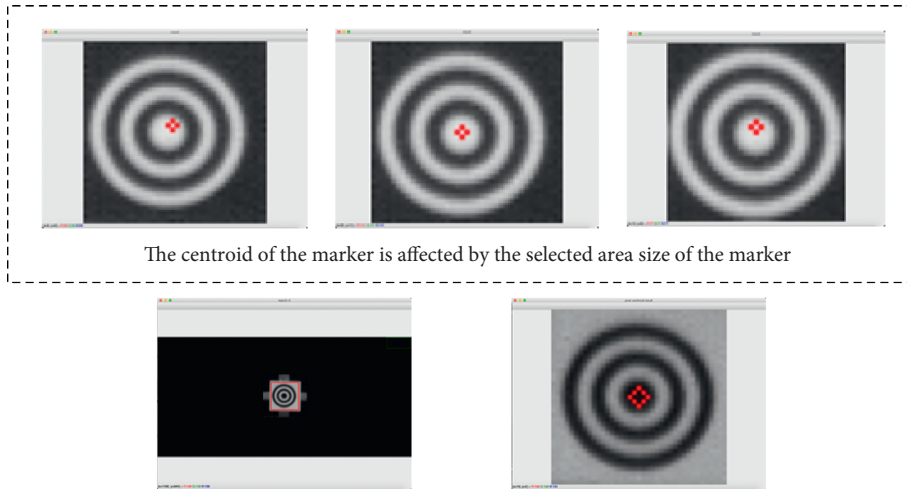

Figure 8: The position of the centroid of the artificial target is affected by the selection of the area.

$$x = \frac{\sum_{j=1}^{n}\sum_{i=1}^{m} f(i,j)\cdot i}{\sum_{j=1}^{n}\sum_{i=1}^{m} f(i,j)},$$
$$y = \frac{\sum_{j=1}^{n}\sum_{i=1}^{m} f(i,j)\cdot j}{\sum_{j=1}^{n}\sum_{i=1}^{m} f(i,j)}. \quad (6)$$

2.5. Displacement Calculation. The displacement of the artificial target in the image coordinate system can be calculated according to the front and rear images. Then, the actual displacement of the artificial target can be obtained by multiplying the displacement in the image coordinate and the scaling factor, as shown in the following equation, which is the displacement of the point where the maker is installed on the structure.

$$\Delta X = X_1 - X_2 = \mathrm{SF}\cdot\Delta X_{\mathrm{pixel}} = \frac{D_{\mathrm{mm}}}{D_{\mathrm{pixel}}}\left(x_{1,\mathrm{pixel}} - x_{2,\mathrm{pixel}}\right). \quad (7)$$

3. Validation Test

3.1. Experiment Setup. The proposed method is applied in the shaking table test of a reduced-scale fifteen-floor reinforced concrete cassette structure model. The experiment was conducted on the shaking table of the Structural Laboratory in Jiulonghu Campus, Southeast University. The parameters of the shaking table are shown in Table 1. The structural model in this paper is shown in Figure 9.

The height of the structure model is 6.9375 m, and the plane size of the structure model is 2.7 × 2.7 m, and the ratio of height to width is 2.5. To avoid the structure torsion of the model and the need to rotate the model because of the different rigidity of the chief axis, the plan layout of the model is set to square, and the orthogonal diagonal sandwich plate is used as the floor slab. The material of the structure model is microconcrete, which is to simulate real concrete material. The design elastic modulus of the microconcrete is 1/5 of the concrete C50. The reinforcement is simulated by a galvanized iron wire, and the design yield strength is 300 Mpa. The weight of the whole structure model is about 21t, which meets the requirements of the seismic station. In order to get the seismic response of the structure under different ground motions, EI Centro #6 wave is selected in this experiment for analysis, and the working conditions are divided by the zoom factor into 8 and 10.

3.2. Installation of the Displacement Sensor. The arrangement of the artificial target, laser displacement meter, and seismic geophone is shown in Figure 2. The laser displacement meter applied is Keyence IL-600, and the seismic geophone applied is

Table 1: The parameters of the shaking table.

Location	Size	Weight capacity (t)	Maximum displacement	Maximum acceleration (g)	Frequency range
Southeast University Jiulonghu Campus	6 m × 4 m	30	±250 mm	1.0	0.1~50 (Hz)

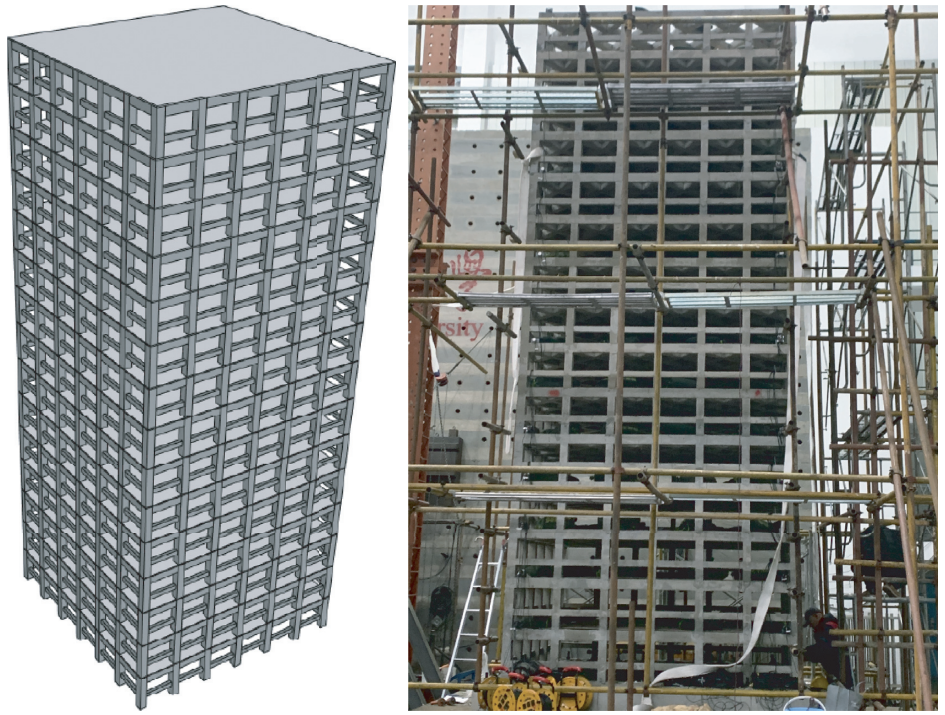

Figure 9: Structure model applied in the experiment.

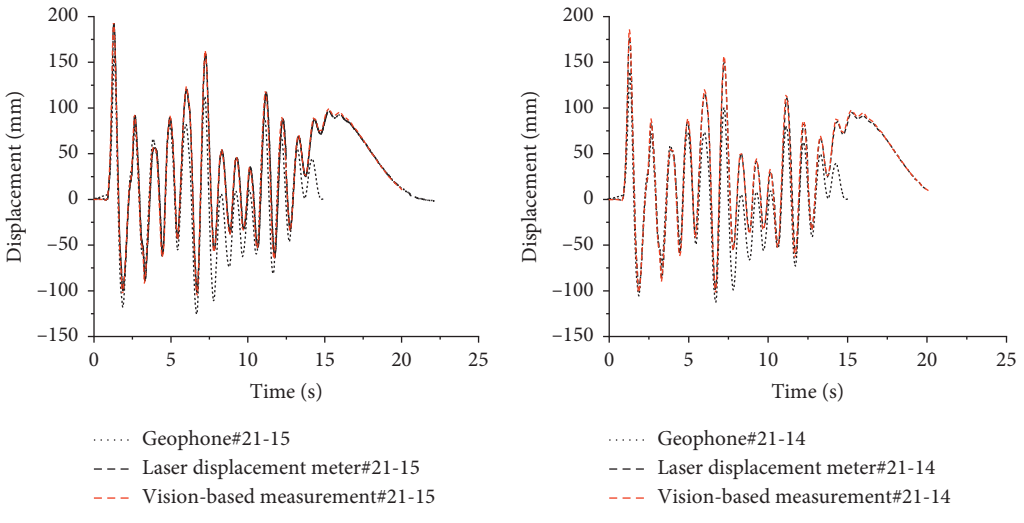

(a) (b)

Figure 10: Continued.

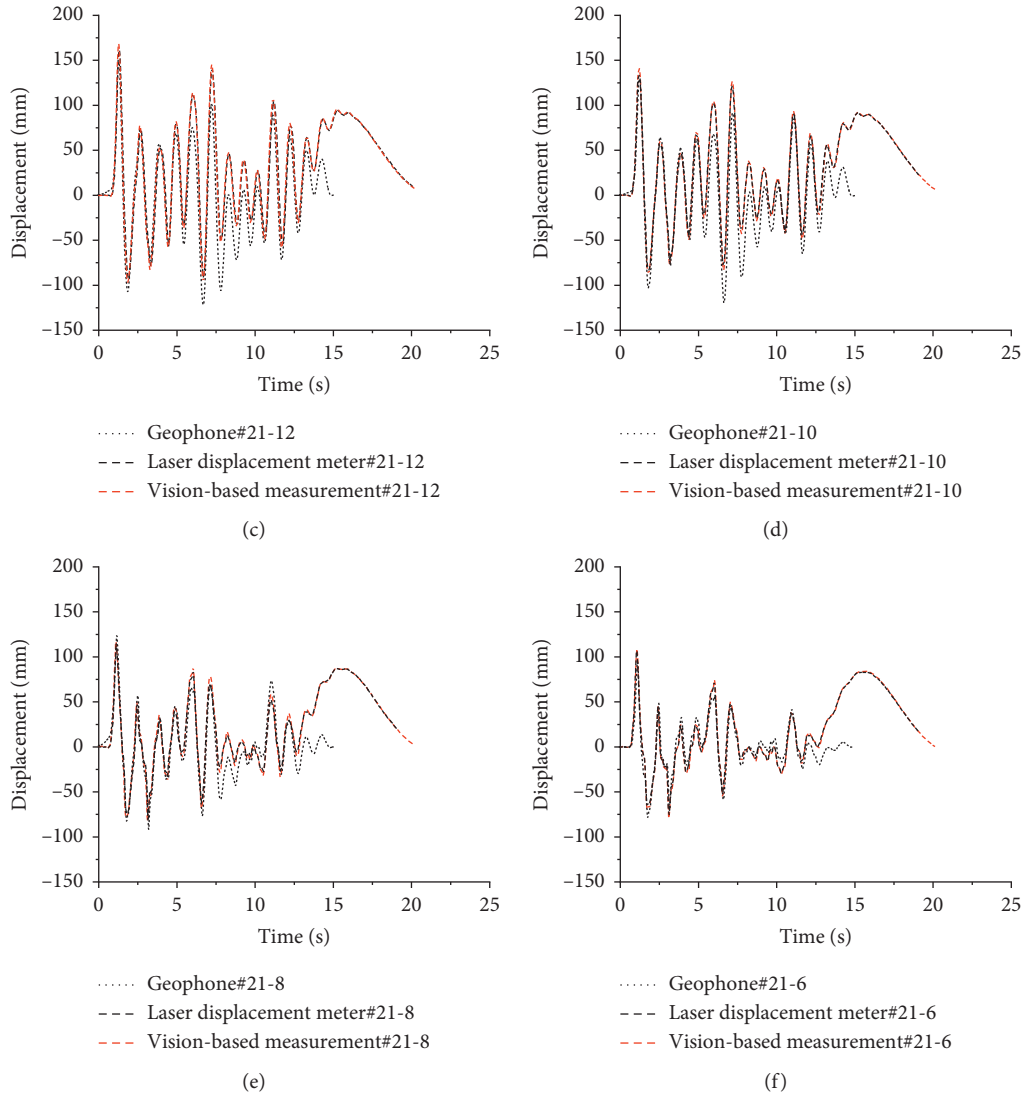

Figure 10: Working condition 21. (a) Fifteenth floor. (b) Fourteenth floor. (c) Twelfth floor. (d) Tenth floor. (e) Eighth floor. (f) Sixth floor.

941B. The measuring range of the Keyence IL-600 is 200 ~ 1000 mm, the sampling frequency of the Keyence IL-600 is 128 Hz, and the repetitive accuracy of the Keyence IL-600 is 50 μm^{*4}. The sensitivity of the 941B seismic geophone is 0.3 m/s^2, and the maximum range of the 941B seismic geophone is 20 m/s^2.

3.3. Displacement Results. In this paper, an industrial camera is used to acquire images of the artificial targets, and a measurement program is compiled in Python language to measure the x-axis model displacement of a reduced-scale fifteen-floor cartridge structure model in the shaking table test. Finally, the measurement results are compared with the traditional measurement sensor, laser displacement meter, and seismic geophone.

3.3.1. Displacement Time-History Curves of Each Floor. Due to space limitations, this article only gives the results of the two working conditions of 21 (EI Centro #6 wave, scaling factor of 10) and 20 (EI Centro #6 wave, scaling factor of 8), as shown in Figures 10 and 11.

4. Discussion

4.1. Error Analysis. It can be seen from Figures 10 and 11 that the X direction horizontal displacement curve of the measuring point obtained by the geophone, the laser displacement meter, and the visual image measurement method basically coincides. In the early period, when the structure began to vibrate, the agreement was generally good, but in the middle and later periods, the curve of the geophone gradually deviated from the curve of the vision-

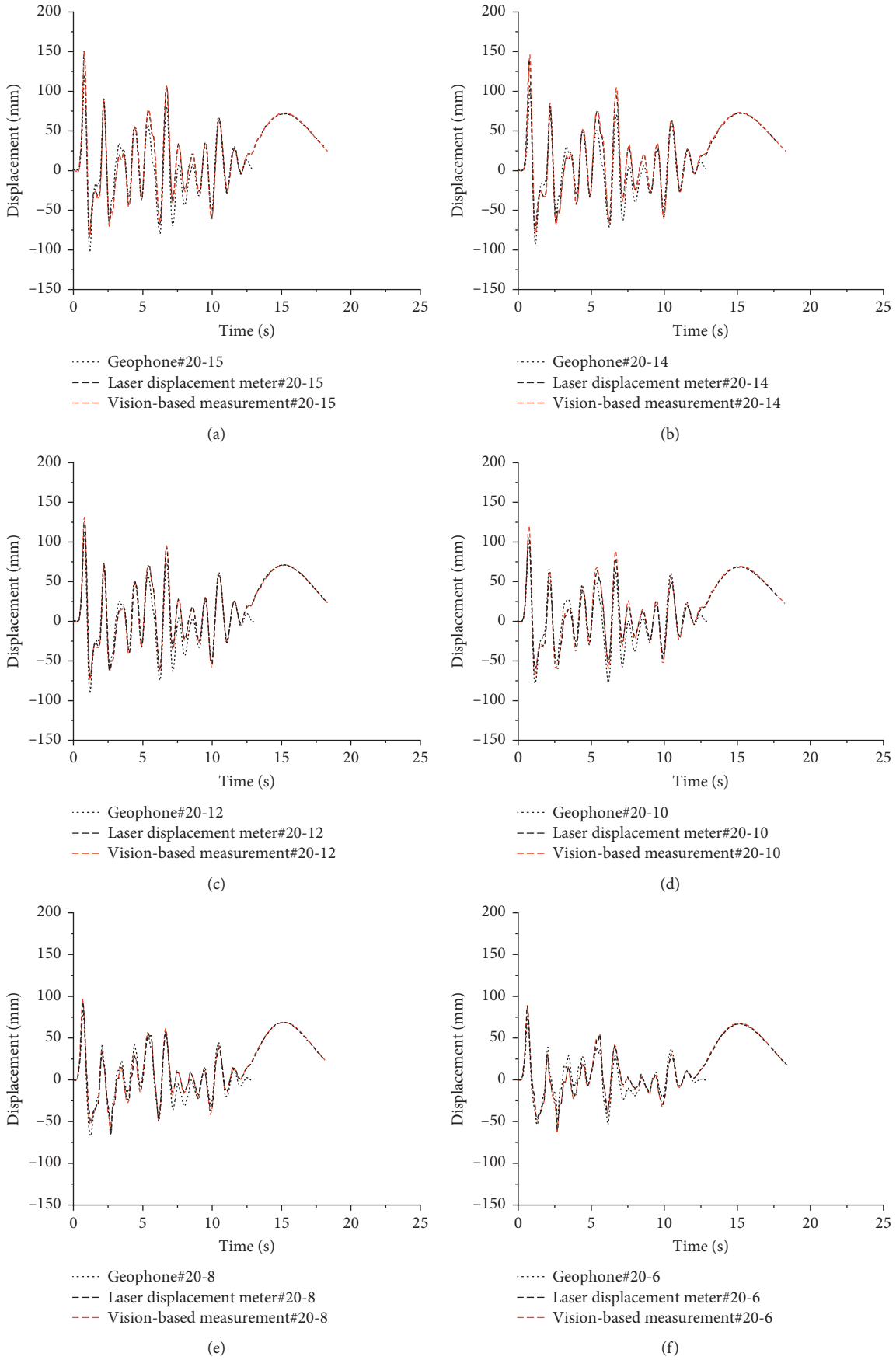

Figure 11: Working condition 20. (a) Fifteenth floor. (b) Fourteenth floor. (c) Twelfth floor. (d) Tenth floor. (e) Eighth floor. (f) Sixth floor.

Table 2: Horizontal maximum displacement error and correlation coefficient of each floor under the working condition 21.

21–15			21–14			21–12		
Vision method	Laser displacement meter	Deviation	Vision method	Laser displacement meter	Deviation	Vision method	Laser displacement meter	Deviation
194.18	195.68	−0.77%	185.56	182.32	1.78%	168.13	164.24	2.37%
−103.62	−96.24	7.67%	−101.68	−93.92	8.26%	−96.81	−90.24	7.28%
93.11	94.96	−1.95%	88.00	88	0.00%	77.57	77.28	0.37%
−91.52	−85.44	7.11%	−89.68	−81.6	9.90%	−82.60	−75.52	9.37%
57.07	59.52	−4.12%	55.01	58.72	−6.32%	52.64	55.12	−4.51%
−62.84	−58.32	7.75%	88.28	89.28	−1.12%	81.55	81.84	−0.35%
90.92	92.8	−2.03%	119.82	120.8	−0.81%	114.08	114.64	−0.49%
122.95	124	−0.84%	−102.62	−93.92	9.26%	−95.40	−87.92	8.51%
−105.60	−98.08	7.67%	156.71	155.44	0.82%	145.15	143.04	1.47%
162.78	162.88	−0.06%	51.29	54.48	−5.85%	47.14	48.64	−3.08%
54.32	57.2	−5.04%	44.10	46.24	−4.63%	39.45	41.2	−4.26%
45.97	49.12	−6.41%	32.68	34.96	−6.53%	27.74	29.76	−6.80%
−53.12	−48.56	9.40%	114.69	115.36	−0.58%	106.97	107.04	−0.06%
118.99	120.72	−1.43%	85.94	87.92	−2.25%	80.04	80.48	−0.55%
−65.27	−60	8.79%	69.05	72.32	−4.52%	65.13	66.88	−2.62%
89.56	91.6	−2.23%	88.72	90.32	−1.77%	85.93	87.52	−1.82%
70.16	72.4	−3.09%	72.89	75.92	−3.99%	72.20	74.64	−3.27%
89.42	91.12	−1.87%	97.48	99.6	−2.13%	95.48	97.28	−1.85%
74.25	74.8	−0.73%	90.31	92.88	−2.77%	89.48	91.44	−2.14%
99.00	100.16	−1.16%	94.29	95.92	−1.70%	92.54	94.48	−2.05%
Average deviation		4.01%	Average deviation		3.75%	Average deviation		3.16%
Correlation coefficient		0.99	Correlation coefficient		0.99	Correlation coefficient		0.99

Table 3: Horizontal maximum displacement error and correlation coefficient of each floor under the working condition 20.

21–15			21–14			21–12		
Vision method	Laser displacement meter	Deviation	Vision method	Laser displacement meter	Deviation	Vision method	Laser displacement meter	Deviation
150.88	149.28	1.07%	145.69	140.56	3.65%	131.67	126.72	3.91%
−84.13	−82.08	2.50%	−80.72	−76.4	5.65%	−74.69	−71.36	4.67%
−35.85	−33.2	7.99%	−25.52	−24.4	4.60%	−27.62	−27.76	−0.49%
90.14	89.92	0.25%	−34.40	−32.56	5.67%	−34.13	−33.04	3.28%
−72.02	−70.24	2.53%	85.24	82	3.95%	73.17	69.84	4.76%
21.81	21.84	−0.15%	−69.09	−65.84	4.93%	−64.53	−61.52	4.89%
−45.47	−43.68	4.11%	21.21	19.84	6.90%	17.90	16.88	6.05%
54.79	54.72	0.13%	−43.42	−41.76	3.98%	−41.50	−40.32	2.93%
−37.32	−34.96	6.76%	53.82	52.4	2.71%	49.57	48.08	3.10%
76.75	75.12	2.17%	76.03	74.72	1.75%	−30.98	−29.76	4.10%
−70.27	−68.64	2.37%	−67.32	−64.8	3.89%	71.43	70.48	1.34%
107.30	106.08	1.15%	104.56	100.96	3.56%	−64.35	−61.6	4.47%
−40.99	−39.68	3.31%	−39.01	−36.16	7.87%	95.70	92.48	3.48%
33.09	33.68	−1.76%	32.90	30.56	7.65%	−36.09	−34.96	3.24%
21.59	21.76	−0.79%	−25.70	−24.16	6.38%	28.52	26.96	5.79%
−28.12	−27.84	1.02%	21.28	20.24	5.13%	−24.32	−23.36	4.12%
34.62	35.04	−1.20%	−27.70	−26.48	4.60%	17.90	17.2	4.07%
−62.57	−60.32	3.73%	34.17	31.6	8.12%	−27.50	−26.48	3.84%
64.33	63.6	1.15%	−60.57	−58.32	3.86%	30.18	28.96	4.22%
−29.75	−28.88	3.02%	63.97	62.48	2.39%	−58.00	−55.92	3.72%
27.61	27.44	0.60%	−28.45	−26.8	6.16%	59.74	58	3.00%
72.66	71.12	2.17%	27.90	26.72	4.40%	−26.65	−25.68	3.77%
Average deviation		2.27%	Average deviation		4.90%	Average deviation		3.78%
Correlation coefficient		0.99	Correlation coefficient		0.99	Correlation coefficient		0.99

based method and laser displacement meter, in which the curve of the vision-based method coincides well with the curve of the laser displacement meter. By analyzing the results, there are three main reasons:

(1) Because the structural model is too large, the vibration of the shaking table causes the installation support of the laser displacement meter to vibrate, but the installation support is assumed to be a zero-displacement point, which introduces errors

(2) Due to the high structural model and whiplash effect, large errors are introduced into the seismic geophone

(3) The displacement of a seismometer is obtained by integrating the velocity or acceleration, during which the error is amplified, and the deviation is caused

4.2. Quantitative Analysis of Error. In order to quantitatively analyze the measurement results of the visual method and the traditional displacement sensor, the correlation coefficient ρ is used to evaluate the correlation between the image measurement and the traditional measurement method. The calculation formula is given as the following equation:

$$\rho = \frac{\left|\sum_i \left(d_T(i) - v_{d_T}\right) \times \left(d_v(i) - v_{d_v}\right)\right|}{\sqrt{\sum_i \left(d_T(i) - v_{d_T}\right)^2} \times \sqrt{\sum_i \left(d_v(i) - v_{d_v}\right)^2}}, \quad (8)$$

where $d_T(i)$ and $d_v(i)$ are the dynamic displacement values of traditional displacement sensors and visual methods, respectively; v_{d_T} and v_{d_v} are the average of the above two sets of data, respectively. The value range of ρ is 0~1, 0 means nothing, 1 means perfect match.

Under the working condition 21 and the working condition 20, the horizontal maximum displacement and the error and correlation coefficient of the displacement data obtained by the proposed and the laser displacement meter on each floor are shown in Tables 2 and 3.

It can be seen from Table 1 and Table 2, under the working conditions 21 and 20, the error of each floor is kept within 5%, which can meet the needs of displacement measurement in the field of civil engineering. The correlation coefficients are very close to 1, which proves that the results obtained by the laser displacement meter are highly consistent with the results of the image measurement.

5. Conclusion

In order to measure the story drift of the reduced-scale fifteen-floor reinforced concrete in the shake table test, this paper proposed a vision-based displacement measurement method, which combined Python programming, computer vision, and machine vision algorithms. The noncontact vision-based measurement method consists of four parts, artificial target image acquired by an industrial camera, the extraction of the artificial targets by computer vision, the positioning of the artificial targets by machine vision, and the corresponding measurement and calculation programs complied in Python, and the effectiveness and accuracy of the method was proved by a series of structural model shaking table tests, and the following conclusions were obtained:

(1) Using the Python programming language, combined with related computer vision algorithms, under complex backgrounds, the marked points installed on the structural model can also be well extracted, which is the foundation for the positioning of the marked points and noncontact measurement

(2) The average error of the horizontal displacement of each floor obtained by the proposed vision-based measurement method is within 5%, which is in good agreement with the laser displacement meter, and the correlation coefficient is much greater than 0.99

(3) The effectiveness and accuracy of the proposed method is verified and applied in the later shaking table test in the shaking table of the Southeast University Jiulonghu Campus

Data Availability

The XLSX data used to support the findings of this study may be accessed by emailing to the corresponding author, Wang Yanhua, who can be contacted at 101010371@seu.edu.cn.

Conflicts of Interest

The authors declare that they have no conflicts of interest.

Acknowledgments

The authors gratefully acknowledge the financial support for this study by the National Natural Science Foundation of China (51708110 and 11827801).

References

[1] X. Zhao and Q. Li, "A review on measurement technology for structural testing in civil engineering," *Journal of Xi'an University of Architecture & Technology (Natural Science Edition)*, vol. 49, no. 1, pp. 48–55, 2017.

[2] D. W. Watt and R. U. Goulet, "In-situ measurements of three-dimensional displacement fields in shear crack growth using phase-shifted speckle interferometry," *Proceedings of Spie the International Society for Optical Engineering*, vol. 2545, 1995.

[3] D. Zhao and W. Song, "Structural analyse by measuring displacement with speckles method," *Applied Laser*, vol. 012, no. 4, pp. 148-149, 1992.

[4] B. Pan, K. Qian, H. Xie et al., "Two-dimensional digital image correlation for in-plane displacement and strain measurement: a review," *Measurement Science and Technology*, vol. 20, no. 6, Article ID 062001, 2009.

[5] B. Pan, L. Yu, and D. Wu, "High-accuracy 2D digital image correlation measurements with bilateral telecentric lenses: error analysis and experimental verification," *Proceedings of the Society for Experimental Mechanics*, vol. 70, no. 2, pp. 1719–1733, 2013.

[6] J. Wang, S. Li, and S. Tian, "Application of binocular vision technology in structural test," *Journal of Applied Optics*, vol. 39, no. 6, pp. 821–826, 2018.

[7] D. Feng, Q. M. Feng, E. Ozer et al., "A vision-based sensor for noncontact structural displacement measurement," *Sensors*, vol. 15, no. 7, pp. 16557–16575, 2015.
[8] Y. Ji, "Computer vision approach for structural dynamic displacement measurement," *Journal of Tongji University (Natural Science)*, vol. 41, no. 11, pp. 1670–1674, 2013.
[9] X. Wang, L. Jin, W. You et al., "3D full field displacement measurement of seismic shaking table experiment," *Journal of Applied Optics*, vol. 37, no. 4, pp. 567–572, 2016.
[10] H. Yoon, H. Elanwar, H. Choi, M. Golparvar-Fard, and B. F. Spencer, "Target-free approach for vision-based structural system identification using consumer-grade cameras," *Structural Control and Health Monitoring*, vol. 23, no. 12, pp. 1405–1416, 2016.
[11] Y. Zhou, L. Zhang, L. Tong et al., "Structural system identification based on computer vision," *China Civil Engineering Journal*, vol. 51, no. 11, pp. 17–23, 2018.
[12] J. Han, Y. Zhang, and H. Zhang, "Displacement measurement of shaking table test structure model based on computer vision," *Earthquake Engineering and Engineering Dynamics*, vol. 39, no. 4, pp. 22–29, 2019.
[13] D. Ribeiro, R. Calçada, J. Ferreira, and T. Martins, "Non-contact measurement of the dynamic displacement of railway bridges using an advanced video-based system," *Engineering Structures*, vol. 75, pp. 164–180, 2014.
[14] T. Khuc, *Computer Vision Based Structural Identification Framework for Bridge Health Mornitoring*, University of Central Florida, Orlando, FL, USA, 2016.
[15] X. Qian, L. Guo, and B. Yu, "Adaptive Gaussian filter based on object scale," *Computer Engineering and Applications*, vol. 46, no. No. 12, pp. 14–16, 2010.
[16] C. G. Harris and M. Stephens, "A combined corner and edge detector," in *Proceedings of the Alvey Vision Conference*, pp. 10–5244, Manchester, UK, September 1988.

Hindawi
Advances in Civil Engineering
Volume 2020, Article ID 8878776, 9 pages
https://doi.org/10.1155/2020/8878776

Research Article

Study on Flexural Behaviour of Box Section Bamboo-Steel Composite Beams

Qifeng Shan,[1,2] **Jialiang Zhang**,[2] **Keting Tong**,[2] **and Yushun Li**[3]

[1]*Zhejiang Industry Polytechnic College, Shaoxing 312000, China*
[2]*School of Civil and Environmental Engineering, Ningbo University, Ningbo 315211, China*
[3]*College of Civil Engineering & Architecture, Qingdao Agricultural University, Qingdao 266109, China*

Correspondence should be addressed to Yushun Li; lys0451@163.com

Received 27 July 2020; Revised 23 September 2020; Accepted 28 October 2020; Published 17 November 2020

Academic Editor: Dongsheng Huang

To take full advantages of the bamboo and cold-formed thin-walled steel, a new type of box section beam combined with bamboo and steel channel was proposed in this paper. Five composite beams with different parameters were tested to evaluate the effects of bamboo plywood thickness of composite beams and thickness and sectional dimension of steel channel. The results of experiment showed that the proposed composite beams exhibited excellent flexural bearing capacities and stiffness. The increase of bamboo plywood thickness and sectional dimension of steel channel could improve bearing capacity and flexural stiffness of composite beams, while the increase of steel thickness could enhance the bearing capacity and safety margin of composite beams. Furthermore, a new method to predict the deformation and bearing capacities of composite beams was proposed and matched well with the experimental results.

1. Introduction

With the development of the society, green, sustainable, and ecologically materials are required to be employed for the construction. Wood and bamboo are one of environment-friendly building materials. Furthermore, wood and bamboo have the advantages of light weight, high strength, and good seismic resistant performance as construction materials.

However, the resources of wood are relatively rare all over the world due to the long growth cycle; thus, the usage of wood is limited. A more environment-friendly building material such as bamboo need to be developed to replace wood.

Bamboo, which has good mechanical performance, has been used by humans for thousands of years. In addition, China has a very rich resource of bamboo [1]. However, the applications of raw bamboo material are limited in civil engineering due to its dimensional instability, irregular shape, and difficult connection [2]. With the development of processing technic, bamboo plywood can be made with good mechanical properties by modified processing of raw bamboo [3–5]. However, the structure members made by modified bamboo had lower bearing capacity compared with the steel members under the same dimensions [6, 7], which meant bamboo members needed more materials to attain the same bearing capacity. Therefore, the bamboo structure members strengthened by other materials such as steel bars [8, 9], fiber polymer [10], and FRP sheets or grid [11–14] were designed and investigated in the recent years.

Thin-walled cold-formed steel is one of the common construction materials with ultrahigh strength, while the steel members generally cannot reach its ultimate strength due to the buckling. Based on these considerations, a new bamboo-steel composite structure is proposed. The bamboo-steel composite structure is made up of bamboo plywood and cold-formed thin-walled steel through epoxy resin. The bamboo-steel composite structure can take the advantages of light weight and high strength of the two materials, while avoiding the disadvantages of easy buckling of cold-formed thin-walled steel. The research studies had showed the co-operation of the two materials could effectively improve the mechanical performance of the composite members [15–19].

In this study, a new type of box section bamboo-steel composite beam, which consisted of four pieces of bamboo plywood and two pieces of cold-formed thin-walled steel channel, is proposed. Then, five composite beams proposed above were tested. The flexural behaviours of the composite beams were analysed and compared. The influence of the bamboo plywood thickness and the thickness and sectional dimension of steel channel were also studied in this paper.

2. Experiment Programs and Results

2.1. Material Properties. Cold-formed thin-walled steel employed in this paper was made of steel sheets, which were processed by a professional steel structure factory. The thickness (t_s), yield stress (f_y), ultimate stress (f_u), and Young's modulus (E_s) of steel sheets were measured according to [20], as shown in Figure 1(a). The mechanical properties of the steel are listed in Table 1.

There is no material test standard to be made for bamboo plywood in China; hence, the modulus of elasticity (E_b) and the modulus of rupture (σ) of bamboo plywood were measured according to the standard of wood-based panels [21], which is shown in Figure 1(b). The mechanical properties of bamboo plywood are listed in Table 2.

2.2. Test Specimens. The main design parameters of box section bamboo-steel composite beams were thickness of bamboo plywood and thickness and sectional dimension of thin-walled steel channel. B-1 and B-2 were designed to investigate the influence of bamboo plywood thickness. B-3 and B-4 were designed to study the effect of steel channel thickness of composite beams. To investigate the effect of steel channel dimension, B-5 was designed as a comparison with B-3. The thickness of bamboo plywood (t_b) was 15.1 mm, 17.6 mm, and 25.0 mm, and the thickness of thin-walled steel channel, namely, t_s (both web and flange), was 1.35 mm and 1.75 mm, and dimensions of steel channel cross-section (flange width × web height, $b_s \times h_s$) were 30 mm × 135 mm, 40 mm × 135 mm, and 40 mm × 175 mm, respectively. The length of five specimens (B-1 to B-5) was designed as 2.44 m, while the calculated span (l) of specimens was 2.2 m. The section of the composite beam is exhibited in Figure 2, and the parameters of specimens are listed in Table 3.

2.3. Specimen Preparation. The box section bamboo-steel composite beams consist of two cold-formed thin-walled steel channel and four bamboo plywood, which is bonded with epoxy resin. The section form of composite beams is shown in Figure 2 and the specific manufacturing processes are as follows. First, polish the interface between thin-walled steel and bamboo plywood to remove zinc coating layer of steel and glaze layer of bamboo plywood. Then, wipe the polished steel and bamboo plywood with alcohol pads to ensure the bonding surface clean. After that, apply the epoxy resin evenly on the surface of bamboo plywood and fix the bamboo plywood and the steel channel with fixtures to make sure that two materials are bonded effectively. Besides, symmetrically place heavy objects on the bond surface to improve the quality of bond. The pressurization process lasted for two days and the curing time lasted for 7 days. The finished specimens are shown in Figure 3.

2.4. Test Setup and Instrumentation. A four-axis universal testing machine was adopted in this study, as shown in Figure 4(a). The mechanical jack was applied for monotonous gradation loading with the step of 5 kN. The force sensor was employed to measure the compressive load. Specimens can still bear load after local failure because of good entirety, and the test was terminated when the beam cannot bear higher level load. The four-point flexure loading scheme was adopted. Clear distance between two supports was 2.2 m, two equivalent loading points were 800 mm from the end of beam, and length of pure bending sections was 600 mm.

Five strain gauges were evenly arranged at the web of midspan of beam. Displacement sensors were installed at support point, loading point, midspan, and midpoint between the support and the loading point to measure vertical deflection under the load. Figure 4(b) shows the scheme of loading device of the test.

Data of strain gauges and displacement sensors was collected by the static strain test system. The load was supposed to be stable in the reading and observation process, and data collection should be carried out after the instrument readings were stable.

3. Test Results and Discussion

3.1. Failure Characteristics and Test Observations. All the five specimens showed the similar failure modes. The failure processes for specimen could be divided into two stages. The first stage began with the application of load. As the load increased to about 50% of the ultimate load, the sporadic sound could be heard due to the extrusion and tension of bamboo plywood. However, no crack could be found on the surface during the first stage. During the second stage, initial debonding cracks could be observed with slight degumming sound in the interface between thin-walled steel and bamboo plywood. With the increase of applied load, the cracks continued to appear and propagated along the interface. As the load was about to reach the ultimate load, the specimens failed due to the local damage and debonding between bamboo plywood and steel channel. However, no overall debonding could be found during the experiment.

Figure 5 shows the failure characteristics of specimens. The difference between B-1 and B-2 is the thickness of bamboo plywood. B-1 failed due to the extrusion of upper bamboo flange (Figure 5(a)), while the upper bamboo flange of B-2 could bear more pressure with thicker bamboo plywood. Debonding at upper flange near the support could be observed when B-2 failed (Figure 5(b)). The difference between B-3 and B-4 is the thickness of steel channel, while they exhibited the similar failure characteristics, both of them failed due to the extrusion of bamboo plywood and local buckling of steel channel in the compression zone of

(a) (b)

Figure 1: Test of material properties. (a) Test for steel sheet. (b) Test for bamboo plywood.

Table 1: Material properties of cold-formed thin-walled steel.

t_s (mm)	E_s (GPa)	f_y (MPa)	f_u (MPa)
1.35	206	255	395
1.75	206	275	405

Table 2: Material properties of bamboo plywood.

t_b (mm)	E_b (MPa)	σ (MPa)
15.1	4858	38
17.6	6784	46
25.0	6905	56

Note: t_b is the thickness of bamboo plywood.

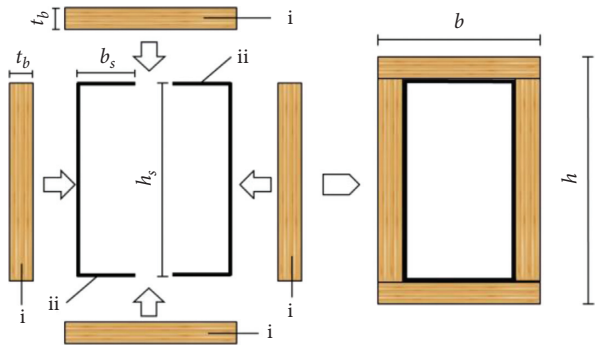

Figure 2: Section form of composite beam: (i) bamboo plywood and (ii) cold-formed thin-walled steel channel.

the midspan section (Figures 5(c) and 5(d)). The steel channel dimension of B-5 is larger than that of B-3. Unlike the B-3, the failure of B-5 attributed to the debonding between bamboo plywood and steel channel (Figure 5(e)), and local buckling of steel channel could be found near the support point (Figure 5(f)); thus, the specimen could not resist more load.

3.2. Load-Deflection Curves and Bearing Capacity. The load-deflection curves for specimens B-1 to B-5 are shown in Figure 6. The deflection here is the deflection of midspan, which is recorded by displacement sensor. As can be seen from Figure 6, the curves of each specimen could be divided into two stages, i.e., the elastic stage and elastic-plastic stage. During the elastic stage, the deflection of the specimen increased linearly with the increase of the load. At this stage, bamboo plywood and thin-walled steel worked together, and the overall performance of composite beam was good. Once the applied load reached approximately 50% of the ultimate load, the flexural stiffness of specimens gradually decreased due to the partial debonding of interface. The curves went into elastic-plastic stages, and the deflection of composite beam increased more, the load-

Table 3: Parameters of specimens.

Specimens	t_b (mm)	t_s (mm)	$b_s \times h_s$ (mm)	$b \times h$ (mm)	l (m)
B-1	15.1	1.35	30.0×135.0	90.2×165.2	2.2
B-2	25.0	1.35	30.0×135.0	110.0×185.0	2.2
B-3	17.6	1.35	40.0×135.0	115.2×170.2	2.2
B-4	17.6	1.75	40.0×135.0	115.2×170.2	2.2
B-5	17.6	1.35	40.0×175.0	115.2×210.2	2.2

Note: b and h represent the width and height of box section, respectively.

Figure 3: Specimens of composite beam. Note: one specimen was omitted due to the invalid result.

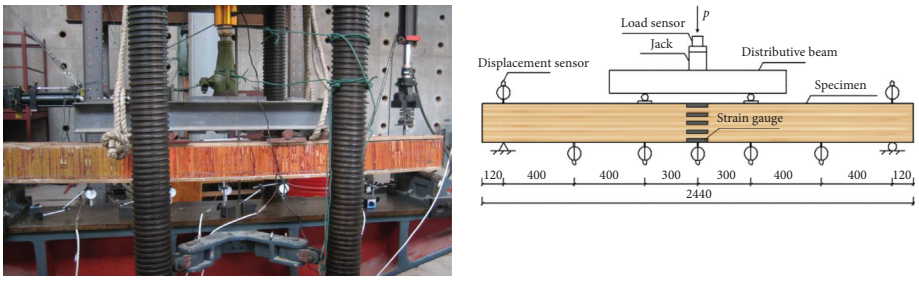

(a) (b)

Figure 4: Test setup. (a) Photograph. (b) Diagrammatic view (all dimensions in mm).

(a) (b) (c)

Figure 5: Continued.

(d) (e) (f)

Figure 5: Failure characteristics of composite beams. (a) Extrusion of upper bamboo flange of B-1. (b) Debonding near support of B-2. (c) Extrusion of upper bamboo flange of B-3. (d) Extrusion of upper bamboo flange of B-4. (e) Debonding of B-5. (f) Local buckling near support of B-5.

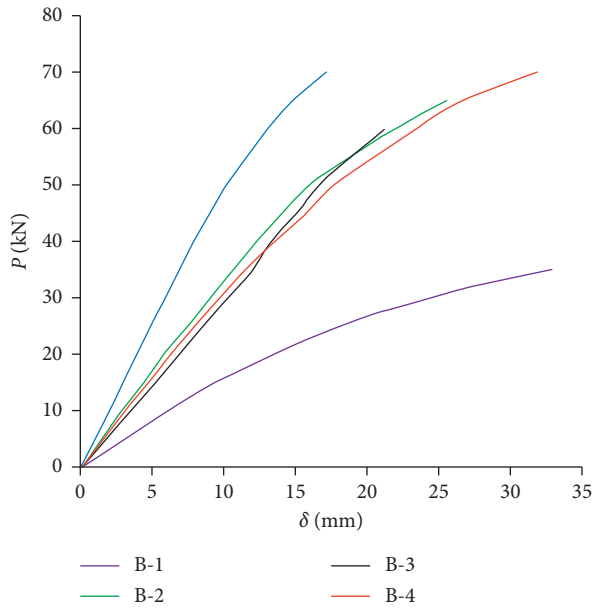

Figure 6: Load-deflection curves for specimens B-1 to B-5.

deflection curves showed nonlinear behaviour. There was no obvious descending section in each curve, and the load could keep near the ultimate load before the specimen failed. Thus, the composite beam had enough safety margin.

The limit state of members can be divided into two states, i.e., the ultimate limit state and the serviceability limit state. The members cannot meet the safety requirements when exceeding the ultimate bearing capacity. And the members cannot meet the suitability and durability requirements when exceeding the serviceability limit state. For flexural members, the flexural capacity calculation is controlled by the ultimate limit state, while the deflection calculation is controlled by the serviceability limit state. The bearing capacity of bamboo-steel composite flexural members (such as composite floors and composite beams) is high, and the deflection is also large. Thus, the bearing capacity under serviceability limit state is controlled by the rigidity condition. The deflection of box section bamboo-steel composite beam under serviceability limit state should be calculated by l/250 of span length according to the standard in China [22]. The main test results are shown in Table 4. The bearing capacity of composite beam under serviceability limit state is close to or exceeds half of that, under the ultimate limit state.

3.3. Strains Distribution at Midspan Section. Five strain gauges were arranged evenly at midspan of composite beams to measure the changes of strain along the height of beams under different loads. It was found that the cross-sectional strain curves of each beam were similar. Taking specimen B-3 as example, the average strain distribution along the height at midspan, which is shown in Figure 7, changed almost linearly, and the position of neutral axis of section was at the centre of beam height, which indicated that the midspan sectional deformation of the composite beam accorded with the plane-section assumption.

4. Parametric Analysis

4.1. Effect of Bamboo Plywood Thickness. The bamboo plywood thickness of B-2 was increased from 15.1 mm (thickness of B-1) to 25 mm, as comparing B-1 and B-2, both of which had the same geometrical dimensions of the steel channel. Load-deflection curves (Figure 8) show that the ultimate load of B-2 was increased from 35 kN of B-1 to 65 kN. And the deflection of B-2 was also significantly smaller than that of B-1 under the same load. This may attribute to the fact that the ticker bamboo plywood has great contribution to the sectional moment of inertia, which could improve the flexural stiffness and bearing capacity. Thus, with the increase of bamboo flange and web thickness of the composite beam, the ultimate load and flexural stiffness of composite beams can be greatly improved.

4.2. Effect of Thickness and Sectional Dimension of Steel Channel. The load-deflection curves of B-3 and B-4 are compared in Figure 9, and it can be found that the increased thickness of thin-walled steel can improve ultimate load and safety margin of composite beams, while having little effect on flexural stiffness. Because the sectional area of steel is far less than that of bamboo plywood in composite beams, the thicker steel channel has little contribution to the sectional moment of inertia. Thus, the thickness of steel channel has

Table 4: Calculation results of specimens.

Specimens	P_u (kN)	M_u (kN·m)	δ_{max} (mm)	M_u' (kN·m)	δ (mm)	M_u'/M_u
B-1	35.0	14.0	35.80	5.68	8.80	0.41
B-2	65.0	26.0	25.47	11.40	8.80	0.44
B-3	60.0	24.0	21.16	10.76	8.80	0.45
B-4	70.0	28.0	31.76	11.72	8.80	0.42
B-5	70.0	28.0	17.10	17.64	8.80	0.63

Note: P_u is the ultimate applied load; M_u is the ultimate flexural bearing capacity; δ_{max} is the deflection of midspan corresponding to P_u; M_u' is the flexural bearing capacity in serviceability limit state; δ is the deflection of midspan in the serviceability limit state.

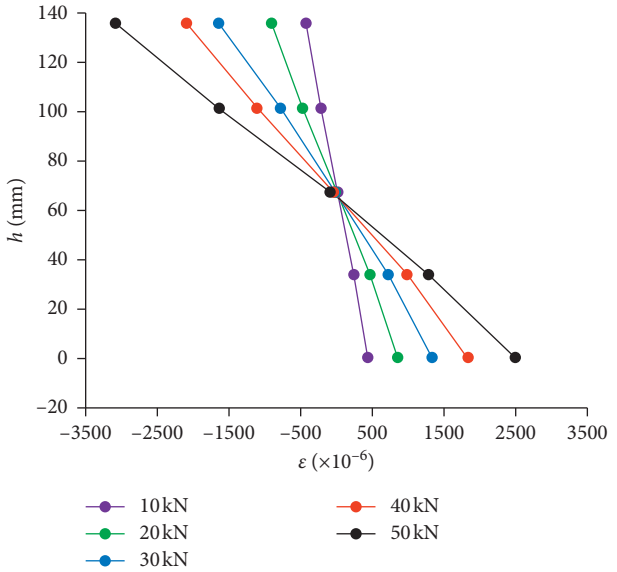

Figure 7: Strain distribution at midspan section of B-3.

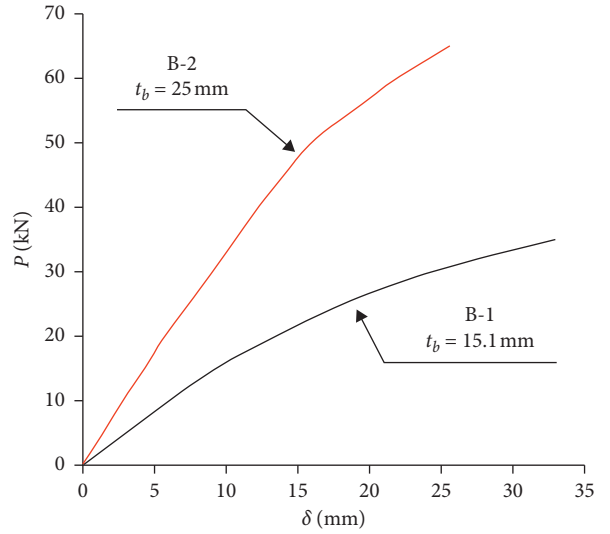

Figure 8: Effect of bamboo plywood thickness on load-deflection curves.

little influence on the flexural stiffness of beams. However, the ultimate stress of steel (f_u) is larger than the rupture modulus of bamboo plywood (σ) according to Table 1 and Table 2. Therefore, the bearing capacity of the composite beam can be improved effectively by increasing the thickness of steel channel.

Similarly, the load-deflection curves of B-3 and B-5 are compared in Figure 10, and it can be found that the increase of the height of steel channel could improve the ultimate bearing capacity and flexural stiffness. That is because the increase of height of steel channel can increase both the inertia moment and area of cross-section effectively.

5. Theoretical Calculation and Analysis

5.1. Midspan Deflection. The test showed that the steel and bamboo plywood of the bamboo-steel composite beam are both in the elastic stage under the serviceability limit state. Therefore, superposition principle can be employed to calculate the flexural stiffness (EI) of the composite beam [2], which is given by

$$\mathrm{EI} = E_{fb}I_{fb} + E_{wb}I_{wb} + E_sI_s, \tag{1}$$

where E_{fb}, E_{wb}, and E_s are the elasticity modulus of flange bamboo plywood, web bamboo plywood, and steel channel, respectively; I_{fb}, I_{wb}, and I_s are the inertia moment of flange bamboo plywood, web bamboo plywood, and steel channel, respectively.

Considering the different deflection calculation of composite components between test and theory, a coefficient β_b is introduced in the formula for calculating the midspan deflection of the simply supported beam [23]. Thus, the midspan deflection (δ) of the composite beam under the serviceability limit state can be expressed as follows:

$$\delta = \beta_b \frac{\mathrm{pal}^2}{48\mathrm{EI}}\left(3 - 4\left(\frac{a}{l}\right)^2\right), \tag{2}$$

where the P is the applied load on the composite beam, a is the distance between the point of applied load and near support, l is the calculated span of composite beam, and EI is the flexural stiffness of composite beam.

Figure 11 showed the comparison of midspan deflections between experimental values and theoretical values calculated by equation (1) and equation (2). It can be observed that the calculated values matched well with the experimental values with less than 10% relative errors.

5.2. Flexural Bearing Capacities. The test results showed that when the beam damaged, the upper flange of the cross-section was deboned, so the strength reduction factor γ_d ($\gamma_d = 0.95$) [2] of bamboo plywood was introduced to

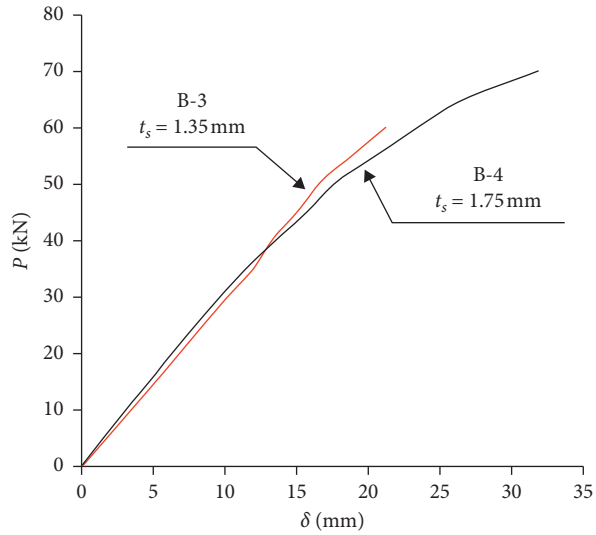

Figure 9: Effect of steel channel thickness on load-deflection curve.

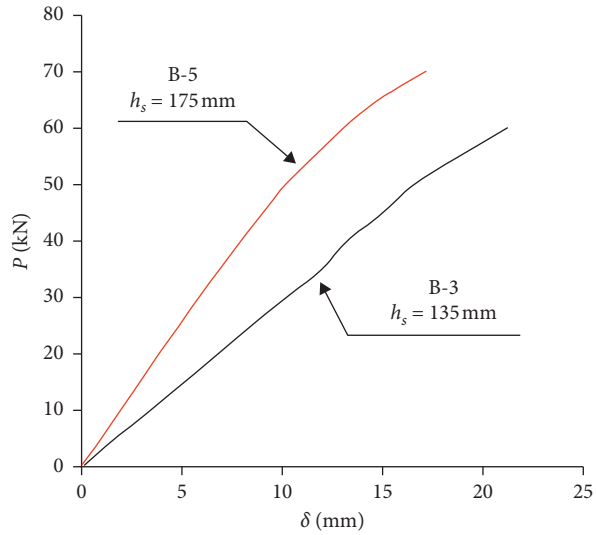

Figure 10: Effect of sectional dimension of steel channel on load-deflection curve.

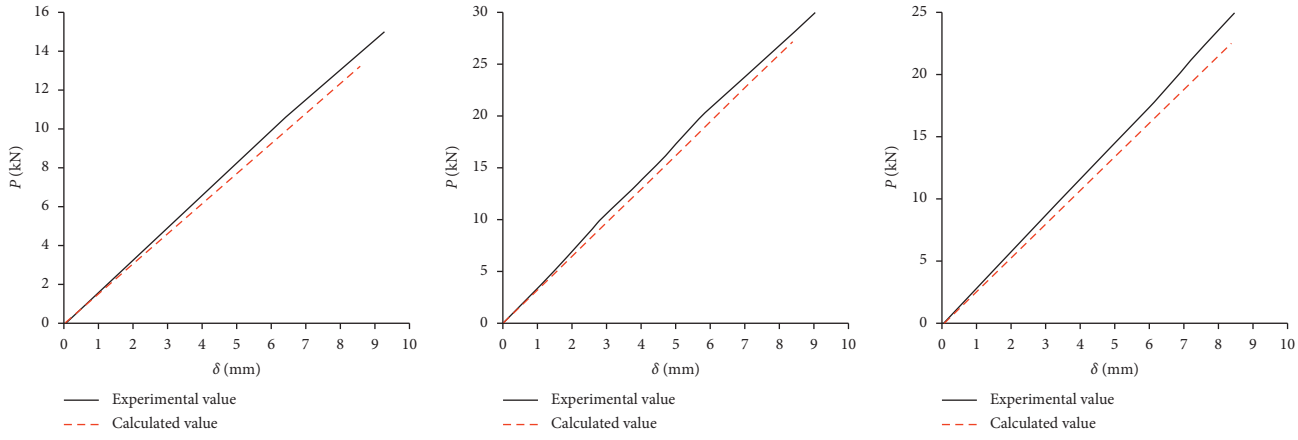

Figure 11: Continued.

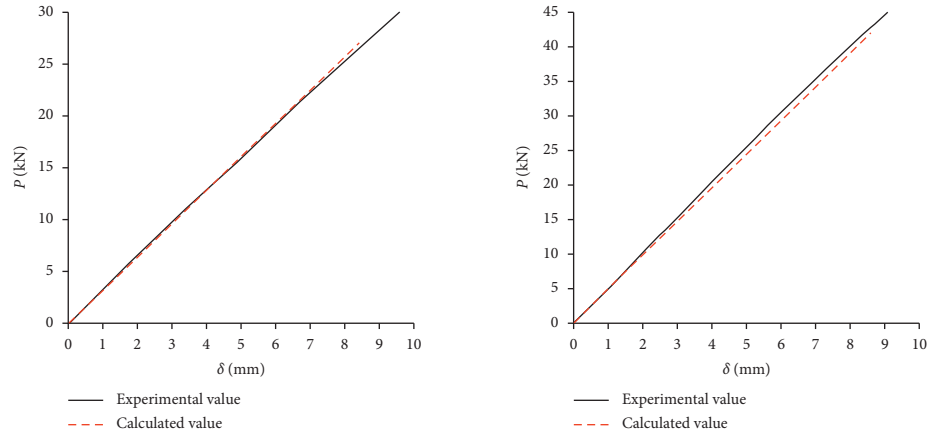

Figure 11: Comparisons of midspan deflections between the experimental and calculated value (in serviceability limit state). (a) B-1. (b) B-2. (c) B-3. (d) B-4. (e) B-5.

Table 5: Comparison of flexural bearing capacities between calculated and experimental values.

Specimens	M_b (kN·m)	M_s (kN·m)	M (kN·m)	M_{exp} (kN·m)	M_b/M	M_{exp}/M
B-2	5.10	7.65	12.75	14.00	0.40	1.10
B-3	12.78	7.65	20.43	26.00	0.63	1.27
B-4	10.04	8.69	18.73	24.00	0.54	1.28
B-5	12.01	13.53	25.54	28.00	0.47	1.10
B-6	10.29	13.17	23.46	28.00	0.44	1.19

consider the debonding of upper flange. It also could be found that the strain of steel channel in the tension zone exceeded the yield strain ($\varepsilon_s > 0.002$) when the beam damaged, which indicated that the tension zone of the steel channel had reached the plastic stage while the other components were still in the elastic stage. Thus, the plastic ratio of steel channel γ_s ($\gamma_s = 1.05$) [24] was introduced to consider the plastic behaviour. Strain distribution at midspan section of specimens indicates that the midspan sectional deformation of specimens agrees with the plane-section assumption. The flexural bearing capacities (M) of box section composite beams are proposed based on the superposition principle, which is shown as follows:

$$\begin{aligned} M &= M_b + M_s, \\ M_b &= \gamma_d \sigma_b W_b, \\ \sigma_b &= \varepsilon_b E_{fb}, \\ M_s &= \gamma_s f_u W_s, \end{aligned} \tag{3}$$

where M_b and M_s are the flexural bearing capacities of bamboo section and steel channel section, respectively; σ_b and ε_b are the failure normal stress and strain of bamboo plywood, respectively; W_b and W_S are the elastic section modulus of bamboo plywood section and steel channel section, respectively; and f_u is the ultimate stress of steel channel.

The comparison of flexural bearing capacities between calculated values (M) and experimental values (M_{exp}) are shown in Table 5. It can be found that the calculated capacities matched well with the experimental values. Furthermore, the bamboo section contributes 40–63% of the total flexural bearing capacity of composite beams.

6. Conclusions

In this paper, the flexural behaviour of box section bamboo-steel composite beams was experimentally investigated and theoretically analysed. Five box section bamboo-steel composite beams were tested, and the conclusion based on the results is summarized as follows:

(1) The box section bamboo-steel composite beams have an excellent structural integrity, and no overall failures can be observed in the interface between bamboo plywood and thin-walled steel channel. The composite beams could combine the advantages of light weight and high strength of bamboo plywood and steel, while the disadvantage of easy buckling of thin-walled steel are overcome.

(2) The midspan cross-section strain curve of composite beams showed that strains changed linearly along the height of cross-section; therefore, the plane-section assumption can be used to study the composite beams.

(3) The thickness of bamboo plywood, thickness, and sectional dimension of steel channel have varying degrees influence on bearing capacities, flexural

stiffness, and safety margin of the box section bamboo-steel composite beams. The bearing capacity and flexural stiffness increased with the increase of the thickness of bamboo plywood and sectional dimension of steel channel, while the thickness of steel channel has little influence on the flexural stiffness. However, the thickness of steel channel can improve bearing capacity and safety margin of composite beams.

(4) The bearing capacity of composite beams under serviceability limit state is close to or exceeds half of that, under ultimate limit state, which indicated that the strength of both bamboo plywood and thin-walled steel channel was fully utilized. The proposed equations for predicting the deformation and bearing capacities of composite beams matched well with the experimental results.

Data Availability

The data used to support the findings of this study are available from the corresponding author upon request.

Conflicts of Interest

The authors declare that there are no conflicts of interest regarding the publication of this paper.

Acknowledgments

The authors gratefully acknowledge the financial support provided by the National Key R&D Program of China (2019YFD1101002), National Natural Science Foundation of China (NSFC) (51678310 and 51978345), and K. C. Wong Magna Fund at the Ningbo University.

References

[1] K. Wang, Q. Li, and X. Gao, "Present utilizational situation and deep exploitation of bamboo resources," *Journal of Bamboo Research*, vol. 19, no. 4, pp. 72–75, 2000.

[2] Y. Li, W. Shan, H. Shen, Z.-W. Zhang, and J. Liu, "Bending resistance of I-section bamboo-steel composite beams utilizing adhesive bonding," *Thin-walled Structures*, vol. 89, pp. 17–24, 2015.

[3] Y. Huang, Y. Qi, Y. Zhang, and W. Yu, "Progress of bamboo recombination technology in China," *Advances in Polymer Technology*, vol. 2019, Article ID 2723191, 10 pages, 2019.

[4] F. F. Wang and W. H. Wang, "The status quo and problems of bamboo-based panels production in China," *China Wood-based Panels*, vol. 14, no. 12, pp. 1–4, 2007.

[5] F. Z. Meng, W. J. Yu, and G. S. Chen, "Processing and properties comparison between four kinds of bamboo-based panel," *Wood Processing Machinery*, vol. 22, no. 1, pp. 32–35, 2011.

[6] A. Zhou and Y. Bian, "Experimental study on the flexural performance of parallel strand bamboo beams," *The Scientific World Journal*, vol. 2014, Article ID 181627, 6 pages, 2014.

[7] J. Lei, B. Chen, and P. Yuan, "Experimental study on flexural properties of side-pressure laminated bamboo beams," *Advances in Civil Engineering*, vol. 2020, Article ID 5629635, 10 pages, 2020.

[8] V. De Luca and C. Marano, "Prestressed glulam timbers reinforced with steel bars," *Construction and Building Materials*, vol. 30, pp. 206–217, 2012.

[9] Y. Wei, M. Zhou, and D. Chen, "Flexural behaviour of glulam bamboo beams reinforced with near-surface mounted steel bars," *Materials Research Innovations*, vol. 19, no. 1, pp. S198–S103, 2015.

[10] Y. Wei, X. Ji, M. Duan, and G. Li, "Flexural performance of bamboo scrimber beams strengthened with fiber-reinforced polymer," *Construction and Building Materials*, vol. 142, pp. 66–82, 2017.

[11] Y.-F. Li, Y.-M. Xie, and M.-J. Tsai, "Enhancement of the flexural performance of retrofitted wood beams using CFRP composite sheets," *Construction and Building Materials*, vol. 23, no. 1, pp. 411–422, 2009.

[12] Y. Nadir, P. Nagarajan, M. Ameen, and M. Arif M, "Flexural stiffness and strength enhancement of horizontally glued laminated wood beams with GFRP and CFRP composite sheets," *Construction and Building Materials*, vol. 112, pp. 547–555, 2016.

[13] H. Fang, X. Xu, W. Liu et al., "Flexural behavior of composite concrete slabs reinforced by FRP grid facesheets," *Composites Part B: Engineering*, vol. 92, pp. 46–62, 2016.

[14] Q. Lv, W. Wang, and Y. Liu, "Flexural performance of cross-laminated bamboo (CLB) slabs and CFRP grid composite CLB slabs," *Advances in Civil Engineering*, vol. 2019, Article ID 6980782, 17 pages, 2019.

[15] T. Liu, Y. Li, K. Xu et al., "Research on mechanical performance of steel-bamboo composite box short column," *Industrial Construction*, vol. 46, no. 1, pp. 25–29, 2016.

[16] Y. Li, H. Shen, W. Shan, L. Bo, and T. Jiang, "Experimental study on shear behavior of I-shaped section bamboo-steel composite beams," *Journal of Building Structures*, vol. 11, no. 7, pp. 80–86, 2011.

[17] Y. Li, W. Shan, Z. Huang, B. Ge, and Y. Wu, "Experimental study on mechanical behavior of profiled steel sheet-bamboo plywood composite slabs," *Journal of Building Structures*, vol. 29, no. 1, pp. 96–102, 2008.

[18] Y. Li, H. Shen, W. Shan, and T. Han, "Flexural behavior of lightweight bamboo-steel composite slabs," *Thin-Walled Structures*, vol. 53, pp. 83–90, 2012.

[19] Y. Li, H. Shen, W. Zhang et al., "Experimental study on seismic performance of compression plate and bamboo board composite wall," *Engineering Mechanics*, vol. s1, pp. 108–112, 2010.

[20] China National Standard, *Metallic Materials-Tensile Testing-Part 1: Method of Test at Room Temperature (GB/T228.1-2010)*, China National Standard, Beijing, China, 2010.

[21] China National Standard, *Test Methods of Evaluating the Properties of Wood-Based Panels and Surface Decorated Wood-Based Panels (GB/T 17657-2013)*, China National Standard, Beijing, China, 2013.

[22] China National Standard, *Standard for Design of Timber Structures (GB50005-2017)*, China National Standard, Beijing, China, 2017.

[23] China Architecture & Building Press, *Handbook of Static Calculation of Building Structures*, China Architecture & Building Press, Beijing, China, 2nd edition, 2000.

[24] China National Standard, *Standard for Design of Steel Structures (GB 50017-2017)*, China National Standard, Beijing, China, 2017.

Hindawi
Advances in Civil Engineering
Volume 2020, Article ID 8854156, 10 pages
https://doi.org/10.1155/2020/8854156

Research Article

Field Test and Simulation Analysis of Thermal Performance of Bamboo Steel Composite Wall in Different Climate Regions

Qifeng Shan,[1] **Keting Tong**,[1] **Xiaocun Zhang**,[1] **and Yushun Li**[2]

[1]*School of Civil and Environmental Engineering, Ningbo University, Ningbo 315211, China*
[2]*School of Civil Engineering, Qingdao Agricultural University, Qingdao 266109, China*

Correspondence should be addressed to Yushun Li; lys0451@163.com

Received 8 September 2020; Revised 27 September 2020; Accepted 30 September 2020; Published 14 October 2020

Academic Editor: Min-Juan He

In this paper, a bamboo steel composite testing building was designed and built to study the thermal performance of a new proposed bamboo steel composite wall. The heat flux meter method was adopted in the field test to measure the heat transfer coefficient of the composite wall. The energy consumption of testing building was measured to verify the validity of the simulation model. Then, the simulation analysis was conducted to study the energy performance of the composite walls compared with reinforced concrete wall in different climate regions. The result showed that the measurement value of heat transfer coefficient matched well with the theoretical calculation value, and both values meet the requirement of the standard. The simulation result showed that the composite walls had better energy performance and had great potential utilization in residential buildings in different climate regions.

1. Introduction

With the development of the society, excessive resource consumption has become an important problem in developing economy and improving people's living standards. The resource consumption of building and building-related activities has a huge share in total resource consumption [1, 2]. It is essential to promote renewable materials to replace non-renewable and heavily polluted building materials such as steel, concrete, and brick masonry.

Bamboo is one of the fastest growing renewable resources and the yearly output yield is higher compared with wood. Besides, bamboo has the advantages of high strength-to-weight ratio and good seismic resistant performance. It is a sustainable building material and can be competitive with traditional materials [3, 4].

To reduce the resource consumption, low-energy buildings have received widespread concerns. The main design of low-energy buildings is to improve a building's thermal performance [1]. Some studies showed that the bamboo exhibited good thermal performance: Shah et al. [5] reported that the engineered bamboo with high density had lower thermal conductivities than equivalent timber products. Takagi et al. [6] investigated the insulating properties of the PLA-bamboo fiber and found that the thermal conductivity of PLA-bamboo fiber is smaller than that of conventional composites.

Some researchers carried out the study on the thermal performance of bamboo composite walls: Xiang et al. [7] tested the thermal properties of compound bamboo wall in different moisture content. The study indicated that the thermal insulation performance of bamboo plywood was better than traditional building materials. Risnandar and Wonorahardjo [8] proposed a plastered-bamboo wall composed of bamboo as a frame and mortar as a frame cover. The proposed wall had better thermal properties than brick wall while the density of proposed wall was lower than brick wall. Wang et al. [9] studied the insulating properties of bamboo-based shear wall, which indicated the possible application of bamboo-based shear wall in light-frame building.

However, the bamboo structure members have lower bearing capacity than the steel members under the same dimensions [10, 11]. Thus, the bamboo structure members

strengthened by other materials such as steel bars [12, 13], fiber polymer [14], and FRP sheets or grid [15–18] were designed and investigated in recent years.

Bamboo steel composite members are a new kind of composite structure, which are made of bamboo plywood and cold-formed thin-walled steel. The bamboo steel composite members combine the advantages of light weight and high strength of bamboo plywood and steel, while the disadvantage of easy buckling of thin-walled steel is overcome. Recently, some researchers have proposed some bamboo steel composite components, such as bamboo steel composite columns [19], beams [20], and slabs [21, 22]. The researches had shown the cooperation of the two materials could effectively improve the mechanical performance of the composite members.

The authors proposed a new type of bamboo steel composite walls; these new walls can be fabricated in factory and quickly installed on-site. Relative research had shown that the composite walls had better bearing capacity and ductility compared with reinforced concrete wall [23]. However, the thermal performance of the proposed walls has not been studied. This paper is aimed at investigating the thermal performance of bamboo steel composite wall and its potential application in different climate regions. In this study, a testing building made of bamboo steel composite walls was built to test the thermal performance of the proposed wall. Then, the simulation was conducted to assess the energy performance of the composite walls compared with reinforced concrete wall in different climate regions.

2. Project Overview

As is shown in Figure 1, a bamboo steel composite building for field measurement was built in Ningbo, where is a typical city with hot summer and cold winter in China. All the members for the testing building including beams, plates, and columns were precast in the laboratory. The prefabricated members were transported to the destination for on-site installation. Thermal insulation and waterproof measures were taken for the testing building as common houses. This was the first truly new type of bamboo steel composite building which consisted of steel bamboo composite members and reinforced concrete floor. The single-storey building covered an area of 24 m^2 and the height of the building was 3 m. The ratio of window area to wall area was 0.24 for the north wall and 0.31 for the south wall, respectively, while there were no windows in east and west walls. The windows adopted here were ordinary windows with 6 mm single glazing. The floor of the testing building was made of concrete with a thickness of 120 mm.

2.1. Design of Wall. The bamboo steel composite walls structure is shown in Figure 2. The composite wall is composed of two bamboo plywoods with a thickness of 10 mm as cover panels and strengthened by several bamboo steel composite skeletons. The composite skeletons shown in Figure 3(a) are made of C-type steel which was sandwiched by two bamboo plywoods with a thickness of 20 mm. The dimension ($h \times b \times c \times t$) of C-type steel shown in Figure 3(b) is 100 mm × 50 mm × 20 mm × 1 mm. As is illustrated in Figure 1(b), the testing building belongs to frame structure. The walls of testing building are employed as building envelopes. Thus, the design of walls is mainly to satisfy the requirement of thermal performance. The cavity of wall is filled with mineral wool as insulation material. Several layers are covered on the outer surface of the wall including cement mortar and polystyrene board; the total thickness of the composite wall is 170 mm. The construction of the composite wall is shown in Figure 4.

The east wall dimension of the testing building was 3.27 m × 2.68 m. Due to the difficulty in production and installation of the entire wall, the composite wall was divided into three pieces with the same size of 1.09 m × 2.68 m. The mechanical experiments of composite walls suggest that the suitable distance between composite skeletons varies from 250 mm to 400 mm. Two composite skeletons should be employed in the edge of wall. The width of every wall is 1090 mm; thus, two extra composite skeletons need to be added to strengthen the composite walls. The walls were evenly divided into three cavities by four skeletons and the center-to-center distance between skeletons is 333 mm. Then, the three pieces of walls were spliced by thin steel sheet and bolts during the on-site installation. The composite walls were employed as building envelopes; thus, the connection between walls was designed to maintain their integrity. While the insulation performance of splice between walls was taken seriously, polystyrene board was entirely covered over the splice, steel sheet, and bolts to ensure thermal performance of composite walls (Figure 1(c)).

2.2. Manufacture of Wall. As described above, the manufacture of composite wall mainly includes 3 processes, i.e., the production of composite skeletons, the combination of two bamboo plywood cover panels with skeletons, and filling with insulation material in the cavity of walls. The production processes of the walls are illustrated in Figure 5 and the specific manufacture processes are as follows:

(1) Polish the interface between the C-type steel and bamboo plywood, and then wipe the polished steel and bamboo plywood with alcohol wipes to ensure that the bonding surface is clean (Figure 5(a)).

(2) Apply the pre-mixed structural adhesive evenly on the surface of the C-type steel. Fix the bamboo plywood and steel with fixtures to make sure that the two materials were bonded effectively. Besides, symmetrically place heavy objects on the bond surface to improve the quality of bond (Figure 5(b)).

(3) Fill three layers of mineral wool into the cavity of the C-type steel (Figure 5(c)), and then bond them with another bamboo plywood followed by the above steps (Figure 5(d)). Finally, the composite skeleton with insulation material is completed (Figure 5(e)).

(4) The skeletons are bonded on the bamboo plywood cover panels as designed and the adhesive procedure follows the steps above (Figure 5(f)).

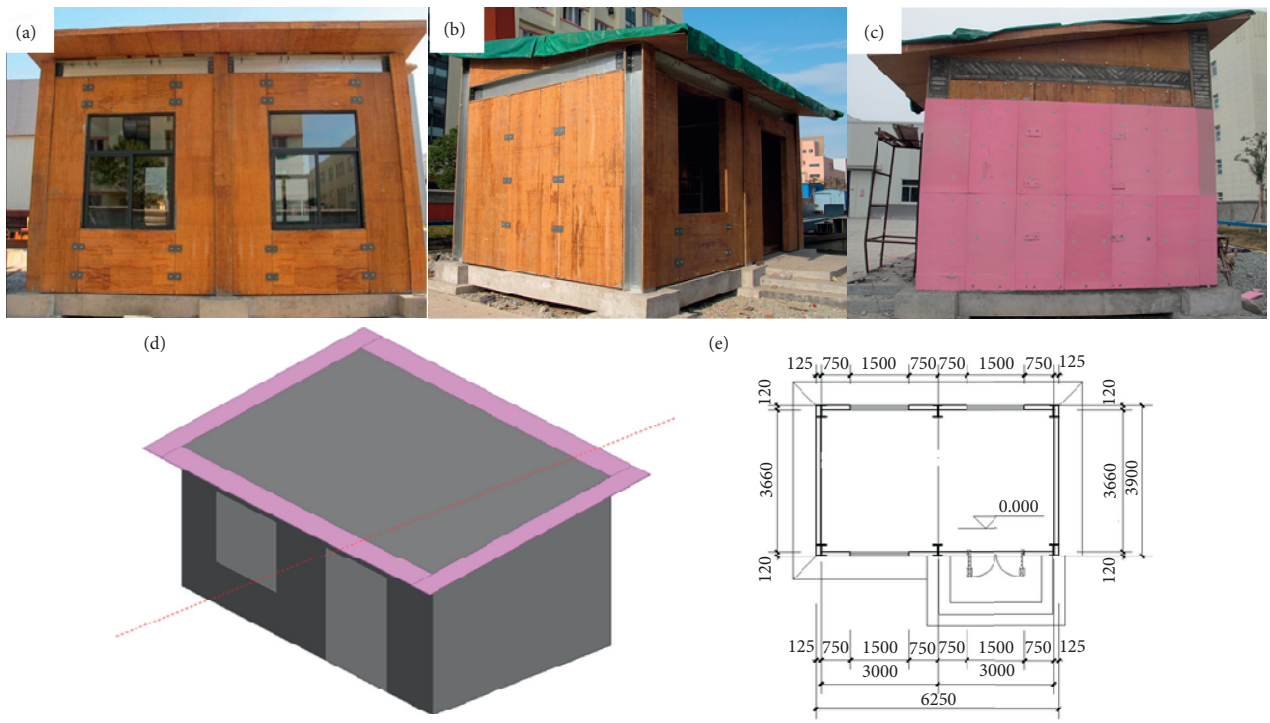

Figure 1: Testing building. (a) Front view. (b) Lateral view. (c) Installation of polystyrene board. (d) Simulation model. (e) Plan view of building.

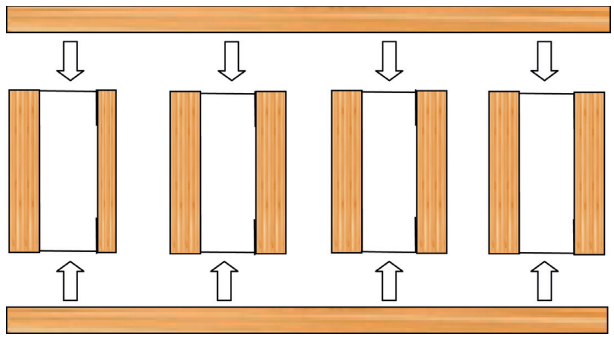

Figure 2: Structure of bamboo steel composite wall.

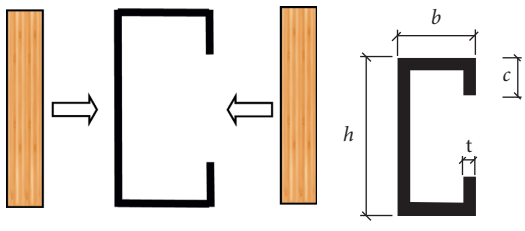

Figure 3: Bamboo steel composite skeleton. (a) Structure of the skeleton. (b) Dimension of C-type steel.

(5) The cavities between steel-bamboo composite skeletons and bamboo plywood cover panels are also filled with three layers of mineral wool (Figure 5(g)). Thus, the bamboo steel composite wall is finished (Figure 5(h)).

3. Field Test and Simulation Analysis

Both field test and numerical simulation were conducted to measure the thermal performance of the bamboo steel composite walls. The thermal and energy performance of the testing building were field-tested during winter.

3.1. Heat Transfer Coefficient. Heat transfer coefficient (*K* value for short) is an important index to assess the thermal performance of external walls. *K* value is the amount of heat that is transferred per unit area, per time period, and per unit degree temperature difference between the internal and external of walls, which reflected how easily heat energy passes through the wall. The lower the *K* value, the higher the heat insulation performance. Therefore, the *K* value of bamboo steel composite walls should be experimentally measured and theoretically calculated to determine whether it satisfied the requirement of the standard [24].

3.1.1. Experimental Method. In this paper, the heat flux meter method is employed to measure the *K* value. Heat flux meter method is one of the most commonly used methods for measuring heat transfer coefficient [25, 26]. The test method is shown in Figure 6. A heat flux meter is arranged on the inner surface of the wall to measure the heat flux of the wall. Two temperature sensors are glued on the internal and the external surfaces of the wall to measure the temperature of the wall. Both the data of heat flux meter and temperature sensors were collected and recorded by patrol-

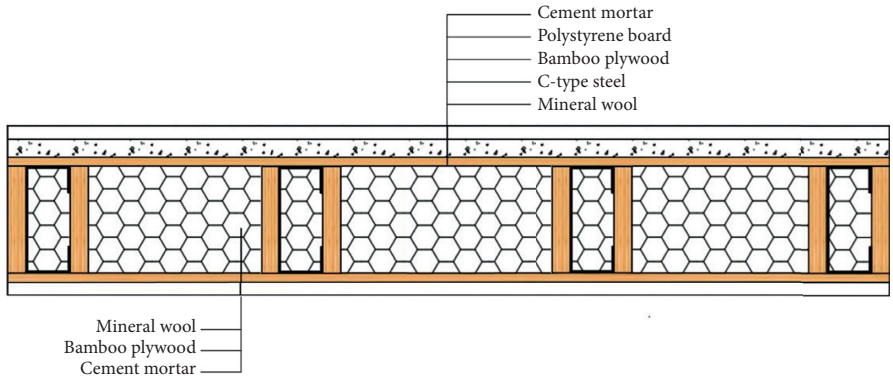

Figure 4: Construction of the composite wall.

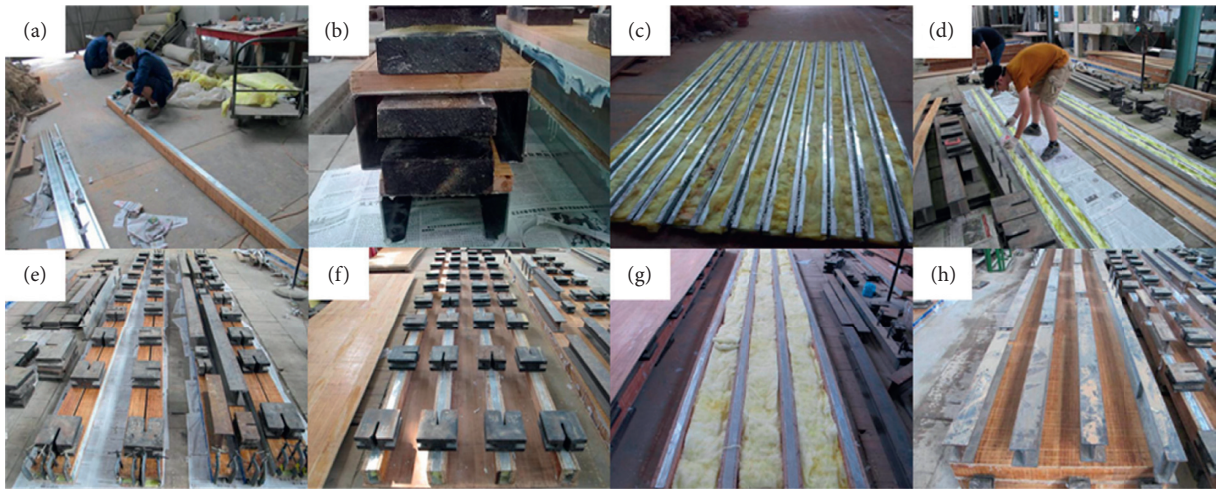

Figure 5: Production processes of composite walls.

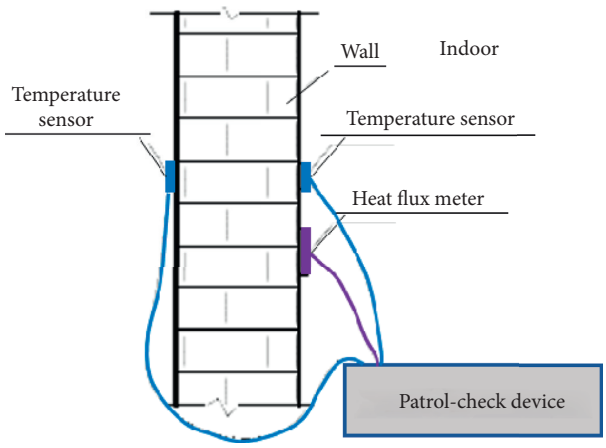

Figure 6: Heat flow meter method.

check device. The interval time of record data is set as 15 minutes in the test.

The K value can be calculated as follows:

$$K = \frac{1}{R_i + R + R_e}, \quad (1)$$

where R_i and R_e are the thermal resistance of internal and external wall, respectively. R_i and R_e here can be given as 0.11 m^2K/w and 0.04 m^2K/w, respectively, according to the Chinese standard [27]. R is the thermal resistance of the composite wall which can be calculated through the field test. The calculation equation can be expressed as follows:

$$R = \frac{\sum_{j=1}^{n}\left(\theta_{1j} - \theta_{2j}\right)}{\sum_{j=1}^{n} q_j}. \quad (2)$$

The subscript j is the time of measurement. The superscript n is the total measurement time. θ_{1j} and θ_{2j} are the inner and outer surface temperature tested by temperature sensors. q_j is the heat flux passed through the wall measured by heat flux meter.

3.1.2. Test Apparatus. The apparatuses including temperature sensors, heat flux meter, and patrol-check device were employed in the field test. The specification and precision of the apparatuses are introduced as follows:

Temperature sensor: the temperature sensor used in this test was a self-made T-type thermocouple, which is shown in Figure 7. This kind of T-type thermocouple was made of copper and welded with constantan wire. The temperature of the sensor ranged from −5°C to 100°C after calibration, while the precision of the sensor

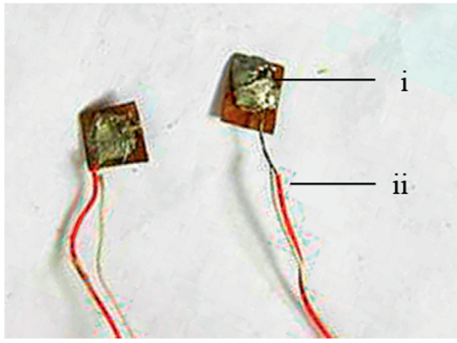

Figure 7: T-type thermocouple. (i) Copper; (ii) constantan wire.

was 0.1°C and the uncertainty of the sensor was −0.3~0.3°C.

Heat flux meter: the heat flux meter ranged from 0 to 2 kw/m^2 with a precision of 5%, while the size of the heat flow meter was 110 mm × 55 mm × 4 mm. The heat flow meter was glued on the inner surface of the wall sealed with grease and adhesive tape. Direct sunlight should be avoided which may have effect on the test result.

Patrol-check device: a JTRG-II thermal temperature and heat flux monitor device was adopted in this paper, which could display and record both temperature and heat flux at the same time. The monitor device could record 60 routes of temperature data and 30 routes of heat flow data at the same time.

3.1.3. Arrangement of Monitoring Point. According to the Chinese standard [25, 26], to measure heat transfer coefficient, the arrangement of monitoring point is essential in the field test. The monitoring point should be arranged near the center of the wall where it is far away from the columns, windows, corners, beams, and cracks. Considering the particularity of the composite wall structure, the center of the east wall of the test building is chosen to arrange the monitoring point, where neither the composite skeletons nor the location of the connection is located. The locations of the monitoring points are shown in Figure 8.

3.1.4. Requirement of Field Test. The field test complied with Chinese standards [25]. The bamboo steel composite walls belong to lightweight building envelope, and the field test of K value should be carried out during the night. Thus, the data used to calculate the K value in this paper were collected from 20 : 00 to 6 : 00. During the measurement, the temperature difference between inside and outside should be more than 10°C to make sure that heat energy passed through the wall steadily. The steady state of heat transfer cannot be reached until the deviation of calculated daily average K value between 2 continuous measurements is less than 5%. The field test of K value can be finished after 4 continuous measurements during the steady state of heat transfer. The measured K value of the composite walls can be determined by the average value of calculated daily average K value.

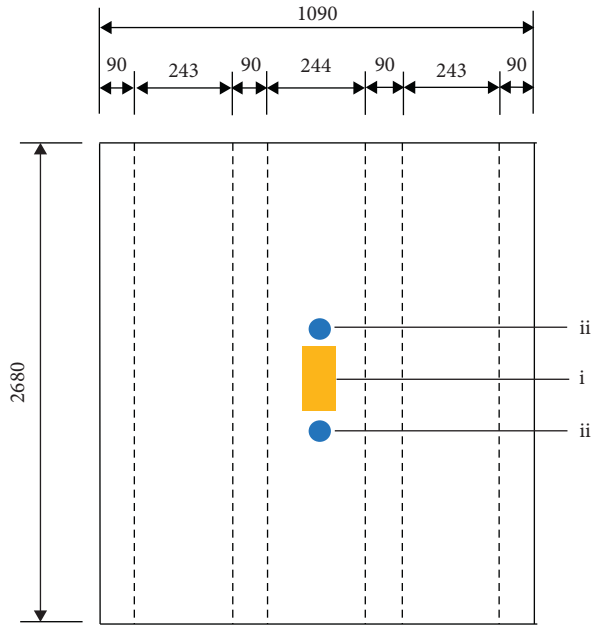

Figure 8: Arrangement of monitoring points on the east wall. (i) Heat flux meter; (ii) T-type thermocouple. Note: the dotted line is the location of the composite skeletons.

3.2. Energy Performance. An air condition for heating was installed in the testing building. The COP (coefficient of performance) of the air condition was 2.89. During the field test of K value, the air condition was kept on and the temperature was set at 18°C to ensure the temperature difference between indoor and outdoor was more than 10°C. An electric meter was installed to observe and record the heating energy consumption of the testing building. The measured energy consumption would be used to verify the validity of the simulation model for further investigation.

3.3. Computer Simulation. The testing building was simulated by the software EnergyPlus. It is an open-source, whole building energy modelling engine that can simulate both energy consumption (such as heating and cooling) and water usage in buildings.

The energy performance of the composite wall was simulated and compared with reinforced concrete wall, a typical wall structure commonly used in China. The construction of these two types of walls is listed in Table 1 (denoted as wall1 and wall2, respectively). The design of wall2 was required to meet the thermal performance of the standard (no more than 1.5 W/m^{2}K) [24]. The simulation between wall1 and wall2 was based on the same building model except the materials of wall and roof. The building model with wall1 adopted bamboo steel composite roof with an insulation layer (as shown in Table 1), while the other building model with wall2 employed reinforced concrete roof. Both building models have the same reinforced concrete floor.

Four typical cities in different climate regions in China were selected to analyse the energy performance of these two wall structures including hot summer/warm winter region

Table 1: Thermal properties of building materials.

Building members	Materials	δ (m)	λ (W/mK)	c (J/kgK)	ρ (kg/m^3)
Bamboo steel composite wall (wall1)	Cement mortar	0.015	0.93	1050	1800
	Polystyrene board	0.02	0.042	1500	20
	Bamboo plywood	0.01	0.17	2510	600
	C-type steel	0.001	58.2	480	7800
	Mineral wool	0.098	0.05	840	32
	C-type steel	0.001	58.2	480	7800
	Bamboo plywood	0.01	0.17	2510	600
	Cement mortar	0.015	0.93	1050	1800
Reinforced concrete wall (wall2)	Cement mortar	0.015	0.93	1050	1800
	Polystyrene board	0.02	0.042	1500	20
	Reinforced concrete	0.24	1.74	1094	1700
	Cement mortar	0.015	0.93	1050	1800
Roof1 for building with wall1	Fine aggregate concrete	0.03	1.51	920	2400
	Polystyrene board	0.02	0.042	1500	20
	Bamboo plywood	0.01	0.17	2510	600
	C-type steel	0.001	58.2	480	7800
	Mineral wool	0.098	0.05	840	32
	C-type steel	0.001	58.2	480	7800
	Bamboo plywood	0.01	0.17	2510	600
	Cement mortar	0.03	0.93	1050	1800
Roof2 for buildings with wall2	Fine aggregate concrete	0.03	1.51	920	2400
	Polystyrene board	0.02	0.042	1500	20
	Reinforced concrete	0.12	1.74	920	2500
	Cement mortar	0.03	0.93	1050	1800
Floor	Cement mortar	0.03	0.93	1050	1800
	Reinforced concrete	0.12	1.74	920	2500

Note. δ is the thickness; λ is the thermal conductivity; c is the thermal capacity; ρ is the density.

(Guangzhou), hot summer/cold winter region (Shanghai), cold region (Beijing), and severe cold region (Harbin).

The simulation setting followed the testing building and the setting items are listed in Table 2. The operation schedule of air condition was assumed to run throughout the year to meet the indoor temperature setting. The total power density of miscellaneous loads (including lighting systems and occupants) was set to 4.3 W/m^2. All these thermal settings complied with the design standard in China [24].

4. Results and Discussion

4.1. Heat Transfer Coefficient

4.1.1. Test Results. The test of K value of the composite wall was carried out during 5 typical winter days from 2016/1/26 to 2016/1/30. The average internal and external surface temperature of the composite wall are shown in Figure 9(a). The temperature curves showed that the internal surface temperature of the wall increased obviously with the increase of time. After about 8 hours, it reached the setting temperature of the air condition, and the temperature was kept at about 18°C with a little fluctuation, which indicated that the air conditioner could meet the demand for the indoor continuous heating. The external surface of the wall changed slightly due to the cloudy weather during the measurement period.

Figure 9(b) exhibits the heat flux rate of the test wall during the measurement. The heat flux rate is high at the beginning of the test due to unstable transfer of heat flux. Then, the heat flux rate dropped to about 5 W/m^2 after 9 hours and fluctuated with the temperature difference between the internal and external wall.

The calculated results of K value during the field test period are exhibited in Figure 9(c); the K value constantly decreased with the increase of indoor temperature in the beginning and tended to be stable after about 9 hours, which indicated that the heat transfer of the wall reached the steady state. The K value kept approximately constant with a small fluctuation during the night at a steady state. Thus, the data measured during the night from 20 : 00 to 6 : 00 was used to calculate the daily average K value. The differences between daily average K values are listed in Table 3. From Table 3, we can find that the difference of the daily average K value compared to it of the previous day was less than 5% in the last 3 measurements, so the measured K value is the average of the last 4 daily average K values and the test result is 0.447 W/m^{2}K.

4.1.2. Theoretical Calculation Value. As is described in Section 2.1, the bamboo steel composite walls are made of multi-layer materials, which is shown in Figure 4.

According to the design code [27], the thermal resistance of a single material can be defined as $R_i = \delta_i/\lambda_i$. Thermal resistance of multi-layer enclosure structure is calculated as $R = R_1 + R_2 + R_3 + \cdots + R_n$. The thickness and thermal conductivity of each material are shown in Table 4. The mineral

Table 2: Setting items of building models.

Setting items	Value	
Purpose	Verification	Energy performance
Location	Ningbo	Harbin, Beijing, Shanghai, Guangzhou
Area of building	24 m^2	
Building envelope	Wall1 + Roof1 + Floor	Wall1 + Roof1 + Floor, Wall2 + Roof2 + Floor
Window-to-wall ratio	North wall: 0.24, south wall: 0.31, west and east wall: 0	
Air condition	Temperature: 18°C Run time: 2016/1/26–2016/1/30	Temperature: 16°C (winter), 26°C (summer) Run time: whole year
Weather condition	Measured	Typical meteorological year
Miscellaneous loads	0	4.3 W/m^2

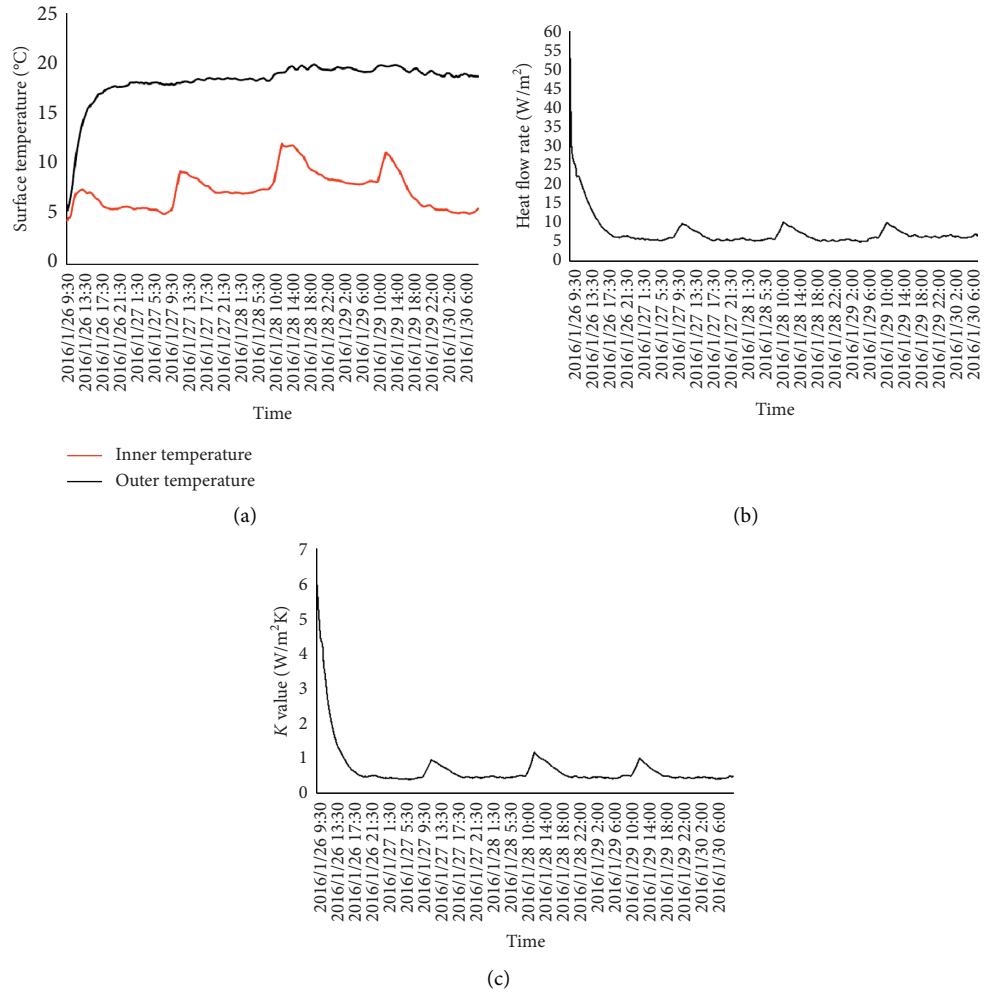

Figure 9: Field test results of K value during winter. (a) Average temperature of inner and outer surface wall. (b) Test result of heat flux rate. (c) Calculated K value during the measurements.

wool and polystyrene board employed as heat insulating material of wall will sink during the service stage, so the thermal conductivity should be modified. The correction factor of mineral wool and polystyrene board is 1.2 and 1.1, respectively, which is shown in Table 4.

The calculative processes of the thermal resistance of bamboo steel composite wall are listed in Table 4. The total thermal resistance of composite wall is 2.216 m^2K/W according to the table. Thus, the K value of the composite wall can be calculated by equation (2) and the theoretical result is 0.423 W/m^2K.

4.1.3. Comparison of K Value. The theoretical calculation and measured K values of the bamboo steel composite wall are listed, respectively, in Table 5. It can be found that the

Table 3: Comparison of the daily average K values.

Date	1/26	1/27	1/28	1/29	1/30
Daily average (W/m^2K)	0.485	0.443	0.460	0.443	0.440
Difference (%)	—	8.82	3.99	3.74	0.66
Measurement K value (W/m^2K)			0.447		

Table 4: Calculative processes of thermal resistance.

Building member	Materials	δ (m)	λ (W/mK)	Correction factor	R (m^2K/W)
Bamboo steel composite wall (wall1)	Cement mortar	0.015	0.93	—	0.016
	Polystyrene board	0.02	0.042	1.1	0.433
	Bamboo plywood	0.01	0.17	—	0.059
	C-type steel	0.001	58.2	—	0.000
	Mineral wool	0.098	0.05	1.2	1.633
	C-type steel	0.001	58.2	—	0.000
	Bamboo plywood	0.01	0.17	—	0.059
	Cement mortar	0.015	0.93	—	0.016
Total					2.216

Note. The thermal resistance of C-type steel can be neglected due to the thin thickness and high thermal conductivity.

Table 5: Comparison among theoretical value and measured value and standard limit value.

Items	K value (W/m^2K)
Measurement value	0.447
Theoretical calculation value	0.423
The standard limit value [24]	1.5

Table 6: Reads of the electric meter.

Items	Value (kWh)
Initial reading of electric meter	35.4
Final reading of electric meter	47.2
Energy consumption	11.8

calculation value matched well with the measurement value and the relative error is about 5%.

The comparison results show that the heat flux meter method is suitable for the field test of K value. Both the measurement value and theoretical calculation value are less than the limit value which indicates that the composite walls have an excellent thermal performance and can satisfy the requirement of the standard.

4.2. Energy Performance

4.2.1. Verification of the Simulation Model. As is described in Section 3.2, the air condition in testing building was adopted to keep the indoor temperature. The energy consumption of building was recorded by the electric meter. The reads of the electric meter are listed in Table 6, and the energy consumption based on measurement is 11.8 kWh according to Table 6. Then, the simulation model based on the testing building was conducted to verify the validity of the model. The simulated result was 10.52 kWh, which is a little lower than the test result by 10.8%. Because the heating performance (COP) of the air condition changes with outdoor conditions, there is an acceptable difference between simulated and measured heating energy consumption. Therefore, the proposed simulation model to analyse energy performance of the composite wall in different climate regions is verified.

4.2.2. Parametric Analysis. The annual energy consumption of the two walls in different climate regions are illustrated in Figure 10.

According to the simulation result in Figure 10, the energy consumption in different climate regions was different. Guangzhou had the lowest energy consumption among the four typical cities. That is because the average annual temperature is close to the setting temperature of air condition. Buildings in Shanghai consumed both heating and cooling energy due to the hot summer and cold winter climate feature, but the total consumption is lower than Beijing and Harbin. Both Beijing and Harbin consumed heating energy while demanding little cooling energy.

Due to the lower K value, Wall1 had the better heating energy performance than wall2. The heating energy consumption of wall1 was lower than that of wall2 by 30.18%, 37.48%, 33.3%, and 32.03% in the four cities (namely, Guangzhou, Shanghai, Beijing, and Harbin), respectively.

For the cooling energy demand in Guangzhou, Shanghai, and Beijing, wall1 had the better performance than wall2 with the improvement of 36.22%, 37.57%, and 28.36%, respectively. This is due to the fact that wall1 with lower K value can prevent heat energy from passing through the wall more effectively. However, the cooling energy consumption of wall1 is larger than that of wall2 in Harbin. That is because the typical summer temperature of Harbin used in the simulation merely exceeded 26°C; the heat energy was generated by the equipment in the room. The heat energy cannot be dissipated easily due to the lower K value of Wall1. Thus, the cooling energy was demanded more in wall1.

For the total energy demand, the consumption of wall1 was lower than that of wall2 by 35.93%, 37.51%, 32.75%, and 31.71%, respectively, which showed that the bamboo steel composite walls had the potential to be employed as building envelope in China.

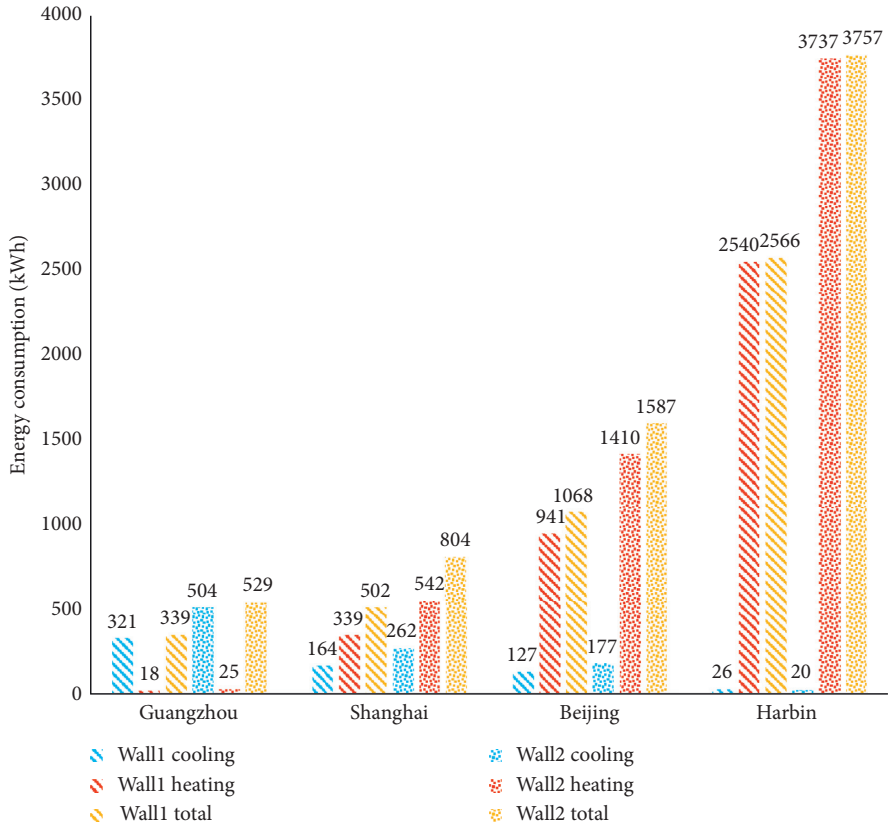

Figure 10: Comparison of annual energy consumption of the two walls in four cities.

5. Conclusion

In this paper, the thermal performance of a novel bamboo steel composite wall was experimentally investigated and numerically simulated. The key conclusions based on the analysis are summarized as follows:

(1) In the field test, the heat transfer method was employed to measure the heat transfer coefficient (K value) of the wall. The measurement value was less than the limit value, which indicated that the composite walls had an excellent thermal performance and could satisfy the requirement of the standard.

(2) A theoretical formula for K value of the bamboo steel composite wall was presented and the calculation value matched well with the measurement value.

(3) The validity of the simulation model was verified through the field test; then, the proposed model was adopted to analyse the energy performance of the composite wall. The simulation result indicated that the composite walls had better energy performance compared with reinforced concrete wall and could be employed as building envelope in China.

Data Availability

The data used to support the findings of this study are available from the corresponding author upon request.

Conflicts of Interest

The authors declare that there are no conflicts of interest regarding the publication of this paper.

Acknowledgments

The authors gratefully acknowledge the financial support provided by the National Key R&D Program of China (2019YFD1101002), the National Natural Science Foundation of China (NSFC) (51678310 and 51978345), and Ningbo Science and Technology Project (202002N3090).

References

[1] K. D. Flander and R. Rovers, "One laminated bamboo-frame house per hectare per year," *Construction and Building Materials*, vol. 23, no. 1, pp. 210–218, 2009.

[2] J. Li, "Towards a low-carbon future in China's building sector—a review of energy and climate models forecast," *Energy Policy*, vol. 36, no. 5, pp. 1736–1747, 2008.

[3] P. van der Lugt, A. A. J. F. van den Dobbelsteen, and J. J. A. Janssen, "An environmental, economic and practical assessment of bamboo as a building material for supporting structures," *Construction and Building Materials*, vol. 20, no. 9, pp. 648–656, 2006.

[4] X. Sun, M. He, and Z. Li, "Novel engineered wood and bamboo composites for structural applications: state-of-art of manufacturing technology and mechanical performance evaluation," *Construction and Building Materials*, vol. 249, Article ID 118751, 2020.

[5] D. U. Shah, M. C. D. Bock, H. Mulligan, and M. H. Ramage, "Thermal conductivity of engineered bamboo composites," *Journal of Materials Science*, vol. 51, no. 6, pp. 2991–3002, 2016.

[6] H. Takagi, S. Kako, K. Kusano, and A. Ousaka, "Thermal conductivity of PLA-bamboo fiber composites," *Advanced Composite Materials*, vol. 16, no. 4, pp. 377–384, 2007.

[7] L. L. Xiang, N. P. Li, Z. Chen, and X. W. Chen, "Research of thermal and moisture transport within compound bamboo wall with different moisture content," *Key Engineering Materials*, vol. 517, pp. 887–891, 2012.

[8] F. F. Risnandar and S. Wonorahardjo, "Thermal performance of plastered bamboo-wall," *KnE Social Sciences*, vol. 3, no. 21, pp. 284–296, 2019.

[9] J. S. Wang, C. Demartino, Y. Xiao, and Y. Y. Li, "Thermal insulation performance of bamboo- and wood-based shear walls in light-frame buildings," *Energy and Buildings*, vol. 168, pp. 167–179, 2018.

[10] A. Zhou and Y. Bian, "Experimental study on the flexural performance of parallel strand bamboo beams," *The Scientific World Journal*, vol. 2014, Article ID 181627, 6 pages, 2014.

[11] J. Lei, B. Chen, and P. Yuan, "Experimental study on flexural properties of side-pressure laminated bamboo beams," *Advances in Civil Engineering*, vol. 2020, Article ID 5629635, 10 pages, 2020.

[12] V. De Luca and C. Marano, "Prestressed glulam timbers reinforced with steel bars," *Construction and Building Materials*, vol. 30, pp. 206–217, 2012.

[13] Y. Wei, M. Zhou, and D. Chen, "Flexural behaviour of glulam bamboo beams reinforced with near-surface mounted steel bars," *Materials Research Innovations*, vol. 19, no. 1, pp. S1–S103, 2015.

[14] Y. Wei, X. Ji, M. Duan, and G. Li, "Flexural performance of bamboo scrimber beams strengthened with fiber-reinforced polymer," *Construction and Building Materials*, vol. 142, pp. 66–82, 2017.

[15] Y.-F. Li, Y.-M. Xie, and M.-J. Tsai, "Enhancement of the flexural performance of retrofitted wood beams using CFRP composite sheets," *Construction and Building Materials*, vol. 23, no. 1, pp. 411–422, 2009.

[16] Y. Nadir, P. Nagarajan, M. Ameen, and M. Arif, "Flexural stiffness and strength enhancement of horizontally glued laminated wood beams with GFRP and CFRP composite sheets," *Construction and Building Materials*, vol. 112, pp. 547–555, 2016.

[17] H. Fang, X. Xu, W. Liu et al., "Flexural behavior of composite concrete slabs reinforced by FRP grid facesheets," *Composites Part B: Engineering*, vol. 92, pp. 46–62, 2016.

[18] Q. Lv, W. Wang, and Y. Liu, "Flexural performance of cross-laminated bamboo (CLB) slabs and CFRP grid composite CLB slabs," *Advances in Civil Engineering*, vol. 2019, Article ID 6980782, 17 pages, 2019.

[19] T. Liu, Y. Li, K. Xu et al., "Research on mechanical performance of steel-bamboo composite box short column," *Industrial Construction*, vol. 46, no. 1, pp. 25–29, 2016.

[20] Y. Li, H. Shen, W. Shan et al., "Experimental study on shear behavior of I-shaped section bamboo-steel composite beams," *Journal of Building Structures*, vol. 32, no. 7, pp. 80–86, 2011.

[21] Y. Li, W. Shan, Z. Huang et al., "Experimental study on mechanical behavior of profiled steel sheet-bamboo plywood composite slabs," *Journal of Building Structures*, vol. 29, no. 1, pp. 96–102, 2008.

[22] Y. Li, H. Shen, W. Shan, and T. Han, "Flexural behavior of lightweight bamboo-steel composite slabs," *Thin-Walled Structures*, vol. 53, pp. 83–90, 2012.

[23] Y. Li, J. Guo, T. Jiang et al., "Experimental study on seismic behavior of cold-formed Thin-walled C steel-bamboo plywood composite walls," *Journal of Shenyang Jianzhu University (Natural Science)*, vol. 29, no. 6, pp. 969–976, 2013.

[24] Engineering Construction Standard of Zhejiang Province, *Design Standard for Energy Efficiency of Residential Buildings (DB33/1015-2015)*, China Planning Press, Beijing, China, 2015.

[25] China National Standard, *Test Standard for Overall Heat Transfer Coefficient of Building Envelope and Heat Supply for Space Heating (GB/T23483-2009)*, Standards Press of China, Beijing, China, 2009.

[26] China Industrial Standard, *Standard for Energy Efficiency Test of Residential Buildings (JGJ/T 132-2009)*, China Architecture & Building Press, Beijing, China, 2010.

[27] China National Standard, *Code for Thermal Design of Civil Building (GB 50176-2016)*, China Architecture & Building Press, Beijing, China, 2016.